UNIVERSITAT DE BARCELONA

The physics of rotational atomic and photonic quantum fluids

Albert Gallemí Camacho

The physics of rotational atomic and photonic quantum fluids

Albert Gallemí Camacho

PhD Thesis

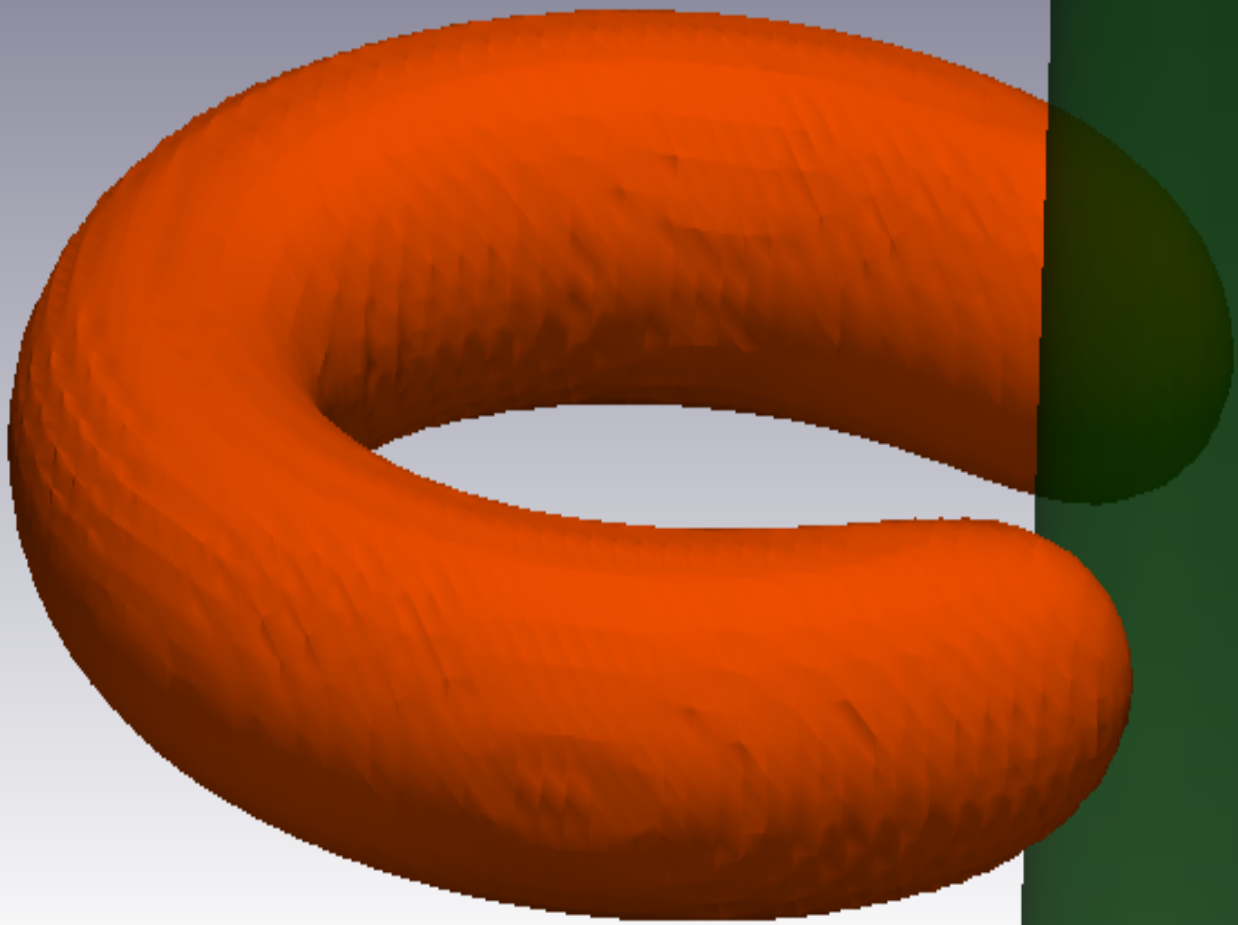

Universitat de Barcelona

Programa de doctorat en Nanociències

PhD program in Nanoscience

Tesi doctoral

PhD Thesis

The physics of rotational atomic and photonic quantum fluids

Albert Gallemí Camacho

Directors de la tesi:
Montserrat Guilleumas Morell
Ricardo Mayol Sánchez

Tutor de la tesi:
Martí Pi Pericay

Universitat de Barcelona

Abril de 2017

Outline

List of Figures

List of Tables

Agraïments

Abans d'entrar en matèria, hi ha certa gent a qui he d'agrair el camí que ha suposat la confecció d'aquesta tesi. Primer de tot, he d'agrair als meus directors de tesi, la Muntsa Guilleumas i en Ricardo Mayol, als quals conec des de ja fa ben bé una dècada, haver compartit amb mi tots aquests anys de viatge que ha suposat la tesi. Sobretot per haver-me ensenyat, ja no només a introduir-me en un camp de la física apassionant, si no per ajudar-me a madurar com a científic i com a persona. També els vull agrair la gran quantitat d'hores dedicades a la tesi, i l'amistat que m'han concedit ja des del primer moment. Dintre del mateix grup, també vull agrair maques discusions que he pogut tenir amb en Martí Pi i en Manel Barranco, els quals sempre em van donar el seu ajut quan el vaig necessitar.

De manera especial, hi ha un company de fatigues que m'ha acompanyat durant una part de la tesi, ja no només com a col·loborador, si no com a company de despatx i amic: l'Antonio Muñoz. La seva contribució a la tesi ha estat tan determinant com per a reorientar-la cap a un camp que originalment en el grup desconeixia. Per tot això, i les converses que hem mantingut sobre qualsevol tema que se'ns acudia, ja sigui sobre física o no, moltes gràcies! Hi ha altres persones tant de la Universitat de Barcelona com la Universitat Autònoma de Barcelona, amb qui he col·laborat, i a qui vull donar les gràcies per tot el que m'han ensenyat i ajudat: l'Anna Sanpera, l'Artur Polls, el Bruno Juliá i el Joan Martorell.

També m'agradaria agrair a tota la gent amb qui he compartit despatx en tots aquests anys: la Carla Marín, el Vicente Rives, l'Arianna Carbone, l'Antonio Leal, l'Antonio Muñoz, la Clàudia Gonzàlez i l'Albert Escrivà. Sobretot els Antonios i la Clàudia, els meus companys de despatx més longeus, i amb qui he compartit converses sobre política d'allò més interessants.

I would like to acknowledge also the members of the Laboratoire de Physique et Modélisation des Milieux Condensés, in Grenoble, and specially Anna Minguzzi and Maxime Richard for the nice hospitality that I received there during the first months of 2016. Also the PhDs and postdocs that I met there, who embraced me from the first day: Katharina Rojan, Eiji Kawasaki, Guillaume Lang, Malo Tarpin, Natalia Matveeva, José María Escalante, Ivan Khaymovich...

A més a més, voldria donar les gràcies als amics que m'han acompanyat en tots aquests anys: en Joan, l'Isabel, en Frede, en Lluís, l'Anna, la Judit, en Roger, en Genís, en Ricard, en Xavi, i altra gent amb qui he interaccionat de manera més esporàdica, però amb converses precioses, com l'Adrià, l'Eli, l'Edu, i companys de passadís, com en Dani, l'Albert i en Pere. Finalment, gent amb qui he coincidit en congressos i amb qui he passat grans estones: Guillem Ferré, Joan Polo, Mariona Moreno, Marta Abad, Yun Li, Pedro Nevado, Davit Aghamalyan, Tomasso Comparin... També he d'agrair companys amb qui he fet teatre durant tots aquests anys, de La Inestable de Bellaterra, Helena Teatre i Cloteatre.

Finalment, també vull agrair a la meva família, el suport que m'han donat durant tots aquests anys.

Aquesta tesi ha estat possible gràcies a una beca FI de la Generalitat de Catalunya que vaig gaudir durant sis mesos, i una FPU del Ministerio de Educación, Cultura y Deporte, que vaig gaudir durant tres anys.

Resum / Abstract

En aquesta tesi estudiarem fenòmens relacionats amb la superfluïdesa de sistemes atòmics i fotònics condensats, a través de la manipulació d'estats rotacionals, com poden ser vòrtexs i corrents persistents. Estudiarem condensats de Bose-Einstein tant en sistemes fortament correlacionats, on models basats en la segona quantització com el model de Bose-Hubbard seran necessaris per a estudiar aquest tipus de sistemes, com en sistemes feblement interactuants, on les aproximacions de camp mig resultaran prou acurades, i on el sistema pot ser descrit per l'equació de Gross-Pitaevskii.

Començarem amb l'anàlisi de les propietats fonamentals de sistemes de gasos bosònics atrapats en xarxes constituïdes per pocs pous. Per exemple, el diagrama de fases, les fraccions condensades, i l'entrellaçament. Pel que respecta a les fases, estudiarem les propietats de les transicions entre aquestes, i en particular, els exponents crítics que les caracteritzen.

Més endavant, adaptarem la geometria del sistema com un sistema de pous formant un anell, i estudiarem l'efecte de manipular la junció que uneix dos d'ells. Aquest tipus d'unió manipulable és el que s'anomena *weak link*, i analitzarem què succeeix en l'aproximació de camp mig, en comparació amb el cas fortament correlacionat. En tots dos casos observarem que el *weak link* resulta ser un element crucial en el sistema, per a realitzar superposicions d'estats de corrent. A més a més, en el cas de camp mig, podrem identificar una barrera energètica que separa els dos estats de corrent, on hi habiten estats de tipus solitònic, és a dir, estats caracteritzats per la presència de singularitats topològiques. Aquesta barrera serà la causant de la presència d'un cicle d'histèresi, en processos de trànsit entre diferents corbes de corrent, anomenats *phase slips*.

A continuació, estudiarem el cas de dues components d'un condensat de Bose-Einstein acoblades de manera coherent i atrapades en un potencial de tipus toroidal. Veurem que quan imprimim un corrent persistent en una de les components, hi ha una transferència de moment angular entre les dues components. Aquesta transferència pot ser identificada com esdeveniments de tipus *phase slip*. Investigarem com aquests sistemes són prou robusts com per a fer-se servir com *qubits*, donat que els estats de corrent són menys fràgils.

En condensats de dues components acoblades de manera coherent, és possible trobar un tipus d'estat solitònic anomenat *Josephson vortex*. Aquest estat ve caracteritzat per una depressió de densitat entorn d'un punt on les corrents són no nul·les. A més a més, aquests estats són energèticament més favorables que els estats de tipus *dark soliton*, els quals es diferencien en el fet de que no presenten corrents. En el cas en el qual afegim acoblament de tipus spí-òrbita en el sistema, els estats de tipus *dark soliton* ja no són possibles, i només es poden trobar estats de tipus *Josephson vortex*. En aquesta tesi veurem que aquests estats decauen a causa d'excitacions transversals, produint parelles de vòrtex-antivòrtex, llur evolució dinàmica dependrà de la orien-

tació inicial del *Josephson vortex*.

Per acabar, concluïrem l'estudi en el camp de condensats de polaritons, els quals són quasi-partícules producte de l'acoblament de fotons i excitons (que són acoblaments electró-forat) en cavitats semiconductores. Els polaritons poden formar un condensat de Bose-Einstein fora d'equilibri, degut a la curta vida dels polaritons. A més a més, poden ser descrits per una equació de tipus Gross-Pitaevskii però per a dues components, donades les components de polarització inherent de la naturalesa fotònica dels polaritons. Les cavitats on es formen aquests condensats generen un acoblament de tipus espín-òrbita entre les dues components, que permet acoblar estats de diferent moment angular entre les dues components. Això dóna lloc a un fenomen de conversió de moment angular d'espín en moment angular orbital que estudiarem en polaritons confinats en forma d'anell, i finalment provarem la superfluïdesa dels condensats polaritònics, analitzant la resposta dels corrents generats davant la presència de desordre.

♠ ♠ ♠

In this thesis, we will study the superfluidity of condensed atomic and photonic systems, through the manipulation of rotational states, such as vortices or persistent currents. We will study Bose-Einstein condensates both in the strongly-correlated regime, where models based on second quantization, like Bose-Hubbard model, will be required; and in weakly-interacting systems, where mean-field approximations will be accurate enough, and the system is described by means of the Gross-Pitaevskii equation.

We will start with the analysis of the fundamental properties of Bose gases trapped in few-site lattices, such as the phase diagram, the condensed fractions and the entanglement. Concerning the phases, we will study the properties of the transitions between them and, in particular, their characteristic critical exponents.

Afterwards, we will consider the sites of a lattice constituting a ring geometry and study the effect of manipulating the tunnelling rate between two of the wells. This kind of tunable link is called *weak link*, and we will analyze what happens in the mean-field approximation, in comparison with the strongly-correlated case. In both regimes we will observe that the weak link behaves as a key element in the system in order to generate superpositions of flow states. Moreover, in the mean-field case, we can identify an energy barrier that separates two current states (also known as *winding number states*), where solitonic states, i.e. states characterized by the presence of topological singularities, live. Such a barrier will be the origin of the appearance of a hysteresis cicle in processes of transfer between different winding number curves, called *phase slips*.

After that, we will study two coherently-coupled components of a toroidally-trapped Bose-Einstein condensate. We will see that when we imprint a persistent current in one of the components, there is an angular momentum transfer between both components. This transfer can be identified as a phase slip event, and the tunability of the system allows it to behave as a robust *qubit*, due to the fact that states supported by currents are less fragile.

In two-component condensates, it is possible to find a particular solitonic state called *Josephson vortex*. This state is characterized by a density depletion around a point with nonzero currents. Moreover, these states are energetically more favourable than dark soliton states, whose

main difference with respect to Josephson vortices is the fact that dark solitons do not present currents. However, when spin-orbit coupling is added, dark soliton states are no longer possible, but Josephson vortices persist. In this thesis, we will see that these states decay through transversal excitations (i.e. *snake instability*), producing vortex-antivortex pairs, and their subsequent dynamical evolution depends on the initial orientation of the Josephson vortex.

Finally, we will move to the field of polariton condensates. Polaritons are quasiparticles product of the coupling between photons and excitons (which are electron-hole excitations) in semiconductor microcavities. These particles can constitute an out-of-equilibrium (due to the short lifetime of polaritons) Bose-Einstein condensate described by the Gross-Pitaevskii-like equation for two components, because of the two polarization components inherent to the photonic nature of polaritons. The cavities where these condensates are created generate a spin-orbit coupling between the two polariton components, in such a way that current states with different orbital angular momentum are coupled. This yields to a phenomenon of spin-to-orbital angular momentum conversion that we will study in ring-trapped polariton condensates. At the end of this thesis, we will probe the superfluid properties of polariton condensates, by analyzing the response of the generated currents against the presence of disorder.

Chapter 1

Introduction

Superfluidity and superconductivity have become an intensive field of research in many-body quantum systems since their first experimental evidences in the laboratories. The main feature that characterizes these phenomena is that particles can flow without dissipation or resistance. For this reason, the study of the fundamentals of the superfluidity and superconductivity have been pointed out as a key point in order to develop future technological applications. Remarkably, in the recent years, it has been possible to build superconducting quantum interference devices [Jak64, Jak65] (also known as SQUIDs), by constructing a quantum state as a macroscopic quantum superposition of two counterpropagating current flows by using Josephson junctions.

In order to reach a superfluid phase, a quantum fluid must be cooled down below a certain temperature, which, in the early years, was assumed to be the temperature needed to reach Bose-Einstein condensation in the system. This phenomenon is achieved when a dilute gas of bosons is driven to quantum degeneracy at ultralow temperatures, of the order of tens or hundreds of nanoKelvins. When the system is cooled, the thermal de Broglie wave length of the different particles increases and, at some point, when the temperature reaches the critical temperature for condensation, the wave lengths become of the same order of the size of the system itself. Therefore, the wave packets associated to each particle overlap, enhancing the quantum coherence. Below this temperature, the particles that constitute the system macroscopically occupy the single-particle ground state, and the condensate behaves as a single particle itself. This effect was predicted by Satyendra N. Bose and Albert Einstein, who discovered that for very low temperatures the occupation number of the ground state of a bosonic system diverges (macroscopic occupation of the ground state, Bose-Einstein condensation).

The first time that Bose-Einstein condensation was achieved was in the experiment of Kammerling-Onnes in 1911, when Helium was liquefied until reaching superfluidity. However, only a small fraction of the fluid exhibited properties of a Bose-Einstein condensate. Several decades of development of cooling techniques were required in order to finally achieve almost-full condensation in 1995. It was possible with a gas of ^{87}Rb at the University of Colorado and a gas of ^{23}Na atoms at the Massachussets Institute of Technology. These results were worth the Nobel Prize in Physics 2001 to Eric A. Cornell, Wolfgang Ketterle and Carl E. Wieman in 2001 *for the achievement of Bose-Einstein condensation in dilute gases of alkali atoms, and for early fundamental studies of the properties of the condensates* [And95, Dav95]. The first atoms candidates to be condensed were alkali atoms since their atomic structure was appropriate for optical cooling.

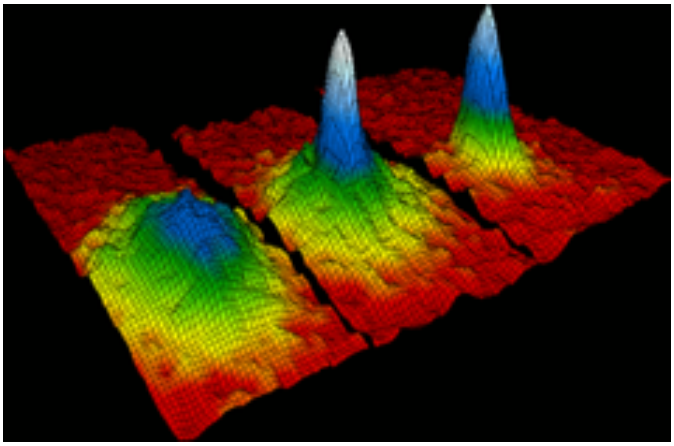

Figure 1.1: Experimental momentum distribution for three different values of the temperature. From left to right: $T > T_c$, $T \sim T_c$ and $T < T_c$, where T_c is the critical temperature for condensation. From Ref. [Cor96].

In those systems, by means of the cooling procedure: Doppler cooling, Magneto-Optical Trap, evaporative cooling; the temperature was reduced from the *room* temperature (300 K) to the nanoKelvin scale in few seconds. When the system is at a temperature above the critical point for condensation, quantum degeneracy is still not achieved, and the momentum distribution of the cloud follows Maxwell-Boltzmann statistics (broad gaussian). When the temperature is below the critical one, the momentum distribution follows the geometry of the trap. In the case of a harmonic trap, and in the noninteracting case, the distribution is a gaussian, but narrower than the classical Maxwell-Boltzmann distribution. In the intermediate temperatures, both regimes coexist (Bose-Einstein and Maxwell-Boltzmann), and the momentum distribution is bimodal (both thermal and condensed atoms can be encountered in the bulk of the atomic cloud). Figure 1.1 shows the experimental momentum distribution for three different values of the temperature: $T > T_c$, $T \sim T_c$ and $T < T_c$, from left to right. In the first case, the distribution is gaussian and broad, following the Maxwell-Boltzmann distribution. In the second case, the distribution is a superposition of two gaussians, the one corresponding to noncondensed atoms (classical) and the one corresponding the condensed atoms (quantum). In the last case, a single peak appears again, narrower than in the high temperature case, following the geometry of the trap. This is a clear signature of Bose-Einstein condensation.

It has been shown that under certain conditions, Bose-Einstein condensates clearly manifest superfluid phenomena, although condensation is not an actual requirement for exhibiting superfluidity. A clear manifestation of superfluid behaviour is the possibility to excite rotational quantized vortices [Fet01, Mat99] and persistent currents in a quantum fluid. Liquid Helium and atomic and photonic Bose-Einstein condensates are examples of quantum systems that can exhibit superfluid properties. Hence, the study of rotational states in quantum fluids has become an important tool in order to probe the superfluidity of such systems. Rotating quantum fluids are good constituents for building quantum devices for technological applications. For instance, superfluid liquid helium [Per97, Sim01] or atomic Bose-Einstein condensates can emulate the same physics that can be encountered in SQUIDs. For the particular case of atomic condensates, it has become popular the name of atromtronic quantum interference devices (AQUIDs) in order to label the atomic analog of SQUIDs [Sea07]. Unfortunately, nowadays, the relation between superfluidity and condensation is still not fully understood, since superfluidity seems to be related to the interactions, rather than the coherence between the particles in the system.

Atomic Bose-Einstein condensates must be very dilute systems, in order to prevent three-body recombination, which destroys the condensate. However, despite this diluteness, two-body collisions are processes that can not be neglected, but they can be very well approximated in terms of the s-wave scattering length a_s, which quantifies the strength of two-body collisions at first order (s-wave). The scattering length is a quantity that can be experimentally tuned by using Feshbach resonances. Such resonances can be performed by using an external uniform magnetic field that shifts the energy levels of different states corresponding to the different hyperfine levels by Zeeman effect, in such a way that the energy of a level in a closed chanel (a potential of a hyperfine state that bounds an atom) coincides with the energy of a level in an open chanel (a potential of a hyperfine state that does not bound an atom). At those values of the magnetic field at which this resonance occurs, the value of the scattering length diverges, and therefore, close to the resonance, the two-body collisional rate can be *freely* tuned, imposing no restrictions on the value of the scattering length. One must be aware, however, of losses, since a very large scattering length increases three-body recombination, which destroys the condensate.

In terms of the strength of the interaction, there are two main frameworks that can be used to describe a bosonic gas. In weakly-interacting systems, the mean-field theory provides a good description. In particular, when two-body interactions can be approximated by a contact-interaction term, it is possible to solve the Gross-Pitaevskii equation, whose result is the condensate wave function, or order parameter. This equation is a Schrödinger-like equation with a nonlinear term that precisely accounts for contact interactions. In contrast, for large interactions, the system enters the strongly correlated regime, and the mean-field theory does not properly describe the system. In this case, the Bose-Hubbard model is more suitable, since it considers atoms as individual particles that occupy the different modes that constitute the whole system. This model has been widely used in order to study systems confined in lattices, by identifying the lattice sites as the modes in the Bose-Hubbard model. This kind of geometrical setups can be engineered by using counterpropagating laser beams. Configurations that have been used in order to generate lattices are displayed in the left panels of Fig. 1.2, for a 2D (a) and a 3D (b) lattice.

The Bose-Hubbard model is built in second quantization, in terms of creation and annihilation operators that become the elemental blocks to construct a system where particles can hope from mode to mode and increase the interaction energy when two particles coincide in the same mode[1]. This yields to a hamiltonian that can be written in terms of a matrix that has to be diagonalized. It provides the eigenenergies and the corresponding eigenstates, of the system. This allows to draw a phase diagram as a function of the parameters of the model, which in its simplest version are the tunnelling rate, usually denoted by J, and the on-site interaction, commonly labeled by U. The Bose-Hubbard model is suitable to study the quantum phase transitions between the different phases that constitute the phase diagram, and analyze several magnitudes, like fragmentation, entanglement, and critical exponents.

In the limit of weak interactions, the Gross-Pitaevskii hamiltonian contains a kinetic and a potential term, as the Schrödinger hamiltonian, but with a new nonlinear term, which is cubic in the condensate wave function, and accounts for interactions. Its strength is given by a parameter g proportional to the scattering length a_s. This equation, being nonlinear, possesses not only

[1]This model can also account for long-range or intermode interactions. In this case, the model is said to be extended (Bose-Hubbard model). An example of long-range interaction is the dipolar interaction, which will be introduced in Sect. 6.1.

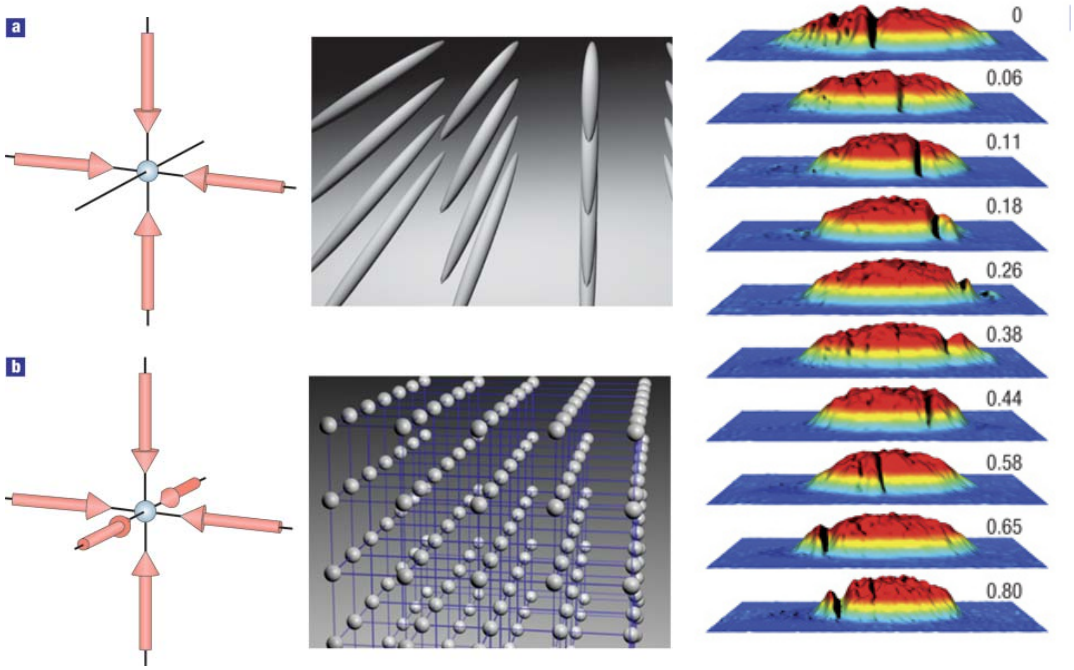

Figure 1.2: The left and middle panels show the laser beam configuration needed in order to create a 2D lattice (a) and a 3D lattice (b). From Ref. [Blo08]. The right panel shows the experimental spatial oscillation in time (in units of the oscillation period) of a dark soliton imprinted in a Bose-Einstein condensate. From Ref. [Bec08].

a single family of solutions, but an infinite number of them. The Gross-Pitaevskii equation has been used to study not only systems with a single condensed component, but more than one, which can correspond to a mixture of several condensed atoms (atomic mixture), or different isotopes of the same atom (isotopic mixture), or the different hyperfine levels of the same atom (spinor condensate). In the latter case, the different components can be identified as different (pseudo)spin components of the atom, and atoms populating one of components can flip their spin (keeping the total spin constant), producing an exchange of particles between components.

For the particular case of two hyperfine levels involved in the effective dynamics of the system, one has a coherently-coupled two-component condensate, whose main features have been deeply studied both from a theoretical [Son02, Aba15] and an experimental point of view. In the mean-field regime, in order to describe both the static and dynamic properties of the two-component condensate, one can still use the Gross-Pitaevskii theory, but with two coupled Gross-Pitaevskii equations, each of them associated to each component of the condensate. Both equations are coupled via two terms. The first term is a nonlinear term that accounts for contact (intercomponent) interaction between particles corresponding to a different hyperfine level. The second term allows exchange of particles between both components, which is modulated by a Raman process that leads to a Rabi coupling between the condensates.

Among the different possible solutions of the Gross-Pitaevskii equation, there are few of them that are characterized by a nontrivial phase pattern produced by the presence of singularities

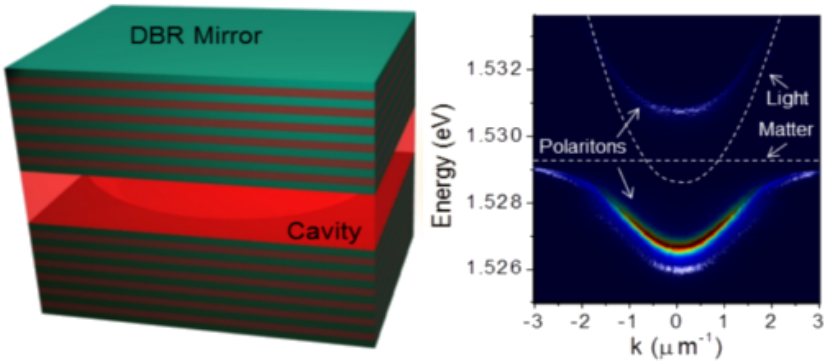

Figure 1.3: The left panel shows a sketch of a semiconductor microcavity with the two Distributed Bragg Reflectors (DBR) around the quantum well. The right panel shows the dispersion relation of polaritons (both the upper and the lower branch).

in the condensate wave function. As an example, there exist dark solitons, which posses a density depletion, where the phase of the wave function suffers a jump of π when crossing the plane of the depletion. The right panel of Fig. 1.2 shows experimental snapshots of a dark soliton in an elongated condensate, which, after being generated away from the center, oscillates around this position. In multidimensional systems, dark solitons can be unstable against small perturbations. The soliton plane distorts itself through the *snake instability*, and the dark soliton decays into a single vortex or a pair of vortices. These states have an axis (vortex core) where the density vanishes and when going around the previous axis, the phase increases an amount equal to κ times 2π, where κ is an integer number, called winding number, and quantizes the circulation of the vortex. Singly-quantized $\kappa = 1$ vortices are stable, however, when they are multiply-quantized, they decay into κ singly-quantized vortices. However, this effect depends on the geometry. For instance, in multiply-connected geometries, like toroidal traps, (giant) vortices become stable, independently of the winding number, and the state is said to be a persistent current along the torus. These states have been studied in the strongly correlated case [Kol06, Par03, Com14], in the single-component [Ryu07, Mun15] and the two-component [Bea13, Aba14, Aba16, Smy14, Wu15, Gal16c] mean-field case, for atomic condensates, and in superfluid Helium [Rep64]. And also in the present thesis [Mun15, Gal16c].

As mentioned above, the possibility to nucleate excited quantum states with nontrivial topology is a clear signature of superfluidity. In the case of vortices and persistent currents, whose topological structure is characterized by the winding number, it is possible to abruptly change their topology through a dissipative mechanism called *phase slip event*. This effect was first studied in the field of superconductors [Aru08]. Its appearance can be produced due to thermal effects, or quantum effects. It has an analog in atomic superfluids, and the dissipation process is carried out by a single-quantized vortex that crosses the system (entering or leaving it), and subsequently modifying the circulation around a given point in 2π.

Apart from atoms, it is possible to generate Bose-Einstein condensates with other bosonic particles. As an example, Bose-Einstein condensates of photons [Kla10], magnons [Dem06] or polaritons [Kas06], have been achieved in current experimental setups. In the present thesis,

we address the latter case: polaritons. A polariton is a composite bosonic mixture product of the coupling between an exciton (which is a bound state between an electron and a hole in semconductor) and a photon. As a consequence, polaritons exhibit some features which are characteristic of excitons (mass, interaction), and photons (short lifetime, polarization).

In the case of polaritons, condensation exists at high temperature, due to the fact that polaritons have a mass of the order of the electron mass, and therefore, the critical temperature for condensation is of the order of the *room* temperature. Polariton condensates can be experimentally realized in a device called *semiconductor microcavity*. This device is constituted by a quantum well located between two Distributed Bragg Reflectors, which are layered dielectrics, where the layers alternate two different values of the refractive index (see left panel of Fig. 1.3).

The main difference between atomic and polaritonic condensates is the lifetime of the particles that constitute the condensate itself. Whereas atomic condensates are stable for times of the order of the minute, which is several orders of magnitude larger than the characteristic time scale of the system, polaritons survive only for times of the order of the picosecond, of the same order of the characteristic time scale. Hence, one can not consider that polaritonic condensates are at equilibrium, in contrast to atomic condensates, where losses can be neglected. Thus, to overcome the losses, one has to pump the polariton condensate. In the mean-field regime, these features are included in a new version of the Gross-Pitaevskii equation at nonequilibrium, called driven-dissipative Gross-Pitaevskii equation.

Due to the photonic nature, polariton condensates are also characterized by their polarizability. Therefore, a polariton condensate can be described by means of two coherently-coupled driven-dissipative Gross-Pitaevskii equations, following the same formalism of two-component condensates. In this case, each component correspond to an element of the polarization basis, which can be, for instance, horizontal-vertical, or circular left-right. There exists a mechanism that allows to flip the polarization of a photon (due to a precession process [Kav04, Kav05] caused by the energy splitting between the transversal and the longitudinal modes, also known as Transversal Electric-Transversal Magnetic or TE-TM splitting), that induces and effective Rabi coupling between both polarization components. Such a precession, is the responsible for the apperance of spin-orbit coupling between the two components. Rotational properties of polariton condensates under these conditions analyzed in this thesis.

Outline of the thesis

This thesis is structured in five parts. The first part (Chapters 2−4) gives a theoretical introduction to the models that we have used to describe ultracold Bose gases: the Bose-Hubbard model in the strongly correlated regime (Chap. 2), and the Gross-Pitaevskii equation for a single component (Chap. 3) and for two components (Chap. 4) in the mean-field framework. The second part (Chap. 5) presents some properties and results in the Bose-Hubbard model, and its relation with quantum magnetic models. The next part (Chapters 6−8) show results that have been obtained during the thesis concerning topological states and the possibility to nucleate persistent currents. Afterwards, the fourth part of the thesis (Chapter 9) gives an introduction to polariton condensates with TE-TM splitting, and gives the results that have been obtained in the particular case of toroidal trapping. The last part of the thesis (Chapter 10) enumerates the different conclusions that can be extracted, and provides different future perspectives for this work. The information is organized as follows:

In Chapter 2, the main features of Bose gases loaded in optical lattices are presented. We define Bloch functions and Wannier functions in the lattice. From this point, we provide the main steps for the derivation of the Bose-Hubbard hamiltonian in its simplest version, with tunnelling rate and on-site interaction. We briefly comment the main transition that was studied in this hamiltonian: the superfluid-to-Mott insulator transition. After that, we include dipolar interaction, which yields to the extended Bose-Hubbard hamiltonian. Finally, we define the main quantities that can be extracted from this hamiltonian and will be used during the thesis in order to characterize the systems.

Chapter 3 is devoted to the study of single-component Bose-Einstein condensates in the mean-field regime. We derive the Gross-Pitaevskii equation, and other versions of this equation, like the dimensionless, the reduction to lower dimensions, and the inclusion of the rotating frame. After that, we discuss some characteristics of the ground state, and introduce the Thomas-Fermi approximation, which is analytical. Afterwards, we analyze the expression of some excited states that can be encountered in these systems and also possess an analytical solution: vortices and solitons.

In Chapter 4, we present coherently-coupled two-component condensates, and the two coupled Gross-Pitaevskii equations that describe the system in this case. We analyze the ground state properties, and the phase diagram in terms of the miscibility and the polarizability. Then, we introduce in the system Rashba-Dresselhauss spin-orbit coupling, which was first achieved in the experiment of Ref. [Lin11]. Finally, we discuss the phase diagram of the spin-orbit coupled Bose gas in the homogeneous case.

In Chapter 5, we analyze few-site lattices, and in particular, the double-well and the triple-well potential. In the former case, we provide the expression of the effective potential of the system as a function of the population imbalance, and show how this model can be mapped onto a spin model: the Lipkin-Meshkov-Glick hamiltonian. We analyze the scaling with the number of particles of different observables of the system and another magnitude called *Schmidt gap* (see Chap. 2). We extract the critical exponents and compare them with those of the Lipkin-Meshkov-Glick hamiltonian. We also propose a possible way to define a correlation function that gives the proper behavior far from the critical point and at criticality. After that, we focus on four configurations of the extended Bose-Hubbard hamiltonian for a triple-well potential, and analyze the phase diagram and the entanglement. We see that in these configurations, there exist some quantum phase transitions where the Schmidt gap scales with the same critical exponents than in the case of the double well, and therefore, these transitions, and the transition of the double well and the Lipkin-Meshkov-Glick hamiltonian fall in the universality class.

Chapter 6 deals with systems constituted by Bose gases confined in ring geometries with a weak link. The first part of the chapter is devoted to the study of a lattice ring with a tunable link in the strongly correlated regime. We analyze the phase diagram, the excitations and the condensed fractions of the system as a function of the interaction and tunnelling rate in the tunable link. We observe that for a particular value of the tunnelling rate in the link, the ground state is given by a superposition of half-quantized persistent currents. The robustness of such a superposition is characterized in the interacting case. In the second part of the chapter, we study the mean-field case, with a rotating barrier in a toroidal trap. We observe that in these systems, winding number states are coupled by a swallow tail curve that joins winding number states through dark soliton states. Such a barrier is the responsible of the appearance of the hysteresis cycle observed in Ref. [Eck14].

In Chapter 7, we study the physics of toroidally-trapped coherently-coupled two-component condensates. We analyze the transfer of angular momentum between both components when we imprint a persistent current onto one of them. We identify and characterize different dynamical regimes, focusing in particular in one of them, which occurs at large value of the Rabi coupling: Coherent Quantum Phase Slip. In this regime, there is a coherent transfer of vortices between both components, and the system effectively operates as a phase slip junction.

In coherently-coupled two-component condensates there exists a characteristic solitonic solution called Josephson vortex. In Chapter 8 we analyze in detail the physics of Josephson vortices in these systems as a function of the dimensionality of the system, and the presence of spin-orbit coupling. We show that Josephson vortices decay in multidimensional systems by snake instability, as dark solitons. The result of the decay is a vortex dipole, and its subsequent evolution depends on the initial orientation of the Josephson vortex with respect to the direction of the spin-orbit coupling, the interaction constants, and on the strength of the Rabi coupling with respect to the strength of the spin-orbit coupling.

Chapter 9 addresses the polariton condensate case. We introduce the main physics of polaritons, and the equation that describes these condensates: the driven-dissipative Gross-Pitaevskii equation. We show how does spin-orbit coupling appear in these systems, and the main consequences on the steady state of the polariton condensate. We study a particular phenomenon produced by the spin-orbit coupling, called *spin-to-orbital angular momentum conversion*. We implement this phenomenon in the particular geometry of a ring, and show how persistent currents are generated in this case. We study the decay of these currents, as a function of the interaction strength and the disorder in the system, and identify the outcome as a main feature of many-body localization. Thus, this setup results in a good proposal to test the superfluidity of polariton condensates.

Chapter 2

Strongly correlated Bose gases

The realization of optical lattices in experimental setups has allowed to analyze in laboratories the strongly correlated regime of Bose gases. Optical lattices can be engineered in experiments by producing standing waves with two counterpropagating laser beams per dimension. The distance between the nodes in the standing wave scales with the wave length of the laser. The atoms are located in the maxima (minima) of the intensity in the case of a red (blue) detuned laser. The experimental tunability of the atom-atom interaction and the geometry of the optical lattices (like the depth or the distance between maxima) has allowed the exploration and discovery of novel quantum phases of many body systems, predicted by Hubbard [Hub63] and spin models, and visit limiting regimes in quantum gases, like Tonks-Girardeau [Par04, Kin04]. Hubbard models were originally developed to theoretically study the physics of an electronic cloud tightly bound by the atoms of a solid. They can be extended to describe strongly correlated quantum matter at ultralow temperatures, and in particular, the Bose-Hubbard model can properly describe systems with bosonic particles [Lew07, Lew12, Blo08] (and equivalently the Fermi-Hubbard model for fermionic particles).

In the present thesis we will restrict our studies on strongly correlated systems that can be described by the Bose-Hubbard model. This model considers a system constituted by a certain number of atoms distributed in several sites corresponding to the mimima of a potential where atoms can accomodate. It is important to remark that the same model can describe as well atoms that populate different states, corresponding to different quantum labels (as different spin or orbital angular momentum, or excited states in a single site), without requiring any spatial separation. It is common to use the name of "mode" instead of "site" in this latter case. In this thesis, we will generally use the name of "mode", but when referring to lattices we will use both names indistinctly. Once the configuration of sites or modes is properly clarified, the Bose-Hubbard model considers a term that accounts for tunnelling between the sites (in the case of modes tunnelling between modes can account for spin flip transitions, etc.), whose magnitude is quantified by a constant parameter, commonly labelled by J for bosonic systems and t for quantum magnetic models; and another term quantified by the parameter U that describes the two-body interactions in the system.

The superfluid-to-Mott insulator transition, which was experimentally confirmed in Ref. [Gre02], is the paradigmatic quantum phase transition of the Bose-Hubbard model [Fis89]. The superfluid phase appears for weak interactions, and is characterized by the coherence between

all the single-site wave functions in the lattice. In contrast, when the interaction U is much larger than the tunnelling J, the Mott insulator emerges, and the coherence is destroyed, since the boson number in each site gets very well defined.

2.1 Band structure and Wannier functions of an optical lattice

The study of the physics of an electron (or an electronic cloud) in a potential generated by atoms periodically localized constituting a lattice potential, has been widely discussed in solid state physics [Ash76]. Electrons, as quantum particles, obey the Schrödinger equation, which describes the electronic wave function in the given potential. For the case of a bosonic gas, the periodic potential can be engineered with an optical lattice $V_{\text{lat}}(\vec{r})$. Analogously to the electronic system, the band structure of an optical lattice can be obtained by analyzing the Schrödinger equation corresponding to a single boson described by the wave function $\phi(\vec{r})$:

$$-\frac{\hbar^2}{2m}\vec{\nabla}^2\phi(\vec{r}) + V_{\text{lat}}(\vec{r})\phi(\vec{r}) = E\phi(\vec{r})\,. \tag{2.1}$$

The hamiltonian corresponding to an optical lattice is translational invariant, provided the periodicity in $\vec{a}$ of the potential. As a consequence, Bloch theorem guarantees that the wave function has periodicity in $\vec{a}$ too, and $\phi_{\vec{k}}(\vec{r}+\vec{a}) = e^{i\vec{k}\cdot\vec{a}}\phi_{\vec{k}}(\vec{r})$. In the previous expression, $\phi_{\vec{k}}(\vec{r})$ is the eigenfunction corresponding to the eigenvalue $E_{\vec{k}}$ of the hamiltonian, both labelled by the wave vector $\vec{k}$, which defines a quasimomentum in the lattice. One can then rewrite the wave function as $\phi_{\vec{k}}(\vec{r}) = e^{i\vec{k}\cdot\vec{r}}u_{\vec{k}}(\vec{r})$, with $u_{\vec{k}}(\vec{r})$ a function periodic in $\vec{a}$.

The wave functions $\phi_{\vec{k}}(\vec{r})$ (one for each energy level, indexed by n) are known as Bloch functions, which are spatially delocalized, and can be genuinely superposed in order to generate a new set of orthonormal wave functions:

$$\omega(\vec{r}-\vec{r}_i) = \frac{1}{\sqrt{L}}\sum_{\vec{k}} e^{-i\vec{k}\cdot\vec{r}_i}\phi_{\vec{k}}(\vec{r})\,, \tag{2.2}$$

which are called Wannier functions, and are localized on the minima of the lattice $\vec{r}_i$, where i runs over the L lattice sites. Due to this property, they are also referred to as single-site wave functions.

Periodic potentials like optical lattices are well described by sinusoidal potentials $V_{\text{lat}}(\vec{r}) = V_0\sin^2(\vec{k}_0\cdot\vec{r})$, where $|\vec{k}_0| = 2\pi/\lambda$, with λ the wave length of the laser. The increase of the lattice depth V_0 leads to flatter energy bands with an increasing gap between them, and Wannier functions become more localized in the minima of the lattice potential, locally approaching the harmonic oscillator wave function. These features can be observed in Fig. 2.1. Panels a) and b) schematically show the band structure of the optical lattice, corresponding to a small and large lattice depth, respectively. Whereas in the former, the energy levels conserve the quadratic dependence on the momentum, characteristic of the free dispersion, in panel b), the lower bands are almost flat, and the gap between them increases. Panels c) and d) depict characteristic Bloch and Wannier functions (solid blue lines), together with the lattice potential (dashed orange lines). As said before, Bloch functions are periodic and delocalized while Wannier functions are localized

with their maxima in the same position of one of the minima of the lattice potential.

The band structure of the system confined in an optical lattice is very rich. However, the system can be described by considering only the lower-lying states, if the gap between these states and the excited ones, which increases with the lattice depth, is large enough. When this assumption is valid, the system is said to belong to the tight-binding regime, and the Bose-Hubbard model can be simplified by taking into account these states only.

2.2 Bose-Hubbard model

In the previous section, we have studied the physics of a single (bosonic) particle in an optical lattice. When many particles are loaded on the lattice, one has to consider the many-body hamiltonian, which contains the single-particle hamiltonian, and an additional term that accounts for two-body interactions $\mathcal{V}_{\rm int}(\vec{r},\vec{r}\,')$. Then, the many-body hamiltonian of a system of interacting bosonic particles in a lattice potential is:

$$\begin{aligned}\hat{\mathcal{H}} = &\int d\vec{r}\,\hat{\Psi}^\dagger(\vec{r})\left(-\frac{\hbar^2}{2m}\vec{\nabla}^2 + V_{\rm lat}(\vec{r})\right)\hat{\Psi}(\vec{r}) + \\ &+\frac{1}{2}\int d\vec{r}\,d\vec{r}\,'\,\mathcal{V}_{\rm int}(\vec{r},\vec{r}\,')\hat{\Psi}^\dagger(\vec{r})\hat{\Psi}^\dagger(\vec{r}\,')\hat{\Psi}(\vec{r}\,')\hat{\Psi}(\vec{r})\,,\end{aligned} \tag{2.3}$$

where $\hat{\Psi}(\vec{r})$ ($\hat{\Psi}^\dagger(\vec{r})$) is the bosonic field operator annihilating (creating) a boson at position $\vec{r}$. At low temperatures, and when the system is dilute, the two-body term can be approximated by a contact interaction, i.e. $\mathcal{V}_{\rm int}(\vec{r},\vec{r}\,') = g\delta(\vec{r}-\vec{r}\,')$, where g is the coupling constant and it is proportional to the s-wave scattering length a_s ($g = 4\pi\hbar^2 a_s/m$ in 3D, but its expression depends on dimensionality, see Chap. 3 for further details). Writing the field operators as a linear combination of bosonic creation ($\hat{b}^\dagger$) and annihilation ($\hat{b}$) operators modulated by Wannier functions, one gets $\hat{\Psi}^\dagger(\vec{r}) = \sum_{n,l}\omega_n(\vec{r}-\vec{r}_l)\,\hat{b}^\dagger_{n,l}$, where the index n (l) runs over the energy levels (sites of the lattice). When the lattice depth V_0 is large enough, it is valid to describe the system by restricting the problem to the first band only. In this case, one can consider a single band (e.g. the band corresponding to $n = 1$), and therefore, the index that labels the band is no longer necessary and can be dropped from the equation. As a consequence, one can write the Bose-Hubbard hamiltonian as:

$$\hat{\mathcal{H}} = -\sum_{l,l'} J_{l,l'}(\hat{b}^\dagger_l\hat{b}_{l'} + \hat{b}^\dagger_{l'}\hat{b}_l) + \frac{1}{2}\sum_l U_l\hat{n}_l(\hat{n}_l - 1) - \mu\sum_l \hat{n}_l\,, \tag{2.4}$$

where $\hat{n}_l = \hat{b}^\dagger_l\hat{b}_l$ is the particle number operator at position l, and μ is the chemical potential. The parameters

$$J_{l,l'} = -\int d\vec{r}\,\omega^*(\vec{r}+\vec{r}_l)\left(-\frac{\hbar^2}{2m}\vec{\nabla}^2 + V_{\rm lat}(\vec{r})\right)\omega(\vec{r}+\vec{r}_{l'})\,, \tag{2.5}$$

and

$$U_l = g\int d\vec{r}\,|\omega(\vec{r}+\vec{r}_l)|^4\,, \tag{2.6}$$

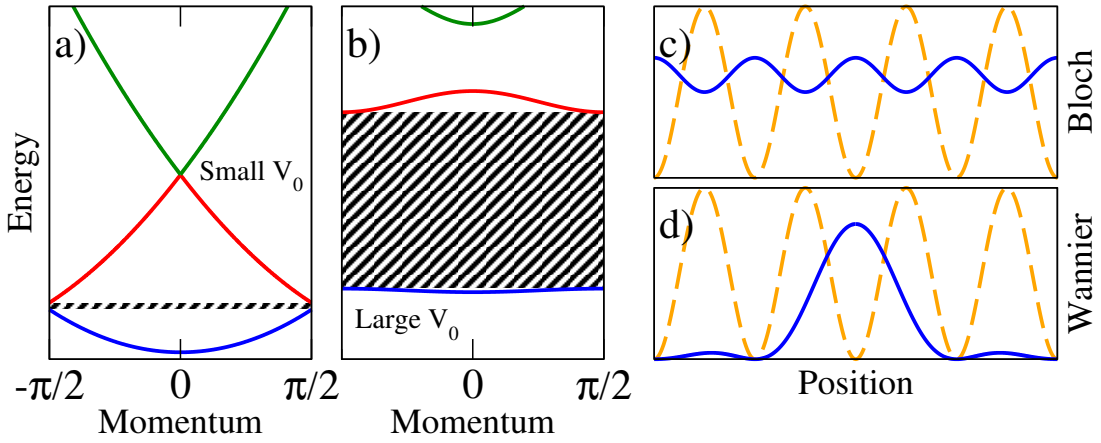

Figure 2.1: Panels a) and b) depict the band structure corresponding to a particle in an optical lattice for small ($V_0 \lesssim E_{\mathrm{Rec}}$) and large lattice depth ($V_0 \gg E_{\mathrm{Rec}}$), where the recoil energy $E_{\mathrm{Rec}} = \hbar^2 k_0^2/2m$. The shadowed region corresponds to the gap. Panel c) schematically shows the shape of a Bloch function (solid blue line) of the corresponding particle in the lattice (dashed orange line), and panel d) the Wannier function (solid blue line) localized in one of the sites of the lattice (dashed orange line).

where $\vec{r}_l$ is a vector that indicates the position of the minima of the lattice potential (the sites), quantify the *tunnelling rate* processes between sites l and l' and the *on-site collision two-body interactions* (in site l) in the system, respectively. It is common to assume that tunnelling appear only at the nearest neighbors sites, in such a way that the tunnelling rate is independent on l and l'. Moreover, if the Wannier functions are independent on the lattice site, the on-site interaction parameter gets independent on l. Unless otherwise stated, these approximations will be used, and these parameters will be considered to be simply J and U. Nevertheless, in Chap. 6, we will see which is the effect of tuning the tunnelling rate between two sites (also known as a weak link).

In addition to the previous approaches, tunnelling terms are also commonly reduced to the case where tunnelling rate is only appreciable in nearest-neighbor sites, in such a way that l and l' correspond to indices labelling neighboring sites. This case occurs when the system can be described within the tight-binding regime, and then the spatial localization of the Wannier functions is high. Under this approach, the Bose-Hubbard model is valid when all the energy parameters are small compared to the energy gap between the ground and excited states (single-band approach). It is also required that the size of the ground state (described by the width of Wannier functions) is larger than the scattering length but at the same time smaller than the distance between sites (tight-binding approximation).

2.2.1 Superfluid-to-Mott insulator transition

The paradigmatic phase transition of the Bose-Hubbard model is the superfluid-to-Mott insulator transition [Fis89, Fre94], which appears due to a competition between the tunnelling rate J and the on-site interaction U. This transition can be probed by tuning the lattice depth V_0 (the tunnelling rate decreases with increasing V_0) or the s-wave scattering length. The Mott

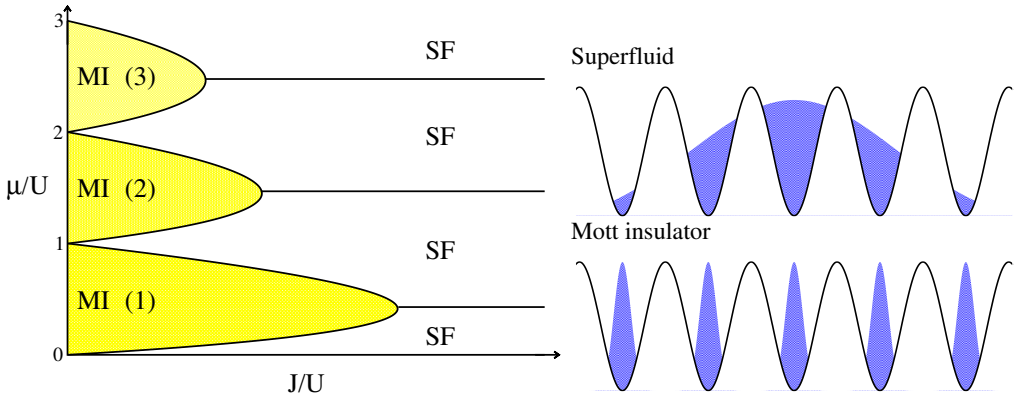

Figure 2.2: Left: Phase diagram of the Bose-Hubbard model for a 1D lattice ($z = 2$). In yellow, the Mott insulator lobes (for filling factor 1, 2 and 3, respectively) and in white, the superfluid phase. Right: Schematic density profiles of the superfluid and the Mott insulator phase in a 1D optical lattice. Whereas the coherence in the superfluid phase is preserved despite the lattice, this is destroyed in the Mott insulator phase, where the Bose gas behaves as many condensates localized in the minima of the lattice.

insulator is a phase described by a very well defined number of particles in each site and a loss of coherence, and it appears when the tunnelling rate is small compared with the on-site interaction ($J \ll U$). In the opposite situation ($J \gg U$), the superfluid phase is characterized by a coherent ground state with a common phase and large uncertainty in the number of particles per site, due to the shallowness of the lattice (see right panel of Fig. 2.2. The boundary between the superfluid and the insulating phase is implicitly represented by the following curve [Fis89, Lew12]:

$$J/U = \frac{(2n-1)(\mu/U) - n(n-1) - (\mu/U)^2}{2z(1+\mu/U)}\,, \tag{2.7}$$

where z is the coordination number, i.e. the number of neighboring sites.

Figure 2.2 represents the phase boundary in the $J/U - \mu/U$ plane. Inside each Mott lobe (yellow areas), the number of particles per site (filling factor) is also written. In right panel, we show schematically the probability distribution in an optical lattice in the superfluid phase (delocalized, extended) and in the Mott insulator phase (localized around the minima of the lattice potential).

2.2.2 Extended Bose-Hubbard model

Equation (2.4) describe the physics of a system of particles in an optical lattice that can hope between the different sites of the lattice and interact via contact interaction when two particles occupy the same site. It is indeed possible to add additional terms in the Bose-Hubbard hamiltonian in order to account for other kind of interactions, which yields to the extended Bose-Hubbard model. In particular, in the present section, we will add the dipolar interaction

[Aik12, Lu11, Lah09] in the two-body term of the many-body hamiltonian, whose expression is:

$$\mathcal{V}_{\text{int}}^{\text{dip}}(|\vec{r}-\vec{r}\,'|,\theta) = d^2\frac{1-3\cos^2\theta}{|\vec{r}-\vec{r}\,'|^3}\,, \tag{2.8}$$

where d is the dipole-dipole (electric or magnetic) coupling constant and θ is the angle between the dipole orientation and the vector given by $\vec{r}-\vec{r}\,'$. This term is introduced in the many-body hamiltonian as:

$$\mathcal{H}_{\text{dip}} = \frac{1}{2}\int d\vec{r}\,d\vec{r}\,'\hat{\Psi}^\dagger(\vec{r},t)\hat{\Psi}^\dagger(\vec{r}\,',t)\,\mathcal{V}_{\text{int}}^{\text{dip}}(|\vec{r}-\vec{r}\,'|,\theta)\,\hat{\Psi}(\vec{r}\,',t)\hat{\Psi}(\vec{r},t)\,, \tag{2.9}$$

and it contributes in the on-site interaction and it adds another term in the Bose-Hubbard hamiltonian. The on-site interaction U_l, in this case, gets renormalized as:

$$U_l = g\int d\vec{r}\,|\omega(\vec{r}+\vec{r}_l)|^4 + \int d\vec{r}\,d\vec{r}\,'|\omega(\vec{r}+\vec{r}_l\,)|^2\mathcal{V}_{\text{int}}^{\text{dip}}(|\vec{r}-\vec{r}\,'|,\theta)|\omega(\vec{r}\,'+\vec{r}_l)|^2\,, \tag{2.10}$$

and another term that takes into account the anisotropic and long-range character of the dipolar interaction appears in the hamiltonian

$$\hat{\mathcal{H}} = -\sum_{l,l'}J_{l,l'}(\hat{b}_l^\dagger\hat{b}_{l'}+\hat{b}_{l'}^\dagger\hat{b}_l) + \frac{1}{2}\sum_l U_l\,\hat{n}_l(\hat{n}_l-1) + \sum_l\sum_{l'}U_{l,l'}\,\hat{n}_l\hat{n}_{l'} - \mu\sum_l\hat{n}_l\,, \tag{2.11}$$

where

$$U_{l,l'} = \int d\vec{r}\,d\vec{r}\,'|\omega(\vec{r}+\vec{r}_l\,)|^2\mathcal{V}_{\text{int}}^{\text{dip}}(|\vec{r}-\vec{r}\,'|,\theta_{l,l'})|\omega(\vec{r}\,'+\vec{r}_{l'}\,)|^2\,. \tag{2.12}$$

Equation (2.11) is known as the extended Bose-Hubbard hamiltonian, and it describes the physics of polar particles loaded on an optical lattice.

2.3 Many-body properties in the Bose-Hubbard model

Once the Bose-Hubbard hamiltonian has been introduced, one has to solve the eigenvalue problem, i.e. to find the eigenvalues (eigenenergies) of the given operator and their corresponding eigenvectors. For systems characterized by particles populating different modes, it is convenient to work in the Fock basis, which labels its elements according to the number of particles per site: $|n_1,\cdots,n_M\rangle$, where n_i is the number of particles at site i, corresponding to this element of the basis and M is the number of modes. The elements of the Fock basis are eigenvectors of the particle number operator $\hat{n}_i$, and their corresponding eigenvalues are n_i. The whole set of eigenvalues of the particle number operator fulfills that $\sum_{i=1}^M n_i = N$, where N is the total number of particles, which is conserved. Mathematically, the elements of the Fock basis can be constructed from the vacuum $|\text{vac}\rangle = |0,\cdots,0\rangle$ (i.e. the state where all the sites have zero occupancy) as:

$$|n_1,\cdots,n_M\rangle = \prod_{l=1}^M\frac{1}{\sqrt{n_l!}}\left(\hat{b}_l^\dagger\right)^{n_l}|\text{vac}\rangle\,, \tag{2.13}$$

and they can be expressed as a product state $|n_1, \cdots, n_M\rangle = |n_1\rangle \otimes \cdots \otimes |n_M\rangle$. The number of elements of the Fock basis is equal to the dimension of the Hilbert space D_{BH}, which can be computed as:

$$D_{\mathrm{BH}} = \left(\!\!\binom{M}{N}\!\!\right) = \binom{M+N-1}{N} = \frac{(N+M-1)!}{N!(M-1)!}\,. \tag{2.14}$$

One can then map each element of the Fock basis $|n_1, \cdots, n_M\rangle$ to an (indicial) basis $|k\rangle$, where k runs from 1 to D_{BH}. Thus, a general many-body wave function is written as

$$|\Psi\rangle = \sum_{k}^{D_{\mathrm{BH}}} C_k\,|k\rangle, \tag{2.15}$$

where C_k is the corresponding amplitude of the Fock state corresponding to $|k\rangle$. It is interesting to remind that in a continuous system, the sequence of the number of particles in each position gives the density profile, then, the Fock basis is constituted by states that describe the density profile in a discrete way.

2.3.1 Coherence

The first property that one can obtain from the Fock basis is the coherence. Coherent states are the closest analogs to classical solutions, in the same way wavepackets are the closest quantum analog to classical trajectories. They are mathematically defined as the eigenvectors of the annihilation operators $\hat{b}_l|\alpha\rangle = \alpha|\alpha\rangle$, in such a way that they do not change if a particle is removed from the state (coherence). A general coherent state can be constructed by assuming that all N atoms populate the same single-particle state,

$$\hat{\alpha}^\dagger \equiv \sum_{l=1}^{M} c_l\,\hat{b}_l^\dagger\,. \tag{2.16}$$

The coherent state then reads,

$$|\alpha\rangle = \frac{1}{\sqrt{N!}}\left(\hat{\alpha}^\dagger\right)^N|\mathrm{vac}\rangle\,. \tag{2.17}$$

Since $c_l \in \mathbb{C}$, this many-body state has $2M$ parameters to be determined. Properly normalizing the single-particle wave function and also realising that there is always an arbitrary global phase, the number of free parameters can be reduced to $2(M-1)$. It is worth stressing that a coherent state as the one defined above corresponds to a fully condensed atomic cloud.

2.3.2 Fragmentation

Regarding the Bose-Hubbard hamiltonian, there is a quantity that can be obtained and provides an idea about the suitability for the system to be described through mean-field methods: fragmentation. The fragmentation properties of an ultracold atomic gas [Mue06] with N particles occupying M different modes can be investigated by means of the eigenvalues of the one-body density matrix $\hat{\rho}^{(1)}$, whose matrix elements can be computed as:

$$\hat{\rho}^{(1)}_{ij} = \frac{1}{N}\langle\Psi|\hat{b}_i^\dagger\hat{b}_j|\Psi\rangle\,, \tag{2.18}$$

with $i, j = 1, \cdots, M$. Since $|\Psi\rangle$ is properly normalized, it follows that $\mathrm{Tr}\,\hat{\rho}^{(1)} = 1$. The eigenvectors $|\psi_i\rangle$ of the one-body density matrix, are referred in the literature as natural orbitals, and their eigenvalues p_i are positive, normalized $\sum_i p_i = 1$ and ordered, satisfying $p_i \geq p_{i+1}$ for $i = 1, \cdots, M-1$. Each eigenvalue of the one-body density matrix gives the relative occupation number of the corresponding natural orbital $p_i = N_i/N$. In a singly condensed system, there is only one large eigenvalue that corresponds to the condensed fraction of the single-particle state $|\psi_1\rangle$: $p_1 \sim 1$ and the associated occupation number scales with the number of particles $N_1 \sim \mathcal{O}(N)$, with all the other eigenvalues p_j $(j \neq 1)$ being small $\sim \mathcal{O}(1/N)$ and its associated occupation numbers vanishing as N increases (they do not scale with N). Instead an s-fragmented system has more than one large eigenvalue (more than one occupation number that scales with N), and $N_i \sim \mathcal{O}(N)$, with $i = 1, \ldots, s$, with the rest of eigenvalues p_j $(j > s)$ small $\sim \mathcal{O}(1/N)$. The particular cases of $s = 2$ and $s = 3$ are also called bifragmentation and trifragmentation, respectively. When the system is fully condensed, the mean-field approximation provides a good description of the physics of the system. In contrast, when the situation where the system is not fully condensed, but fragmented, quantum correlations become important and the mean-field approximation fails to describe the system.

2.3.3 Entanglement: von Neumann entropy and Schmidt gap

Correlations between different subsystems of a many-body quantum system can be quantified by performing different bipartite splittings, i.e. splittings in two subsystems, whose union yields the whole system. Then, considering the system as made of two subsystems, tracing out one of the parts, and studying the von Neumann entropy and the entanglement spectrum [Li08a] of the resulting subsystem, we will be able to quantify quantum correlations and entanglement properties between both. It is important to remark that the number of bipartite splittings that we can perform in the system, depends on the number of modes in the Bose-Hubbard hamiltonian.

From the density matrix of the full system $\hat{\rho}$, correlations between mode i and the rest can be determined by first taking the partial trace of $\hat{\rho}$ over the Fock-state basis of the other modes. This yields the reduced density matrix on subsystem i, $\hat{\rho}_i$, that describes the state of this subsystem. For instance, by tracing out the sites $2, 3, \cdots$ to M, a bipartite splitting of the M-mode system is obtained, and the reduced density matrix on site 1 takes the form $\hat{\rho}_1 = \mathrm{Tr}_{2,\cdots,M}\hat{\rho}$. In the particular case of the Bose-Hubbard hamiltonian, it is found to be diagonal in the single mode space of N particles,

$$\hat{\rho}_1 = \sum_{k=0}^{N} \lambda_k^{(1)} |k\rangle\langle k| \ , \quad \lambda_k^{(1)} \geq 0 \tag{2.19}$$

where $|k\rangle$ are states with k particles in mode 1. The set of eigenvalues $\{\lambda_k^{(1)}\}$ is called entanglement, or Schmidt spectrum [Li08a, DeC12], and the eigenvalues are the Schmidt coefficients. The Schmidt coefficient $\lambda_k^{(1)}$ is in this case the probability of finding k particles in site 1 without measuring the number of atoms in the other modes. The Schmidt spectrum fulfills $\sum_i \lambda_i^{(1)} = 1$, and contains information about the correlations and the entanglement properties of the state in subsystem 1 with respect to the rest of the system. It is worth recalling that a many-body state is entangled when it cannot be written as a product state.

A measure of the entanglement between the two subsystems is provided by the single-site von Neumann entropy, which can be calculated as $S_j = -\mathrm{Tr}(\hat{\rho}_j \log \hat{\rho}_j)$, with $j = 1, \cdots, M$. Noting

that the density matrix $\hat{\rho}_1$ is already diagonal if obtained from a Bose-Hubbard hamiltonian, the von Neumann entropy can be evaluated from the Schmidt coefficients as

$$S_j = -\sum_i \lambda_i^{(j)} \log \lambda_i^{(j)} \,. \tag{2.20}$$

Another magnitude that can measure the degree of entanglement and correlations in quantum systems is defined from the set of Schmidt coefficients λ_k: the so-called Schmidt gap, defined as the difference between the two largest and more relevant Schmidt coefficients in the entanglement spectrum of subsystem i, $\Delta\lambda^{(i)}$ [DeC12]. In the case of no entanglement between the subsystems, the Schmidt gap takes the value of 1, its maximum. Instead, the vanishing of the Schmidt gap marks large entanglement between the subsystems.

Entanglement vs fragmentation

No relation exists between fragmentation and entanglement, in the sense that a system can be entangled and fragmented independently. For instance, a system where all the bosons occupy the same mode is nor fragmented neither spatially entangled. In the case of 2 modes (also called bosonic Josephson junction) in the strong repulsive interaction regime $U/J \to \infty$ (also called Fock regime) is a clear example of a non entangled but fragmented state: $|N/2, N/2\rangle$. In contrast, in the noninteracting regime the bosonic Josephson junction is in a fully condensed state,

$$|\Psi\rangle = \frac{1}{\sqrt{N!}} \left(\frac{\hat{b}_1^\dagger + \hat{b}_2^\dagger}{\sqrt{2}} \right)^N |\text{vac}\rangle \,, \tag{2.21}$$

which has large entanglement between the two sites as seen by the Schmidt coefficients which can be computed analytically to find their expression:

$$\lambda_k = 2^{-N} \binom{N}{k} \,. \tag{2.22}$$

Finally, cat states, which appear in a bosonic Josephson junction in the atractive regime ($U/J \to -\infty$), $|\Psi\rangle = (|N, 0\rangle + |0, N\rangle)/\sqrt{2}$, are a well known example of fragmented and entangled many-body systems.

Chapter 3

Bose-Einstein condensates in the mean-field regime: single-component condensates

We have seen that dilute and weakly interacting atomic Bose gases macroscopically occupy the single-particle ground state when the system is cooled below a critical temperature, which is characteristic of the system. When it occurs, the wave length of the wave packets associated to each atom increases until being of the order of the size of the system. At this point, the wave packets overlap, constituting a giant matter wave known as Bose-Einstein condensate. When the number of particles is large and the noncondensed fraction is negligible, the condensate is said to belong to the mean-field regime, and the statical properties and the dynamical evolution of the macroscopic wave function that describe the properties of the condensate is described through the Gross-Pitaevskii equation. This equation has a single-particle part, which contains the kinetic term and the potential that traps the particles, and a nonlinear term that includes two-body interactions. This is the reason why the Gross-Pitaevskii equation is also known as the nonlinear Schrödinger equation in part of the bibliography.

In this chapter we present the single-component Gross-Pitaevskii equation (in contrast to the next chapter, where we present the theory to describe condensate condensed in two different single-particle states, also known as two-component condensates) both in the time-dependent and in the time-independent version. Afterwards, we comment about other versions of the Gross-Pitaevskii, like the dimensionless equation, the reduction to lower dimensions or the introduction of the rotating frame. After that, we introduce the ground state properties, together with the analytical approach in the large number of particles limit (the Thomas-Fermi approximation). Then, we visit the excited states, and in particular, the topological states, which possess a nontrivial phase pattern and density profile (i.e. with singularities): vortices and solitons. These topological states can be engineered in experiments, by using different techniques, some of them discussed in the present chapter.

3.1 Gross-Pitaevskii equation

From the many-body hamiltonian describing N bosons interacting according to the potential $\mathcal{V}_{\rm int}(\vec{r}-\vec{r}\,')$ confined in an external potential $V_{\rm trap}(\vec{r})$, which can be written in second quantization as: (Eq. (2.3)):

$$\hat{\mathcal{H}} = \int d\vec{r}\,\hat{\Psi}^\dagger(\vec{r})\left[-\frac{\hbar^2}{2m}\vec{\nabla}^2 + V_{\rm trap}(\vec{r})\right]\hat{\Psi}(\vec{r}) + \frac{1}{2}\int d\vec{r}\,d\vec{r}\,'\hat{\Psi}^\dagger(\vec{r})\hat{\Psi}^\dagger(\vec{r}\,')\mathcal{V}_{\rm int}(\vec{r}-\vec{r}\,')\hat{\Psi}(\vec{r}\,')\hat{\Psi}(\vec{r})\,, \tag{3.1}$$

one can derive the corresponding Schrödinger-like equation by using the Heisenberg equation of motion:

$$i\hbar\frac{\partial}{\partial t}\hat{\Psi} = [\hat{\Psi}, \hat{\mathcal{H}}]\,. \tag{3.2}$$

In the case of a Bose-Einstein condensate, a single-particle state becomes macroscopically occupied, thus one can neglect the non-condensed fraction in the system. As a consequence, the field operators can be replaced by their mean value $\Phi(\vec{r}) = \langle\hat{\Psi}(\vec{r})\rangle$, which is known as the order parameter or condensate wave function, and is normalized to the total number of particles N:

$$\int d\vec{r}\,\Phi^*(\vec{r})\Phi(\vec{r}) = N\,. \tag{3.3}$$

The time evolution of the condensate wave function can be computed with Eq. (3.2), which yields to the Gross-Pitaevskii equation for a generalized two-body interaction:

$$i\hbar\frac{\partial}{\partial t}\Phi(\vec{r},t\,) = \mathcal{H}_0(\vec{r})\Phi(\vec{r},t\,) + \int d\vec{r}\,'\Phi^*(\vec{r}\,',t)\mathcal{V}_{\rm int}(\vec{r}-\vec{r}\,')\Phi(\vec{r}\,',t\,)\Phi(\vec{r},t\,)\,, \tag{3.4}$$

where $\mathcal{H}_0(\vec{r}) = -\hbar^2/2m\,\vec{\nabla}^2 + V_{\rm trap}(\vec{r})$ is the noninteracting single-particle hamiltonian. When the system is dilute and at low temperature, interactions can be approximated to be contact-like or s-wave. Therefore, the two-body interaction potential takes the form of a delta function $\mathcal{V}_{\rm int}(\vec{r}-\vec{r}\,') = g\delta(\vec{r}-\vec{r}\,')$, with $g = 4\pi\hbar^2 a_s/m$ the coupling constant in 3D (we present the expression of the coupling constant in lower dimensions in Sect. 3.1.2) and a_s the s-wave scattering length. Then, one obtains the Gross-Pitaevskii equation for s-wave contact interaction:

$$i\hbar\frac{\partial}{\partial t}\Phi(\vec{r},t\,) = \mathcal{H}_0(\vec{r})\Phi(\vec{r},t\,) + g|\Phi(\vec{r},t\,)|^2\Phi(\vec{r},t\,)\,. \tag{3.5}$$

At this point, one can get the time-independent Gross-Pitaevskii equation through the ansatz $\Phi(\vec{r},t\,) = \Psi(\vec{r})e^{-i\mu t/\hbar}$, where μ is the chemical potential. Then, one obtains:

$$\mu\Psi(\vec{r}) = \mathcal{H}_0(\vec{r})\Psi(\vec{r}) + g|\Psi(\vec{r})|^2\Psi(\vec{r})\,. \tag{3.6}$$

The solution of this equation crucially cares about whether the system is open or closed. In the first case, the grandcanonical ensemble applies, the system can exchange particles with the environment (then the number of particles is not conserved), and the chemical potential remains constant. In the second case, where the canonical ensemble applies, it is the number of particles

the conserved quantity (and then normalization), whereas the chemical potential is fixed by normalization.

There exists an alternative way to derive the time-independent Gross-Pitaevskii equation for contact-interacting condensates, by looking for stationary points of the following energy functional [Dal99, Pit03]:

$$E[\Psi,\Psi^*] = \int d\vec{r}\left[\frac{\hbar^2}{2m}|\vec{\nabla}\Psi(\vec{r})|^2 + V_{\rm trap}(\vec{r})|\Psi(\vec{r})|^2 + \frac{g}{2}|\Psi(\vec{r})|^4\right] \tag{3.7}$$

under the constraint of the conservation of the total number of particles, where the Lagrange multiplier is the chemical potential:

$$\frac{\delta}{\delta\Psi^*}\left[E[\Psi,\Psi^*] - \mu\left(\int d\vec{r}\,\Psi^*(\vec{r})\Psi(\vec{r}) - N\right)\right] = 0\,. \tag{3.8}$$

The solution of the previous variation is the time-independent Gross-Pitaevskii equation, Eq. (3.6) derived before by using the Heisenberg equation of motion.

3.1.1 Dimensionless Gross-Pitaevskii equation

It is interesting to derive the dimensionless version of the Gross-Pitaevskii equation, which clearly reveals the physical dimensionless parameters that describe the static and dynamic properties of a Bose-Einstein condensate. In order to do that, we will restrict to the case of a harmonic confinement, since many traps can be locally approximated as harmonic oscillators around their minima.

The expression of the harmonic oscillator in 3 dimensions is:

$$V_{\rm harm}(x,y,z) = \frac{1}{2}m\left(\omega_x^2x^2 + \omega_y^2y^2 + \omega_z^2z^2\right)\,, \tag{3.9}$$

where m is the mass of the particle and ω_i with $i = x, y, z$ are the trapping frequencies along the axes x, y and z. The harmonic confinement provides a natural length scale $a_\omega = \sqrt{\hbar/m\omega}$, and an energy scale $e_\omega = \hbar\omega$, where ω here is an arbitrary frequency.

When introducing these scales within the time-independent Gross-Pitaevskii equation (3.6), one obtains the following dimensionless equation:

$$\tilde{\mu}\tilde{\Psi}(\tilde{\vec{r}}) = \left[-\frac{1}{2}\tilde{\vec{\nabla}}^2 + \frac{1}{2}\left(\tilde{\omega}_x^2\tilde{x}^2 + \tilde{\omega}_y^2\tilde{y}^2 + \tilde{\omega}_z^2\tilde{z}^2\right)\right]\tilde{\Psi}(\tilde{\vec{r}}) + \frac{4\pi N a_s}{a_\omega}|\tilde{\Psi}(\tilde{\vec{r}})|^2\tilde{\Psi}(\tilde{\vec{r}})\,, \tag{3.10}$$

where $\tilde{\vec{\nabla}}^2 = a_\omega^2\vec{\nabla}^2$, $\sqrt{N}\,\tilde{\Psi}(\tilde{\vec{r}}) = a_\omega^3\Psi(\vec{r})$, $\tilde{\mu} = \mu/e_\omega$, $\tilde{x} = x/a_\omega$, $\tilde{y} = y/a_\omega$, $\tilde{z} = z/a_\omega$, and $\tilde{\omega}_i = \omega_i/\omega$ are dimensionless quantities. It is important to recall that the choice of ω is, up to now, arbitrary. However, there exist some standards in this election, as a function of the geometry of the system. In the case of cylindrically symmetric condensates, where the trapping frequencies fulfill $\omega_x = \omega_y = \omega_\perp$, and $\lambda = \omega_z/\omega_\perp$, is the aspect ratio (the z-direction has been chosen as the symmetry axis), there are two limits that allow some approximations. When $\lambda > 1$, the trapping in z-direction is tighter, and the condensate is said to be pancake-shaped. In contrast, for $\lambda < 1$, it is the radial direction the one that is tightly confined, and the condensate

is said to be cigar-shaped in this case. In addition, when $\lambda \gg 1$ or $\lambda \ll 1$, the dimensionality of the Gross-Pitaevskii equation can be reduced to 2D and 1D (see Sect. 3.1.2 for more details).

From Eq. (3.10), we can see that there is a single dimensionless parameter that actually plays a role in the system: $4\pi a_s N/a_\omega$. This parameter quantifies the strength of the interaction energy in the system, and its expression is indeed reasonable, since it increases with the product of a_s, the scattering length and N, the total number of particles.

3.1.2 Gross-Pitaevskii equation in lower dimensions

In the previous section we have derived the Gross-Pitaevskii equation in 3D. Under certain conditions, the condensate is tightly confined in one or two of the dimensions, and it behaves effectively as a 2D or 1D condensate, respectively. However, the reduction of the Gross-Pitaevskii equation to lower dimensions is not trivial due to the nonlinear term. It is, therefore, necessary, to renormalize the s-wave contact interaction constant g, which is linear with the s-wave scattering length a_s, for lower dimensions. In order to reduce the dimensionality of a Bose-Einstein condensate, one has to assume the shape in the squeezed directions, commonly approximated as gaussians, which are the noninteracting ground states in the tightly confined directions. In what follows, we derive the Gross-Pitaevskii equation for a harmonic trap, of a 1D condensate squeezed in y-z plane, and the one corresponding to a 2D condensate squeezed in the z-direction.

1D case

3D condensates with high transverse confinement (ω_y,$\omega_z \gg \omega_x$) are called cigar-shaped condensates, and they can be effectively approached as one-dimensional condensates. In that situation, the wave function can be separated as a product of two functions, one that depends on the longitudinal direction x and time t, $\psi(x,t\,)$, and another one, freezed in time, that depends on the transversal coordinates $\psi_\perp(y,z)$, and is assumed to have the shape of a gaussian (because the energy of the excited transversal modes increase with confinement, becomes much larger than the energy of the longitudinal modes and, therefore, the ground state of the harmonic oscillator is a good ansatz to describe transversal modes):

$$\psi_\perp(y,z) = \left(\frac{m}{\pi\,\hbar}\right)^{1/2} (\omega_y\omega_z)^{1/4}\, e^{-\frac{m(\omega_y y^2+\omega_z z^2)}{2\hbar}}\,. \tag{3.11}$$

When this ansatz is introduced in the Gross-Pitaevskii equation, one can multiply the equation by $\psi_\perp^*(y,z)$ and integrate in the y-z plane to obtain the 1D Gross-Pitaevskii equation

$$i\hbar\frac{\partial}{\partial t}\psi(x,t\,) = \left(-\frac{\hbar^2}{2m}\,\frac{\partial^2}{\partial x^2} + V_{\rm trap}(x)\right)\psi(x,t\,) + g_{\rm 1D}|\psi(x,t\,)|^2\psi(x,t\,)\,, \tag{3.12}$$

with a renormalized coupling constant

$$g_{\rm 1D} = g\frac{m}{2\pi\hbar}\sqrt{\omega_y\omega_z} = 2\hbar a_s\sqrt{\omega_y\omega_z}\,. \tag{3.13}$$

2D case

When there is a strong confinement only in a single dimension ($\omega_z \gg \omega_x$,ω_y), in such a way that the condensate acquires a disk-shape geometry, it is reasonable to use the 2D version of the Gross-Pitaevskii equation. In the present 2D case, this equation can be obtained analogously to the 1D equation, i.e. assuming the gaussian:

$$\psi_\perp(z) = \left(\frac{m\,\omega_z}{\pi\,\hbar}\right)^{1/4} e^{-\frac{m\omega_z z^2}{2\hbar}}\,. \tag{3.14}$$

Then, substituting in the Gross-Pitaevskii equation, multiplying by $\psi_\perp^*(z)$ and integrating along z, one obtains the 2D Gross-Pitaevskii equation

$$i\hbar\frac{\partial}{\partial t}\psi(x,y,t\,) = \left[-\frac{\hbar^2}{2m}\left(\frac{\partial^2}{\partial x^2}+\frac{\partial^2}{\partial y^2}\right) + V_{\rm trap}(x,y)\right]\psi(x,y,t\,) + g_{\rm 2D}|\psi(x,y,t\,)|^2\psi(x,y,t\,)\,, \tag{3.15}$$

with the corresponding 2D coupling constant

$$g_{\rm 2D} = g\left(\frac{m\,\omega_z}{2\pi\hbar}\right)^{1/2}\,. \tag{3.16}$$

3.1.3 Gross-Pitaevskii equation in the rotating frame

3D Bose-Einstein condensates are superfluids, i.e. fluids that can flow without dissipation. From the experimental point of view, Bose-Einstein condensates have been rotated in order to probe their superfluidity. In order to describe this new situation, one has to build the Gross-Pitaevskii equation in a rotating frame, which can be done for a constant angular velocity by imposing the conservation of the angular momentum $\hat{L}_z$. This constraint adds an additional term that includes such rotation, and is proportional to the angular momentum with a lagrangian multiplier Ω, which is the rotation frequency. Moreover, this new term enters in the equation as a vector potential in the kinetic term. Then, the Gross-Pitaevskii equation in the rotating frame is [Fet09]:

$$\mu\Psi(\vec{r}) = \mathcal{H}_0(\vec{r})\Psi(\vec{r}) + g|\Psi(\vec{r})|^2\Psi(\vec{r}) - \Omega\hat{L}_z\Psi(\vec{r})\,, \tag{3.17}$$

where we have implicitly assumed that the rotation is around the z-axis. The last term favors states with positive angular momentum, i.e. solutions that present counterclockwise rotation. The energy corresponding to the rotation can be computed as:

$$E_{\rm rot} = \Omega\int d\vec{r}\,\Psi^*(\vec{r})\hat{L}_z\Psi(\vec{r})\,, \tag{3.18}$$

which corresponds to the energy of a classical rotator.

3.2 Ground state

The ground state of the Gross-Pitaevskii equation corresponds to the solution of this equation with the lowest energy. This state is characterized by a density that follows the trap geometry, and a constant arbitrary phase that can be safely removed from the Gross-Pitaevskii equation.

There are some particular cases, where the ground state of a system can be obtained analytically: the noninteracting case (the ground state solution of the Schrödinger equation), the homogeneous case (no trapping), whose ground state is $\Psi(\vec{r}) = \sqrt{n}$, where $n = \mu/g$ is the background density (the system is open, then the chemical potential is fixed and the total number of particles is not), and the strong interacting limit, given by the Thomas-Fermi wave function. When the solution can not be obtained analytically, numerical methods, like the Imaginary Time Step Method [Chi00] (a split-step-like method), are needed.

In this section we derive, for the particular case of a harmonic oscillator, the virial theorem, which relates the different energy contributions in the energy functional, and the Thomas-Fermi approximation, which is an analytical solution that exists in the Gross-Pitaevskii equation in the limit of large number of particles.

3.2.1 Virial theorem

From the expression of the energy functional (3.7), it is clear to see that the energy of an interacting Bose-Einstein condensate can be decomposed in three terms: $E = E_{\text{kin}} + E_{\text{trap}} + E_{\text{int}}$, where the first term is the kinetic energy:

$$E_{\text{kin}} = \frac{\hbar^2}{2m} \int d\vec{r} |\vec{\nabla}\Psi(\vec{r})|^2 \,, \tag{3.19}$$

the second term is the energy due to the external confinement:

$$E_{\text{trap}} = \int d\vec{r} V_{\text{trap}}(\vec{r}) |\Psi(\vec{r})|^2 \,, \tag{3.20}$$

and the last term is the interaction energy:

$$E_{\text{int}} = \frac{g}{2} \int d\vec{r} |\Psi(\vec{r})|^4 \,. \tag{3.21}$$

In addition, the direct integration of the Gross-Pitaevskii equation relates the previous quantities with the chemical potential in such a way that $\mu N = E_{\text{kin}} + E_{\text{trap}} + 2E_{\text{int}} = E + E_{\text{int}}$. However, for the case of the ground state, there is an additional equation that relates the different energy contributions of the system, given by the virial theorem.

When a system is in equilibrium, any coordinate scaling $\vec{r} \to \nu\vec{r}$, where $\nu \in \mathbb{R}$ is a spatial scaling factor, must not modify the total energy of a condensate. It means, that, in d dimensions, $\Psi(\vec{r}) \to \Psi_\nu(\vec{r}) = \mathcal{C}\Psi(\nu\vec{r})$, where $\mathcal{C}$ is a normalization constant. Normalizing the wave function to the total number of particles:

$$\begin{aligned} N = \int d\vec{r} |\Psi(\vec{r})|^2 = \int d\vec{r} |\Psi_\nu(\vec{r})|^2 = |\mathcal{C}|^2 \int d\vec{r} |\Psi(\nu\vec{r})|^2 = \\ |\mathcal{C}|^2 \nu^{-d} \int d(\nu\vec{r}) |\Psi(\nu\vec{r})|^2 = |\mathcal{C}|^2 \nu^{-d} N \,, \end{aligned} \tag{3.22}$$

and thus, $|\mathcal{C}|^2 = \nu^d$.

Then, one can compute how do scale the other energy contributions; the kinetic energy scales

as:

$$E_{\mathrm{kin},\nu} = \frac{\hbar^2}{2m}\int d\vec{r}\,|\vec{\nabla}\Psi(\vec{r})|^2 = \frac{\hbar^2}{2m}\int d\vec{r}\,|\vec{\nabla}\Psi_\nu(\vec{r})|^2 = \frac{\hbar^2}{2m}|\mathcal{C}|^2\int d\vec{r}\,|\vec{\nabla}\Psi(\nu\vec{r})|^2 = \frac{\hbar^2}{2m}\nu^d\int \nu^{-d}d(\nu\vec{r})\,\nu^2|\vec{\nabla}_\nu\Psi(\nu\vec{r})|^2 = \nu^2 E_{\mathrm{kin}}\,, \tag{3.23}$$

and for the trap potential, it depends on the geometry. In the case of a d-dimensional harmonic oscillator

$$V_{\mathrm{harm}}(\vec{r}) = \frac{1}{2}m\sum_{r_i}^{d}\omega_{r_i}^2 r_i^2\,, \tag{3.24}$$

the scaled energy is:

$$E_{\mathrm{harm},\nu} = \int d\vec{r}\,V_{\mathrm{harm}}(\vec{r})|\Psi(\vec{r})|^2 = \int d\vec{r}\,V_{\mathrm{harm}}(\vec{r})|\Psi_\nu(\vec{r})|^2 = |\mathcal{C}|^2\int d\vec{r}\,V_{\mathrm{harm}}(\vec{r})|\Psi(\nu\vec{r})|^2 = \nu^d\int \nu^{-d}d(\nu\vec{r})\,\nu^{-2}V_{\mathrm{harm}}(\nu\vec{r})|\Psi(\nu\vec{r})|^2 = \nu^{-2}E_{\mathrm{harm}}\,. \tag{3.25}$$

Finally, the term corresponding to the contact interaction scales as

$$E_{\mathrm{int},\nu} = \frac{g}{2}\int d\vec{r}\,|\Psi(\vec{r})|^4 = \frac{g}{2}\int d\vec{r}\,|\Psi_\nu(\vec{r})|^4 = \frac{g}{2}|\mathcal{C}|^4\int d\vec{r}\,|\Psi(\nu\vec{r})|^4 = \frac{g}{2}\nu^{2d}\int \nu^{-d}d(\nu\vec{r})|\Psi(\nu\vec{r})|^4 = \nu^d E_{\mathrm{int}}\,. \tag{3.26}$$

Putting everything together $E_\nu = \nu^2 E_{\mathrm{kin}} + \nu^{-2}E_{\mathrm{harm}} + \nu^d E_{\mathrm{int}}$ and imposing the equilibrium condition (this condition imposes that the energy is extremal when there is no scaling, $\nu = 1$), which is:

$$\left.\frac{dE_\nu}{d\nu}\right|_{\nu=1} = 0\,, \tag{3.27}$$

yields to the virial theorem:

$$2E_{\mathrm{kin}} - 2E_{\mathrm{harm}} + dE_{\mathrm{int}} = 0\,. \tag{3.28}$$

This expression has been widely used to check the computation of the ground state of a system, obtained by numerically solving the Gross-Pitaevskii equation.

3.2.2 Thomas-Fermi approximation

The Thomas-Fermi approximation is an analytical limit of the solution of the Gross-Pitaevskii for large repulsive interactions. When they increase (and in particular, the dimensionless parameter $a_s N/a_\omega$ increases (Eq.(3.10))), the density is no longer peaked at the minimum of the harmonic potential, particles are "expelled" from the center, and the density becomes rather flat, increasing the effective size of the condensate. As a consequence, the kinetic term can be neglected, due to the flatness of the density (the spatial curvature of the density is also known as quantum pressure), and the term with the laplacian in the Gross-Pitaevskii equation (3.6) can

be neglected. Therefore, this equation becomes algebraic, i.e.

$$V_{\text{trap}}(\vec{r})\Psi(\vec{r}) + g|\Psi(\vec{r})|^2\Psi(\vec{r}) = \mu\Psi(\vec{r})\,, \tag{3.29}$$

and it is thus possible to analytically isolate the atomic density $n(\vec{r}) = |\Psi(\vec{r})|^2$ as:

$$n(\vec{r}) = \begin{cases} \dfrac{\mu - V_{\text{trap}}(\vec{r})}{g} & \forall\, \vec{r} \mid \mu > V_{\text{trap}}(\vec{r}) \\ 0 & \forall\, \vec{r} \mid \mu \leq V_{\text{trap}}(\vec{r}) \end{cases}. \tag{3.30}$$

In the case of a harmonic oscillator, the corresponding Thomas-Fermi density is:

$$n(\vec{r}) = \frac{\mu}{g}\left(1 - \frac{x^2}{R_x^2} - \frac{y^2}{R_y^2} - \frac{z^2}{R_z^2}\right), \tag{3.31}$$

with $R_i = \sqrt{2\mu/m\omega_i^2}$. In the case of axially symmetric condensates around the z-axis, with a radial trapping frequency $\omega_\perp$, the density profile becomes

$$n(\vec{r}) = \frac{\mu}{g}\left(1 - \frac{r_\perp^2}{R_\perp^2} - \frac{z^2}{R_z^2}\right), \tag{3.32}$$

and the chemical potential can be computed from the normalization of the density to the total number of particles N:

$$\mu = \frac{1}{2}\hbar\omega_\perp\left(15\lambda\frac{Na_s}{a_\perp}\right)^{2/5}, \tag{3.33}$$

where $\lambda = \omega_z/\omega_\perp = R_\perp/R_z$, $g = 4\pi\hbar^2 a_s/m$, and $a_\perp = \sqrt{\hbar/m\omega_\perp}$. Analogously, the corresponding expressions of the Thomas-Fermi densities for the 1D and 2D case, can be derived from the corresponding dimensional reduction of the Gross-Pitaevskii equation (see Sect. 3.1.2). Moreover, the corresponding 1D and 2D solution meet the ones of the 3D Thomas-Fermi approximation for the cigar-shaped (λ small) and pancake-shaped (λ large) limit. The expression of the chemical potential corresponding to the different dimensions are represented in Table 3.1.

1D	2D	3D
$\mu = \frac{1}{2}\hbar\omega_{\text{long}}\left(\frac{3}{\lambda}\frac{Na_s}{a_{\text{long}}}\right)^{2/3}$	$\mu = \frac{1}{2}\hbar\omega_\perp\left(\frac{16\sqrt{\lambda}}{\sqrt{2\pi}}\frac{Na_s}{a_\perp}\right)^{1/2}$	$\mu = \frac{1}{2}\hbar\omega_\perp\left(15\lambda\frac{Na_s}{a_\perp}\right)^{2/5}$

Table 3.1: Expression of the Thomas-Fermi chemical potential for 1, 2 and 3 dimensions of a Bose-Einstein condensate with cylindrical symmetry. In these expressions, ω_{long} is the trapping frequency along the symmetry axis of the condensate, with $a_{\text{long}} = \sqrt{\hbar/m\omega_{\text{long}}}$, and $\omega_\perp$ is the trapping frequency along the direction perpendicular to the symmetry axis. In all the expressions, $\lambda = \omega_{\text{long}}/\omega_\perp$.

Figure 3.1(a) represents the density corresponding to the ground state obtained by numerically solving the 1D Gross-Pitaevskii equation, at the chemical potential $\mu = \hbar\omega_{\text{ho}}$ (solid black line) and $\mu = 8\hbar\omega_{\text{ho}}$ (solid red line), where ω_{ho} is the harmonic oscillator frequency. The dashed lines plot the associated Thomas-Fermi densities. One can observe that when the chemical poten-

tial increases (which means the interaction energy increases as well), the Thomas-Fermi density practically overlaps with the numerical ground state at the region of the bulk (at the boundary, the density is small and the Thomas-Fermi approximation fails), whereas for a small chemical potential, the Thomas-Fermi wave function deviates from the actual ground state of the system.

3.3 Bogoliubov excitations

Once the ground state properties of a system have been discussed, it is important to investigate the physics of perturbations on the ground state $\Psi_0(\vec{r})$, also known as elementary excitations. One can consider small oscillations around the ground state solution, and calculate the dynamical evolution of the perturbations by performing [Dal99, Pit03]:

$$\Phi(\vec{r},t) \rightarrow \left(\Psi_0(\vec{r}) + u(\vec{r})e^{-i\omega t} + v^*(\vec{r})e^{i\omega t}\right) e^{-i\mu t/\hbar}\,, \tag{3.34}$$

where $u(\vec{r})$ and $v^*(\vec{r})$ are the complex amplitudes of the perturbation, and ω is the excitation frequency. Introducing this equation in the time-dependent Gross-Pitaevskii equation (3.5), one obtains:

$$\begin{aligned}\left(\mu\Psi_0(\vec{r}) + (\mu+\hbar\omega)u(\vec{r})e^{-i\omega t} + (\mu-\hbar\omega)v^*(\vec{r})e^{i\omega t}\right)e^{-i\mu t/\hbar} = \\ \mathcal{H}_0\left(\Psi_0(\vec{r}) + u(\vec{r})e^{-i\omega t} + v^*(\vec{r})e^{i\omega t}\right)e^{-i\mu t/\hbar} + \\ g\left(\Psi_0^*(\vec{r}) + u^*(\vec{r})e^{i\omega t} + v(\vec{r})e^{-i\omega t}\right)\left(\Psi_0(\vec{r}) + u(\vec{r})e^{-i\omega t} + v^*(\vec{r})e^{i\omega t}\right)\times \\ \left(\Psi_0(\vec{r}) + u(\vec{r})e^{-i\omega t} + v^*(\vec{r})e^{i\omega t}\right)e^{-i\mu t/\hbar}\,.\end{aligned} \tag{3.35}$$

The zero-th order terms in the perturbation amplitudes can be identified as the time-independent Gross-Pitaevskii equation, which is fulfilled for the ground state of the system and thus they simply cancel.

At this point, if we keep the terms at first order in the complex amplitudes (the linear terms), Eq. (3.35) can be rewritten as:

$$\begin{aligned}\left((\mu+\hbar\omega)u(\vec{r})e^{-i\omega t} + (\mu-\hbar\omega)v^*(\vec{r})e^{i\omega t}\right) = \mathcal{H}_0\left(u(\vec{r})e^{-i\omega t} + v^*(\vec{r})e^{i\omega t}\right) + \\ g|\Psi_0(\vec{r})|^2\left(u^*(\vec{r})e^{i\omega t} + v(\vec{r})e^{i\omega t} + 2u(\vec{r})e^{-i\omega t} + 2v^*(\vec{r})e^{-i\omega t}\right).\end{aligned} \tag{3.36}$$

By separating the terms that are accompanied by the exponential $e^{-i\omega t}$ and $e^{-i\omega t}$, we can obtain the following two coupled equations, also known as Bogoliubov-de Gennes equations:

$$\begin{aligned}\hbar\omega u(\vec{r}) &= -\mu u(\vec{r}) + \mathcal{H}_0 u(\vec{r}) + g|\Psi_0(\vec{r})|^2\left(2u(\vec{r}) + v(\vec{r})\right) \\ -\hbar\omega v(\vec{r}) &= -\mu v(\vec{r}) + \mathcal{H}_0 v(\vec{r}) + g|\Psi_0(\vec{r})|^2\left(2v(\vec{r}) + u(\vec{r})\right)\,.\end{aligned} \tag{3.37}$$

These two equations, in general, must be solved numerically. However, they have an analytical solution for the homogeneous case, where there is no trapping, and the wave function is written in terms of the background density, which is defined as $n = |\Psi_0(\vec{r})|^2$. In this case, the complex amplitudes are plane waves $u(\vec{r}) = e^{i\vec{k}\cdot\vec{r}}$ and $v(\vec{r}) = e^{-i\vec{k}\cdot\vec{r}}$, and the excitation frequencies can

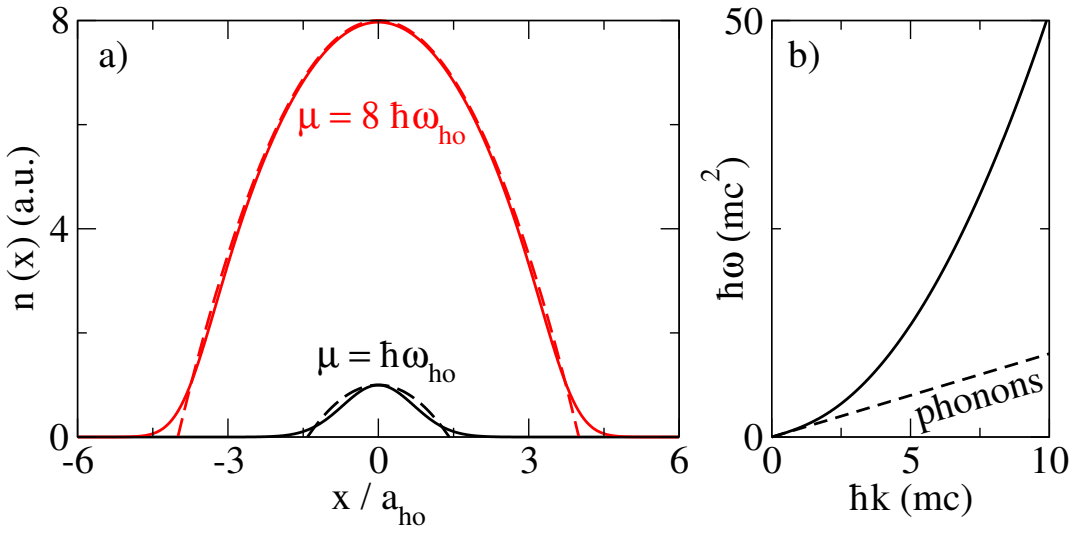

Figure 3.1: a) Density profile of a 1D condensate in a harmonic trap with chemical potential $\mu = \hbar\omega_{\rm ho}$ (solid black line) and $\mu = 8\hbar\omega_{\rm ho}$ (solid red line). Dashed lines correspond to the Thomas-Fermi densities at the given chemical potential. b) Bogoliubov spectrum corresponding to the Gross-Pitaevskii equation with contact interactions (solid black line). The dashed line corresponds to the linear asymptote of the spectrum as $k \to 0$.

be found as:

$$\begin{vmatrix} \hbar\omega - \frac{\hbar^2 k^2}{2m} - gn & -gn \\ -gn & -\hbar\omega - \frac{\hbar^2 k^2}{2m} - gn \end{vmatrix} = 0\,, \tag{3.38}$$

whose solutions are:

$$(\hbar\omega)^2 = \frac{\hbar^2 k^2}{2m}\left(\frac{\hbar^2 k^2}{2m} + 2gn\right)\,. \tag{3.39}$$

Equation (3.39) is known as the excitation (or Bogoliubov) spectrum, and gives the energy of the perturbation as a function of the wave vector of the excitation. The plot of the Bogoliubov spectrum is represented in Fig. 3.1(b), and it reveals that the dispersion is that of a free particle $\hbar\omega = \hbar^2 k^2/2m$ for large wave vector (quadratic), however, when the wave vector is small, the dispersion is phononic $\omega = ck$, with sound velocity given by:

$$c = \frac{1}{k}\lim_{k\to 0}\omega(k) = \sqrt{\frac{gn}{m}}\,, \tag{3.40}$$

which is the slope of the dashed line in Fig. 3.1(b).

3.4 Topological states

Using the Madelung transformation [Don91], it is possible to write the wave function in polar form, in terms of the density profile $n(\vec{r})$, and the phase pattern $S(\vec{r})$:

$$\Psi(\vec{r}) = \sqrt{n(\vec{r})}\, e^{iS(\vec{r})}\,. \tag{3.41}$$

This expression has been used to derive hydrodynamic properties of superfluids, like 3D condensates. For the particular case of the ground state, the Madelung transformation is simplified since the phase pattern of the ground state is flat, and then, the phase can be set arbitrarily to zero. However, this is no longer true for excited states. Nevertheless, there exist some excited states that can emerge in Bose-Einstein condensates that despite their nontrivial phase pattern and density profile, have a local analytical solution, like vortices and solitons. These states, apart from having an analytical solution, they have a classical analog (not for the case of dark solitons). In this section we discuss the physics of quantum vortices and solitons, and in particular, these states with nontrivial phase pattern, which are also referred in the literature as topological states [Tsu71].

3.4.1 Vortices

A vortex is a region of a fluid where particles flow along a closed *trajectory* around a given axis. They appear both in classical and quantum fluids, however, they present different features. The main one, is the circulation around the rotation axis. Whereas in classical vortices, the circulation is not quantized, in quantum vortices, the circulation is quantized, proportional to an integer number κ, called winding number of the vortex. Due to the fact that the wave function is single-valued, its phase must wind a factor of κ times 2π around the rotation axis, where a topological singularity appears. As a consequence, the density vanishes in order to hold such a singularity, and the hole produced by this vanishing density is the so-called core of the vortex.

Quantum vortices can be very well described by means of their velocity field, which can be obtained through the current as $\vec{j}(\vec{r}) = n(\vec{r})\vec{v}(\vec{r})$, where the current is defined as:

$$\vec{j}(\vec{r}) = -i\frac{\hbar}{2m}\left(\Psi^*(\vec{r})\vec{\nabla}\Psi(\vec{r}) - \Psi(\vec{r})\vec{\nabla}\Psi^*(\vec{r})\right) = n(\vec{r})\frac{\hbar}{m}\vec{\nabla}S(\vec{r})\,. \tag{3.42}$$

The corresponding velocity field is

$$\vec{v}(\vec{r}) = \frac{\hbar}{m}\vec{\nabla}S(\vec{r})\,. \tag{3.43}$$

The previous expression clearly shows that states that present phase gradients have associated a current field. On the other hand, states with flat phase pattern, like ground states, are currentless.

In the case of a quantum vortex centered at the origin of coordinates and rotating around the z-axis, the wave function is (in cylindrical coordinates):

$$\Psi(\vec{r}) = \sqrt{n(\rho, z)}\, e^{i\kappa\varphi}\,, \tag{3.44}$$

which fulfills the condition that the phase must wind from 0 to $2\pi\kappa$ around the vortex core. Equation (3.44) shows that the phase pattern of a quantum vortex is $S(\vec{r}) = \kappa\varphi$, and then, the velocity field, which is proportional to the gradient, is:

$$\vec{v}(\vec{r}) = \frac{\kappa\hbar}{m\rho}\hat{\varphi}\,. \tag{3.45}$$

From this expression, it is straightforward to see that the circulation along the core is indeed quantized:

$$\Gamma = \oint \vec{v}\cdot d\vec{\ell} = \frac{\hbar\kappa}{m}\oint \frac{1}{\rho}d\vec{\ell} = \frac{\hbar\kappa}{m}\oint \frac{1}{\rho}\rho d\varphi = \frac{\hbar\kappa}{m}\oint d\varphi = \frac{h}{m}\kappa\,, \tag{3.46}$$

where h/m is the quantum of circulation, and the winding number κ becomes the quantization number. In addition, the angular momentum per particle is also quantized, in such a way that

$$\langle \hat{L}_z \rangle = \langle \Psi(\vec{r})| - i\hbar \frac{\partial}{\partial \varphi} |\Psi(\vec{r})\rangle = -i\hbar \int d\vec{r}\, n(\vec{r}) e^{-i\kappa\varphi} \frac{\partial e^{i\kappa\varphi}}{\partial \varphi} = \hbar\kappa \int d\vec{r}\, n(\vec{r}) = \hbar\kappa N\,, \quad (3.47)$$

and $\langle \hat{L}_z \rangle / N = \hbar\kappa$.

Regarding the density profile, the characteristic feature of a vortex is, as previously mentioned, that the density goes to zero when approaching the axis of rotation. This density depletion is known as the core of the vortex, and its size strongly depends on interactions. In the case of a condensate trapped in a harmonic oscillator, the size of the vortex core scales with the radial oscillator length for small interactions, and with a characteristic length $\xi = \hbar/\sqrt{2gnm}$, called healing length (see below), for large interactions. In the case of noninteracting condensates, the analytical solution of the vortex is:

$$n(\rho, z) \propto \rho^2 e^{-m\left(\omega_\perp \rho^2 + \omega_z z^2\right)/\hbar}\,. \quad (3.48)$$

In contrast, in the interacting case, there is no analytical solution, but it is possible to analytically reveal that the size of the core scales with the healing length. If we write the Gross-Pitaevskii equation (3.6) in cylindrical coordinates, we get:

$$-\frac{\hbar^2}{2m}\frac{1}{\rho}\frac{d}{d\rho}\left(\frac{d\sqrt{n(\vec{r})}}{d\rho}\right) + \frac{\hbar^2}{2m\rho^2}\sqrt{n(\vec{r})} + gn(\vec{r})\sqrt{n(\vec{r})} = \mu n(\vec{r})\,. \quad (3.49)$$

At this point, and following the derivation of Ref. [Pit03], we can express the density as $\sqrt{n(\vec{r})} = \sqrt{n_{\rm GS}(\vec{r})} f(\beta)$, where $n_{\rm GS}(\vec{r})$ is the density of the ground state and $\beta = \rho/\xi$. Under the assumption that near the core, the ground state density is constant and $n = \mu/g$, we can derive a differential equation for the function $f(\beta)$:

$$\frac{d^2 f(\beta)}{d\beta^2} + \frac{1}{\beta}\frac{df(\beta)}{d\beta} + \left(1 - \frac{1}{\beta^2}\right) f(\beta) - f^3(\beta) = 0\,. \quad (3.50)$$

The numerical solution of this equation shows that the parameter ξ, the healing length, is the distance that the condensate needs to recover the background density if at some point, the density vanishes. In future subsections, we will see that the existence of a healing length is intrinsically linked to the appearance of any topological defect (accompanied by a sudden increase or decrease of the density), and it is not a particularity of vortices.

Figure 3.2(a) depicts the $\kappa = 1$ vortex state of a 2D condensate in a harmonic trap, for the case of $gN = 200\hbar\omega_{\rm ho} a_{\rm ho}^2$. The inset, shows in a gray scale the density in the 2D plane, clearly revealing the hole in the center of the vortex core with a characteristic size given by the healing length.

3.4.2 Solitons

Solitons, also known as solitary waves, are states that can propagate in time and/or space without dispersion and collide with other solitons without distorting their intrinsic shape, remaining unaltered from the collision except for a phase shift. They can appear both in the classical

and the quantum regime, however, in the latter case, the spectra of solitonic solutions of the Gross-Pitaevskii equation is richer. Depending of the character of the interaction (attractive or repulsive), two kind of solitons can appear: bright and dark (gray) solitons, respectively. The origin of their names resides in the field of optics. Bright solitons are characterized by a localized increase of the intensity, which yields to a brighter region in space [Bjo74], whereas dark solitons present a depletion of the light intensity [Emp87] in a localized region, which subsequently becomes dark.

Bright solitons (attractive interaction)

Bright solitons [Bil13] are solutions characterized by an increase of the density in a localized point. This localized rise of the density gets stabilized by virtue of the natural dispersion that matter waves suffer (to minimize the kinetic energy), which compensates attractive interactions, and prevents collapse of the Bose-Einstein condensate. In a 1D homogeneous condensate, the solution is analytical:

$$\Psi_{\mathrm{BS}}(x) = \sqrt{n}\,\mathrm{sech}\left(\frac{x - x_0}{\sqrt{2}\xi}\right), \tag{3.51}$$

where n is the background density, x_0 is the position of the bright soliton (the position of the maximum of the density) and $\xi = \hbar/\sqrt{2gnm}$ is again the healing length, that gives a measure of the distance from the position of the maximum to recover the background density. Therefore, the healing length gives the order of magnitude of the width of a bright soliton. The above equation is represented in Fig. 3.2(b).

Dark (gray) solitons (repulsive interaction)

In contrast to bright solitons, which appear for attractive interaction, when the interaction is repulsive, dark solitons are favoured. They are states characterized by a depletion of the density at a certain point in 1D, and in a plane in 3D (called soliton plane). In the case of static dark solitons, the density depletion is complete (i.e. the density at the soliton plane is zero), and the phase suffers a change of π across the soliton plane. In contrast, for moving dark solitons, the density depletion is not complete, and the phase jump is smaller than π. Dark solitons with incomplete density depletion, like moving dark solitons, are called gray solitons.

Dark soliton solutions of the Gross-Pitaevskii equation, for the homogeneous and 1D case, have also an analytical expression [Fra10]:

$$\Phi_{\mathrm{DS}}(x,t) = \sqrt{n}\left\{i\frac{v}{c} + \gamma\tanh\left(\frac{\gamma}{\sqrt{2}\xi}(x - x_0 - vt)\right)\right\}, \tag{3.52}$$

where n is the background density, x_0 is the position of the soliton point, v is the velocity of the soliton and $c = \sqrt{gn/m}$ is the sound velocity. $\xi = \hbar/\sqrt{2gnm}$ is the healing length of the soliton, which indicates at which distance from the center the soliton recovers the background density, and $\gamma = \sqrt{1 - v^2/c^2}$ plays the role of a "relativistic" parameter that remarks that the velocity of a dark soliton can not exceed the sound velocity. The density associated to Eq. (3.52) is represented in Fig. 3.2 (c) for three different velocities: $v = 0$ (static dark soliton), $v = 0.4\,c$ and $v = 0.8\,c$, which correspond to the solid black line, dashed red line and dot-dashed blue line, respectively.

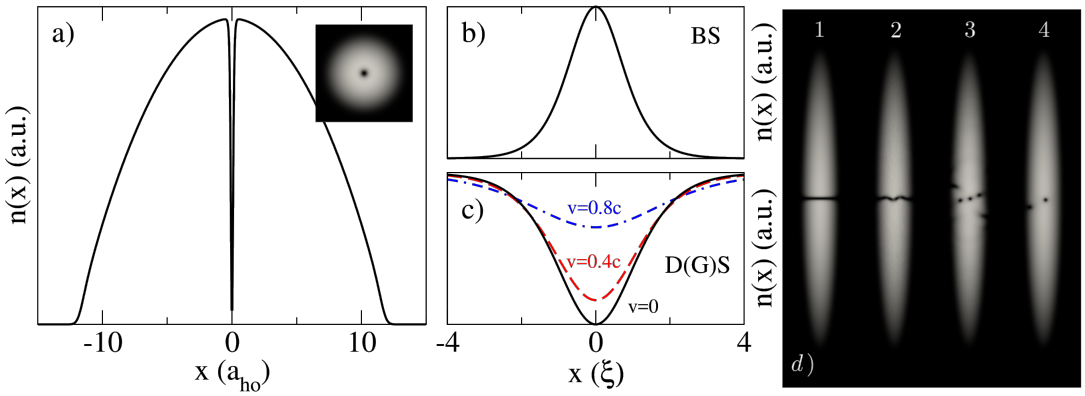

Figure 3.2: a) Density profile along the x-axis of a single vortex with winding number $\kappa = 1$ in a Bose-Einstein condensate confined in a harmonic trap with $gN = 200\hbar\omega_{\rm ho}a_{\rm ho}^2$, where N is the total number of particles. In the inset, the density profile in the x-y plane. b) Density profile of a bright soliton in a homogeneous condensate. c) Density profile of dark (grey) solitons in a homogeneous condensate, corresponding to the following velocities: $v = 0$ (black), $v = 0.4\,c$ (red) and $v = 0.8\,c$ (blue). d) Density profile of a dark soliton in the x-y plane in a cigar-shaped condensate, at different stages of the decay into a solitonic vortex [Bra01]: 1. Initial state, 2. Distortion of the soliton plane (snake instability), 3. Decay into vortices, 4. All the vortices except for one, scape from the condensate, leading to a perturbation of the surface of the condensate. The remaining vortex in the bulk is the so-called solitonic vortex.

Dark solitons are dynamically stable in 1D condensates. However, in 2 and 3 dimensions and at large interactions, small perturbations can distort the soliton plane, by exciting transversal modes. This distortion yields to the so-called snake instability. When it occurs, the dark soliton decays to another topological object. In the case of a dark soliton in a cigar-shaped condensate, it has been demonstrated that the product of the snake instability is a (solitonic) vortex [Bra01], which is a vortex that appears after the dark soliton decay, conserving the initial energy and angular momentum, except for the small amount of these quantities added by the perturbation. The decay of a dark soliton into a solitonic vortex for the case of a cigar-shaped condensate is represented in Fig. 3.2 (d). In snapshot 1 there is the dark soliton before adding the perturbation. In snapshot 2, after the perturbation, the soliton plane, gets distorted (snake instability). Snapshot 3 shows how the curved soliton plane decays into an array of vortices, which scape from the condensate, remaining only one of them, the solitonic vortex (snapshot 4). In the case of pancake-shaped condensates, the product of the decay of the dark soliton is richer, and one can find vortex-antivortex pairs, or lumps, which appear as dark solitons joining a vortex and an antivortex [Hua03].

3.4.3 Experimental techniques to generate topological states

Experimental realization of topological defects and nontrivial phase patterns in a Bose-Einstein condensate requires a good control of the quantum phase. Among the different techniques that exist, there are three that will be discussed in the present section. The first one, phase imprinting [Den00], is an experimental technique that was developed at the end of the

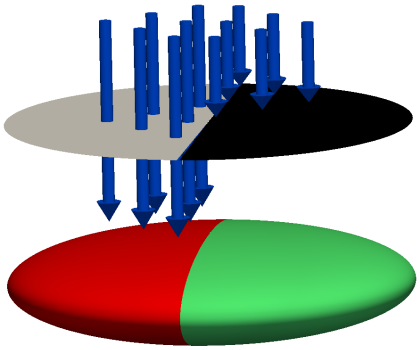

Figure 3.3: Schematic picture that represents phase imprinting. The laser beam (blue arrows) passes through an absorption plate (in the picture, the plate blocks the light that shines half of the condensate), and the condensate acquires a space-dependent phase profile (in the picture, half of the condensate has a different phase than the other half).

last century that allows to engineer atomic gases with different phase profiles. It has been particularly relevant to obtain vortices [Dob99] and solitons [Bur99, Den00], which, as previously mentioned, are states with a nontrivial phase pattern. Phase imprinting can be experimentally realized by shining the condensate with a far-off-resonant laser pulse that has passed through an space-dependent absorption plate. The space-dependence light-shift produced by the pulse leads to a space-dependent phase shift in the condensate wave function. The equation that gives the values of the imprinted phase in the case of the generation of a dark soliton in x_0 by phase imprinting is [Bur02]:

$$\varphi(x) = \frac{\pi}{2}\left[1 + \tanh\left(\frac{x - x_0}{bW}\right)\right], \tag{3.53}$$

where W is the *stepness* of the phase gradient and b is an empirical coefficient that accounts for absorption in the imprinting process. Figure 3.3(a) illustrates the phase imprinting process for the case of a dark soliton. The laser pulse (blue arrows) cross a space-dependent absorption plate (disk with inhomogeneous colors that represent the inhomogeneous absorption). Then, the light shines the condensate (ellipsoid) in such a way that it acquires an inhomogeneous phase (represented by the different colors of the surface of the ellipsoid.

Another way to generate topological states consists in stirring a condensate to excite collective modes through the anisotropy of the condensate, which yields to the nucleation of a vortex if the frequency of rotation is above a critical one. It has been also shown that for increasing rotation frequency, instead of a single vortex, many vortices appear constituting an array called Abrikosov lattice. In addition, another technique called density-engineering method has allowed the creation of a dark soliton in a condensate. This method consists in manipulating the phase pattern of the Bose gas through the generation of shock waves that appear after the sudden reduction of the density at a certain point of the system.

Chapter 4

Bose-Einstein condensates in the mean-field regime: two-component condensates

We have studied in the previous chapter the physics of single-component Bose-Einstein condensates. In the case of systems where the atoms can condense in more than a single quantum state, the system can be described as several coupled condensates. This kind of systems are known in the literature as multicomponent condensates. Mixtures and spinor condensates are paradigmatic cases of this type of condensates. Mixtures are systems constituted by condensates of different type of atoms or isotops that can interact without exchanging particles. In the case of spinor condensates, condensation simultaneously occurs in different hyperfine levels, and as a consequence, the condensate acquires an additional degree of freedom: the spin. As in mixtures, the different condensate components can interact between them. Nevertheless, there is another mechanism, the spin-flip, which can modify the population of each condensate component keeping constant the total number of particles. The hamiltonian of a spinor system can be written in terms of spin matrices, whose off-diagonal terms describe the spin-flip physics.

In the particular case of a spinor condensate with two components, the off-diagonal term receives the name of Rabi coupling (due to the fact that it can be experimentally realized by coupling the different hyperfine states of an atom with Raman processes, the off-diagonal term is also called Raman coupling). Apart from that, it has been also shown that spin-orbit coupling [Ho11, Gal13a, Sta08] between the spin and the linear or angular momentum can be generated in cold atoms. In quantum mechanics, two main types of spin-orbit coupling are reported on literature: Rashba [Ras60, Byc84], and Dresselhaus [Dre55] spin-orbit coupling, which have become a focus of research in many fields of solid state physics, as semiconductors [Ber11] or quantum dots [Kha00]. They are characterized for effectively operating in 2 dimensions, e.g. they couple both the k_x and k_y-component of the momentum to the spin: Rashba spin-orbit coupling is proportional to $\alpha_R(k_x\hat{\sigma}_y - k_y\hat{\sigma}_x)$, and Dresselhaus spin-orbit coupling is proportional to $\alpha_D(k_x\hat{\sigma}_y + k_y\hat{\sigma}_x)$, where $\hat{\sigma}_x$ and $\hat{\sigma}_y$ are the Pauli matrices and α_R and α_D are the strengths of the Rashba and Dresselhaus spin-orbit coupling, respectively. Nevertheless, in cold atoms, the first spin-orbit coupling that was experimentally implemented was a superposition of the two

previous ones ($\alpha_R = \alpha_D$), named Rashba-Dresselhaus spin-orbitcoupling [Lin11], and with the particular feature of being 1-dimensional: it means that it couples the component of the linear momentum in a single dimension to the spin. Few years later, Bose-Einstein condensates with pure Rashba spin-orbit coupling have been also achieved [Hua16].

In this chapter, we will present the equations that describe a two (spin)-component Bose-Einstein condensate. In particular, we address the physics of the coherent coupling between both components that accounts for spin-flip processes, by analyzing how the miscibility condition and excitations are modified under the presence of Rabi coupling. Finally, we present a derivation of the equations of a Bose-Einstein condensate with two components coupled via a Rashba-Dresselhaus mechanism.

4.1 Gross-Pitaevskii equations for a two-component Bose-Einstein condensate

As single-component condensates, multicomponent systems can be also dealed in the mean-field regime. In the case of two spinor components, the system can be considered as an effective pseudospin-1/2 system (and then the symbols $\uparrow$ and $\downarrow$ will denote the two components), and can be described by means of two coupled Gross-Pitaevskii equations but with some additional terms with respect to the single-component case:

$$\begin{aligned} i\hbar\frac{\partial}{\partial t}\Psi_\uparrow &= \mathcal{H}_0\Psi_\uparrow + g_{\uparrow\uparrow}|\Psi_\uparrow|^2\Psi_\uparrow + g_{\uparrow\downarrow}|\Psi_\downarrow|^2\Psi_\uparrow + \frac{\hbar\Omega}{2}\Psi_\downarrow \\ i\hbar\frac{\partial}{\partial t}\Psi_\downarrow &= \mathcal{H}_0\Psi_\downarrow + g_{\downarrow\downarrow}|\Psi_\downarrow|^2\Psi_\downarrow + g_{\uparrow\downarrow}|\Psi_\uparrow|^2\Psi_\downarrow + \frac{\hbar\Omega}{2}\Psi_\uparrow\,, \end{aligned} \tag{4.1}$$

where $\mathcal{H}_0(\vec{r}) = -\hbar^2/2m\,\vec{\nabla}^2 + V_{\text{trap}}(\vec{r})$. The parameters $g_{\uparrow\uparrow}$ ($g_{\downarrow\downarrow}$) are the intraspecies coupling constants between atoms with the same spin-$\uparrow$ (spin-$\downarrow$) and $g_{\uparrow\downarrow}$ is the interspecies coupling between atoms with different spin, and couples the two components through their density. The last term, which is proportional to the Rabi frequency Ω, is a linear term that couples the condensate wave function of the spin-$\uparrow$ component $\Psi_\uparrow$ with $\Psi_\downarrow$, the condensate wave function of the spin-$\downarrow$ component. This term is also known as the coupling through the phase, and it allows the exchange of particles between both components. In many cases of interest, like ^{87}Rb condensates, the coupling constants $g_{\uparrow\uparrow}$ and $g_{\downarrow\downarrow}$ are known to be very similar, and because of that, we will work under the approximation $g = g_{\uparrow\uparrow} = g_{\downarrow\downarrow}$, except for the derivation of the miscibility condition (see below).

Performing an analogous procedure to the one developed for the single-component case, one can derive the two coupled time-independent Gross-Pitaevskii equations that describe the two components of the system:

$$\begin{aligned} \mu_\uparrow\Psi_\uparrow &= \mathcal{H}_0\Psi_\uparrow + g_{\uparrow\uparrow}|\Psi_\uparrow|^2\Psi_\uparrow + g_{\uparrow\downarrow}|\Psi_\downarrow|^2\Psi_\uparrow + \frac{\hbar\Omega}{2}\Psi_\downarrow \\ \mu_\downarrow\Psi_\downarrow &= \mathcal{H}_0\Psi_\downarrow + g_{\downarrow\downarrow}|\Psi_\downarrow|^2\Psi_\downarrow + g_{\uparrow\downarrow}|\Psi_\uparrow|^2\Psi_\downarrow + \frac{\hbar\Omega}{2}\Psi_\uparrow\,, \end{aligned} \tag{4.2}$$

where $\mu_\uparrow$ and $\mu_\downarrow$ are the chemical potential of each component, respectively.

The physics of the coherent Rabi coupling has been described with detail in several papers

in the literature [Aba13, Tyl16, Son02]. When there is no Rabi coupling, the phase of each component is independent of the other phase, and, as a consequence, the symmetry of the system is $U(1) \times U(1)$, which yields to the conservation of the number of particles in each component. However, this symmetry no longer holds when the Rabi coupling is activated. The concept of the phase of each component disappears and in this case there is a global phase that evolves according to a single chemical potential $\mu = \mu_\uparrow = \mu_\downarrow$. Therefore, the symmetry of the system is $U(1)$, and the total number of particles is conserved rather than the number of particles per component, which can vary (through spin-flip processes) keeping the total one constant.

4.1.1 Miscibility and polarization

In the absence of the Rabi coupling, the competition between the interspecies and the intraspecies interaction results in a transition between two phases: the miscible and the immiscible phase. The miscible phase is characterized by a spatial overlap of the two components, whereas in the immiscible phase, the two components exhibit a spatial separation (or phase separation). In contrast, in the presence of Rabi coupling, phase separation is no longer energetically favourable, and the system exhibits population spin imbalance (which is possible through spin-flips). Then, the two new phases are characterized by the Rabi frequency and the interacting coupling constants, and they are named as the unpolarized and the polarized phase. In this section, we will first calculate the miscibility condition in the case of no Rabi coupling, and the polarization condition when Ω is nonzero.

In order to find the miscibility condition, let us suppose a 1D condensate in a box of volume V, constituted by two components with $N_\uparrow$ and $N_\downarrow$ atoms, respectively. In the homogeneous case, the energy in the miscible phase E_M depends on the coupling constants, only:

$$E_\mathrm{M} = \frac{1}{2V} g_{\uparrow\uparrow} N_\uparrow^2 + \frac{1}{2V} g_{\downarrow\downarrow} N_\downarrow^2 + \frac{1}{V} g_{\uparrow\downarrow} N_\uparrow N_\downarrow \,. \tag{4.3}$$

In contrast, in the immiscible phase, the two components are separated. Assuming $V_\uparrow$ ($V_\downarrow$) the volume of the $\uparrow(\downarrow)$ component, the energy of the system E_I is:

$$E_\mathrm{I} = \frac{1}{2V_\uparrow} g_{\uparrow\uparrow} N_\uparrow^2 + \frac{1}{2V_\downarrow} g_{\downarrow\downarrow} N_\downarrow^2 \,. \tag{4.4}$$

In the immiscible phase, when the interaction is large, one can notice that the two components do not overlap, and one can consider that $V = V_\uparrow + V_\downarrow$. Then, the pressure (energy per volume) equilibrium must be fulfilled, which implies that

$$\frac{\partial E_\mathrm{I}}{\partial V_\uparrow} = \frac{\partial E_\mathrm{I}}{\partial V_\downarrow} \,. \tag{4.5}$$

Combining these two conditions, one obtains that in equilibrium,

$$V_{\uparrow(\downarrow)} = V \left(1 + \sqrt{\frac{g_{\downarrow\downarrow(\uparrow\uparrow)}}{g_{\uparrow\uparrow(\downarrow\downarrow)}}} \frac{N_{\downarrow(\uparrow)}}{N_{\uparrow(\downarrow)}} \right)^{-1} , \tag{4.6}$$

and then

$$E_{\mathrm{I}} = \frac{1}{2V} g_{\uparrow\uparrow} N_{\uparrow}^2 + \frac{1}{2V} g_{\downarrow\downarrow} N_{\downarrow}^2 + \frac{1}{V} \sqrt{g_{\uparrow\uparrow} g_{\downarrow\downarrow}} N_{\uparrow} N_{\downarrow} \,. \tag{4.7}$$

Looking at Eqs. (4.3) and (4.7), one can easily see that for

$$g_{\uparrow\uparrow} g_{\downarrow\downarrow} \geq g_{\uparrow\downarrow}^2 \,, \tag{4.8}$$

the two components are miscible, i.e. the miscible phase is energetically favourable $E_{\mathrm{I}} \geq E_{\mathrm{M}}$, whereas when the previous condition is not fulfilled, the immiscible phase is energetically favourable and both components will spatially separate. Equation (4.8) is known as the miscibility condition.

When the Rabi coupling is active, both components can exchange particles, and one can not talk about miscibility instead of polarizability. Spin-polaritzation is energetically favourable, since, spatial separation leads to an increase of the kinetic energy due to the curvature of the wave function in the boundary of each component. It means that, unless $g_{\uparrow\downarrow}$ is much larger than $g_{\uparrow\uparrow}$ and $g_{\downarrow\downarrow}$, the condensate will remain in the miscible phase, but two new phases in this regime will appear: the spin-unpolarized and the spin-polarized phase (with different degrees of polarization).

Therefore, in this case, there is a condition that fixes the boundary between these two phases. In the homogeneous case, the densities of each component are $n_{\uparrow}$ and $n_{\downarrow}$, and the energy per unit volume is (assuming miscibility) [Aba15]:

$$\mathcal{E} = \frac{1}{2} g_{\uparrow\uparrow} n_{\uparrow}^2 + \frac{1}{2} g_{\downarrow\downarrow} n_{\downarrow}^2 + g_{\uparrow\downarrow} n_{\uparrow} n_{\downarrow} - 2\Omega \sqrt{n_{\uparrow} n_{\downarrow}} \,. \tag{4.9}$$

The minimization of the previous energy with respect to the density, under the condition $n_{\uparrow} + n_{\downarrow} = n$, yields to the ground state of the system. For the particular case of $g_{\uparrow\uparrow} = g_{\downarrow\downarrow} = g$, the minimization condition can be written as:

$$\left(g - g_{\uparrow\downarrow} + \frac{\Omega}{2\sqrt{n_{\uparrow} n_{\downarrow}}} \right) (n_{\uparrow} - n_{\downarrow}) = 0 \,. \tag{4.10}$$

This yields to the unpolarized phase $n_{\uparrow} - n_{\downarrow} = 0$ for

$$g_{\uparrow\downarrow} < g + \frac{\Omega}{n} \,, \tag{4.11}$$

and the polarized phase otherwise, with the solution corresponding the given polarization

$$n_{\uparrow} - n_{\downarrow} = \pm \sqrt{1 - \left(\frac{\Omega}{(g - g_{\uparrow\downarrow}) n} \right)^2} \,. \tag{4.12}$$

In the left panel of Fig. 4.1 we show the spin-polarization imbalance of the ground state as a function of $(g - g_{\uparrow\downarrow})n/\Omega$. When Eq. (4.11) is fulfilled, the system is unpolarized (yellow region), whereas when the previous condition does not hold, the system is polarized (blue region).

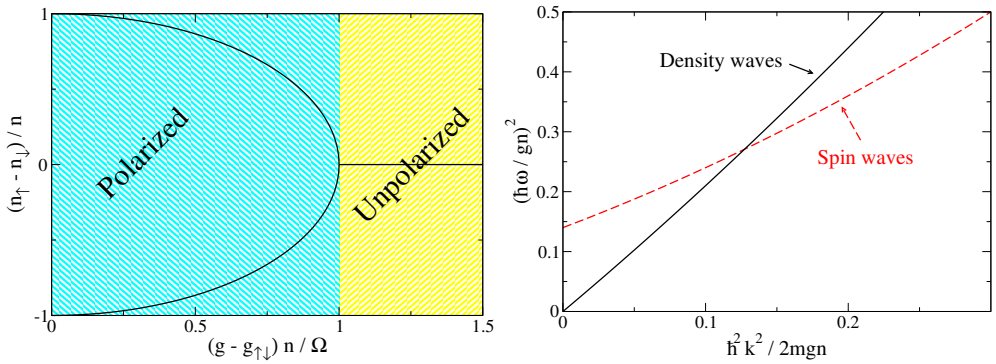

Figure 4.1: Left: Phase diagram of the homogeneous system. When the polarization condition (4.11) is not fulfilled the system exhibits spin polarization. In contrast, when this condition is fulfilled, the ground state of the system is that with equal background density per component $n_\uparrow = n_\downarrow = n/2$. Right: Bogoliubov excitations of density waves (solid black line) and spin waves (dashed red line) for $g_{\uparrow\downarrow} = 0.5\, g$ and $\hbar\Omega = 0.1\, gn$. We can observe that whereas at $k = 0$, density wave excitations are gapless, spin wave excitations acquire a gap.

4.1.2 Excitation spectrum

As in the single-component case, it is also possible to derive the Bogoliubov excitations corresponding to a two-component homogeneous Bose-Einstein condensate, by using an analogous method used in Sect. 3.3. The main difference is that when analyzing the excitation spectrum for $\Omega = 0$, one finds two kind of gapless excitations, known as density (the ordinary excitation in a bulk superfluid), with sound velocity:

$$c_{\mathrm{DW}} = \sqrt{\frac{(g + g_{\uparrow\downarrow})n}{2m}}\,, \tag{4.13}$$

and spin waves (waves originated by a local polarization in the system), with sound velocity

$$c_{\mathrm{SW}} = \sqrt{\frac{(g - g_{\uparrow\downarrow})n}{2m}}\,, \tag{4.14}$$

where the background densities of each component have been assumed to be equal to $n/2$. It is important to notice that in the case of $g = g_{\uparrow\downarrow}$, one recovers the sound velocity of the single-component case for density waves, where spin waves can not propogate, due to the vanishing of the spin save sound velocity.

However, the Rabi coupling does play an important role regarding the excitations: whereas the density wave excitation spectrum remains unaltered and gapless, the excitation spectrum of spin waves acquires a gap that increases with the Rabi frequency Ω:

$$\omega_{\mathrm{SW}} = \sqrt{\frac{n}{2m}\left(g + \frac{\Omega}{n} - g_{\uparrow\downarrow}\right)(k^2 + 2m\Omega)}\,. \tag{4.15}$$

We can see that in order to have stable spin wave excitations, the miscibility (zero-polarization)

condition (4.11) must be fulfilled.

In the right panel of Fig. 4.1, we represent the excitation energy of density waves (solid black line) and spin waves (dashed red line) in units of gn as a function of the momentum, for the case of $\hbar\Omega = 0.1gn$ and $g = 0.5g_{\uparrow\downarrow}$. Whereas the former goes to zero as the wave vector vanishes, the latter goes to a nonzero value of the energy, which means that one has to apport a given energy to the system, even at $k = 0$, in order to excite a spin wave.

4.2 Spin-orbit coupled Bose-Einstein condensates

Spin-orbit coupled Bose gases are condensates with more than one component (typically two), in such a way that there exists a coupling between the momentum operator and the spin operator (given in two-component systems by the 2×2 Pauli matrices). In this section we will explain how this kind of coupling can be generated experimentally. We will derive the linear part of the spin-orbit coupled hamiltonian that has been engineered experimentally, and finally, we will introduce its phase diagram both in the noninteracting and interacting case.

4.2.1 Experimental realization of Rashba-Dresselhaus spin-orbit coupling

Few years ago, the first spin-orbit coupled Bose gas was experimentally realized in the group of Ian Spielman [Lin11]. This was achieved with a spin $F = 1$ spinor ^{87}Rb Bose gas, by applying on the system a strong magnetic field that induces a Zeeman shift between the hyperfine levels and a two-photon Raman beam in order to couple the different hyperfine levels of the atom. Due to the strength of the magnetic field both the linear and the quadratic terms of the Zeeman shift must be kept in the hamiltonian.

In a spin $F = 1$ Bose gas, the basis of the problem has three elements (hyperfine states), corresponding to the three projections of F_z, whose quantum label is $M_F = -1, 0, 1$. Over these states, we build the hamiltonian, which is the sum of different contributions: kinetic energy, external trap, linear and quadratic Zeeman effect, and the hamiltonian corresponding to the two-photon Raman beam

$$\mathcal{H} = \mathcal{H}_0 + \mathcal{H}_Z^1 + \mathcal{H}_Z^2 + \mathcal{H}_{2P}\,. \tag{4.16}$$

In the hyperfine basis, the kinetic term and the one corresponding to the external trap are diagonal in the hamiltonian, so, $\mathcal{H}_0 = (\hbar^2 k^2/2m + V_{\text{trap}})\mathbb{1}$. Regarding the splitting of the energy levels due to Zeeman effect, the linear term is proportional to the third component of the spin (so proportional to the third Pauli matrix $\hat{\sigma}_z$) $\mathcal{H}_Z^1 = \hbar\Delta_1\hat{\sigma}_z$, whereas the quadratic term, also known as quadratic Zeeman effect, is proportional to $\hat{\sigma}_z^2$, therefore $\mathcal{H}_Z^2 = \hbar\Delta_2\hat{\sigma}_z^2$, where Δ_1 and Δ_2 are the magnitudes of the linear and quadratic Zeeman shift, respectively.

In order to take into account the two-photon Raman coupling one has to introduce the following term in the hamiltonian [Zha12, Zha15]:

$$\mathcal{H}_{2\text{P}} = \hbar \begin{pmatrix} \delta\omega & \Omega e^{i(2k_L x - \delta\omega t)} & 0 \\ \Omega e^{-i(2ik_L x - \delta\omega t)} & 0 & \Omega e^{i(2k_L x - \delta\omega t)} \\ 0 & \Omega e^{-i(2k_L x - \delta\omega t)} & -\delta\omega \end{pmatrix}, \tag{4.17}$$

where Ω is the average Rabi coupling, $\delta\omega$ is the energy difference between the two Raman lasers, and $k_L = \sqrt{2}\pi/\lambda$ is the laser wave vector, which has been chosen to be in the x-direction (see a justification of the $\sqrt{2}$ in Ref. [Rad11]). Then, the complete hamiltonian can be rewritten as:

$$\begin{aligned}\mathcal{H} = &\left(\frac{\hbar^2 k^2}{2m} + V_{\text{trap}}\right)\mathbb{1} + \hbar\begin{pmatrix}\Delta_1 + \Delta_2 + \delta\omega & 0 & 0\\ 0 & 0 & 0\\ 0 & 0 & \Delta_2 - \Delta_1 - \delta\omega\end{pmatrix}\\ &+ \hbar\Omega\left[\begin{pmatrix}0 & 1 & 0\\ 1 & 0 & 1\\ 0 & 1 & 0\end{pmatrix}\cos 2k_L x + \begin{pmatrix}0 & i & 0\\ -i & 0 & i\\ 0 & -i & 0\end{pmatrix}\sin 2k_L x\right]. \end{aligned} \tag{4.18}$$

When adjusting $\delta\omega$ and Zeeman parameters Δ_1 and Δ_2 such that $\delta\omega + \Delta_1 \simeq \Delta_2$, we can see (in Fig. 4.2) that the energy of the $|M_F = +1\rangle$ state becomes large compared to other energy scales of the system. Thus, we can consider only the physics in a two-state system spanned by $|M_F = 0\rangle$ and $|M_F = -1\rangle$, where the state $|M_F = +1\rangle$ has become uncoupled from the rest of the system. Figure 4.2 sketches a diagram with the splittings that the different hyperfine levels suffer when the two-photon Raman beam, the linear and the quadratic Zeeman effect are introduced, respectively. Under these conditions, the hamiltonian (4.18) can be approximated as:

$$\mathcal{H} = \left(\frac{\hbar^2 k^2}{2m} + V_{\text{trap}}\right)\mathbb{1} + \hbar\begin{pmatrix}0 & 0\\ 0 & \delta\end{pmatrix} + \hbar\Omega(\hat{\sigma}_x \cos 2k_L x - \hat{\sigma}_y \sin 2k_L x)\,, \tag{4.19}$$

where now the Pauli matrices are written in the 2×2 representation, and $\delta = \Delta_2 - \Delta_1 - \delta\omega$ is called *detuning*.

Mathematically, this hamiltonian can be further simplified, in such a way that the term that includes spin-orbit coupling appears as a diagonal term in the hamiltonian. In order to do that, on has to perform a local spin rotation with angle $\theta = k_L x$ around the z-axis, which is a unitary transformation. Afterwards, the new form of the hamiltonian is:

$$\mathcal{H}' = U\mathcal{H}U^\dagger\,, \tag{4.20}$$

where

$$U = \begin{pmatrix}e^{-i\theta} & 0\\ 0 & e^{i\theta}\end{pmatrix} \tag{4.21}$$

is the unitary transformation corresponding to the rotation in the spin space. All the terms of the hamiltonian remain unaltered except for two of them: the kinetic and the Rabi term. The kinetic energy, which depends on k, suffers a spin-dependent boost of magnitude k_L, in such a way that

$$\begin{aligned}k^2\mathbb{1} \to &\begin{pmatrix}e^{-ik_L x} & 0\\ 0 & e^{ik_L x}\end{pmatrix} k^2 \begin{pmatrix}e^{ik_L x} & 0\\ 0 & e^{-ik_L x}\end{pmatrix} = \begin{pmatrix}(\vec{k} + k_L\hat{e}_x)^2 & 0\\ 0 & (\vec{k} - k_L\hat{e}_x)^2\end{pmatrix}\\ =&\frac{\hbar^2 k^2}{2m}\mathbb{1} + \frac{\hbar^2 k_L^2}{2m}\mathbb{1} + \frac{\hbar^2 k_x k_L}{m}\hat{\sigma}_z\,. \end{aligned} \tag{4.22}$$

The two additional terms that appear are the recoil energy $E_{\text{Rec}} = \hbar^2 k_L^2/2m$ (which is the energy scale characteristic of the spin-orbit coupling) and the term that couples the momentum in the

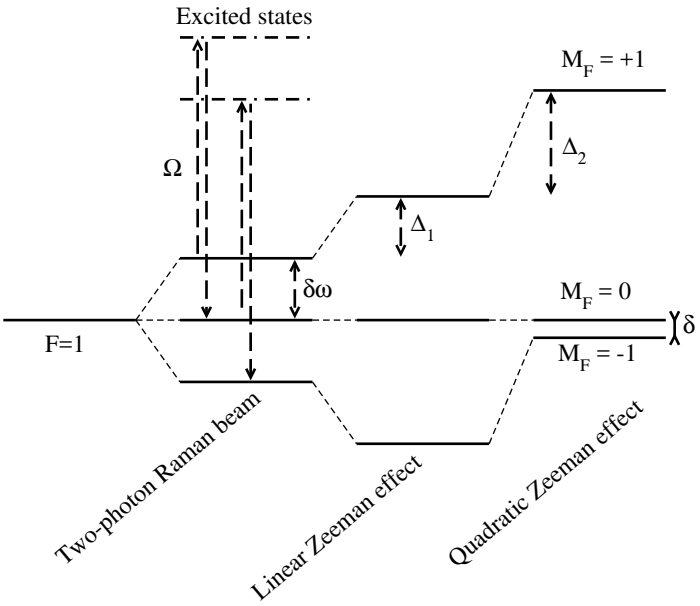

Figure 4.2: Sketch of the splittings that the hyperfine levels $|M_F = +1\rangle$, $|M_F = 0\rangle$ and $|M_F = -1\rangle$ suffer after the introduction of the two-photon Raman beam, and linear and quadratic terms of the Zeeman effect.

x-direction with the spin (given by the Pauli matrix $\hat{\sigma}_z$). The other term affected by the spin rotation is the one corresponding to the Rabi coupling. That term can be written as

$$\hat{\sigma}_x \cos 2k_L x - \hat{\sigma}_y \sin 2k_L x = \begin{pmatrix} 0 & e^{i2\theta} \\ e^{-i2\theta} & 0 \end{pmatrix} , \tag{4.23}$$

and as a consequence,

$$\begin{pmatrix} e^{-i\theta} & 0 \\ 0 & e^{i\theta} \end{pmatrix} \begin{pmatrix} 0 & e^{i2\theta} \\ e^{-i2\theta} & 0 \end{pmatrix} \begin{pmatrix} e^{i\theta} & 0 \\ 0 & e^{-i\theta} \end{pmatrix} = \hat{\sigma}_x \, . \tag{4.24}$$

Thus, the complete hamiltonian reads:

$$\mathcal{H}' = \left(\frac{\hbar^2 k^2}{2m} + V(r) \right) \mathbb{1} + \frac{\hbar^2 k_L}{m} k_x \hat{\sigma}_z + \Omega \hat{\sigma}_x + \begin{pmatrix} 0 & 0 \\ 0 & \delta \end{pmatrix} , \tag{4.25}$$

where we have dropped from the final expression the recoil energy (because it is a constant). The previous hamiltonian works as the single-particle part of the complete hamiltonian. From now on, we will consider the case of $\delta = 0$ only. We will comment, however, the effect of this parameter in the noninteracting case on the phase diagram of the system.

4.2.2 Phase diagram of a homogeneous Rashba-Dresselhaus spin-orbit coupled Bose gas

At the single-particle level, the phase diagram of the hamiltonian (4.25) can be readily obtained by analytically diagonalizing it, which yields to:

$$\frac{E(\vec{k})}{E_{\mathrm{Rec}}} = \left(\frac{k}{k_L}\right)^2 \pm \sqrt{4\left(\frac{k_x}{k_L}\right)^2 + \left(\frac{\Omega}{E_{\mathrm{Rec}}}\right)^2}. \tag{4.26}$$

The ground state (corresponding to the $-$ sign in front of the square root) of the 1D picture has one minimum for $\Omega \geq 2E_{\mathrm{Rec}}$ and two minima otherwise (see left panel of Fig. 4.3). The former phase is known as the single-minimum phase, with a single minimum at zero momentum. It means that the phase profile of each condensate component is flat. However, in the other phase, where two minima appear, the condensate wave function is described by a plane wave with a wave vector corresponding to one of the two minima, and the density imbalance is flat and nonzero. The plot shows the energy as a function of the momentum for values of $\hbar\Omega/E_{\mathrm{Rec}}$ that range from 0 (solid grey lines) to 2.8 (solid purple line) in steps of 0.4. When there exists a detuning $\delta \neq 0$ between the two spin states, the degeneracy between the two minima in the plane-wave phase is broken, and one of the minima gets energetically favoured in front of the other.

The phase diagram of the system dramatically changes in the interacting case. An additional phase appears at low values of the Rabi coupling given a threshold density that depends on the Rabi coupling itself: the stripe phase. This phase is characterized by the appearance of fringes, which come from a sinusoidal density profile, product of the interference of the two plane waves corresponding to the nonlinear extension of the minima of the single-particle hamiltonian.

For large and close (but fulfilling the miscibility condition) values of the interacting couplings g and $g_{\uparrow\downarrow}$, the boundaries between the stripe and plane-wave phases and the plane-wave and single-minimum phases, respectively, can be calculated as [Li12, Li15]:

$$\frac{\hbar\Omega^{(S-PW)}}{E_{\mathrm{Rec}}} = \frac{1}{1+\gamma}\sqrt{\frac{n}{n_c}\left(2(1+\gamma) - \frac{n}{n_c}\right)} \tag{4.27}$$

$$\frac{\hbar\Omega^{(PW-SM)}}{E_{\mathrm{Rec}}} = 2 - \frac{1}{1+\gamma}\frac{n}{n_c}, \tag{4.28}$$

where $n_c = \hbar^2 k_L^2/2mg\gamma$ and $\gamma = (g - g_{\uparrow\downarrow})/(g + g_{\uparrow\downarrow})$. There is a quantum tricritical point at $n = n_c$, at which the previous curves meet, and for higher densities, there is a transition from the stripe phase to the single-minimum phase at the density-independent value of $\Omega = E_{\mathrm{Rec}}$. The previous curves are represented in the right panel of Fig. 4.3, constituting the whole phase diagram of the system in the Ω-n/n_c plane. In addition, the insets schematically depict the structure of the ground state in each phase of the system.

It is important to remind that the single-minimum phase and the stripe phase do not present spin polarization whereas the plane-wave phase does. In addition, the distance between the fringes in the stripe phase depends on the Rabi coupling, in such a way that the increase of the Ω increases the distance between the fringes, until the plane-wave phase or the single-minimum phase is reached.

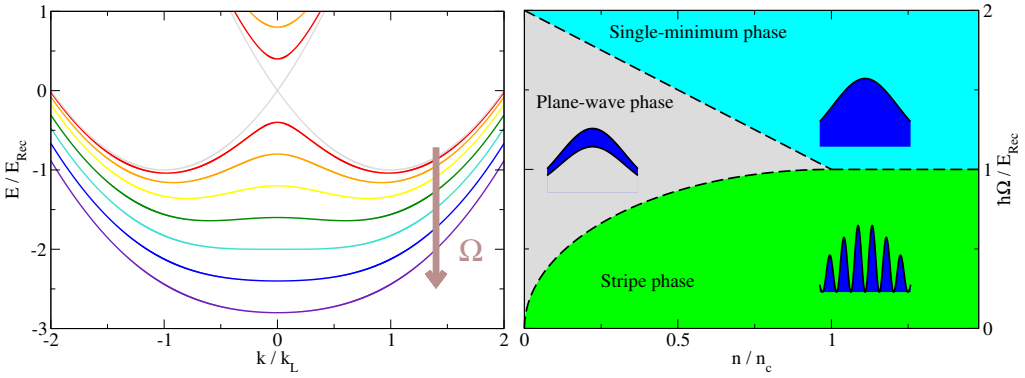

Figure 4.3: Left: Eigenenergies of the 1D single-particle condensate with Rashba-Dresselhaus spin-orbit coupling as a function of the momentum, for the following values of the Rabi coupling (in units of the recoil energy): $\Omega = 0$ (grey), $\Omega = 0.4$ (red), $\Omega = 0.8$ (orange), $\Omega = 1.2$ (yellow), $\Omega = 1.6$ (green), $\Omega = 2$ (cyan), $\Omega = 2.4$ (blue), and $\Omega = 2.8$ (violet). For Ω below $2E_{\mathrm{Rec}}$, there are two minima in the energy landscape (plane-wave phase), whereas above this value, there is only one (single-minimum phase). Right: Phase diagram of the system, as a function of the Rabi coupling and the background density. The insets schematically show the main features of the ground state in the given phase: fringes in the stripe phase, spin polarization in the plane-wave phase, and equal density profiles in the single-minimum phase.

Moreover, the role of a (harmonic) trap has been discussed in the literature (see for instance Ref. [Cao15]). Since the density in a harmonic trap is not homogeneous, and the phase diagram depends on the background density, one can find that in a harmonic trap, different phases of the phase diagram can coexist in the condensate. As an example, at low values of the Rabi coupling, in the central part of the Bose gas (with higher density) the system will exhibit stripes, but at the boundaries, where the density is smaller, spin polarization can appear: a signature of the plane-wave phase.

Chapter 5

Spin models in few-site lattices

In Chap. 2, we have presented the theory of ultracold Bose gases loaded in optical lattices. One of the main applications of lattice gases is the suitability to simulate quantum magnetic models, by identifying each boson at each lattice site by a spin. The achievement of quantum magnetism with ultracold lattice atoms can be regarded as one of the cornerstones of modern physics. Indeed, the seminal proposal [Jak98] that ultracold atoms confined in optical lattices can be described by a Bose-Hubbard model [Fis89] has prompted the field of quantum simulators. Since then, the scope of condensed matter phenomena that can be addressed with ultracold gases and ions has broadened enormously (see e.g [Blo08, Lew07, Lew12, Gre13] and references therein). Nevertheless, the capability of few-site lattices for simulating spin models still requires a deeper study.

For the particular case of the Bose-Hubbard hamiltonian corresponding to the double-well potential, it is possible to perform a mapping to the Lipkin-Meshkov-Glick hamiltonian [Lip65, Mes65, Gli65], which is a spin model developed in the nuclear physics framework. In this chapter, we will first address this mapping and show how, as a consequence, one can deduce that the Bose-Hubbard hamiltonian of the double-well potential possesses a quantum phase transition that shares the same critical exponents with that of the Lipkin-Meshkov-Glick hamiltonian, and thus, both hamiltonians fall in the same universality class [Mus10].

The possibility of performing a similar mapping between a spin model and another configuration involving more than two sites in the Bose-Hubbard model is, up to now, unknown. Nevertheless, one can study the properties of quantum phase transitions by performing finite-size scaling near the transition [Sac99], and then find the corresponding critical exponents, which can be compared with the critical exponents of known quantum phase transitions of other spin models, in order to elucidate whether both transitions fall in the same universality class or not. In the second part of this chapter, we will introduce different configurations that can be considered in a dipolar Bose gas confined in a triple-well potential, as a function of the dipole orientation. In the particular cases that we deal with here, there is a quantum phase transition that possesses the same critical exponents that those of the Lipkin-Meshkov-Glick hamiltonian, and fall, therefore, in the same universality class.

5.1 Bose gases in double-well potentials

In what follows, we present the Bose-Hubbard hamiltonian corresponding to N bosons trapped in a double-well potential, by particularizing the hamiltonian of Eq. (2.4) to two sites ($M = 2$):

$$\hat{H}_2 = -J\left[\hat{b}_1^\dagger \hat{b}_2 + \hat{b}_2^\dagger \hat{b}_1\right] + \frac{U}{2}\left[\hat{n}_1(\hat{n}_1 - 1) + \hat{n}_2(\hat{n}_2 - 1)\right] . \tag{5.1}$$

This hamiltonian possesses two main phases as a function of the parameter $\Lambda = UN/2J$ [Jul10]. These features can be observed from the effective potential of this hamiltonian V_{eff}, which can be obtained in the semiclassical regime. A detailed derivation of such a potential can be seen in Ref. [Zin08]. Ths potential is:

$$V_{\text{eff}}(Z) = NJ\left(\frac{1}{2}\Lambda Z^2 - \sqrt{1 - Z^2}\right) , \tag{5.2}$$

where $Z = (n_1 - n_2)/N$ is the population imbalance, between both sites. This effective potential presents two minima at $Z = \pm\sqrt{1 - 1/\Lambda^2}$ when $\Lambda < -1$, and a single minimum at $Z = 0$ otherwise. The point $\Lambda = -1$ corresponds to the location of the quantum phase transition between the two phases commented above. For $\Lambda < -1$, one obtains spontaneous symmetry breaking, where the system is in a superposition of two states: a cat state[1]. In contrast, for $\Lambda > -1$, the two wells are coherently occupied with equal populations.

An analysis of this quantum phase transition has been widely discussed in Ref. [Jul10], by numerically solving through exact diagonalization the Bose-Hubbard hamiltonian of the two-site system. In this paper, the authors show which is the structure of the ground state as a function of the Λ parameter defined above. In Fig. 5.1 we show the contribution of the different elements of the Fock basis (labelled by its corresponding population imbalance), for different values of Λ. In addition, we plot also the effective potential of the hamiltonian, given by Eq. (5.2).

5.1.1 Mapping to the Lipkin-Meshkov-Glick hamiltonian

In the double-well potential, it is possible to map the hamiltonian onto another hamiltonian widely used in nuclear physics: the Lipkin-Meshkov-Glick hamiltonian. In order to perform such a mapping, one can use the Schwinger representation [Bot83], which allows to map the two-mode annihilation and creation operators onto spin operators:

$$\hat{S}_+ = \hat{b}_1^\dagger \hat{b}_2 , \quad \hat{S}_- = \hat{b}_2^\dagger \hat{b}_1 , \quad \hat{S}_z = \frac{1}{2}(\hat{b}_1^\dagger \hat{b}_1 - \hat{b}_2^\dagger \hat{b}_2) , \tag{5.3}$$

with the constraint $\hat{b}_1^\dagger \hat{b}_1 + \hat{b}_2^\dagger \hat{b}_2 = 2\hat{S} = \hat{N}$, which fixes the total number of bosons or equivalently the total spin. Using such representation, the two-site Bose-Hubbard Hamiltonian can be rewritten as

$$\hat{H}_2 = -J(\hat{S}_+ + \hat{S}_-) + U(\hat{S}_z^2 + \hat{S}^2 - \hat{S}) = -2J\hat{S}_x + U\,\hat{S}_z^2, \tag{5.4}$$

[1] A cat state is a macroscopic quantum superposition between two symmetric states: in one of them, all the atoms populate one of the wells, and in the other state, they occupy the second well. This state, which can be written as $(|N, 0\rangle + |0, N\rangle)/\sqrt{2}$, is also called *NOON state*.

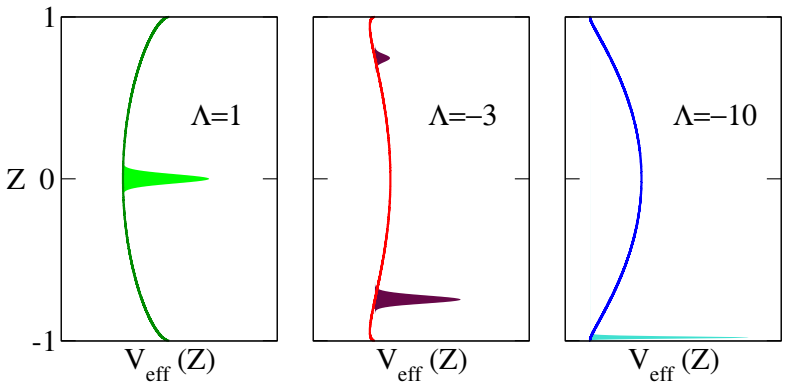

Figure 5.1: Plot of the effective potential of the double well as a function of the population imbalance Z for the following values of Λ: 1, -3 and -10. The filled curve corresponds to the coefficients of the ground state in the Fock basis (each element labelled by its population imbalance) in each case, i.e. this curve displays which is the contribution of each population imbalance to the ground state of the system.

where in the last equation, we have used that $[\hat{H}_2, \hat{N}] = [\hat{H}_2, \hat{S}] = 0$ to remove all terms proportional to the total spin $\hat{S}$. By defining $\hat{S}_\alpha = \sum_{i=1}^{N} \hat{\sigma}_i^\alpha/2$ as the collective spin along the α-direction, where the set of operators $\hat{\sigma}^\alpha$ corresponds to the Pauli matrices, the double-well Hamiltonian $\hat{H}_2$ can be interpreted as a system of N spin-1/2 particles mutually interacting along the z-axis and embedded in a transverse magnetic field along the x-direction. Thus, the double-well Hamiltonian (5.4) is just a particular case of the general Lipkin-Meshkov-Glick model [Lip65, Mes65, Gli65], introduced to study quantum phase transitions in mean-field models, where all spins interact with each other, and since then exploited in many different contexts e.g. [Bot83, Res05, Dus04, Oru08]. The corresponding Hamiltonian is:

$$\hat{H}_{LMG} = -h \sum_i \hat{\sigma}_i^x - \frac{\lambda}{N} \sum_{i<j} \left(\hat{\sigma}_i^z \hat{\sigma}_j^z + \gamma \hat{\sigma}_i^y \hat{\sigma}_j^y \right) , \tag{5.5}$$

where the factor $1/N$ ensures the convergence of the free energy per spin in the thermodynamic limit $N \to \infty$. This magnetic model and its corresponding phase transitions have been very well studied. For $\lambda > 0$, i.e. when the interaction between spins is ferromagnetic, there exists a second order phase transition at $\lambda = -h$, if $0 \leq \gamma \leq 1$. The mapping between Eqs. (5.4) and (5.5) is straightforward in the case of $\gamma = 0$, and provides the relation $\lambda/h = UN/2J = \Lambda$, which at the transition yields to $\Lambda = -1$. Thus, approaching $UN/2J \to -1$, there is a quantum phase transition between ferromagnetic and paramagnetic order, which in the thermodynamic limit converges to $U/2J \to 0$. The paramagnetic region is thus proportional to $1/N$, nondegenerate and has a gap that vanishes at the transition point. We notice that in the double-well potential, the thermodynamic limit corresponds to the limit in which a mean-field description is valid and does not require to reach $N \to \infty$ but rather a sufficiently large N. Finally, we remark that models in which each spin interacts with each other have infinite dimensionality and, therefore, the concept of length is not defined.

5.1.2 Correlation length and critical exponents in a double-well potential

As already mentioned, when approaching the limit $\Lambda \to -1$, the mean-field description of the double well collapses and the Gross-Pitaevskii equation cannot provide anymore the description of the ground state of the system. The two-well Bose-Hubbard description shows also a massive fluctuation of the particle number on each well in the border of the transition regime. Indeed, it is the existence of quantum fluctuations on all length scales, the most characteristic feature of (continuous) quantum phase transitions occurring at zero temperature. This behavior, commonly denoted as criticality, is also reflected on the behavior of some observables $\hat{O}$ that scale near the transition point $U_{\text{crit}} = -2J/N$ as a power law $\hat{O} \propto |U - U_{\text{crit}}|^{\alpha}$, where α is a set of parameters called critical exponents that determine the qualitative nature of the critical behavior. Those parameters α are independent of the microscopic details of the system, but are rather linked to the symmetries of the emerging order as well as to the dimensionality of the system. Thus, quantum phase transitions associated to different Hamiltonians that share the same set of critical exponents are said to belong to the same universality class. The quantum phase transition is also accompanied by the vanishing of some energy scale and the divergence of some length (the correlation length) which indicates the spread of correlations in the system [Sac99].

We aim at interpreting the quantum phase transitions in the double-well potential in a similar way as in spin chains, provided a definition of correlations. This definition allows to link critical behavior to the divergence of a correlation length. With this purpose we first calculate the phase diagram of the double well for different values of N near criticality. Inspired by two-point correlations in spin chains, we define correlations in our system in such a way that their behavior properly displays the relevant features of the quantum phase transitions.Then, we analyze the scaling behavior of some operators and perform finite-size scaling (see below) to obtain the corresponding critical exponents. Finally, we check if other models of the restricted Bose-Hubbard family share the same critical exponents and belong, therefore, to the same universality class.

Notice that in a spin chain of spin $\vec{S}$ particles, the length is naturally settled by the number of sites L (number of spins), and two-body spin-spin correlations are given by $\mathcal{C}_{ij} = \langle \vec{S}_i \vec{S}_j \rangle - \langle \vec{S}_i \rangle \langle \vec{S}_j \rangle$. Translational invariance in such systems ensures that the behavior of spin-spin correlations depends only on the distance between the two sites $|i - j|$, but not on the specific sites i, j. This fact allows to define a correlation length ξ, which fixes the length scale at which the spins are correlated between them. Far from criticality, the decay of correlations is exponential $\mathcal{C}_{ij} \sim \exp(-|i - j|/\xi)$, meaning that two far away spins are not correlated. At criticality, for continuous second order phase transitions, the decay is algebraic $\mathcal{C}_{ij} \sim (|i - j|^{-p})$, and the correlation length diverges as $\xi \propto |U - U_{\text{crit}}|^{-\nu}$, where ν is a critical exponent and U_{crit} is the critical point where the quantum phase transition occurs, expressing the fact that now spins are correlated between them even when they are far.

In a double well, such length scale is irrelevant. In order to mimic the behavior of second order quantum phase transitions in spin chains in our system, we start by realizing that the quantity that settles the dimension of the Hilbert space here is the number of bosons on each well. Furthermore, this permits to order the Fock states in the following way: $|N, 0\rangle, |N - 1, 1\rangle, \cdots, |0, N\rangle$.

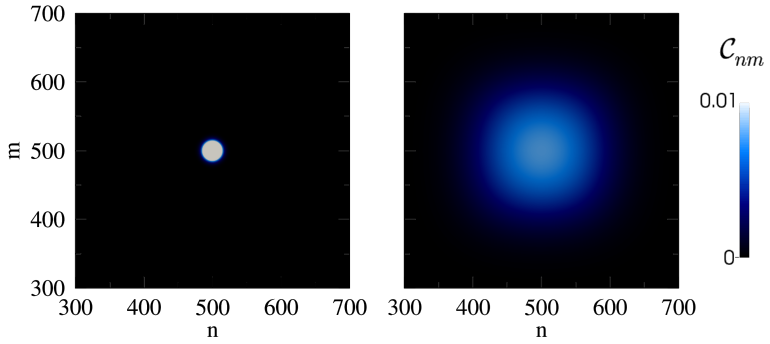

Figure 5.2: Behavior of the correlations $\mathcal{C}_{nm}$ as a function of n and m for a double well. Left panel: $UN/2J = 100$ far from criticality; right panel: $UN/2J = -1$, at criticality. The figures correspond to $N = 1000$, thus, the ground state corresponds to 500 atoms in each well (in the center of color map).

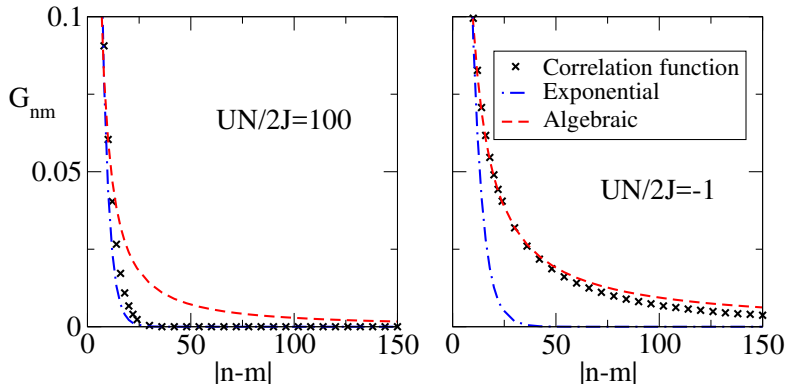

Figure 5.3: Correlation function for the double-well potential G_{nm} versus $|n-m|$. Left panel: $UN/2J = 100$ far from criticality. Right panel: $UN/2J = -1$ at the critical point. The figures correspond to $N = 1000$. To better understand the different behavior far and close to criticality, an exponential decay (dashed-dotted line) and an algebraic decay (dashed line) has been drawn to guide the eye. As clearly displayed in the figure, at criticality (right panel) the best adjustment is algebraic, otherwise it is exponential (left panel).

We then define two-body correlations in the ground state of our system as:

$$G_{nm} = \sum_{|n-m|} \frac{\langle\, |n\rangle\langle m| \otimes |N-n\rangle\langle N-m|\,\rangle}{|n-m|} = \sum_{|n-m|} \frac{\mathcal{C}_{nm}}{|n-m|}\,, \tag{5.6}$$

where the operator $|n\rangle\langle m|$ acts on the first trap and $|N-n\rangle\langle N-m|$ on the second one. So, we analyze how the number of bosons are correlated within a trap, i.e. the simultaneous presence of n and m bosons in the ground state and the sum extends over all possible contributions with $|n-m|$ fixed. Notice that $\mathcal{C}_{nm}$ is not equivalent to the population imbalance operator in the double-well potential. The latter indicates the difference of population between the wells $Z = \langle \hat{S}_z \rangle = \langle |\hat{n}_1 - \hat{n}_2| \rangle / N = \sum_{n_1,n_2} |C_{n_1,n_2}|^2 (|n_1 - n_2|)/N$, while the former, $\mathcal{C}_{nm} = C_{n,N-n} C_{m,N-m}$, correlates

boson occupation numbers within a well. In order to recover the "translational invariance", concept rooted in spin chains, we weight the correlation function by the "effective distance" $|n-m|$. This renormalization factor ensures the proper behavior of correlations as it neglects contributions from any intermediate level between n and m.

The general behavior of the correlations $\mathcal{C}_{nm}$ as a function of n and m, far from and close to criticality, is shown in Fig. 5.2, in the left and right panel, respectively. While far from criticality, the ground state is correlated with the closer states only, at criticality the spreading of correlations becomes evident. Nevertheless, it is indeed the weighted function G_{nm} the one which allows to recover the concept of "translational invariance" and define a correlation length ξ for the system. In Fig. 5.3, we display G_{nm} as a function of $|n-m|$ far from and near criticality. One can see that G_{nm} decays exponentially far from the critical point and algebraically at criticality. To better stress the character of the correlation decay we fit the functions by an exponential and a power law.

To obtain a deeper understanding about the concept of correlation and the exact location of the quantum phase transition in the mean-field limit, we analyze the behavior of the population imbalance Z, its fluctuations ΔZ, the magnetization along the z-axis, defined as $m_z = (\langle \hat{S}_z^2 \rangle)^{1/2}/N$ [Res05], and the entanglement spectrum, by means of the Schmidt gap $\Delta\lambda = \lambda_1 - \lambda_2$ (see Chap. 2), which closes at the critical point in the thermodynamic limit [DeC12, Lep13].

In spin chains, finite-size effects strongly modify the location of the critical point where a quantum phase transition occurs, while distorts the general properties of the transition [Fis72]. In order to account for finite-size effects, we repeat our simulations for different number of atoms $N = 500, 1000, 1500$ and look at the exponents that make all data to cross at the same point (critical point), and to collapse (overlap) in order to obtain the critical exponents of observables, which scale as $\hat{O} \simeq N^{-\beta/\nu} f(|U - U_{\rm crit}|N^{1/\nu})$, where ν is the mass gap exponent (associated to the correlation length divergence), and β is the critical exponent of the corresponding operator $\hat{O}$. This analysis is called finite-size scaling. In Fig. 5.4 we display the scaling behavior of the population imbalance Z, the magnetization along the z-axis, and the Schmidt gap for the double-well case. One should point out that $\Delta\lambda$ is not an observable, however, all the quantities exhibit scaling. This allows us to extract the critical exponents, which are summarized in Table 5.1.

	Z	ΔZ	m_z	$\Delta\lambda$
ν	1.000	1.000	1.000	1.000
β	0.499	0.502	1.500	1.498

Table 5.1: Critical exponents of the correlation length (ν) and the scaling operator (β) obtained from the scaling of the population imbalance (Z), its fluctuations (ΔZ), the magnetization along the z-direction m_z, and the Schmidt gap $\Delta\lambda$ (obtained from the entanglement spectrum).

As expected, from the scaling of population imbalance, we obtain the mean-field exponents for Z and ΔZ, which converge to $\beta = 1/2$ and $\nu = 1$ in agreement with previous works [Dus04, Buo12]. Interestingly, the critical exponents obtained from the scaling of the magnetization m_z and the entanglement spectrum $\Delta\lambda$ coincide and result into $\beta = 3/2$ and $\nu = 1$ in agreement with the results presented in Refs. [Bot83, Res05].

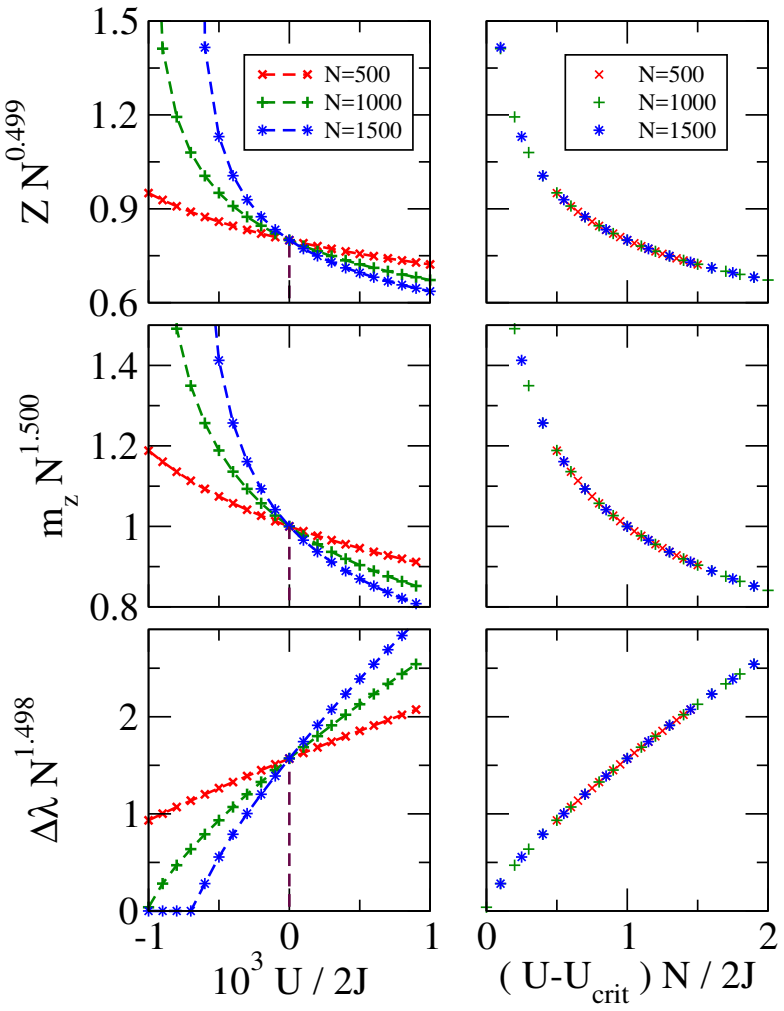

Figure 5.4: Finite-size scaling behavior of the population imbalance (first row), the magnetization along the z-axis (second row) and the Schmidt gap (third row) in the double-well potential. The critical exponents obtained via this method are summarized in Table 5.1.

5.2 Dipolar Bose gases in triple-well potentials

In the previous section, we have restricted the system to the particular case of two sites. Nevertheless, the physics of the three-site Bose-Hubbard model is richer, since the geometry appears as an additional degree of freedom. If the atoms possess a nonzero dipole moment, dipolar interaction is a new degree of freedom, provoking the appearance of new phases in the phase diagram. Remarkably, the role of the dipole-dipole interaction will strongly depend on the geometry [Aba10], since this interaction is both anisotropic and has a long-range character. We could have also considered the dipolar interaction in the double-well potential, but it has been shown that in this case, dipolar interaction simply modifies the effective on-site interaction constant U, without changing the main features of the phase diagram of the system [Maz13].

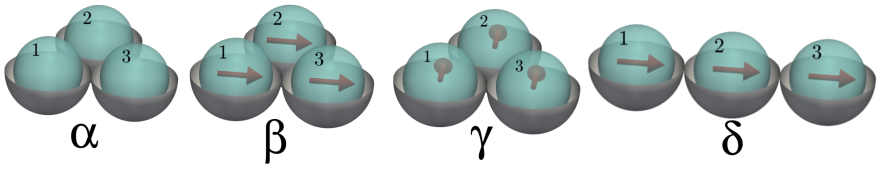

Figure 5.5: The four configurations presented in the text are schematically depicted. From left to right α, β, γ and δ.

The (extended) Bose-Hubbard hamiltonian (see Sect. 2.2.2) that describes N dipolar bosons in a system constituted by three wells is:

$$\begin{aligned}\hat{\mathcal{H}}_3 = &- \left[J_{12}\left(\hat{b}_1^\dagger \hat{b}_2 + \hat{b}_2^\dagger \hat{b}_1\right) + J_{13}\left(\hat{b}_1^\dagger \hat{b}_3 + \hat{b}_3^\dagger \hat{b}_1\right) + J_{23}\left(\hat{b}_2^\dagger \hat{b}_3 + \hat{b}_3^\dagger \hat{b}_2\right)\right] \\ &+ \frac{U_0}{2}\sum_{i=1}^{3} \hat{n}_i(\hat{n}_i - 1) + U_{12}\,\hat{n}_1\hat{n}_2 + U_{23}\,\hat{n}_2\hat{n}_3 + U_{13}\,\hat{n}_1\hat{n}_3\,. \end{aligned} \tag{5.7}$$

In this section, we will consider four geometrical configurations of the three wells and the dipole orientation. The first three configurations consist of three wells disposed as a triangle, but with different dipole orientations: perpendicular to the plane of the triangle [Del13] (α)[2], in the plane of the triangle but perpendicular to the symmetry axis (β), and in the plane of the triangle and along the symmetry axis (γ). The two last configurations will display which is the role of the anisotropic nature of the dipolar interaction [Gal13b]. Finally, we will also consider an additional configuration, consisting on the three-well array with all the dipoles oriented along the direction of the array (δ) [Lah10, Pet12]. In this latter system, we exploit the long-range character of the dipolar interaction, since the two external wells interact thanks to the dipole moments. These configurations are represented in Fig. 5.5. The relation between the parameters of the extended Bose-Hubbard hamiltonian depends on the configuration, and are summarized in Table 5.2. Notice that the fact that sites 1 and 3 are symmetric with respect to site 2 implies that in all the cases $J_{12} = J_{23}$ and $U_{12} = U_{23}$.

	α	β	γ	δ
J_{12}/J	1	1	1	1
J_{23}/J	1	1	1	1
J_{13}/J	1	1	1	0
U_{12}/U_1	1	1	1	1
U_{23}/U_1	1	1	1	1
U_{13}/U_1	1	-8	$-4/5$	$1/8$

Table 5.2: Values of the inter-site dipole-dipole interaction for each configuration resulting from the anisotropy of the interaction.

We can then write the extended Bose-Hubbard hamiltonian corresponding to the four different configurations:

[2]This configuration can be mapped onto a configuration with the same geometry but with nondipolar atoms. Therefore, in this configuration, the dipole moment of the atoms can be simply dropped.

$$
\begin{aligned}
\hat{\mathcal{H}}_\alpha =& - J \left[\hat{a}_1^\dagger \hat{b}_2 + \hat{b}_2^\dagger \hat{b}_1 + \hat{b}_1^\dagger \hat{b}_3 + \hat{b}_3^\dagger \hat{b}_1 + \hat{b}_2^\dagger \hat{b}_3 + \hat{b}_3^\dagger \hat{b}_2\right] \\
& + (U_1 - U_0)\left[\hat{n}_1\hat{n}_2 + \hat{n}_2\hat{n}_3 + \hat{n}_1\hat{n}_3\right] , \\
\hat{\mathcal{H}}_\beta =& - J \left[\hat{b}_1^\dagger \hat{b}_2 + \hat{b}_2^\dagger \hat{b}_1 + \hat{b}_1^\dagger \hat{b}_3 + \hat{b}_3^\dagger \hat{b}_1 + \hat{b}_2^\dagger \hat{b}_3 + \hat{b}_3^\dagger \hat{b}_2\right] \\
& - U_0\left[\hat{n}_1\hat{n}_2 + \hat{n}_2\hat{n}_3 + \hat{n}_1\hat{n}_3\right] + U_1\left[\hat{n}_1\hat{n}_2 + \hat{n}_2\hat{n}_3 - \frac{1}{8}\hat{n}_1\hat{n}_3\right] , \\
\hat{\mathcal{H}}_\gamma =& - J \left[\hat{b}_1^\dagger \hat{b}_2 + \hat{b}_2^\dagger \hat{b}_1 + \hat{b}_1^\dagger \hat{b}_3 + \hat{b}_3^\dagger \hat{b}_1 + \hat{b}_2^\dagger \hat{b}_3 + \hat{b}_3^\dagger \hat{b}_2\right] \\
& - U_0\left[\hat{n}_1\hat{n}_2 + \hat{n}_2\hat{n}_3 + \hat{n}_1\hat{n}_3\right] + U_1\left[\hat{n}_1\hat{n}_2 + \hat{n}_2\hat{n}_3 - \frac{5}{4}\hat{n}_1\hat{n}_3\right] , \\
\hat{\mathcal{H}}_\delta =& - J \left[\hat{b}_1^\dagger \hat{b}_2 + \hat{b}_2^\dagger \hat{b}_1 + \hat{b}_2^\dagger \hat{b}_3 + \hat{b}_3^\dagger \hat{b}_2\right] \\
& - U_0\left[\hat{n}_1\hat{n}_2 + \hat{n}_2\hat{n}_3 + \hat{n}_1\hat{n}_3\right] + U_1\left[\hat{n}_1\hat{n}_2 + \hat{n}_2\hat{n}_3 + \frac{1}{8}\hat{n}_1\hat{n}_3\right] ,
\end{aligned} \tag{5.8}
$$

where we have removed constants proportional to the number of particles N, since the particle number operator commutes with the hamiltonian (see Refs. [Del13, Maz13, Gal13b] for further details).

5.2.1 Ground states of the system: phase diagram

The ground state of the extended Bose-Hubbard hamiltonian depends on the parameters J, U_0 and U_1, as well as on N, and different ground states belonging to different phases are expected to appear. For $J \neq 0$, but small compared to U_0 and U_1, we expect some insulating phases, i.e. with a well defined number of bosons per site. To preserve symmetry conditions in the insulating phases, we fix the number of atoms to be even and multiple of 3.

The phase diagram has been found by exact diagonalization of Eqs. (5.8) for $N = 12,\ 24\,, 36$ and 48. Results for larger number of atoms become computationally too time-consuming and, in many aspects, irrelevant, since for $N \gg 1$, the extended Bose-Hubbard model becomes practically independent of the tunneling term and reduces to a diagonal hamiltonian in the Fock basis.

A first insight on the phase diagram can be obtained in the atomic limit, i.e. when the tunneling is set to zero. In such case, the hamiltonian becomes diagonal in the Fock basis and the eigenenergies reduce to

$$
E_k = -U_0[n_1n_2 + n_2n_3 + n_1n_3] + U_1[n_1n_2 + n_2n_3] + U_k n_1 n_3\,, \tag{5.9}
$$

where k runs over the four different configurations and U_k is the value of U_{13} for each configuration. Analytical expressions for the phase boundaries can be obtained by minimizing the energy under the constraints $n_1 + n_2 + n_3 = N$ and $n_1 = n_3$, which imposes the symmetry between wells

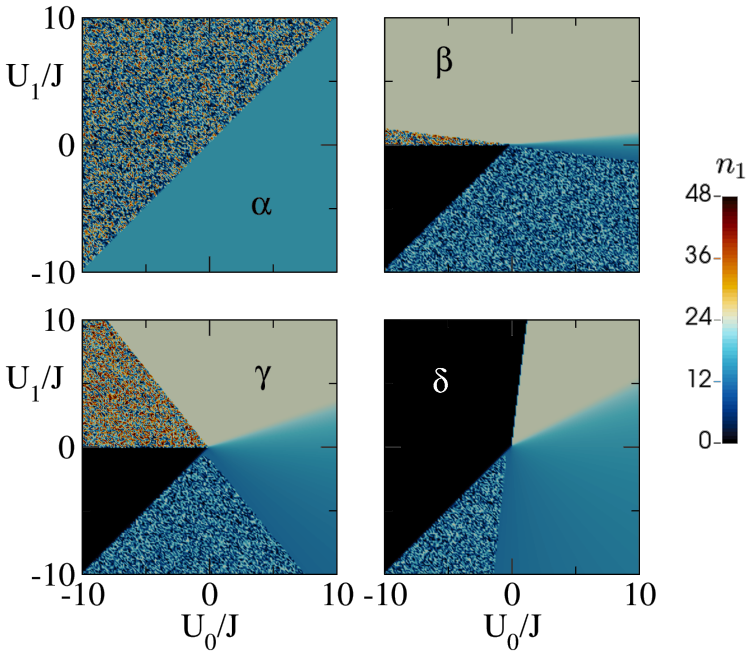

Figure 5.6: Phase diagram in the $(U_0/J, U_1/J)$ plane for the α (left top), β (right top), γ (left bottom) and δ (right bottom) configurations, represented by the population of well 1, given by n_1, for $N = 48$ atoms

1 and 3. This minimization yields to the mean occupation number:

$$n_1 = n_3 = \text{Int}\left[N\frac{U_0 - U_1}{3U_0 - 4U_1 + U_k}\right]$$
$$n_2 = \text{Int}\left[N\frac{U_0 - 2U_1 + U_k}{3U_0 - 4U_1 + U_k}\right] \tag{5.10}$$

where Int$[x]$ denotes the integer part of x.

The whole phase diagram obtained by solving the extended Bose-Hubbard hamiltonian for $N = 48$ for each configuration is displayed in Fig. 5.6, by plotting the mean population of site 1 in every configuration. We can see that the α-configuration exhibits two phase separated by the line $U_0 = U_1$. This can be seen from the hamiltonian, since it can be written in terms of an effective interaction $U_{\text{eff}} = U_0 - U_1$, and there exists a transition at $U_{\text{eff}}N/J = -9/2$ [Del13, Gal15]. This transition is equivalent to the phase transition of the double-well potential (equipopulation against symmetry breaking), but with three wells in this case, see Ref. [Del13] for further details.

Regarding the other configurations, one can observe that the phase diagram is richer, with many phases of different type. In the case of the α, β and δ-configurations, we will analyze in Sect. 5.2.3 a quantum phase transition between two particular phases of the phase diagram (in the α-configuration this transition is the only transition that appears in the phase diagram). In the β-configuration there is a transition between two phases for $U_0 < 0$ and $U_1 > 0$, one of them

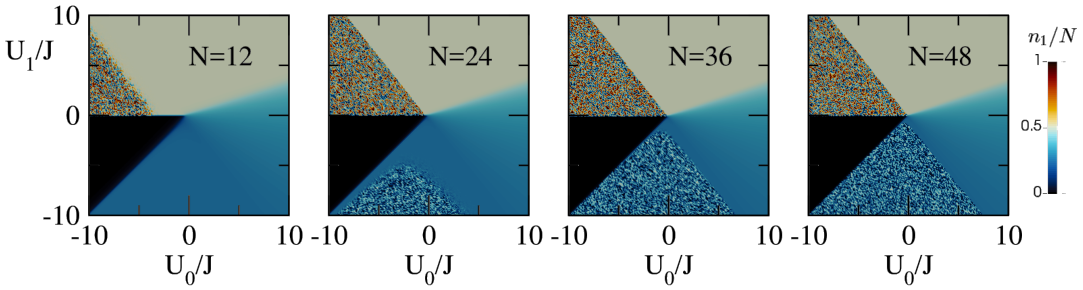

Figure 5.7: Phase diagram, given by n_1 for the γ-configuration obtained from exact diagonalization of the extended Bose-Hubbard hamiltonian for different values of N. From left to right: $N = 12, 24, 36$ and 48.

represented in the phase diagram in ochre, and the second by a pixelate texture. The former phase is characterized by having the well 2 empty, while wells 1 and 3 are equipopulated. The latter phase, is, instead, described by a spontaneous symmetry breaking, where all the atoms coordinately populate well 1 or 3, while well 2 is, again empty [Gal13b]. Concerning the δ-configuration, we will comment about a phase transition that appears for $U_0 < 0$ and $U_1 < 0$, separating a phase colored in black, and another phase with a pixelate texture. The first phase corresponds to a phase where all the atoms accomodate on well 2, whereas in the second one, half of the particles accomodate on well 2, and the other half remains as a macroscopic superposition between wells 1 and 3.

When analyzing the frontiers between the different phases that appear in the phase diagram, one can see that they approach the position predicted by the atomic limit (which corresponds to the thermodynamic limit), when the number of atoms N increases, whereas for small values of N, the atomic limit fails to predict the position of the frontiers between the phases[3]. This effect can be seen in Fig. 5.7, where we plot the phase diagram (given by n_1) in the γ-configuration for $N = 12, 24, 36$ and 48 particles (the latter case is the one plotted in Fig. 5.6).

5.2.2 Phase analysis and entanglement properties

A further insight on the quantum phases and phase transitions in the different configurations can be obtained by analyzing entanglement properties, and in particular the von Neumann entropy, the entanglement spectrum and the Schmidt gap (see Chap. 2). Under this perspective we examine entanglement properties of the ground state of the system for a fixed number of particles N, as a function of the parameters U_0/J and U_1/J. In order to realize such analysis, we perform two bipartite splittings: well 1(2) against the rest of the system, which we will name partition 1(2).

In the top panels of Fig. 5.8, we display the single-site von Neumann entropy of sites in partition 1 (left) and 2 (right), respectively, as a function of U_1/J and U_0/J in the γ-configuration. The bottom panels of Fig. 5.8 represent the Schmidt gap in the two partitions commented above

[3]This is not true when one of the phases corresponds to a product state, which is a *classical* state. This is the reason why the frontier between the black and the blue region remains unaltered even for small number of particles.

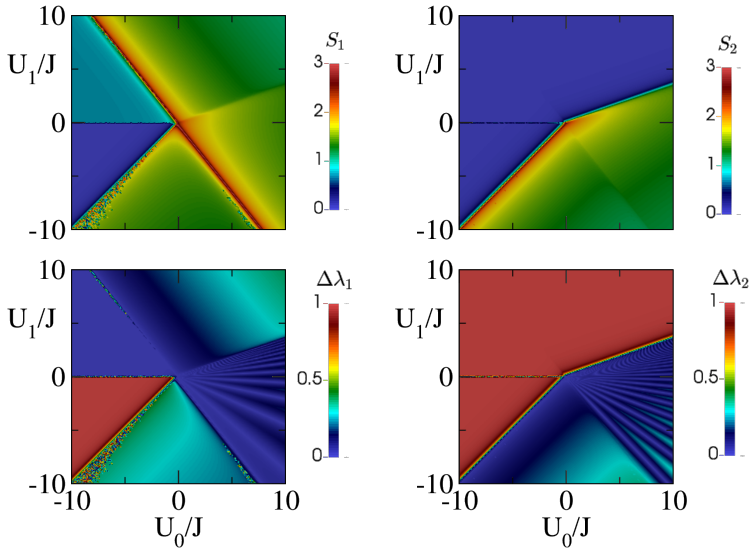

Figure 5.8: Characterization of the phase diagram in the γ-configuration by means of their entanglement properties, by diagonalizing $\mathcal{H}_\gamma$ for $N = 48$ bosons. Top panels represent the von Neumann entropy S_1 in the partition 1 (left) and S_2 in the partition 2 (right). Bottom panels represent the Schmidt gap $\Delta\lambda_1$ in the partition 1 (left) and $\Delta\lambda_2$ in the partition 2 (right). Notice that wells 1 and 3 are symmetric for this configuration.

(left for 1 and right for 2). Inspection of the previous figure shows a remarkable agreement with the phase diagram shown before. As an example, the ground state in the black region of the phase diagram corresponds to a product state where all the particles occupy site 2. Since this state can be written in terms of a single element of the Fock basis, the von Neumann entropy of the system is equal to the entropy of its subsystems and hence identically zero. Moreover, in such cases, the state is already written in terms of the eigenvectors of the reduced density matrix, with a single Schmidt coefficient equal to one (and thus, the Schmidt gap is also equal to one). A deeper discussion about the relation between the entanglement properties and the ground state structure in this system can be found in Ref. [Gal13b].

There is, however, a region of the phase diagram, where the Schmidt gap exhibits a different behavior, with respect to the entropy and the density itself, for $U_0 > 0$. The Schmidt gap displays a series of slopes corresponding to the different *crossovers* occurring in this region of the phase diagram in the γ-configuration. The reason of the appearance of such fan-like structures is that the Schmidt gap is a quantity that is nonaveraged, in contrast to the case of the mean occupation number or the von Neumann entropy, which, being averaged quantities, can not display such structures. In other words, the Schmidt gap contains information of the quantum state itself, and can capture changes of the quantum state that describes the system, whereas the von Neumann entropy is computed from a sum over all the elements of the basis of the reduced density matrix, and isoentropic changes in the quantum state (like those appearing in the region of the fan-like structure) can not be seen.

5.2.3 Quantum phase transitions in the extended Bose-Hubbard hamiltonian: universality

We have seen in Sect. 5.1.2 that the second order quantum phase transition that appears in the phase diagram of the double-well system, can be accurately described in terms of a correlation function inspired by a spin model like the Ising spin chain. The reinterpretation of the occupation number on each well as an effective length in the corresponding Hilbert space allows to provide scaling properties of some important observables like population imbalance, magnetization along a given axis or the Schmidt gap. In turn, the scaling properties of such observables lead to a set of critical exponents that can be associated to the corresponding quantum phase transition. A natural question arises when the number of wells is increased: does the same analysis hold outside of the double-well configuration?

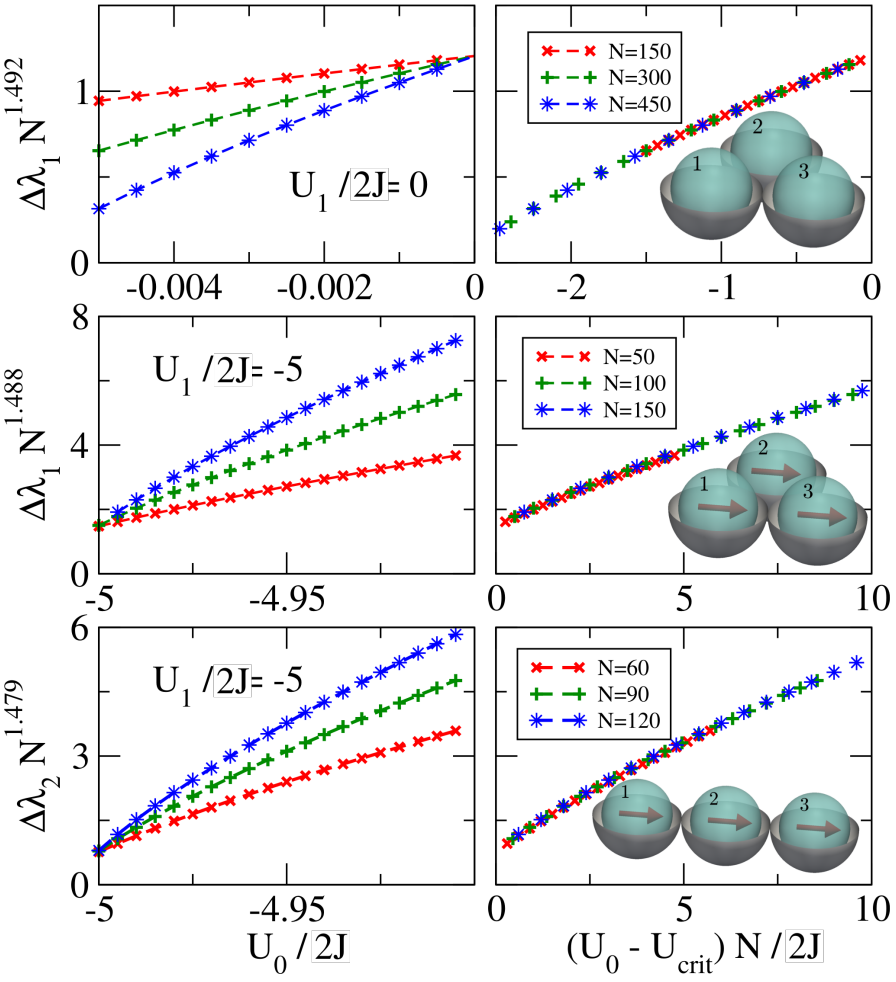

Figure 5.9: Finite-size scaling of the Schmidt gap $\Delta\lambda_1$ (top and middle rows) and $\Delta\lambda_2$ (bottom row) for the three configurations displayed in the insets of the right panels. The critical exponents obtained are reported in the text.

In the double-well case, we have analyzed the scaling properties of some observables, like the imbalance, its fluctuations and the magnetization. For the triple-well case, the definition of the equivalent observables is not so straightforward. Nevertheless, the Schmidt gap can be computed in the way commented before, and we can take profit from its scaling properties. In three-well systems, however, there are more than a single partition of the system.

In this section, we focus on the study of the three quantum phase transitions previously characterized, for the case of dipolar bosons loaded in a triple-well potential. The top (middle) panels of Fig. 5.9 represent the scaling of $\Delta\lambda_1$ in the α (β)-configuration for $N = 150, 300, 450$ ($N = 50, 100, 150$), in the transitions commented above at $U_1 = 0$ ($U_1/2J = -5$). The bottom panels show the scaling of $\Delta\lambda_2$ for the δ-configuration for $N = 60, 90, 120$. In all three cases, the critical exponents are: $\beta = 3/2$ and $\nu = 1$, which are the same that the ones obtained in the scaling for the double well. Despite the number of atoms used to exact diagonalize the system is smaller than in the double-well case, the results for the critical exponents exhibit a clear convergence. The fact that such systems show the same critical exponents that the quantum phase transition of the double well ensures that the transitions of the above cases belong to the same universality class of the double well [Gal16d]. This property becomes evident for the β-configuration, where across the quantum phase transition analyzed previously, the system behaves as an effective double-well system, with one of the wells completely empty.

Chapter 6

The effect of a weak link in Bose gases confined in ring geometries

In the previous chapter we have presented ground state properties of few-site Bose-Hubbard hamiltonians, in different geometries and under the presence of dipolar interactions. This chapter addresses the effect of manipulating a contact-interacting Bose gas in a localized region. By using this method, it is possible to drastically change the phase profile inherent to a condensate. This localized variation of the potential is known as a weak link, and its effect has become very relevant in order to elucidate the physics behind dark solitons and persistent currents, among other topological states.

In the first section of this chapter, we will address the physics of toroidally confined Bose gases with a weak link in the strongly correlated regime. This corresponds to a lattice ring that can be described by means of the Bose-Hubbard model, in which it is possible to tune the tunnelling rate between two sites of the ring. For the particular case in which the strength of the tunable tunnelling rate flips its sign, the ground state is a macroscopic superposition of two current flows [Agh15, Hal11, Sch11] that possess half a quantum circulation [Gal15, Gal16a] (see also Ref. [vdW00] in superconductors). Therefore, they can be identified as semifluxons and antisemifluxons [Gol02, Wal08]. We analyze, under the presence of two-body interactions, the stability and robustness of this macroscopic superposition of current flows in terms of the condensed fraction of the system, the energy spectrum and its entanglement properties.

The second section of the present chapter is devoted to study the continuous system confined in a toroidal potential in the mean-field regime, by using the single-component Gross-Pitaevskii equation. In this case, the weak link simply corresponds to a repulsive potential at some point of the torus that rotates along the ring and behaves as a barrier for the fluid. Above some critical value of the rotation frequency of the weak link, the phase winds producing an increase of the winding number and generating a dissipative process called phase slip [And66, Var15, Hos05], which will be explained in future sections. We describe the static properties of phase slip, by studying the topological structure of the barrier that separates winding number states.

6.1 Bose-Hubbard ring with a weak link

In order to build a lattice ring with a tunable link, we consider N ultracold interacting bosons populating M sites [Ami05], with a tunable link between sites 1 and M, through the parameter γ (see below). Following standard procedures [Lew12], the system is described in the lower-band approximation by the Bose-Hubbard Hamiltonian $\hat{\mathcal{H}} = \hat{\mathcal{T}} + \hat{\mathcal{U}}$, which, takes the form:

$$\begin{aligned} \hat{\mathcal{T}} &= -\gamma J \left(\hat{b}_M^\dagger \, \hat{b}_1 + \hat{b}_1^\dagger \, \hat{b}_M \right) - J \sum_{\lambda=1}^{M-1} \left(\hat{b}_\lambda^\dagger \, \hat{b}_{\lambda+1} + \hat{b}_{\lambda+1}^\dagger \, \hat{b}_\lambda \right) \\ \hat{\mathcal{U}} &= \frac{U}{2} \sum_{\lambda=1}^{M} \hat{b}_\lambda^\dagger \, \hat{b}_\lambda^\dagger \, \hat{b}_\lambda \, \hat{b}_\lambda \, , \end{aligned} \tag{6.1}$$

where the on-site interaction is assumed to be repulsive, $U > 0$. Attractive atom-atom interactions can also be produced and would more naturally lead to macroscopic superposition states but they are fragile against instabilities. In this, section, we will analyze the ground state structure and the excitation spectrum as a function of the dimensionless parameter $\Lambda \equiv NU/J$, which gives the ratio between interaction and tunnelling rate.

A crucial ingredient in the previous model is the presence of a single tunable link. The tunnelling rate between sites 1 and M can be varied through a parameter γ, which is taken to be real. This allows us to study very different configurations, for instance, an open 1D Bose-Hubbard chain when $\gamma = 0$, and a symmetric *non-twisted* (*twisted*) closed chain when $\gamma = 1$ ($\gamma = -1$). There are different experimental techniques that permit to tune the tunnelling rate between two sites of a lattice. For instance, an external shaking of the system along one direction, effectively results in a dressed tunnelling term whose sign can be switched from positive (standard) values to negative (π-phase tunnelling), see Ref. [Eck05] for further details. More recently, a deep laser dip in the centre of a junction has been proposed in Ref. [Szi14] to engineer π-phase tunnelling. Apart from the case of lattices, if the modes of the Bose-Hubbard ring refer to different spin levels of an atom, instead of sites, the Jaksch-Zoller mechanism applies in order to generate a phase-dependent tunnelling [Jak03]. This geometry was experimentally realized in Ref. [Ami14]. It would be also possible to build this kind of hamiltonian by construcing an extra dimension with the spin [Boa12], or with coupled nonliner optical resonators [Eic14].

It can be shown that, for the particular cases $\gamma = \pm 1$, the hamiltonian $\hat{\mathcal{H}}$ is gauge equivalent to a symmetric hamiltonian (i.e. with equal couplings between all the sites) with a total flux along the ring $\Phi = 0$ and $\Phi = \pi$, respectively [Hal06, Par03, Arw14]:

$$\hat{\mathcal{H}}_{\text{sym}} = -J \sum_{\lambda=1}^{M} \left[e^{i\Phi/M} \, \hat{b}_\lambda^\dagger \, \hat{b}_{\lambda+1} + e^{-i\Phi/M} \, \hat{b}_{\lambda+1}^\dagger \, \hat{b}_\lambda \right] + \hat{\mathcal{U}} \, . \tag{6.2}$$

In the previous equation, the site $\lambda = M + 1$ corresponds to site 1, due to the periodicity of the chain. This many-body hamiltonian describes a Bose-Hubbard ring, rotating around its symmetry axis with angular frequency Φ. Therefore, the physics of the hamiltonian (6.1) with $\gamma = \pm 1$ is essentially equivalent to the ones considered in the previous references. However, it is worth emphasizing that such local gauge transformation relating the hamiltonians (6.1) and (6.2) does not exist for a general value of γ.

6.1.1 Single-particle case

For a single particle, the two-body term $\hat{\mathcal{U}}$ can be removed from the hamiltonian, and the problem reduces to finding the eigenvalues μ and eigenvectors $\chi(\lambda)$, with $\lambda = 1, \ldots, M$, of $\hat{\mathcal{T}}$:

$$\begin{pmatrix} -\mu & J & 0 & \cdots & 0 & 0 & \gamma J \\ J & -\mu & J & \cdots & 0 & 0 & 0 \\ 0 & J & -\mu & \cdots & 0 & 0 & 0 \\ \vdots & \vdots & \vdots & \ddots & \vdots & \vdots & \vdots \\ 0 & 0 & 0 & \cdots & -\mu & J & 0 \\ 0 & 0 & 0 & \cdots & J & -\mu & J \\ \gamma J & 0 & 0 & \cdots & 0 & J & -\mu \end{pmatrix} \begin{pmatrix} \chi(1) \\ \chi(2) \\ \chi(3) \\ \vdots \\ \chi(M-2) \\ \chi(M-1) \\ \chi(M) \end{pmatrix} = 0 \,. \tag{6.3}$$

Using standard techniques in solving tight-binding problems, one finds that the solutions can be either even (symmetric): $\chi^{(S)}(\lambda) = \chi^{(S)}(M+1-\lambda)$ or odd (antisymmetric): $\chi^{(A)}(\lambda) = -\chi^{(A)}(M+1-\lambda)$. They can be written conveniently in terms of Bloch phases ϕ as:

$$\begin{aligned} \chi^{(S)}(\lambda) =& \frac{1}{\sqrt{\mathcal{N}_+}} \cos\left[\left(\frac{M+1}{2} - \lambda\right)\phi\right] , \\ \chi^{(A)}(\lambda) =& \frac{1}{\sqrt{\mathcal{N}_-}} \sin\left[\left(\frac{M+1}{2} - \lambda\right)\phi\right] , \end{aligned} \tag{6.4}$$

where the normalization factor of each wave function is $\mathcal{N}_\pm = (M \pm \sin(M\phi)/\sin\phi)/2$. The respective Bloch phases satisfy the implicit equations:

$$\gamma = \frac{\cos(\phi(M+1)/2)}{\cos(\phi(M-1)/2)} \tag{6.5}$$

for the even solutions, and

$$\gamma = -\frac{\sin(\phi(M+1)/2)}{\sin(\phi(M-1)/2)} \tag{6.6}$$

for the odd ones. In terms of the Bloch phases, the eigenvalues (μ) are then given by

$$\mu = -2J\cos\phi \,. \tag{6.7}$$

Figure 6.1 shows the right hand side of the Eqs. (6.5) and (6.6) for symmetric (red dots) and antisymmetric (black open dots) wave functions for a chain with $M = 7$ and $M = 8$. Drawing a horizontal line at the chosen value of γ, the crossings determine graphically the solutions for ϕ, as illustrated for the cases $\gamma = 1$ and -1. Notice the odd/even degeneracies that appear for $\gamma = \pm 1$, a characteristic feature of these two cases, and their absence for any other values of γ. It can be checked that the $\gamma = 1$ solutions are $\phi_q = 2\pi q/M$, with $q = 0, \ldots, M-1$, all twice degenerate except the first. The first degenerate excited states correspond to the vortex / antivortex states (fluxon / antifluxon). Similarly, when $\gamma = -1$ the solutions are $\phi_q = \frac{2\pi}{M}(q + \frac{1}{2})$, with $q = 0, \ldots, M-1$, all twice degenerate except the last. In this case, the first degenerate (ground) states correspond to the half-quantized vortex / antivortex states (semifluxon / antisemifluxon).

For arbitrary γ, all the real solutions that can be extracted from those figures fulfill the

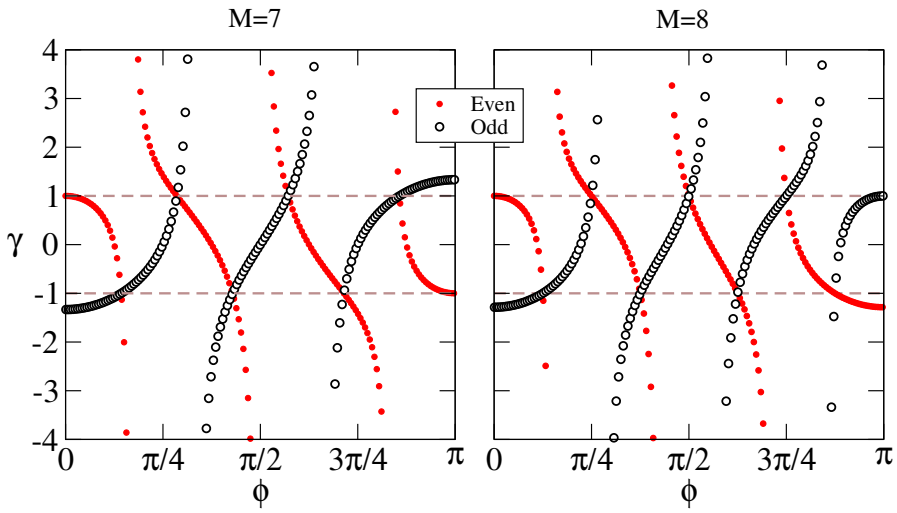

Figure 6.1: Graphical real solutions of Eq. (6.5), even solutions, red dots, and Eq. (6.6), odd solutions, black open dots. As en example we depict horizontal lines for $\gamma = \pm 1$, dashed brown lines. For a given γ, the solutions correspond to the crossings between the horizontal dashed line and the curves drawn by the dots. The number of sites considered is $M = 7$ (left) and $M = 8$ (right).

condition $0 \leq \phi \leq \pi$. Therefore the corresponding energies, Eq. (6.7), are in the band $-2J \leq \mu \leq 2J$, and the associated eigenstates are *bulk states*. This is in agreement with the results in Fig. 6.2, which shows the single-particle spectrum as a function of γ for $M = 3, 4, 5$ and 6. However, there are some special states whose energy is not contained within the previous interval. They correspond to *surface states*, and will be discussed below.

The poles of Fig. 6.1 (which give the solutions when $|\gamma| \to \infty$) are determined by the zeros of the denominators in Eqs. (6.5) and (6.6), i.e. $\phi^{(S,A)}_{k,(|\gamma|\to\infty)} = \pi k/(M-1)$ where k accounts for the odd (even, including $k = 0$) natural numbers for the symmetric (antisymmetric) wave function. As seen in Fig. 6.1 each ϕ corresponding to a finite γ is bounded by those of two consecutive poles $\phi^{(S,A)}_{k-1,(|\gamma|\to\infty)} < \phi^{(S,A)}_{k} < \phi^{(S,A)}_{k,(|\gamma|\to\infty)}$, where $\phi_{-1,(|\gamma|\to\infty)}$ has to be taken as 0. These inequalities show that there are no crossings of single-particle levels of the same parity. This feature can be readily seen in Fig. 6.2, since even single-particle levels (filled symbols) do not intersect levels corresponding to other even-parity states, independently of the number of sites (and the same occurs for odd-parity states, represented by open symbols). Note also that the curves associated to the solid red (dashed blue) lines in Fig. 6.1 are monotonically decreasing (increasing). Thus a monotonic variation of γ gives also a monotonic variation of its corresponding energy in Fig. 6.2.

Extension to imaginary values of ϕ: Surface states

The remaining (up to M) eigenstates of Eq. (6.3) correspond to surface states and require imaginary values of the Bloch phase: $\phi = i\eta$, with η real. Then the implicit equation for the eigenvalues (6.5), becomes

$$\gamma = \frac{\cosh(\eta(M+1)/2)}{\cosh(\eta(M-1)/2)}\,, \tag{6.8}$$

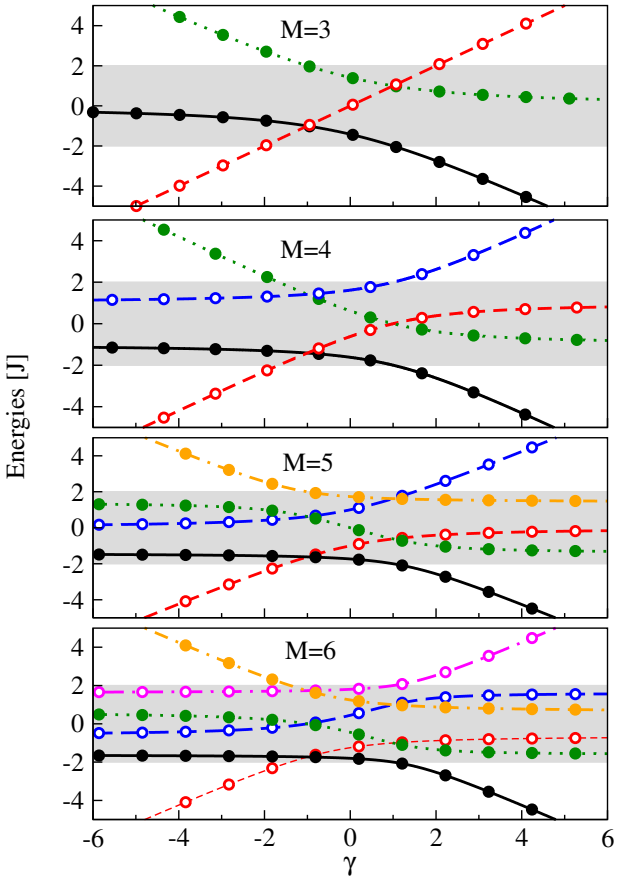

Figure 6.2: Single-particle spectrum for the cases of $M = 3$, 4, 5 and 6 sites, as a function of γ. Filled (open) symbols characterize levels with even (odd)-parity states. The grey region encompasses the range of eigenvalues $|\mu| < 2J$, which contains all the states with real Bloch phase: bulk states. The states outside this region, which have imaginary Bloch phase (see the text), are surface states. Energies are in units of J.

and at small η, the right hand side of the previous equation behaves as $1 + M/2\eta^2$ and leads to $\gamma > 1$. For large η this term rises as e^η and guarantees that there will be solutions for any value of $\gamma > 1$.

For the antisymmetric solutions one has to introduce also $\phi = i\eta$ and the right hand side of Eq. (6.6) becomes

$$\gamma = -\frac{\sinh(\eta(M+1)/2)}{\sinh(\eta(M-1)/2)}, \tag{6.9}$$

and for small η

$$\gamma \simeq -\frac{M+1}{M-1}\left(1 + \frac{1}{6}M\eta^2\right) < -\frac{M+1}{M-1}, \tag{6.10}$$

in agreement with the lower bound in Fig. 6.1. The asymptotic behavior for large η is now $\gamma \simeq -e^\eta$. Figure 6.1 also shows that there is a similar problem with the solutions associated to

states with highest ϕ, corresponding to the surface states above the grey region in Fig. 6.2. In this case one has to set $\phi = \pi + i\eta$ to find the missing solution.

In analogy to the expression of γ as a function of the imaginary Bloch phase, the eigenenergies change as well, which can be calculated as $\mu = -2J\cosh\eta$. This expression, at large values of η, becomes $\mu = \mp 2J\gamma$, for the even $(-)$ and odd $(+)$ surface states. This explains the asymptotic linear behaviour of the energies of these states shown in Fig. 6.2.

6.1.2 Many-body coherent states

In Chap. 2, we have introduced coherent states, which are defined as

$$|\alpha\rangle_q \equiv \frac{1}{\sqrt{N!}}(\hat{\alpha}_q^\dagger)^N|\mathrm{vac}\rangle\,, \tag{6.11}$$

where here, q is an index that provides information about the *flux* carried by the system in the given coherent state. The $\hat{\alpha}_q$ operators can be defined in terms of the single-particle eigensolutions of $\hat{\mathcal{T}}$ described in the previous section:

$$\hat{\alpha}_q^\dagger = \sum_\lambda \chi_q(\lambda)\,\hat{b}_\lambda^\dagger\,, \quad \hat{\alpha}_q = \sum_\lambda \chi_q^*(\lambda)\,\hat{b}_\lambda\ , \tag{6.12}$$

where λ and q run from 1 to M. Unitarity imposes the following relations:

$$\sum_\lambda \chi_q^*(\lambda)\chi_{q'}(\lambda) = \delta_{qq'}\,, \quad \sum_q \chi_q^*(\lambda')\ \chi_q(\lambda) = \delta_{\lambda\lambda'}\ , \tag{6.13}$$

and thus $[\hat{\alpha}_q, \hat{\alpha}_p^\dagger] = \delta_{qp}$, and

$$\hat{b}_\lambda^\dagger = \sum_q \chi_q^*(\lambda)\ \hat{\alpha}_q^\dagger\,, \quad \hat{b}_\lambda = \sum_q\ \chi_q(\lambda)\ \hat{\alpha}_q\,. \tag{6.14}$$

For $\gamma = -1$, the cases $q = 0$ and $q = M-1$ correspond to the semifluxon, $\hat{b}_{\mathrm{sf}}^\dagger$, and antisemifluxon states, $\hat{b}_{\mathrm{asf}}^\dagger$, which are states with opposed half quantum circulation.

Ground state

The expectation value of the Hamiltonian (6.1) in a coherent state leads to the Gross-Pitaevskii energy functional, which is useful in order to obtain the excitations over mean-field coherent states. The expectation value of $\hat{\mathcal{T}}$ can be readily computed by using that $\hat{b}^\dagger|n\rangle = \sqrt{n+1}\,|n+1\rangle$ and $\hat{b}|n\rangle = \sqrt{n}\,|n-1\rangle$. It yields to:

$$\langle\alpha_q\,|\,\hat{b}_{\lambda+1}^\dagger\,\hat{b}_\lambda\,|\,\alpha_q\rangle = N\chi_q^*(\lambda+1)\chi_q(\lambda)\,. \tag{6.15}$$

Therefore, the matrix elements of $\hat{\mathcal{T}}$ are

$$\begin{aligned}\langle\alpha_q|\hat{\mathcal{T}}|\alpha_q\rangle = &- JN\sum_{\lambda=1}^{M-1}\left(\chi_q^*(\lambda)\chi_q(\lambda+1)+\chi_q^*(\lambda+1)\chi_q(\lambda)\right)\\ &-\gamma JN\left(\chi_q^*(M)\chi_q(1)+\chi_q^*(1)\chi_q(M)\right).\end{aligned} \tag{6.16}$$

One can analogously compute the expectation value of the interaction part of the hamiltonian to get:

$$\langle\alpha_q|\,\hat{\mathcal{U}}\,|\alpha_q\rangle = \frac{U}{2}N(N-1)\sum_{\lambda=1}^{M}|\chi_q(\lambda)|^4\,. \tag{6.17}$$

Once the matrix elements of the hamiltonian are obtained, the corresponding Gross-Pitaevskii mean-field equation can be derived by adding a Lagrange multiplier to conserve the norm $\mu_q N\sum_\lambda|\chi_q(\lambda)|^2$ and differentiating with respect to $\chi_q^*(\lambda)$. We arrive at the mean-field equations[1],

$$\begin{aligned}\mu_q\chi_q(\lambda) &= -J(\chi_q(\lambda-1)+\chi_q(\lambda+1))+U\,(N-1)\,|\chi_q(\lambda)|^2\chi_q(\lambda)\\ \mu_q\chi_q(1) &= -J(\gamma\chi_q(M)+\chi_q(2))+U\,(N-1)\,|\chi_q(1)|^2\chi_q(1)\,,\end{aligned} \tag{6.18}$$

which in matrix form becomes Eq. (6.3) for the non-interacting case. Let us point out that for a consistent derivation one has to assume that the $\chi_q(\lambda)$ in Eq. (6.12) are the ones that follow from solving the Gross-Pitaevskii equation including the interaction, $\hat{\mathcal{U}}$. In general, these $\chi_q(\lambda)$ will be different from the ones found without interaction.

Elementary excitations

We will now assume that to a good approximation, even when $U\neq 0$, the simplest excited states can be approximated as one atom being promoted from the coherent state $|\alpha_q\rangle$ made of all the atoms occupying the orbital χ_q to an excited orbital χ_p, both p and q orbitals being eigenstates of the noninteracting single-particle hamiltonian:

$$|\alpha_{q,p}^*\rangle \equiv \frac{1}{\sqrt{(N-1)!}}\,(\hat{\alpha}_q^\dagger)^{N-1}\,\hat{\alpha}_p^\dagger\,|\,\mathrm{vac}\,\rangle\,. \tag{6.19}$$

The expectation value of the hamiltonian (6.1) is the sum of the expectation value of the kinetic term and the interactions. The former element is:

$$\begin{aligned}\langle\alpha_{q,p}^*|\hat{\mathcal{T}}|\alpha_{q,p}^*\rangle = &-J\left(\sum_{\lambda=1}^{M-1}\left(\chi_p^*(\lambda+1)\chi_p(\lambda)+\chi_p^*(\lambda)\chi_p(\lambda+1)\right)+\gamma\left(\chi_p^*(M)\chi_p(1)+\chi_p^*(1)\chi_p(M)\right)\right)\\ &-J\,(N-1)\left(\sum_{\lambda=1}^{M-1}\left(\chi_q^*(\lambda+1)\chi_q(\lambda)+\chi_q^*(\lambda)\chi_q(\lambda+1)\right)+\gamma\left(\chi_q^*(M)\chi_q(1)+\chi_q^*(1)\chi_q(M)\right)\right).\end{aligned} \tag{6.20}$$

The kinetic energy cost of the promotion of one particle from the q mode coherent ground

[1] Notice that there is a missprint in Eq.(20) in Ref. [Gal16a].

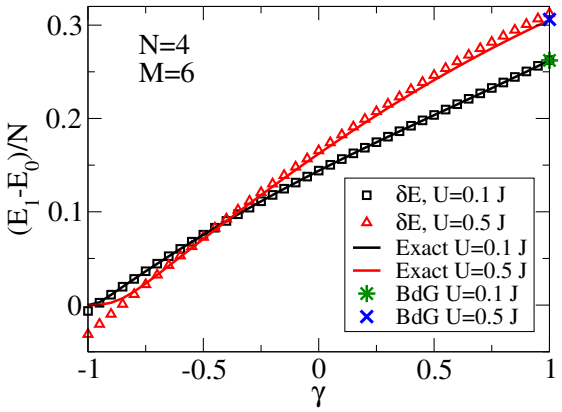

Figure 6.3: Solid lines represent the exact first excitation energy for $U = 0.1$ J (black) and $U = 0.5$ J (red). Squares and triangles correspond to the first excitation energy, computed from Eqs. (6.21) and (6.23), replacing q and p by 0 and 1. Notice also that for $-1 < \gamma < 1$ the ground and first excited states change symmetry, see Fig. 6.1. The cross and star symbols are the more accurate Bogoliubov-de Gennes predictions for $\gamma = 1$. In all cases, $N = 4$ and $M = 6$.

state to the p mode is:

$$\begin{aligned}
&\delta T \equiv \langle \alpha^*_{q,p}|\hat{\mathcal{T}}|\alpha^*_{q,p}\rangle - \langle \alpha_q|\hat{\mathcal{T}}|\alpha_q\rangle \\
&= -J\sum_{\lambda=1}^{M-1}\left[\chi^*_p(\lambda+1)\chi_p(\lambda) - \chi^*_q(\lambda+1)\chi_q(\lambda) + \chi^*_p(\lambda)\chi_p(\lambda+1) - \chi^*_q(\lambda)\chi_q(\lambda+1)\right] \\
&\quad - \gamma J\left[\chi^*_p(M)\chi_p(1) - \chi^*_q(M)\chi_q(1) + \chi^*_p(1)\chi_p(M) - \chi^*_q(1)\chi_q(M)\right] . \qquad (6.21)
\end{aligned}$$

A similar procedure can be followed to obtain the expectation value of $\hat{\mathcal{U}}$:

$$\langle \alpha^*_{q,p}|\hat{\mathcal{U}}\,|\alpha^*_{q,p}\rangle = \frac{U}{2}\left[(N-1)(N-2)\sum_{\lambda=1}^{M}|\chi_q(\lambda)|^4 + 4(N-1)\sum_{\lambda=1}^{M}|\chi_q(\lambda)|^2|\chi_p(\lambda)|^2\right], \qquad (6.22)$$

together with the excitation energy cost due to interactions δU, which yields to

$$\delta U \equiv \langle \alpha^*_{q,p}|\hat{\mathcal{U}}\,|\alpha^*_{q,p}\rangle - \langle \alpha_q|\hat{\mathcal{U}}\,|\alpha_q\rangle = U(N-1)\sum_{\lambda=1}^{M}\left[|\chi_q(\lambda)|^2(2|\chi_p(\lambda)|^2 - |\chi_q(\lambda)|^2)\right]. \qquad (6.23)$$

Figure 6.3 shows the calculated lowest excitation energy, $\delta E = \delta T + \delta U$ for a range of values of γ and two particular values of U. In addition, at $\gamma = 1$ the energy gap predicted by the Bogoliubov-de Gennes approach computed as in Eqs. (20) and (21) of [Par03] has been added (cross for $U = 0.5$ J and star for $U = 0.1$ J). The figure shows that for small values of U and except in the vicinity of $\gamma = -1$ the present approximation can explain most of the effect of the interaction. The singular point $\gamma = -1$ will be discussed in the next section.

6.1.3 The twisted configuration ($\gamma = -1$)

Figure 6.2 shows that the cases of $\gamma = \pm 1$ exhibit degeneracy points where the eigenvectors are linear combinations of the solutions of the hamiltonian (6.1). Remarkably, these new states are no longer currentless. One can construct a basis of flow states (from now on, *flow basis*), which can be obtained from the bare states through the following unitary transformation:

$$\begin{aligned}\tilde{\chi}_q(\lambda;\gamma=+1) &= \frac{1}{\sqrt{M}}\, e^{\,i\frac{2\pi}{M}q\lambda} \\ \tilde{\chi}_q(\lambda;\gamma=-1) &= \frac{1}{\sqrt{M}}\, e^{\,i\frac{2\pi}{M}(q+1/2)\lambda}\ .\end{aligned} \tag{6.24}$$

These expressions imply equidistributed particle population within all the sites but with a phase variation whose gradient between sites leads to an azimutal velocity.

The $\gamma = 1$ case is the commonly considered situation in the literature, as it also appears in the usual tight-binding models in condensed matter systems. The ground state of the system corresponds to $\phi = 0$, which is a currentless state. It is always nondegenerate and its eigenenergy is $\mu_{gs} = -2$ J, independently of the number of sites M. The first two excited states are degenerate and correspond to $\phi = 2\pi/M$ and $-2\pi/M$. They are the discrete version of the usual vortex states (also called *fluxons*) with a circulation of $\pm 2\pi$ [Lee06, Par03]. In contrast, the ground state of a Bose-Hubbard closed chain with $\gamma = -1$ is always degenerate. We will see in the next section that one can demonstrate analytically that the ground state for $\gamma = -1$ is spanned by the eigenvectors corresponding to $q = 0\,(\phi = \pi/M)$ and $q = M-1\,(\phi = -\pi/M)$ in Eq. (6.24), which are discrete *semifluxon/antisemifluxon* states (half-vortices with $\pm\pi$ circulation). The energy gap $\Delta \equiv \mu_{\rm ex} - \mu_{\rm gs}$ between the degenerate ground states and the first excitation is

$$\Delta = 4J\sin(\pi/M)\,\sin(2\pi/M) \simeq 8J\pi^2/M^2\,. \tag{6.25}$$

As explained above, the $\gamma = -1$ case can be related by a local gauge transformation to a Bose-Hubbard hamiltonian in which each hopping induces a π/M phase, as in Eq. (6.2). In that case, considered for instance in Ref. [Hal06] for $M = 3$, the degeneracy takes place between the fully symmetric ground state for $\gamma = 1$, and one of the vortex states.

Analytical model

In order to develop an analytical model that describes the ground state in the $\gamma = -1$ case, it is instructive to start with the case of $M = 3$, which is the minimal closed Bose-Hubbard ring with a weak link that can be constructed [Arw17]. In this case, the single-particle spectrum (see Fig. 6.2) displays two degenerate eigenvalues with eigenenergy $\mu = -J$, and one excited state, which we call $|e\rangle$, with eigenenergy $\mu_{\rm e} = 2J$. The eigenstates associated to these eigenenergies

can be obtained analytically:

$$
\begin{aligned}
|S\rangle &= \frac{1}{\sqrt{6}}\left(|1,0,0\rangle + 2|0,1,0\rangle + |0,0,1\rangle\right) \\
|A\rangle &= \frac{1}{\sqrt{2}}\left(|1,0,0\rangle - |0,0,1\rangle\right) \\
|e\rangle &= \frac{1}{\sqrt{3}}\left(|1,0,0\rangle - |0,1,0\rangle + |0,0,1\rangle\right) ,
\end{aligned} \tag{6.26}
$$

where we have labelled the two degenerate ground states as $|S\rangle$ and $|A\rangle$, since these states are symmetric and antisymmetric with respect to the exchange of the sites 1 and 3, respectively. We can build the corresponding creation and annihilation operators of these states as:

$$
\begin{aligned}
\hat{S}^\dagger &= \frac{1}{\sqrt{6}}\left(\hat{b}_1^\dagger + 2\hat{b}_2^\dagger + \hat{b}_3^\dagger\right) \\
\hat{A}^\dagger &= \frac{1}{\sqrt{2}}\left(\hat{b}_1^\dagger - \hat{b}_3^\dagger\right) \\
\hat{e}^\dagger &= \frac{1}{\sqrt{3}}\left(\hat{b}_1^\dagger - \hat{b}_2^\dagger + \hat{b}_3^\dagger\right) ,
\end{aligned} \tag{6.27}
$$

which obey the proper commutation relations: $[\hat{S}, \hat{S}^\dagger] = [\hat{A}, \hat{A}^\dagger] = [\hat{e}, \hat{e}^\dagger] = \mathbb{1}$. The relation between the basis given by the $\hat{S}$, $\hat{A}$ and $\hat{e}$ operators and the $\hat{b}_i$ operators can be inverted:

$$
\begin{aligned}
\hat{b}_1^\dagger &= \frac{1}{\sqrt{6}}\hat{S}^\dagger + \frac{1}{\sqrt{2}}\hat{A}^\dagger + \frac{1}{\sqrt{3}}\hat{e}^\dagger \\
\hat{b}_2^\dagger &= \sqrt{\frac{2}{3}}S^\dagger - \frac{1}{\sqrt{3}}\hat{e}^\dagger \\
\hat{b}_3^\dagger &= \frac{1}{\sqrt{6}}\hat{S}^\dagger - \frac{1}{\sqrt{2}}\hat{A}^\dagger + \frac{1}{\sqrt{3}}\hat{e}^\dagger .
\end{aligned} \tag{6.28}
$$

At this point, if we want to consider the physics inherent to the two degenerate ground state, from the last change of basis we can simply remove the contribution of the excited state, which yields to:

$$
\begin{aligned}
\hat{b}_1^\dagger &= \frac{1}{\sqrt{6}}\hat{S}^\dagger + \frac{1}{\sqrt{2}}\hat{A}^\dagger \\
\hat{b}_2^\dagger &= \sqrt{\frac{2}{3}}S^\dagger \\
\hat{b}_3^\dagger &= \frac{1}{\sqrt{6}}\hat{S}^\dagger - \frac{1}{\sqrt{2}}\hat{A}^\dagger .
\end{aligned} \tag{6.29}
$$

In this subspace, the interaction hamiltonian reads:

$$
\begin{aligned}
\hat{\mathcal{U}} =& \frac{U}{2}\sum_{\lambda=1}^{M} \hat{b}_\lambda^\dagger \hat{b}_\lambda^\dagger \hat{b}_\lambda \hat{b}_\lambda \\
=& \frac{1}{2}\left(\hat{S}^\dagger\hat{S}^\dagger\hat{S}\hat{S} + \hat{A}^\dagger\hat{A}^\dagger\hat{A}\hat{A}\right) + \frac{2}{3}\left(\hat{S}^\dagger\hat{A}^\dagger\hat{S}\hat{A}\right) + \frac{1}{6}\left(\hat{S}^\dagger\hat{S}^\dagger\hat{A}\hat{A} + \hat{A}^\dagger\hat{A}^\dagger\hat{S}\hat{S}\right) .
\end{aligned} \tag{6.30}
$$

The previous hamiltonian can be diagonalized in the following basis:

$$\hat{b}^\dagger_{\rm sf} = \frac{1}{\sqrt{2}}\left(\hat{S}^\dagger + i\hat{A}^\dagger\right) = \frac{1}{\sqrt{3}}\left(e^{i\frac{\pi}{3}}\,\hat{b}^\dagger_1 + \hat{b}^\dagger_2 + e^{-i\frac{\pi}{3}}\,\hat{b}^\dagger_3\right)$$
$$\hat{b}^\dagger_{\rm asf} = \frac{1}{\sqrt{2}}\left(\hat{S}^\dagger - i\hat{A}^\dagger\right) = \frac{1}{\sqrt{3}}\left(e^{-i\frac{\pi}{3}}\,\hat{b}^\dagger_1 + \hat{b}^\dagger_2 + e^{i\frac{\pi}{3}}\,\hat{b}^\dagger_3\right), \tag{6.31}$$

in which the interacting hamiltonian takes the following expression:

$$\hat{\mathcal{U}} = \frac{1}{6}\,U\left(\hat{n}^2_{\rm sf} + \hat{n}^2_{\rm asf} + 4\hat{n}_{\rm sf}\hat{n}_{\rm asf} - \hat{n}_{\rm sf} - \hat{n}_{\rm asf}\right), \tag{6.32}$$

where $\hat{n}_{\rm sf} = \hat{b}^\dagger_{\rm sf}\hat{b}_{\rm sf}$ and $\hat{n}_{\rm asf} = \hat{b}^\dagger_{\rm asf}\hat{b}_{\rm asf}$ are the number of semifluxons and antisemifluxons operators, respectively.

One can generalize the procedure followed previously by writing the creation and annihilation operators in the coherent flow basis, and truncating such decomposition to the semifluxon and the antisemifluxon states, i.e.

$$\hat{b}^\dagger_\lambda = \frac{1}{\sqrt{M}}\left(e^{i\lambda\pi/M}\,\hat{b}^\dagger_{\rm sf} + e^{-i\lambda\pi/M}\,\hat{b}^\dagger_{\rm asf}\right) \tag{6.33}$$

and the corresponding expression for $\hat{b}_\lambda$. One can then rewrite the $\hat{\mathcal{U}}$ operator by taking into account that sums like $\sum_{\lambda=1}^{M}\exp(i2\lambda\pi/M)$ vanish, as

$$\hat{\mathcal{U}} = \frac{1}{2M}U\left[\hat{n}^2_{\rm sf} + \hat{n}^2_{\rm asf} + 4\hat{n}_{\rm sf}\hat{n}_{\rm asf} - (\hat{n}_{\rm sf} + \hat{n}_{\rm asf})\right]. \tag{6.34}$$

Since $N = N_{\rm sf} + N_{\rm asf}$ is constant, the last term in Eq. (6.34) corresponds to a global energy shift that can be neglected. The eigenstates of $\hat{\mathcal{U}}$ are the new Fock states:

$$|N_{\rm sf}, N_{\rm asf}\rangle = \frac{1}{\sqrt{N_{\rm sf}!N_{\rm asf}!}}(\hat{b}^\dagger_{\rm sf})^{N_{\rm sf}}(\hat{b}^\dagger_{\rm asf})^{N_{\rm asf}}|{\rm vac}\rangle\,. \tag{6.35}$$

In terms of this basis, one can span the ground state of the system as a superposition of the following cat-like states:

$$|\Psi^\pm_k\rangle = \frac{1}{\sqrt{2}}\left(|k, N-k\rangle \pm |N-k, k\rangle\right). \tag{6.36}$$

This is called two-orbital approximation, and $|\Psi^\pm_0\rangle$ corresponds to the two-fold degenerate ground state. A similar approximation and macroscopic superposition of superfluidflow was considered in Ref. [Hal06] for a three-well system in a different gauge.

6.1.4 Bogoliubov-de Gennes spectrum

The spectrum of elementary excitations in the weakly interacting regime can be studied within the Bogoliubov-de Gennes framework. For a Bose-Hubbard ring without weak link ($\gamma = 1$), such an analysis was presented in Ref. [Par03]. To obtain the Bogoliubov spectrum, one can start from the Gross-Pitaevskii equation (6.18) associated to the Bose-Hubbard hamiltonian of the

ring. From Eq.(3.37), we know that the corresponding Bogoliubov equations are:

$$\begin{aligned}\hbar\omega\, u_k(\lambda) =& -\mu_q u_k(\lambda) - J\left[u_k(\lambda+1)+u_k(\lambda-1)\right] + (N-1)U|\chi_q(\lambda)|^2\left(2u_k(\lambda)+v_k(\lambda)\right)\\ -\hbar\omega\, v_k(\lambda) =& -\mu_q v_k(\lambda) - J\left[v_k(\lambda+1)+v_k(\lambda-1)\right] + (N-1)U|\chi_q(\lambda)|^2\left(2v_k(\lambda)+u_k(\lambda)\right)\,.\end{aligned} \tag{6.37}$$

In the interacting case, the chemical potential is given by

$$\mu_q = -2J\cos(\phi_q) + \frac{(N-1)U}{2M}\,, \tag{6.38}$$

and the solution for the wave function is a plane wave:

$$\chi_q(\lambda) = \frac{1}{\sqrt{M}}\, e^{i\phi_q\lambda}\,, \tag{6.39}$$

with $\phi_q = 2\pi q/M$. The solutions of the Bogoliubov equations can be also written as plane waves:

$$\begin{aligned}u_k(\lambda) &= \frac{1}{\sqrt{M}}\, e^{i\frac{2\pi k}{M}\lambda}\, e^{i\phi_q\lambda} u_k\\ v_k(\lambda) &= \frac{1}{\sqrt{M}}\, e^{i\frac{2\pi k}{M}\lambda}\, e^{-i\phi_q\lambda} v_k\,.\end{aligned} \tag{6.40}$$

After introducing these solutions into the Bogoliubov equations (6.37), one obtains:

$$\begin{aligned}\hbar\omega\, u_k &= \left[-2J\left(\cos\left(\frac{2\pi k}{M}+\phi_q\right)-\cos\phi_q\right)\right]u_k + \frac{(N-1)U}{M}\left(2u_k+v_k\right)\\ -\hbar\omega\, v_k &= \left[-2J\left(\cos\left(\frac{2\pi k}{M}+\phi_q\right)-\cos\phi_q\right)\right]v_k + \frac{(N-1)U}{M}\left(2v_k+u_k\right)\,.\end{aligned} \tag{6.41}$$

The corresponding eigensolutions are:

$$\hbar\omega_k^{(\pm)} = 2J\sin\left(\frac{2\pi k}{M}\right)\sin(\phi_q) \pm \sqrt{\varepsilon_k\left(\varepsilon_k + \frac{2(N-1)\,U}{M}\right)}\,, \tag{6.42}$$

with

$$\varepsilon_k = 2J\cos(\phi_q)\left[1-\cos\left(\frac{2\pi}{M}k\right)\right]\,. \tag{6.43}$$

For the case of $\gamma=-1$, the equations are formally the same but with $\phi_q = \frac{2\pi}{M}(q+\frac{1}{2})$ instead of $\phi_q = \frac{2\pi}{M}q$.

The Bogoliubov excitation spectrum is constructed over mean-field states defined as macroscopically occupied modes in the flow basis (6.11), with $q=-1,0,1,\ldots,M-2$ (or equivalently $q=0,1,\ldots,M-1$). In the previous expression the corresponding coefficients of the creation operator $\hat{b}_q^\dagger$ are $\tilde{\chi}_q(\lambda;\gamma=-1)$ defined in Eq. (6.24). The periodicity of the system imposes that q is a cyclic index, with period M: for example, $q=0\,(-1)$ and $M\,(M-1)$ are equivalent. The cyclic index k runs from 0 to $M-1$, and it is interesting to notice that, when $k=0\,(M)$, the Bogoliubov spectrum yields $E_{k=0}^{(\pm)}=0$, which corresponds to remain in the unperturbed mean-field state (i.e. without any excitation).

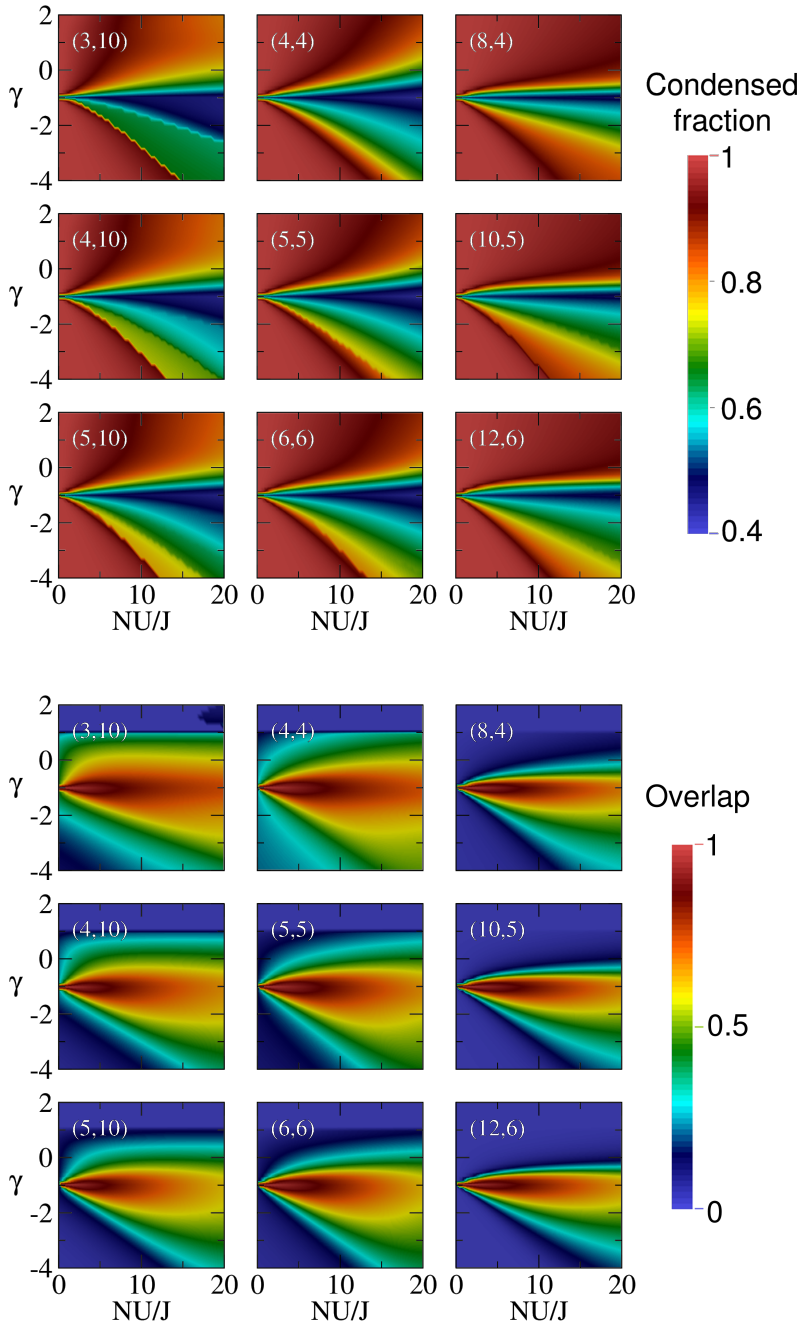

Figure 6.4: The condensed fraction p_1 (top panels) and the overlap determinant $\mathcal{O}$ (bottom panels) are represented in a color map as a function of γ and NU/J, for different values of the pair (M, N), which appears as a label in each plot. In each panel, from top to bottom, the left column has increasing filling factor from 3/10 to 1/2, and the middle and right columns have increasing number of sites M for filling factor 1 and 2, respectively.

6.1.5 Robustness of superconducting flows when $\gamma \neq -1$

The macroscopic superpositions of semifluxon states are predicted to appear for low interactions in the special $\gamma = -1$ case. In this section, we focus on studying the presence of such macroscopic superpositions of superfluid flows when $\gamma \neq -1$. Two indicators will be used to signal the presence of macroscopic cat-like states between the semifluxon and antisemifluxon states. The first one is the fragmentation, defined in Chap. 2. The second one is the overlap between the cat states and the exact solutions resulting from the numerical diagonalization. For $\Lambda = NU/J \lesssim 1$ the ground state is almost doubly-degenerate, then, $\{|\Psi_0^+\rangle, |\Psi_0^-\rangle\}$ is a suitable basis for the lower manifold, as predicted by the two-orbital model. We can therefore define the overlap determinant as,

$$\mathcal{O} = \begin{vmatrix} \langle \Psi_{\rm gs}^{(N)} | \Psi_0^+ \rangle & \langle \Psi_{\rm gs}^{(N)} | \Psi_0^- \rangle \\ \langle \Psi_{\rm 1st}^{(N)} | \Psi_0^+ \rangle & \langle \Psi_{\rm 1st}^{(N)} | \Psi_0^- \rangle \end{vmatrix}, \tag{6.44}$$

with $|\Psi_{\rm gs}^{(N)}\rangle$ and $|\Psi_{\rm 1st}^{(N)}\rangle$ the ground and first excited states obtained by direct diagonalization, respectively. The overlap $\mathcal{O}$ is 1 when the two manifolds are the same.

As expected, the values of the overlap determinant are clearly correlated with those of the condensed fraction, see Fig. 6.4. The system is found to be approximately bifragmented when there is a noteworthy overlap determinant. For small Λ and $\gamma = -1$ we find a condensed fraction of $p_1 \simeq 1/2$ and an overlap determinant very close to 1, regardless of the number of particles and filling factor, N/M. What is somehow unexpected is that finite values of Λ enhance the probability of finding these macroscopic superposition states when $\gamma \neq -1$. For fixed M and filling factors below 1, the area covered by the significantly fragmented configurations broadens for increasing filling, as seen comparing the $(N, M) = (10, 3)$, $(10, 4)$, and $(10, 5)$ panels in Fig. 6.4. For filling factors larger than one, the fragmented region gets reduced, see panels $(N = M, M)$ and $(N = 2M, M)$ in Fig. 6.4. Note that the overlap determinant would be strictly zero if the quasi degeneracy is absent. In this case, even though the ground state may still be well described by $|\Psi_0^+\rangle$, we would get a zero overlap between the two manifolds. This is the reason why the overlap becomes abruptly zero in the vicinity of $\gamma = 1$ signalling a level crossing in the many-body spectrum between the first and second excited states, see Fig. 6.4. This level crossing is directly related to the crossing found at $\gamma = 1$ in the single-particle spectrum, see Fig. 6.2.

Further increasing the interactions, $\Lambda > 100$, the condensed fraction decreases quickly to the expected value $1/M$ for the Mott insulating regime, Fig. 6.5. For integer filling, in the $\Lambda \to \infty$ limit the ground state is nondegenerate and gapped (Mott insulator of the corresponding filling). Thus, it is expected that already for any finite value of Λ the two-fold degeneracy predicted by the two orbital model would be only approximate. For fractional fillings, in contrast, in the large interaction limit the ground state will be degenerate, with the surplus particles delocalized in the chain. In this case the numerics shows that the two-fold degeneracy predicted by our model is present for all values of Λ.

Besides the condensed fraction and the overlap, a crucial feature of a macroscopic superposition is its robustness, characterized by the presence of an energy gap that protects the superposition to be affected by excitations that could involve larger-energy excited states. In Fig. 6.6 we present the energy difference between the ground state and the first excited state (a), and the energy difference between the latter and the second excited one (b). There are two important properties exhibited by the peculiar case of $\gamma = -1$. First, for zero interactions, the ground

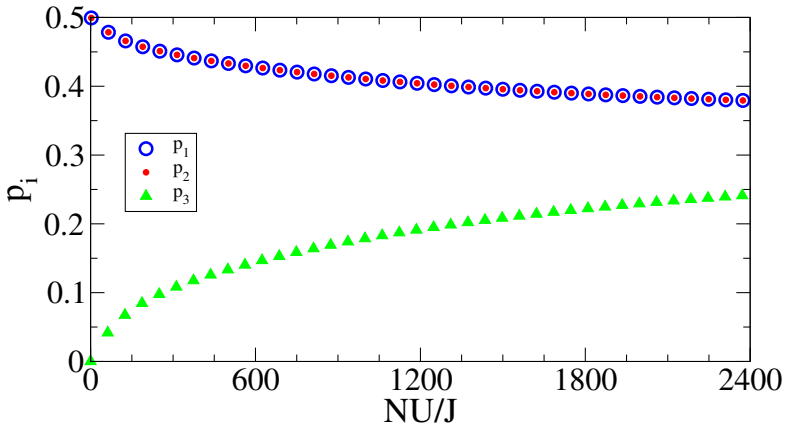

Figure 6.5: Representation of the three eigenvalues of one-body density matrix for $M = 3$ for $N = 48$, as a function of $\Lambda = NU/J$.

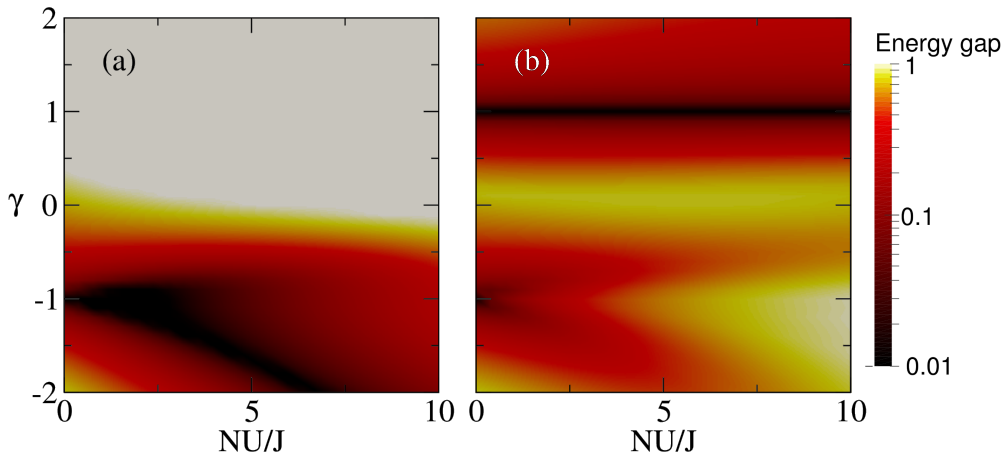

Figure 6.6: Panel (a) displays the energy gap between the many-body ground state and the first excited state, and panel (b) the energy difference between the first and second excited states. Both are computed as a function of Λ and γ for $N = M = 5$.

state has a degeneracy of $N+1$ states, stemming from the combinatorial factor, i.e. N particles populating two single-particle states in $N+1$ ways. For very small interactions, $\Lambda \lesssim 0.5$, this is reflected in the very small gap ($\lesssim 0.01\,J$) both between the ground and first, see Fig. 6.6(a), and between the first and second excited many-body eigenstates, see Fig. 6.6(b). Secondly, for $\gamma = -1$ and $\Lambda \gtrsim 5$, a gap starts to open above the ground state. This gap opening increases the robustness of the macroscopic superposition, which indicates that experimental observation of these states should be feasible.

In the noninteracting case, the densities can be easily constructed by using the wave functions given by Eq. (6.4). When $\gamma > -1$, the ground state is symmetric (see Fig. 6.1), and the density

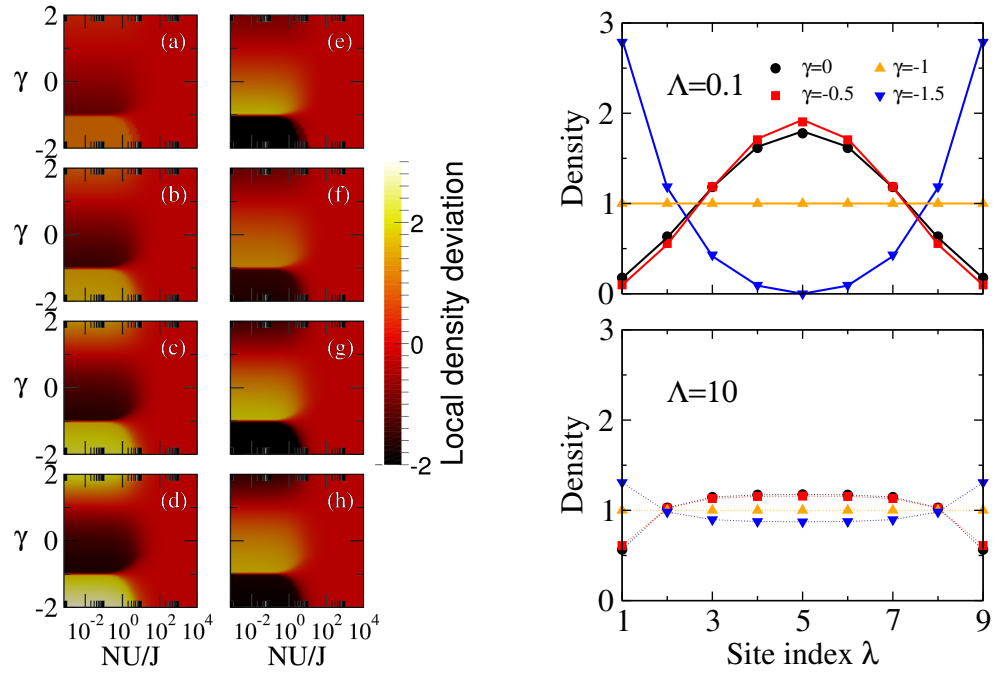

Figure 6.7: Left panels represent the deviation of the local density of the ground state from its global average at the tunable link (a-d), and in the center of the chain, furthest from the tunable link (e-h) as a function of $\Lambda \equiv NU/J$ and γ. The filling factor is the same for all panels, $N/M = 2$. $M = 3$, 4, 5 and 6, are depicted in panels (a,e), (b,f), (c,g) and (d,h), respectively. Right panels show the local average density of the ground state, $\langle \hat{b}_\lambda^\dagger \hat{b}_\lambda \rangle$, as a function of the site index λ for $N = M = 9$. Symbols depict the exact results for the values of $\gamma = -1.5$ (down-triangles), -1 (up-triangles), -0.5 (squares) and 0 (circles). For the small interaction case, $\Lambda = 0.1$, we add the non-interacting result, given explicitly in Eq. (6.45) for bulk states, as solid lines. The dotted lines for $\Lambda = 10$ are just linear interpolations of the exact results.

is given by:

$$\rho^{\gamma}(\lambda) = \frac{N}{\mathcal{N}_+} \cos^2\left[\left(\frac{M+1}{2} - \lambda\right)\phi\right], \tag{6.45}$$

with ϕ determined from Eq. (6.5). These densities are linear in N, have a maximum at $\lambda_m = (M+1)/2$ and are site symmetric with respect to λ_m. The simplest example is the case $\gamma = 0$, where the solution of Eq. (6.5) is $\phi = \pi/(M+1)$ and

$$\rho^{\gamma=0}(\lambda) = \frac{2N}{M+1} \sin^2\left(\frac{\pi}{M+1}\lambda\right), \tag{6.46}$$

which shows that at the maximum $\rho_M = 2N/(M+1)$ and at sites 1 and M, $\rho = 2N/(M+1)\sin^2(\pi/(M+1))$. Similar expressions can be written when $\gamma < -1$, but with the odd single-particle solutions, and, for surface states, the densities can be derived in an analogous way, and they involve hyperbolic functions. The exact results shown in Fig. 6.7 for $\Lambda = 0.1$ are almost identical to these simple predictions, except when γ is very close to -1 where the breaking of

the degeneracy of the odd and even solutions when $U \neq 0$ has to be taken into account.

The effect of varying γ and Λ on the density of the cloud is also particularly pronounced. For $\gamma = 1$, the population is equal within all the sites, as the system is rotationally symmetric. For $\gamma = -1$ the situation is different due to the quasidegeneracy at the ground state level. For small values of the interaction, the ground state is well represented by the cat states between the semifluxon and the antisemifluxon states, which results in a constant density along the chain, see Fig. 6.7. In the Mott regime, the system is equipopulated again, regardless of the value of γ, see the $\Lambda \gtrsim 10$ results in Fig. 6.7. Already for $|\gamma| \gtrsim 1.5$, the density approaches the one built from the surface modes described in the first section, with population peaked on the sites around the tunable link. In Fig. 6.7 we provide a broader picture for filling factor 2. Again for large interactions, both the central density and the density at the extremes approach the $N/M = 2$ limit. Interestingly, the region of macroscopic superposition of fluxon-antifluxon states reflects in an almost equipopulation of all sites for all values of Λ. As discussed above, away from $\gamma = -1$ and for lower interactions, the cat-like state is less robust, resulting in a higher density in the center (extremes) as γ increases (decreases). Monitoring the density of the chain can therefore be a good indicator of the macroscopic superposition states expected. For instance, the chain could be initially prepared at small but nonzero interactions and $\gamma = 1$. Turning the tunable link from $\gamma = 1$ to $\gamma = -1$, the density in the center will grow, reaching very large values of $\gamma \simeq -1$. At $\gamma = -1$ the chain should be again equipopulated. This transition from having almost zero population in the extremes to equipopulation would signal the regime of macroscopic superposition of fluxon-antifluxon states.

6.2 Toroidal trap with a weak link

In the last section, we have seen that a weak link in a Bose-Hubbard ring can generate a macroscopic superposition of current flows. In this section we will show which are the mean-field states that can couple two counterpropagating persistent currents in a torus [Ryu07, Ram11, Mou12, Bea13]. The effect of a weak link, which is an external potential that produces a density depletion, has been theoretically and experimentally addressed in rings of ultracold atomic gases [Pia09, Pia13, Ram11, Wri13]. In the case of a rotating weak link, such a barrier drags the superfluid into a moving state once the resistance of the system to create excitations has been overcome. Whether superfluid excitations are triggered by reaching the speed of sound, according to Landau criterion, or by vortex nucleation, following Feynman criterion, is still an open question [Pia13]. Recent experimental works [Wri13, Eck14] point out that vortices are responsible of the activation of persistent currents in a ring. *Phase slips* are dissipative phenomena that allow the transition between vortex states (or persistent currents) with different winding numbers. These processes seem to be originated by the transit of vortices [Yak15, Aba15] towards the inner (outer) edge of the system, increasing (decreasing) the winding number in one unit.

In Ref. [Eck14], hysteresis loops have been observed in the generation of quantized persistent currents by means of a rotating weak link. Hysteresis is a phenomenon intimately linked to systems presenting multiple local energy minima separated by energy barriers that must be overcome when driving the system from one minimum to the other [Mue02]. The final state depends on the path followed in the dynamical evolution searching for equilibrium states. For superfluids in a ring, it is well known that local energy minima correspond to states with different

winding number [Blo73]. As shown in a seminal paper by Langer and Ambegaokar [Lan67], and widely considered later in the field of superconductors (see e.g. [McC70, Sol94]), the saddle points of the energy functional for the order parameter play a crucial role in the transition amplitudes between winding number states. Unfortunately, in Bose-Einstein condensates, neither the exact nature of the states lying on the barrier nor their stability have been shown yet.

In this section, we demonstrate the existence of stationary states with nonquantized angular momentum in 3D rings. These states are solitary waves that fill the gap of angular momentum between winding number states. We have found that there are also solitonic stationary states in 3D rings. Among them, and in the absence of a weak link, there exist dynamically stable configurations that can support long-life currents. In addition, we show that solitonic states can also be found in the presence of a rotating weak link. As a result of the explicit symmetry breaking of the rotational invariance, solitary waves become dynamically unstable. Solitonic states are located at the saddle points on the energy barrier preventing phase slips, and meet a family of winding number states when the barrier vanishes. These points determine the range of existence of solitons within the weak link region and thus the size of the hysteresis loop. This fact indicates that Landau and Feynman criteria may also match. The former establishes that phase slips are caused when the fluid flow reaches the local speed of sound, at the end of a winding number family of stationary solutions. But this is also in agreement with Feynman criterion, which states that phase slips appear when vortex lines can be excited inside the system, as it occurs at the end of a solitonic family of steady states.

The time-independent Gross-Pitaevskii associated to a toroidally-trapped Bose-Einstein condensate, with a torus of radius R and rotating frequency Ω is:

$$\left(-\frac{\hbar^2}{2m}\nabla^2 - \Omega\hat{L}_z + V_{\rm ext}(\vec{r}) + g|\psi|^2\right)\psi = \mu\psi\,, \tag{6.47}$$

where the external potential $V_{\rm ext}(\vec{r}) = U_{\rm wl}(\vec{r}) + V_{\rm ring}(\vec{r})$ includes the weak link $U_{\rm wl}(\vec{r}) = U_{wl}\exp[-2\,(R(\theta-\theta_0)/w_\theta)^2]$ along the azimuthal coordinate θ, where U_0 and w_θ are the depth and the width of the weak link, respectively; and the ring trap, which in the 1D case is $V_{\rm ring}(\vec{r}) = 0$ (with periodic boundary conditions) and in the 3D case takes the following expression:

$$V_{\rm ring}(\vec{r}) = \frac{1}{2}m\omega_z^2 z^2 + \frac{1}{2}m\omega_\perp^2(\rho - R)^2\,. \tag{6.48}$$

The energy can be calculated from the functional:

$$E[\psi] = \int d\vec{r}\left\{\frac{1}{2m}\left|(-i\hbar\nabla - m\vec{\Omega}\times\vec{r})\psi\right|^2 + \left(V_{\rm ext}(\vec{r}) - \frac{1}{2}m(\vec{\Omega}\times\vec{r})^2\right)|\psi|^2 + \frac{g}{2}|\psi|^4\right\}\,. \tag{6.49}$$

Persistent currents can be generated by states with integer winding number q, quantized angular momentum per particle $\langle\hat{L}_z\rangle/N = \hbar q$, and constant density along θ, that is

$$\Psi_q(\mathbf{r},t) = e^{-i\mu t/\hbar}\,\psi_q(z, r_\perp)\,e^{iq\theta}\,. \tag{6.50}$$

In addition, persistent currents can also be provided by solitonic states, which present non-

quantized angular momentum and produce density dips along the ring

$$\Psi_\kappa(\mathbf{r},t) = e^{-i\mu t/\hbar}\,\psi_\kappa(z,r_\perp,\theta)\,e^{i\kappa\theta}\,, \tag{6.51}$$

where κ in this case is a real number that plays the role of a quasimomentum (see below).

6.2.1 1D case

The physics previously described can be easily visualized in the 1D case. Without weak link, the lowest-energy states for a given angular momentum, or *yrast* states, have been identified as solitary waves connecting states with different winding numbers [Mot99, Kan09, Jac11]. Assuming that a tight transverse harmonic trap enforces a 1D geometry, and using units of $E_R = \hbar^2/mR^2$, the dimensionless 1D version of Eq. (6.47) without external potential reads

$$\frac{1}{2}\left(-i\frac{\partial}{\partial\theta} - \hat{\Omega}\right)^2\psi + \hat{g}|\psi|^2\psi = \hat{\mu}\psi, \tag{6.52}$$

where $\hat{\mu} = \mu/E_R + \hat{\Omega}^2/2$, $\hat{\Omega} = \hbar\Omega/E_R$, $\hat{g} = 2a_sRN/a_\perp^2$, and $a_\perp = \sqrt{\hbar/m\omega_\perp}$ is the characteristic length of the transverse trap.

Among the analytical solutions of Eq. (6.52), a dark soliton moving with linear velocity v_s along the ring is given by Eq. (6.51) with

$$\psi_\kappa(\theta) = \sqrt{\frac{\mu}{\hat{g}E_R}}\left[i\beta + \gamma\tanh\left(\gamma\sqrt{\frac{\mu}{E_R}}\,\theta\right)\right]\,, \tag{6.53}$$

where $\beta = v_s/c$, $c = \sqrt{\mu/m}$ is the speed of sound, $\gamma^2+\beta^2 = 1$, and $\hbar\kappa/mR = \Omega R - v_s$. As can be seen in Fig. 6.8(a), solitons (open circles), given by Eqs. (6.51) and (6.53), connect states $\psi_q(\theta) \propto e^{iq\theta}$ having consecutive winding phases (solid and dashed lines).

By producing localized density depletions in the ring, a single soliton induces a phase jump $\Delta S = 2\arccos(\beta)$ in the condensate wave function [Pit03]. These phase jumps need to be counterbalanced by background currents around the torus, with angular speed $\kappa = -q - \Delta S/2\pi$, to ensure a single-valued order parameter whenever a closed loop is followed. The resulting flow carries angular momentum per particle, $\langle\hat{L}_z\rangle/N\hbar = -\beta\gamma/\pi - \kappa + (\Delta q - 1)/2$, which takes continuous values in the range between integer winding numbers q and $q+\Delta q$, with $\Delta q = \pm 1$. The velocity of moving solitons v_s cannot exceed the speed of sound c, at which nonlinear soliton excitations transform into linear sound waves traveling on a winding number state. Therefore this speed limit bounds the range of existence of solitonic solutions. Provided that solitonic states can show dynamical stability [Kan09], their associated flows will appear as persistent currents. We will see that there exists the counterpart of these states in multidimensional systems.

Weak link

The presence of a rotating weak link introduces variations in the density profile that give rise to phase jumps, and, like in solitons, background currents are brought about in order to compensate such jumps. Fig. 6.8(b) presents our results obtained from the numerical solution of Eq. (6.52) for a system with $\hat{g} = 100$, and weak link of depth $U_{wl} = 0.56\,\mu$ and width $w_\theta = R$. As

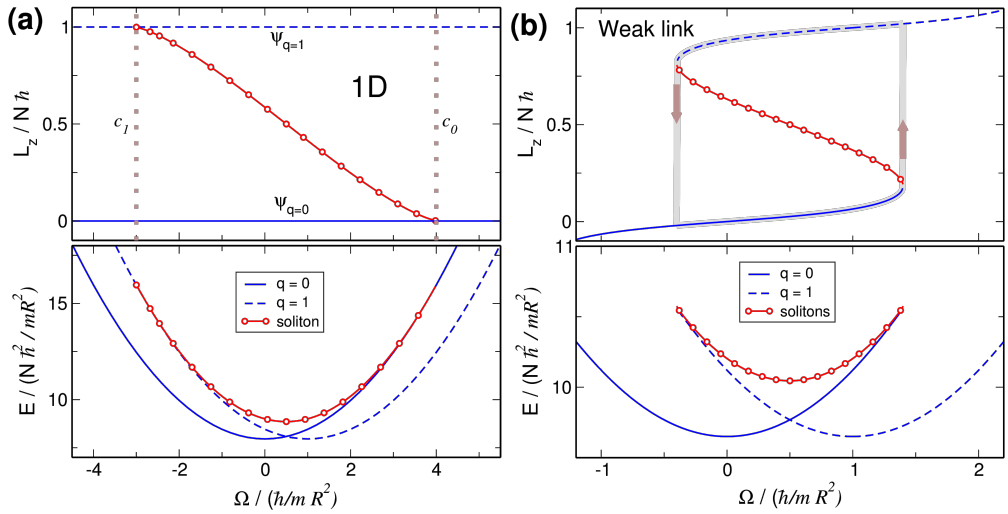

Figure 6.8: Soliton connection between winding number states in a 1D ring for condensates with $\hat{g} = 100$. Only winding numbers 0 and 1 are considered, without (a) and with (b) external weak link of depth $U_{wl} = 0.56\,\mu$ and width $w_\theta = R$ along the angular coordinate. For each case, angular momentum per particle is shown above and energy per particle below. The thick dotted lines of the top graph (a) indicate the values of the speed of sound, c_0 and c_1, relative to the winding number state 0 (right) and 1 (left). The hysteresis loop is displayed in (b) by thick gray lines and arrows.

can be seen, and contrary to the case without weak link, both winding number and solitonic states show variations in the angular momentum with the rotation rate. This effect can be deduced from the expression for the current density $\vec{j}(\vec{r},t) = (\hbar\vec{\nabla}S(\vec{r},t)/m - \vec{\Omega}\times\vec{r})\,n(\vec{r},t)$, expressed in terms of density $n(\vec{r},t)$ and phase $S(\vec{r},t)$ of the order parameter $\Psi(\vec{r},t) = \sqrt{n(\vec{r},t)}\,e^{iS(\vec{r},t)}$. Defining the velocity as $v(\vec{r},t) = j(\vec{r},t)/n(\vec{r},t)$, we get $v(\theta) = \hbar(\partial S(\theta)/\partial\theta - \hat{\Omega})/mR$ for the 1D case. Solving for the phase gradient and integrating along the whole ring we obtain:

$$2\pi q = 2\pi\hat{\Omega} + \frac{mR}{\hbar}\oint d\theta\, v(\theta)\,, \tag{6.54}$$

where, because the order parameter is single-valued, we used $S(\theta = 2\pi) - S(\theta = 0) = 2\pi q$. Whenever the dimensionless angular rotation $\hat{\Omega}$ takes integer values, it is possible to look for static states having $v(\theta) = 0$. Instead, stirring the system at noninteger $\hat{\Omega}$ values imposes a nonvanishing velocity, hence phase gradients.

As a consequence of the weak link, which breaks the rotational symmetry of the system, a gap is opened in the energy spectrum of winding numbers [Mue02, Bah13, Fia12]. This fact is supported and quantified by our numerical results, displayed in Fig. 6.8(b). As can be seen, swallow tails are developed in the presence of a weak link, cutting the otherwise continuous curves traced by winding numbers in Fig. 6.8(a). Generating solitons at the weak link position is energetically more favorable than at higher-density regions. For w_θ greater than the healing length $\xi = \sqrt{\hbar^2/m\mu}$, a local speed of sound $c(\theta) = \hbar\sqrt{\hat{g}\,R\,n_1(\theta)}/mR$ can be defined (n_1 being

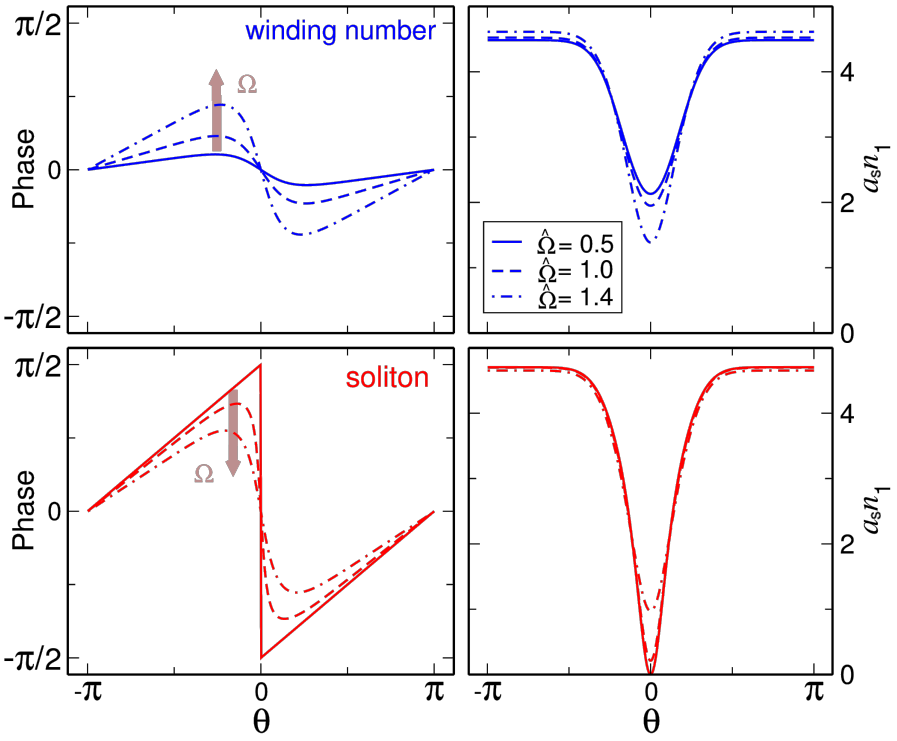

Figure 6.9: Phases (left column) and dimensionless azimuthal densities $a_s n_1(\theta)$ (right column), obtained from numerical solutions of the time-independent 1D Gross-Pitaevskii equation (6.52), corresponding to winding number $q = 0$ (above) and solitonic states (below) for the same parameters as in Fig. 6.8(b), rotating at angular frequencies $\hat{\Omega} = 0.5$, 1.0 and 1.4. Thick arrows (on the left column) indicate the sequence of both type of states for increasing Ω, approaching convergence near $\hat{\Omega} = 1.4$.

the azimuthal density), which takes the lowest value at the weak link center. As the speed of sound is a measure of the range of existence of solitonic solutions, this range is reduced inside the low density region, relative to the system without weak link.

When rotation is introduced, opposite effects can be observed in solitonic and winding-phase states (see Fig. 6.9). For increasing angular frequency, solitons decrease their angular momentum and density dip, whereas winding numbers increase it. In this way, both type of solutions converge at some intermediate value, where the superfluid flow reaches the speed of sound at the weak link. Therefore, the bounds for the existence of solitons are also applicable to states with a winding phase.

Hysteresis loops, as those observed in the experiment [Eck14], can be clearly identified in Fig. 6.8(b) (thick gray lines and brown arrows). In contrast to previous analyses, our results are able to measure the size of the energy barrier preventing phase slips. The solitonic states that we have found are situated at the top of such barriers. These obstacles vanish when both type of states connect, and it is no longer possible to continue beyond these points by increasing the angular velocity. As a result the system decays to the next lower-energy winding-phase state. When the intensity of the weak link grows, the speed of sound and hysteresis cycle width reduce,

and solitons and winding-phase states become energetically closer.

6.2.2 3D case

In multidimensional systems, the 1D picture outlined before is reproduced: solitons are the stationary states making the connection between winding numbers and building the energy barrier separating them. We have numerically solved the 3D Gross-Pitaevskii equation (6.47) in order to find steady states carrying stationary currents in Bose-Einstein condensates with typical experimental parameters. Our results show that 3D toroidal condensates support transverse standing waves equivalent to those found in straight channels, and follow the same energy criterion for their bifurcation. Fig. 6.10(a) exhibits results for a regime where, apart from winding number states, two types of solitary waves can provide stationary currents: dark solitons and solitonic vortices [Bra01, Don14, Ku14, Ku16]. Although their range of existence is quite different, their energies are indistinguishable at the scale of the figure when they coexist. Dark solitons can only be found for values of the angular momentum per particle around $(q + 1/2)\hbar$, while solitonic vortices extend all along the regions between winding numbers, and connect with them. This link is mediated by the two different branches of Fig. 6.10(a) that are represented by means of lines with right and left pointing triangles, along with two characteristic density isocontours. The former connects with the winding number $q = 0$, and consists of vortices that provoke flows rotating in the same direction as Ω, whereas the latter connects with the winding number $q = 1$ and contains counterrotating vortices (antivortices).

It is noteworthy that hysteresis is also present in solitonic vortex states, since the two mentioned branches are separated by an energy barrier occupied by dark solitons (thick green line in Fig. 6.10(a)). This energy difference between solitonic states is responsible of their stability properties. As shown in Fig. 6.11, dark solitons decay into solitonic vortices, which are dynamically stable states. We have evolved in real time a dark soliton state made of 5.3×10^4 atoms of ^{23}Na confined by an isotropic harmonic trap, of angular frequency $\omega_\perp = 2\pi \times 100$ Hz, centered at $R = 6\, a_\perp$. After adding a Gaussian-noise perturbation to the initial dark soliton, it survives during, approximately, the first 20 ms of the simulation, before decaying into another solitary wave, a solitonic vortex, and emitting phonons. The subsequent evolution, sampled at the insets of Fig. 6.11, shows the emergent vortex precessing in the transverse section, and translating around the ring with a different inertial mass than the initial state [Sco11, Lia11].

As in the 1D case, multidimensional solitons can exist only while their velocity around the torus is lower than the speed of sound. For systems confined in isotropic harmonic traps, the speed limit is given by the azimuthal speed of sound $c(\theta)$ that can be calculated by [Mun07]:

$$c(\theta) = \sqrt{\frac{\mu^2(\theta) - (\hbar\omega_\perp)^2}{2m\,\mu(\theta)}}\,, \tag{6.55}$$

where $\mu(\theta)$ is the local chemical potential. In Fig. 6.10(a), the thick dotted vertical lines represent the values given by Eq. (6.55). The manifest agreement with numerical solutions of the Gross-Pitaevskii equation (lines with open triangles), permits Eq. (6.55) to be employed for predicting the range where solitons exist and hence for measuring the size of hysteresis loops.

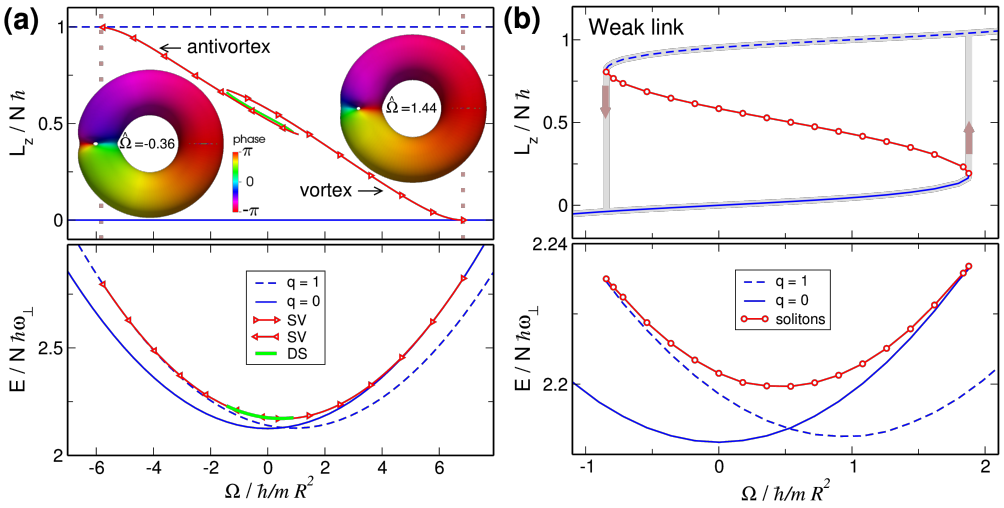

Figure 6.10: Same as Fig. 6.8 for a 3D system, showing numerical results of the time-independent 3D Gross-Pitaevskii equation (6.47) for condensates with 5.3×10^4 atoms of ^{23}Na in an isotropic harmonic trap with $\omega_\perp = 2\pi \times 100$ Hz centered at $R = 6\,a_\perp$. For comparison with Fig. 6.8, energies have been shifted by $m\Omega^2\langle r_\perp^2\rangle/2$. Two solitary waves can be excited in the absence of weak link (a), solitonic vortex (SV) and dark soliton (DS), whereas only a DS is possible at the center of a weak link (b) with depth $U_{wl} = 0.5\,\mu$ and width $w_\theta = 0.6\,R$. The insets represent density isocontours (at 5% of maximum density), coloured by phase, of SVs belonging to two separated branches containing either vortices or antivortices. The external diameter of the tori is $17\,a_\perp$.

Weak link

The presence of the weak link introduces additional effects in 3D systems[2]. The density depletion reduces not only the local speed of sound, as in 1D systems, but also the local energy available for transverse excitations. As a result, not all the solitonic states that can be excited in regions with homogeneous density can survive at the weak link. This is just the case represented in Fig. 6.10(b), where solitonic vortices are excluded from the weak link region, and only dark solitons can be excited inside.

With respect to winding number states, additional nonzero currents are generated in response to rotation. In analogy with the Meissner effect, the system causes a counterflow inside the weak link region in order to exclude the vorticity field induced by rotation. In a multidimensional system, a vortex-antivortex pair origins such a flow [Woo12, Dub12]. The rotating weak link leads to surface excitation modes to nucleate a vortex dipole along the radial direction of the torus [Pia09, Pia13]. This dipole yields a phase jump which is opposite to the background flow, and has the required value for keeping a winding phase. The phase jump grows with increasing angular rotation, up to a critical point where the flow velocity inside the weak link reaches the local speed of sound, and no further increase is allowed. At this point, which is also the end of the trajectory for solitonic states inside the weak link, the localized phase jump vanishes and a

[2]In this case, although qualitatively irrelevant, we have also considered a radial dependence of the weak link $U_{\rm wl}(\vec{r}) = U_{wl}\,\exp\left(-2[R(\theta-\theta_0)/w_\theta]^2 - [(\rho-R)/w_\theta]^2\right)$

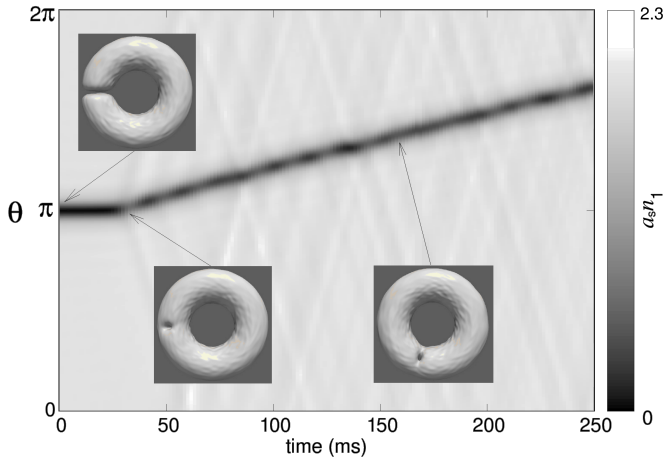

Figure 6.11: Evolution in real time, obtained by solving the 3D time-dependent Gross-Pitaevskii equation with $\hat{\Omega} = 0$, of a dark soliton state, with the same parameters as in Fig. 6.10, after an initial Gaussian-noise perturbation. Dimensionless azimuthal density $a_s n_1(\theta)$ is plotted as a function of time. Density isocontours (at 5% of maximum density) are showed for times (from left to right) 2, 32 and 160 ms. Shallow density depletions (light gray lines on the background) after soliton decay correspond to the emission of phonons traveling at the speed of sound.

phase slip is produced. This effect is due to the dispersion curve of vortex dipoles [Jon82, Li08b], which transform into phonons at low momentum p, i.e. when $E/p \to c$.

Figure 6.12 shows the approach to the critical angular frequency followed by winding number states (upper graph in the figure) and solitons (lower) for a torus with the same parameters as before. At intermediate rotation rates, $\hat{\Omega} = 0.5$, the dark soliton has angular momentum per particle $\langle L_z \rangle / N\hbar = 0.5$, whereas the winding number $q = 0$ triggers a small current, represented on the figure by an almost imperceptible phase gradient. However, as can be seen in the right isocontours of Fig. 6.12, at a higher rotation rate, $\hat{\Omega} = 1.87$, close to the critical frequency, the differences between solitonic and winding numbers begin to disappear. The converging process finishes with a phase slip to winding number $q = 1$, when the local speed of sound $c(\theta)$ is reached. As a consequence, the size of hysteresis loops in 3D rings is determined by the range of existence of solitonic solutions.

As mentioned in the introduction, the weak link opens instability channels for the decay of solitary waves. By explicitly breaking the rotational invariance of the system, a weak link introduces an inhomogeneous environment through which solitons can escape (see Fig. 6.13). In terms of energy, solitonic states within the weak link correspond to saddle points of the Gross-Pitaevskii energy functional, and then they are unstable against small perturbations.

In Fig. 6.13(a), we show the decay of a solitonic vortex state located in a wide weak link (medium grey horizontal band) with a waist much larger than the healing length. Soliton trajectory can be seen as an almost black narrow path that bends upwards at about 40 ms, moving away from the weak link. Inclined light grey lines indicate phonon excitations. It is worth to note that soliton speed (line slope) is slower than the speed of sound (phonon speed). During the passage through the weak link the solitonic vortex changes its speed. In Fig. 6.13(b), with a weak link slightly larger than the healing length, the solitonic vortex decays sooner than in Fig.

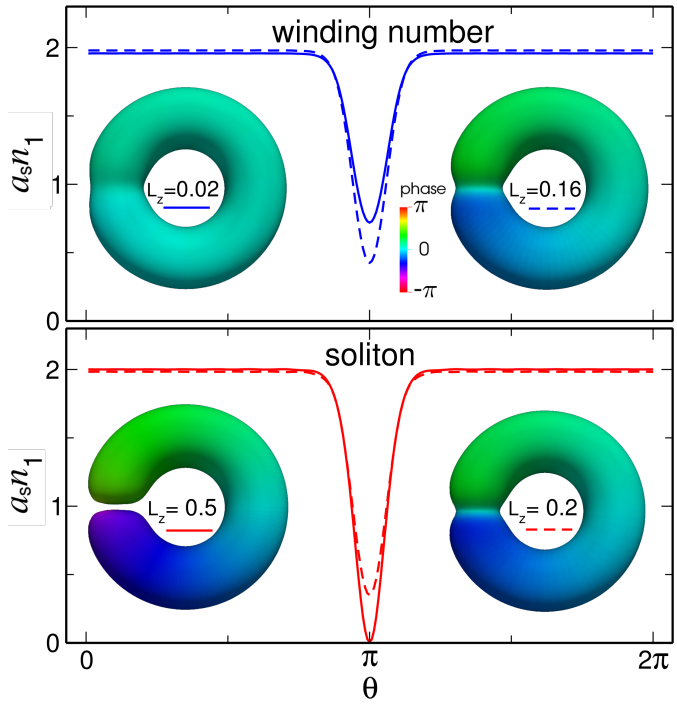

Figure 6.12: Density isocontours at 5% of maximum density, coloured by phase, of winding number $q = 0$ (above) and solitonic states (below), obtained by solving the time-independent Gross-Pitaevskii equation (6.47) in 3D condensates with the same trap and rotating weak link as those of Fig. 6.10. Two rotation rates are considered: $\hat{\Omega} = 0.5$ (left) and $\hat{\Omega} = 1.87$ (right), the latter near the critical frequency. Angular momentum per particle $\langle L_z \rangle / N\hbar$ is indicated in the inner part of the tori. Background graphs show the dimensionless density $a_s n_1(\theta)$, calculated after integration over $(z, r_\perp)$, with n_1 normalized along the radius R.

6.13(a), which has a shorter weak link. Snapshots of density isocontours at different times are also shown in the insets. One can observe that after escaping the density depleted region, the soliton rotates at a different rate than the weak link.

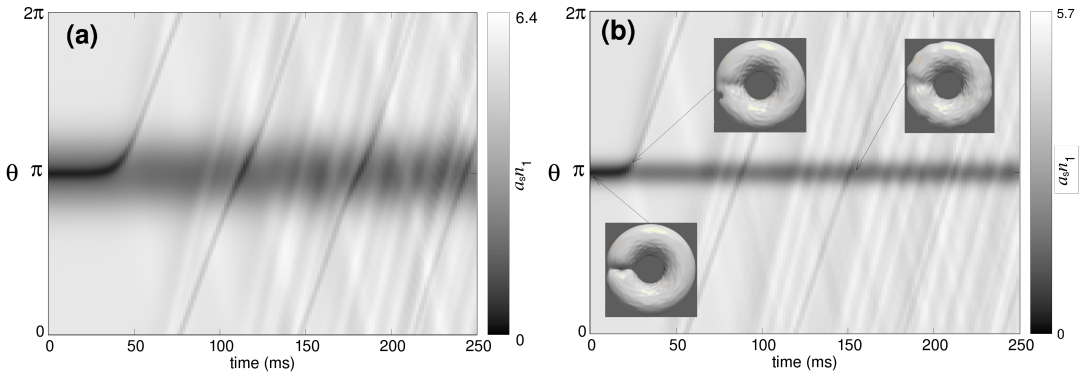

Figure 6.13: Real time evolution, after an initial Gaussian-noise perturbation, of solitonic vortex states containing 1.325×10^5 ^{23}Na atoms trapped by an isotropic harmonic potential, with $\omega_\perp = 2\pi \times 100$ Hz centered at $R = 6\, a_\perp$, in the presence of a weak link with depth $U_{wl} = 0.45\, \mu$. Dimensionless azimuthal density $a_s n_1(\theta)$ is plotted as a function of time. (a) Weak link waist $w_\theta = 1.9\, R$ at $\hat{\Omega} = 0$. (b) Weak link with $w_\theta = 0.6\, R$ rotating at $\hat{\Omega} = 0.36$. Density isocontours (at 5% of maximum density) are shown for times (from left to right) 0, 24 and 160 ms. Images correspond to the reference frame comoving with the weak link.

Chapter 7

Coupled persistent currents in a two-component coherently coupled Bose gas

The aim of this chapter is to introduce the physics of two coherently-coupled components of a spinor Bose-Einstein condensate confined in a toroidal trap. In particular, we will address a phenomenon that has been recently studied in superconducting systems containing loops: Coherent Quantum Phase Slip (CQPS) [Ast12]. This effect is the dual phenomenon of the Josephson effect [Alb05, Lev07, Sme97, Rag99], which is a coherent transport of particles between two superfluids, whereas CQPS is defined as the coherent transfer of vortices through the Josephson link. In CQPS, the stationary states corresponding to flux quanta states become coupled, such that one can continuously change the flux quanta of the system. The first experimental observation of CQPS [Ast12], was realized in a Mooij-Harmans qubit [Moo05, Moo06], which is a device that consists of a superconducting loop with a weak nanowire, and was predicted to be able to manifest CQPS between two current states.

Two coherently-coupled components of a spinor Bose gas can be described by two coupled Gross-Pitaevskii equations for the wave functions $\Psi_\uparrow$ and $\Psi_\downarrow$, as explained in Chap. 4. We consider that the two components are trapped in a toroidal trap of radius R, given in cylindrical coordinates by:

$$V_{\rm trap}(\vec{r}) = \frac{1}{2}\, m\, \omega_\rho^2((\rho - R)^2 + \lambda^2 z^2)\,, \tag{7.1}$$

with a very large aspect ratio $\lambda \gg 1$. Therefore, the dimensionality of the system can be effectively reduced to 2D.

As in the case of a single component, it is also possible to develop the Thomas-Fermi approximation to describe a two-component condensate with high interactions. In the case with no Rabi coupling [Ho96, Rib02, Pol15], the Thomas-Fermi wave function is the same for both components:

$$\Psi^{\rm TF}(\vec{r}) = \sqrt{\frac{\mu - V_{\rm trap}(\vec{r})}{g + g_{\uparrow\downarrow}}}\,, \tag{7.2}$$

up to the phase for each wave function, which can be arbitrarily set to 0. There is a subtle difference under the presence of Rabi coupling, since, in order to minimize the energy $E_\Omega = \int d\vec{r}\Omega\Psi_\uparrow\Psi_\downarrow$ associated to the term proportional to Ω, the two wave functions must have the same density but with a phase differing by a factor of π. Hence, the phases of each wave function can be set to 0 and π, respectively, to obtain that the Thomas-Fermi wave function when there is Rabi coupling is:

$$\psi_\uparrow^{\mathrm{TF}}(\vec{r}) = -\psi_\downarrow^{\mathrm{TF}}(\vec{r}) = \sqrt{\frac{\mu_{\mathrm{eff}} - V_{\mathrm{trap}}(\vec{r})}{g + g_{\uparrow\downarrow}}}\,, \tag{7.3}$$

where $\mu_{\mathrm{eff}} = \mu + \Omega/2$ will play the role of an effective chemical potential for the coupled system.

We investigate the transfer of vortices between two coherently coupled Bose-Einstein condensates by solving numerically the time-dependent Gross-Pitaevskii equation (4.1). To this aim, we have selected typical experimental values for the scattering lengths: $a = 101.41\,a_B$ and $a_{\uparrow\downarrow} = 100.94\,a_B$, where a_B is the Bohr radius, which correspond to the hyperfine states $|F = 1, m_F = 0\rangle$ and $|F = 1, m_F = -1\rangle$ of a two-component ^{87}Rb spinor condensate. The system is confined in a toroidal trap, with frequency $\omega_\rho = 2\pi \times 200\,\mathrm{Hz}$, aspect ratio $\lambda = 4$, and radius $R = 7.5\,\mu m$. In this system, we have studied the dynamical evolution of the superfluid when we phase imprint a vortex state (persistent current) in each component of the condensate, but with different winding numbers κ_1 and κ_2.

7.1 Dynamical regimes of two coupled condensates in a ring

When analyzing the different dynamical behaviors of the condensate as a function of the interaction energy and the strength of the Rabi coupling, one can observe three characteristic evolutions of the difference between the angular momentum of each component (angular momentum imbalance). From this, one can plot a dynamical phase diagram, which reveals at which regime of the dynamical evolution will the system operate for a given value of the chemical potential (which is related to the interaction energy) and the Rabi coupling.

In Fig. 7.1 we show the dynamical regimes of the system, for the initial state $|\kappa_1{=}1,\ \kappa_2{=}0\rangle$ (labelled by the winding numbers imprinted initially onto each component), obtained by numerically solving the Eq. (4.1) in the 2D case (1D case in the inset). Depending on the values of the effective chemical potential and the Rabi coupling, the system explores the three aforementioned regimes, which will be explained in detail in the following sections (see also Ref. [Leg99]). We have found, however, a critical value of the Rabi coupling Ω_c that draws the frontier between a regime below which there is no transfer of vortices between the two components (called Trapping regime) and above which, there is transfer of vortices (phase slip), although in a non-coherent way (see below).

The physical origin of the existence of a critical Rabi frequency to allow phase slip processes in this system is still not clear. However, it is reasonable to think that it can be linked to the energy gap that one has to overcome in order to generate spin waves in two coherently coupled

condensates, whose expression for the homogeneous case is [Son02, Aba13]:

$$\Delta = \Omega \sqrt{1 + \frac{ng}{\Omega}\left(1 - \frac{g_{\uparrow\downarrow}}{g}\right)}\,. \tag{7.4}$$

For the sake of comparison, we have complemented the inset of Fig. 7.1 with the curves given by Eq. (7.4) for the same numerical values of Ω_c: dotted ($g_{\uparrow\downarrow}/g = 1.0$), dashed ($g_{\uparrow\downarrow}/g = 0.9954$) and dot-dashed ($g_{\uparrow\downarrow}/g = 0.9$) lines. The minimal coupling energy $\hbar\Omega_c$ necessary to produce phase slip is of the order of Δ. When $g_{\uparrow\downarrow} = g$, phase slips can be produced for arbitrarily small values of the coherent coupling. As the ratio $g_{\uparrow\downarrow}/g$ decreases the energy cost for producing phase slips increases.

Once this critical Rabi coupling is overcome, phase slip is possible. The system continuously transits from the Non-Coherent Quantum Phase Slip (NCQPS) regime at $\Omega \gtrsim \Omega_c$, where vortex exchange between components can be observed at rates different from Ω, to the Coherent Quantum Phase Slip (CQPS) regime at $\Omega \gg \Omega_c$. We identify a process as coherent if phase slip

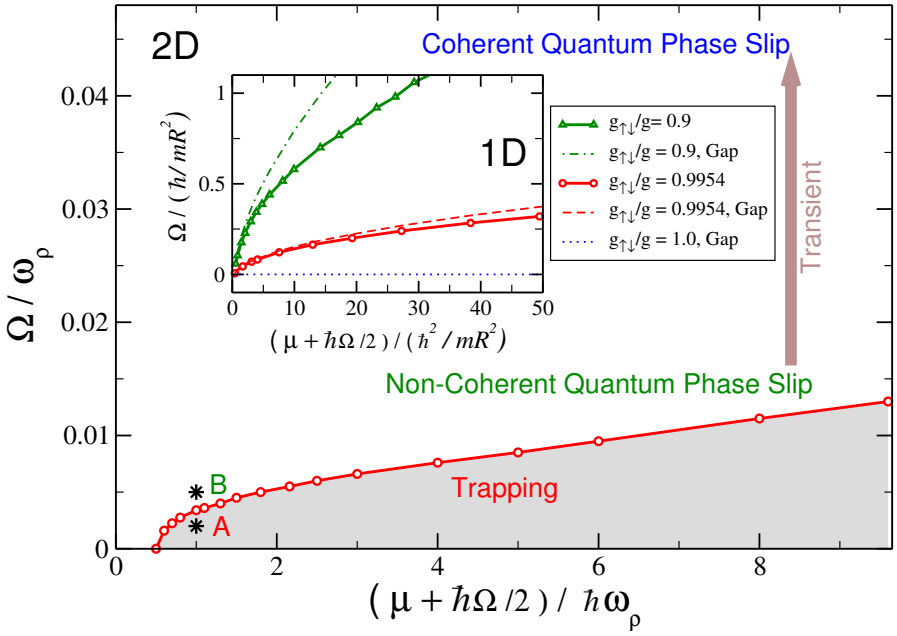

Figure 7.1: Phase diagram containing the different dynamical regimes as a function of the effective chemical potential $\mu_{\text{eff}} = \mu + \hbar\Omega/2$ and the Rabi coupling Ω, for $g_{\uparrow\downarrow}/g = 0.9954$, radius $R = 7.5\mu$m, evolving from the initial state $|\kappa_1{=}1, \kappa_2{=}0\rangle$ in 2D Gross-Pitaevskii equation (4.1). Solid red line draws the boundary Ω_c between the Trapping regime and the regimes where phase slip exists. Above Ω_c there is a continuous transition from a Non-Coherent Quantum Phase Slip regime to a Coherent Quantum Phase Slip regime. The inset compares our numerical results for Ω_c in 1D systems (solid curves with open symbols) with the analytical expression Eq. (7.4) (dotted and dashed lines) for the energy gap associated to the excitation of spin modes at different values of $g_{\uparrow\downarrow}/g$. The labelled points A, B correspond to particular cases addressed in later sections.

events occur with a complete transfer of angular momentum between the components and with a frequency of oscillation equal to the Rabi coupling, together with the fact that only two vortex states are involved in the dynamics. If phase slip events occur without following the previous description, we classify the regime as non-coherent.

The dynamical phase diagram also depends on the radius of the torus. As the ring geometry constitutes a finite system, a zero-point kinetic energy $\hbar^2/mR^2$ is introduced. This energy quantum separates winding number states and, as a result, the degenerate states $|\kappa_1, \kappa_2\rangle$ and $|\kappa_2, \kappa_1\rangle$ are separated by a gap from other winding number states. When the radius of the torus increases, the zero-point kinetic energy goes to zero and the energy spectrum becomes a continuum. The same occurs when the interaction energy is very large, because the energy to produce a vortex is negligible in front of the chemical potential. As we will show later, CQPS decays or is even absent in these cases. The dynamical phase diagram can also exhibit dramatic changes in the immiscible case, where vortex states can split due to phase separation [Gar02].

7.2 Coherent Quantum Phase Slip

In order to have an analytical insight into the dynamics of the system, one can follow the spirit of the two-mode approximation [Rag99]. In the CQPS regime, the condensate wave function can be written as [Wil99b, Wil99c, Wil99a, Dum98]:

$$\begin{pmatrix}\Phi_\uparrow(\vec{r},t)\\ \Phi_\downarrow(\vec{r},t)\end{pmatrix} = \phi_{\kappa_1}(\vec{r})\begin{pmatrix}\psi_{\uparrow,\kappa_1}(t)\\ \psi_{\downarrow,\kappa_1}(t)\end{pmatrix} + \phi_{\kappa_2}(\vec{r})\begin{pmatrix}\psi_{\uparrow,\kappa_2}(t)\\ \psi_{\downarrow,\kappa_2}(t)\end{pmatrix} \tag{7.5}$$

where $\phi_{\kappa_j}(\vec{r}) = \phi_{\kappa_j}(\rho) \times e^{i\kappa_j\theta}$, with $j = 1, 2$, are eigenvectors of both the angular momentum operator $\hat{L}_z$, with eigenvalue $\hbar\kappa_j$, and the Hamiltonian without Rabi coupling, with eigenvalue μ_j. This ansatz neglects any contribution from other modes with winding numbers (or charges) different from κ_1 and κ_2. We will see below that our numerical results agree with this assumption, since the only eigenvectors that significantly contribute to the dynamics are those associated to the winding numbers imprinted initially onto the wave function, i.e. κ_1 and κ_2.

After substituting Eq. (7.5) in the Gross-Pitaevskii equation (4.1) one gets two decoupled linear Josephson equations for each winding number:

$$\begin{aligned} i\hbar\frac{\partial\psi_{\uparrow,\kappa_1}}{\partial t} &= \mu_1\psi_{\uparrow,\kappa_1} + \frac{\hbar\Omega}{2}\psi_{\downarrow,\kappa_1} \\ i\hbar\frac{\partial\psi_{\downarrow,\kappa_1}}{\partial t} &= \mu_1\psi_{\downarrow,\kappa_1} + \frac{\hbar\Omega}{2}\psi_{\uparrow,\kappa_1}\,, \end{aligned} \tag{7.6}$$

and

$$\begin{aligned} i\hbar\frac{\partial\psi_{\uparrow,\kappa_2}}{\partial t} &= \mu_2\psi_{\uparrow,\kappa_2} + \frac{\hbar\Omega}{2}\psi_{\downarrow,\kappa_2} \\ i\hbar\frac{\partial\psi_{\downarrow,\kappa_2}}{\partial t} &= \mu_2\psi_{\downarrow,\kappa_2} + \frac{\hbar\Omega}{2}\psi_{\uparrow,\kappa_2}\,. \end{aligned} \tag{7.7}$$

The straightforward solution of these linear systems has the eigenvalues $\mu_j \pm \hbar\Omega/2$. The energy gap between the two levels is $\hbar\Omega$, where Ω is the driving frequency. Then the solution for

the condensate wave function is:

$$\begin{pmatrix}\Phi_\uparrow(\vec{r},t)\\ \Phi_\downarrow(\vec{r},t)\end{pmatrix} = \phi_{\kappa_1}(\rho)\exp\left(i\kappa_1\theta\right)\begin{pmatrix}\cos\frac{\Omega t}{2}\\ -i\sin\frac{\Omega t}{2}\end{pmatrix} + \phi_{\kappa_2}(\rho)\,\exp\left(-i(\Delta\mu_\kappa t/\hbar - \kappa_2\theta + \varphi)\right)\begin{pmatrix}i\,\sin\frac{\Omega t}{2}\\ -\cos\frac{\Omega t}{2}\end{pmatrix}, \tag{7.8}$$

and the corresponding densities read:

$$\begin{aligned}|\Phi_i(\vec{r},t)|^2 =& \frac{1}{2}\left[|\phi_{\kappa_1}(\rho)|^2\cos^2\left(\frac{\Omega t}{2}\right) + |\phi_{\kappa_2}(\rho)|^2\sin^2\left(\frac{\Omega t}{2}\right)\right.\\ &\left.\pm|\phi_{\kappa_1}(\rho)||\phi_{\kappa_2}(\rho)|\sin\left(\Omega t\right)\sin\left(\frac{\Delta\mu_\kappa t}{\hbar} - \Delta\kappa\,\theta + \varphi\right)\right], \end{aligned}\tag{7.9}$$

where $\Delta\kappa = \kappa_2 - \kappa_1$ is the initial winding number imbalance, $\Delta\mu_\kappa = \mu_2 - \mu_1$ is the associated chemical potential imbalance and φ is an arbitrary phase.

From Eq. (7.8) one can get the mean angular momentum imbalance per particle $\Delta L_z = L_z^1 - L_z^2 = (\langle\Psi_\uparrow|\hat{L}_z|\Psi_\uparrow\rangle - \langle\Psi_\downarrow|\hat{L}_z|\Psi_\downarrow\rangle)/\hbar N$, as a function of time:

$$\Delta L_z = \hbar\frac{\Delta\kappa}{2}\cos(\Omega t)\,. \tag{7.10}$$

This expression predicts that the exchange of vortices between the two components oscillates with the Rabi frequency Ω. As a consequence, a π-pulse ($\Omega t = \pi$) exchanges the winding numbers between components, and a $\pi/2$-pulse ($\Omega t = \pi/2$) will drive each component to a quantum superposition of flows with winding numbers κ_1 and κ_2.

7.2.1 Phase slip between adjacent winding numbers

In this section we will describe the dynamical evolution for the particular case of two adjacent winding numbers: $\kappa_1 = 1$ and $\kappa_2 = 0$, obtained by numerically solving the two-component Gross-Pitaevskii equation. Figure 7.2 shows our numerical results, within the CQPS regime, for the mean angular momentum imbalance per particle as a function of time, and $\Omega = 0.16\,\omega_\rho$ (which corresponds to 200 Hz), for different number of particles. The comparison with the analytical prediction given by Eq. (7.10) is also shown. As can be seen, the agreement is very good. The frequency of the oscillation of ΔL_z is precisely the Rabi coupling Ω that coherently connects both spin components. The population imbalance is initially zero, and we have seen that it remains unaltered during the whole simulation, thus one can deduce that the spin exchange occurs "at pairs" even though the population of both spin components is not fixed. By "at pairs" we mean that for each particle of one condensate component flipping its spin there exists another particle of the other component doing the same.

In order to elucidate how the topological structure of the wave function changes as a function of time, we show in Fig. 7.3 the dynamical evolution of the density and the local phase for a condensate with $N = 5\times10^4$ atoms. White lines represent density isocontours at 5% of maximum density and colours depict the phase. Initially, at t=0, we have imprinted a persistent current (κ_1=1) in the $\uparrow$-component while the other is at rest (panel (a)). A quarter of period later, Ωt=$\pi/2$, an azimuthal density node[1] is formed spontaneously in each component, at opposite

[1]This objects should not be confused with dark solitons, since they can also appear in the linear case and the associated healing length is, in general, much larger than the one of solitary waves.

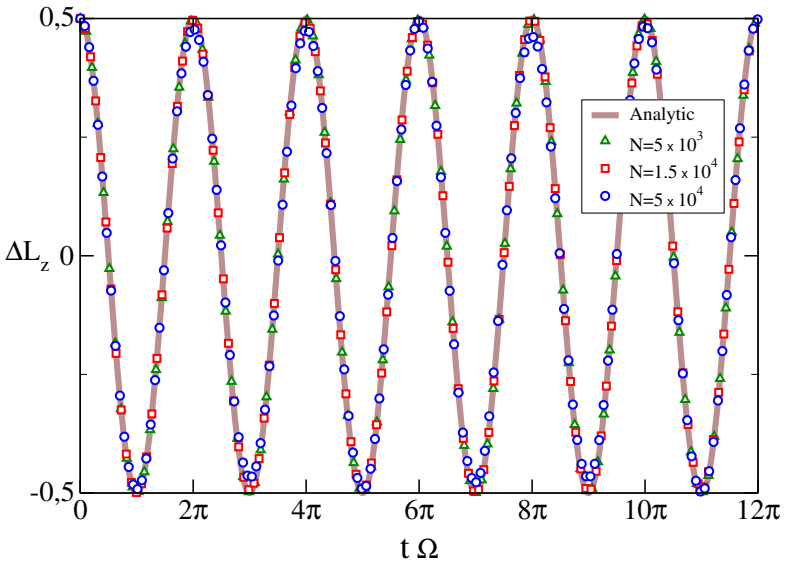

Figure 7.2: Comparison between the dynamical evoluion of the mean angular momentum imbalance per particle calculated by solving the Gross-Pitaevskii equation for $N = 5 \times 10^3$ (green triangles), $N = 1.5 \times 10^4$ (red squares) and $N = 5 \times 10^4$ (blue circles) together with the result predicted by Eq. (7.10) (thick brown line). The Rabi coupling is $\Omega = 200\,\mathrm{Hz}$ and the initial state is $|\kappa_1{=}1,\, \kappa_2{=}0\rangle$.

positions (panel (b)). The vortex that was inducing the rotation in the initial state escapes from the ↑-component through the density depletion, while another vortex crosses the corresponding node in the ↓-component, transferring vorticity from the ↑-component to the ↓-component (panel (c)). This is the mechanism followed by the coupled system to produce 2π-phase slips. After that, in panel (d) the evolution is reversed, returning the vorticity to the ↑-component (panel (e)), and so on [Hal10]. Anologous results in a harmonic trap have been analyzed in Ref. [Cal17].

CQPS in atomtronic circuits allows the system to effectively operate as a qubit. A quantum mechanical system is a good candidate for qubit manipulation if two conditions are fulfilled. First, the system must be considered as an effective two-state system $|0\rangle$ and $|1\rangle$, and second, at every time, the qubit must be expressed as a quantum superposition of both states. In our system these two states are $|\kappa_1, \kappa_2\rangle$ and $|\kappa_2, \kappa_1\rangle$, and as a result the state of the system can be written as $\Psi = \alpha|\kappa_1, \kappa_2\rangle + \beta|\kappa_2, \kappa_1\rangle$ at every time. From the analytical model (7.8), we know that $\alpha = \cos(\Omega t/2)\hat{\sigma}_z$ and $\beta = i\sin(\Omega t/2)\hat{\sigma}_z$, where $\hat{\sigma}_z$ is a Pauli matrix. It can be mapped to the most general expression of a qubit $\Psi = \cos(\theta/2)|0\rangle + \exp(i\varphi)\sin(\theta/2)|1\rangle$. The mapping is characterized by a periodic evolution with a period of $2\pi/\Omega$. At half a period, the phases of both components are exchanged, and in between, topological defects appear in the wave function in order to drive the phase slip. The Rabi coupling Ω is a parameter that can be externally manipulated, and its control allows to simulate a tunable single-qubit quantum gate for quantum information processes. In this regime, the system displays two characteristic properties:

i) The system behaves as linear despite the non-linearity, since the frequency is the Rabi cou-

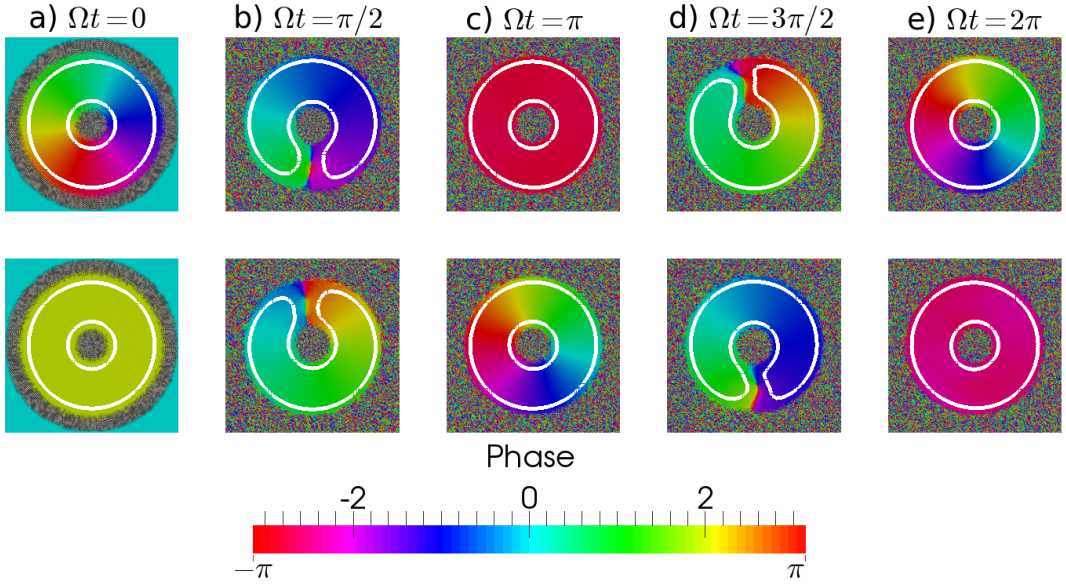

Figure 7.3: Evolution of a condensate with $N = 5 \times 10^4$ atoms as a function of time, after imprinting a vortex on the $\uparrow$ component (first row). The second row corresponds to the $\downarrow$ component. The value of the Rabi coupling is $\Omega = 200\,\mathrm{Hz}$ and the length of the square graphs is $30\mu m$. The white line corresponds to density isocontours at 5% of maximum density, whereas colours represent the phase. Panels (a-e) display snapshots of the state of the system during a Rabi cycle. This number of particles is in the limit of the CQPS regimes, since ΔL_z deviates in 6% from the analytical model.

pling, independently of the interaction.

ii) The evolution occurs following quasi-stationary states.

The two previous remarkable properties can be demonstrated by following this protocol:

a) Evolve the system with a certain value of Ω in the CQPS regime, thus the angular momentum imbalance will oscillate with frequency Ω.

b) At an arbitrary time t_1, switch the Rabi coupling to zero, suppressing the exchange of phase between components.

c) At another arbitrary time t_2, switch on again the Rabi coupling to its initial value in the process.

Figure 7.4 represents the whole sequence of this protocol. At t_1 the state gets frozen in a quasi-stationary state rotating at a given velocity according to the imbalance between the chemical potential associated to the two winding number states. Then, at t_2 the evolution resumes, with exactly the same properties of the system at t_1. The curves predicted by the analytical model accurately fit in with the solution of the Gross-Pitaevskii equation.

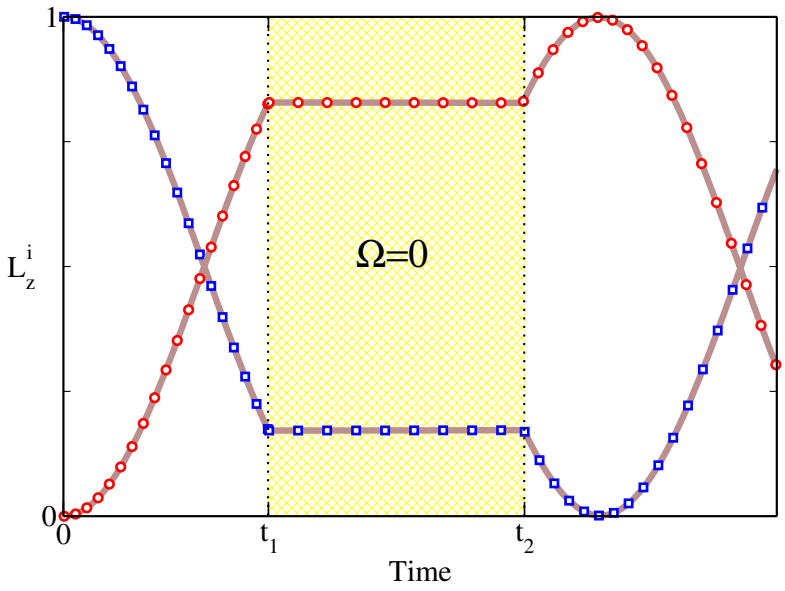

Figure 7.4: Comparison between the analytical model given by Eq. (7.10) (thick brown lines) and the numerical solution of the Gross-Pitaevskii equation (open symbols) for the time evolution following the protocol described in the text. Blue squares correspond to the mean angular momentum per particle of the ↑ component, and red circles to the ↓ component. The initial state is $|\kappa_1{=}1,\, \kappa_2{=}0\rangle$, the number of atoms is $N = 5\times10^3$ and the Rabi coupling is $\Omega = 200\,\mathrm{Hz}$, except between time $t_1\Omega = 14.37/2\pi$ and $t_2\Omega = 32.32/2\pi$, where Ω is switched off.

7.2.2 Phase slip between non-adjacent winding numbers

All the results presented in Sect. 7.2.1 are devoted to the case of CQPS between adjacent winding number states. However, the analytical model is more general and also applies between non-adjacent winding numbers. In this section we present the performance of CQPS in the case where the winding numbers imprinted onto both wave functions differ in more than one unit.

We have shown that in order to change the winding number in one unit, a 2π-phase slip event involving the formation of an azimuthal density node has to occur. Therefore, to drive each component from winding number κ_1 to κ_2 (and viceversa), multiple number of such nodes ($|\kappa_1-\kappa_2|$) must appear simultaneously. Multiple 2π-phase slip can not occur through a sequence of single 2π-phase slip events, since other states with winding number different from κ_1 and κ_2 would contribute, as described by the ansatz (7.5). This fact can be seen in Fig. 7.5, where we compare the numerical results of the Gross-Pitaevskii equation (white isocontours at 4% of maximum density and colours for the phase), with the analytical prediction for the same density isocontour given by Eq. (7.9) (black line), assuming that the system is in the Thomas-Fermi limit and Eq. (7.3) applies, for the initial state $|\kappa_1{=}1,\, \kappa_2{=}0\rangle$ (panel (a)) and $|\kappa_1{=}2,\, \kappa_2{=}0\rangle$ (panel (b)). The agreement is again excellent.

Figure 7.6 represents Ω_c, which fixes the critical value of the Rabi coupling that allows phase slip events, as a function of the effective chemical potential, for different initial winding number imbalances $\Delta\kappa = 1, 2, 3$ (red circles, blue squares and green triangles, respectively), after solving the 1D Gross-Pitaevskii equation with $g_{\uparrow\downarrow}/g = 0.9954$. Ω_c increases with μ_{eff}, but this increasing

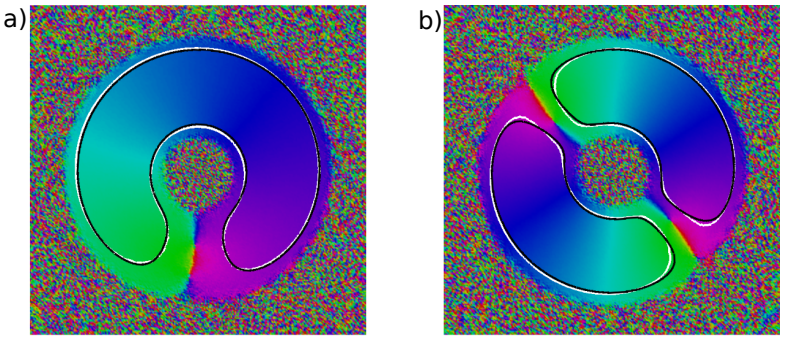

Figure 7.5: Comparison of the numerical results of the Gross-Pitaevskii equation with the analytical prediction of Eq. (7.9), for the wave function of the ↑ component at a quarter of a Rabi cycle. The initial state is $|\kappa_1{=}1,\ \kappa_2{=}0\rangle$ (panel (a)) and $|\kappa_1{=}2,\ \kappa_2{=}0\rangle$ (panel (b)), the Rabi coupling is $\Omega = 200\,\mathrm{Hz}$ and the condensate holds $N = 5 \times 10^4$ atoms. White lines correspond to density isocontours at 4% of maximum density and colours to the phase, both of them obtained numerically. Black lines correspond to density isocontours at 4% of maximum density predicted by the model, assuming the initial density in the Thomas-Fermi limit, given by Eq. (7.3).

is faster for larger initial $\Delta\kappa$. The azimuthal nodes that the system has to generate in order to produce phase slips involve more energy, and the strength of the coherent coupling has to be larger to overcome higher energy barriers associated to smaller characteristic lengths.

We have studied the dynamics of the system for different initial winding number imbalance

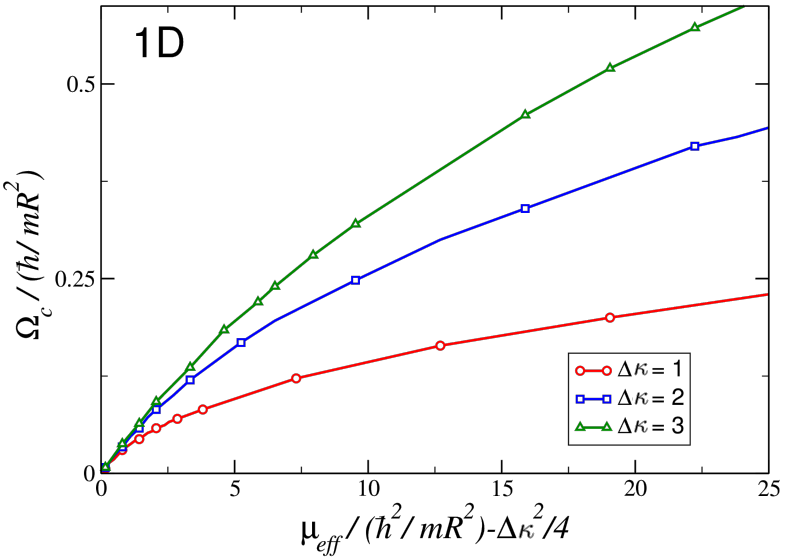

Figure 7.6: Critical coupling Ω_c as a function of the effective chemical potential μ_{eff} for different values of the winding number imbalance $\Delta\kappa = 1$ (red circles), $\Delta\kappa = 2$ (blue squares) and $\Delta\kappa = 3$ (green triangles), with $\kappa_2 = 0$. The results have been obtained by solving numerically the 1D Gross-Pitaevskii equation with $g_{\uparrow\downarrow}/g = 0.9954$.

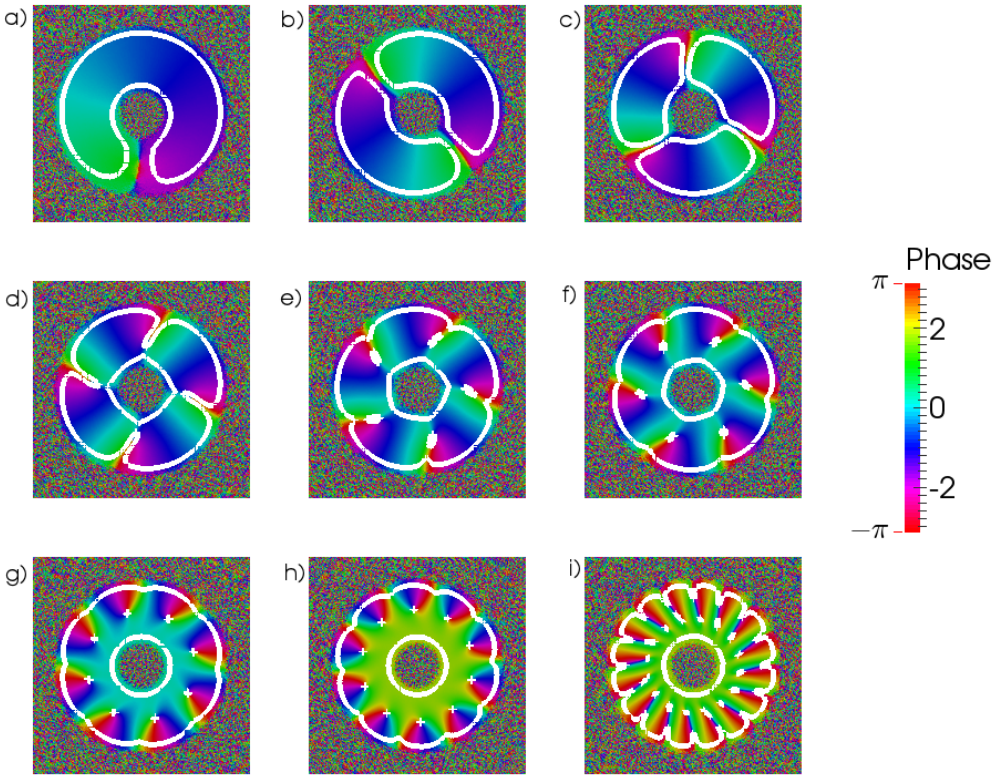

Figure 7.7: Density isocontours at 5% of maximum density and phase (colour) of the ↑ component at a quarter of a Rabi cycle for a condensate of $N = 5\times10^4$ atoms, $\Omega = 200\,\mathrm{Hz}$ and different values of the initial angular momentum imbalance, with the ↓ component initially at rest ($\kappa_2 = 0$). a) $\kappa_1 = 1$, b) $\kappa_1 = 2$, c) $\kappa_1 = 3$, d) $\kappa_1 = 4$, e) $\kappa_1 = 5$, f) $\kappa_1 = 6$, g) $\kappa_1 = 8$, h) $\kappa_1 = 10$ and i) $\kappa_1 = 16$. Only the cases of the first row do exhibit CQPS.

at $\Omega = 200\,\mathrm{Hz}$. Figure 7.7 shows the density (white isocontours) and the phase (colour) of the ↑-component at a quarter of a Rabi cycle, for different values of the initial winding number κ_1 (with $\kappa_2 = 0$) imprinted onto condensates with $N = 5 \times 10^4$ atoms. One can observe that density nodes appear equispaced forming an ordered pattern. As the initial angular momentum imbalance increases, the characteristic length scale associated to the azimuthal density nodes decreases as predicted by Eq. (7.9), and becomes closer to that of solitary waves as dark solitons or solitonic vortices. To generate such objects additional winding number modes have to be excited, and therefore, the CQPS process decays after few cycles. Then, the ansatz (7.5) is no longer valid. That is why the second and the third row of Fig. 7.7 will not exhibit CQPS (they belong to the NCQPS regime), and only the cases of the first row will display this phenomenon.

7.3 Other dynamical regimes

As was shown in Fig. 7.1, CQPS can not be found in the whole parameter space of the system, given that $g \neq g_{\uparrow\downarrow}$. Our numerical results point to the fact that CQPS exists as far as the ansatz (7.5) is valid, and this occurs for high values of the coherent coupling in comparison with Ω_c. Below this critical value, we have found a dynamical regime where there is no vortex exchange between spin components. This fact is due to the presence of an energy barrier between degenerate winding number states $|\kappa_1, \kappa_2\rangle$ and $|\kappa_2, \kappa_1\rangle$, that prevents phase slips. In the previous chapter, we have seen that in order to produce a phase slip event, one has to overcome an energy barrier, whose states correspond to topological states, like dark solitons, i.e., this barrier is a result of the nonlinear nature of the matter wave [Mun15]. In contrast, in the CQPS regime, such phase slips are produced in a different way: they are a result of the interference between the two flows in the different hyperfine components, which is a linear effect. When approching the critical Rabi frequency, the nonlinearity of the Gross-Pitaevskii equations start to have a significant role in the excitation of spin modes. As mentioned before, the excitation of such modes has been demonstrated to play a key role in spinor condensates coupled by density, and seems to be also relevant in this case. Such excitations are separated from the winding number states by the energy gap given in Eq. (7.4), which must be overcome in order to produce

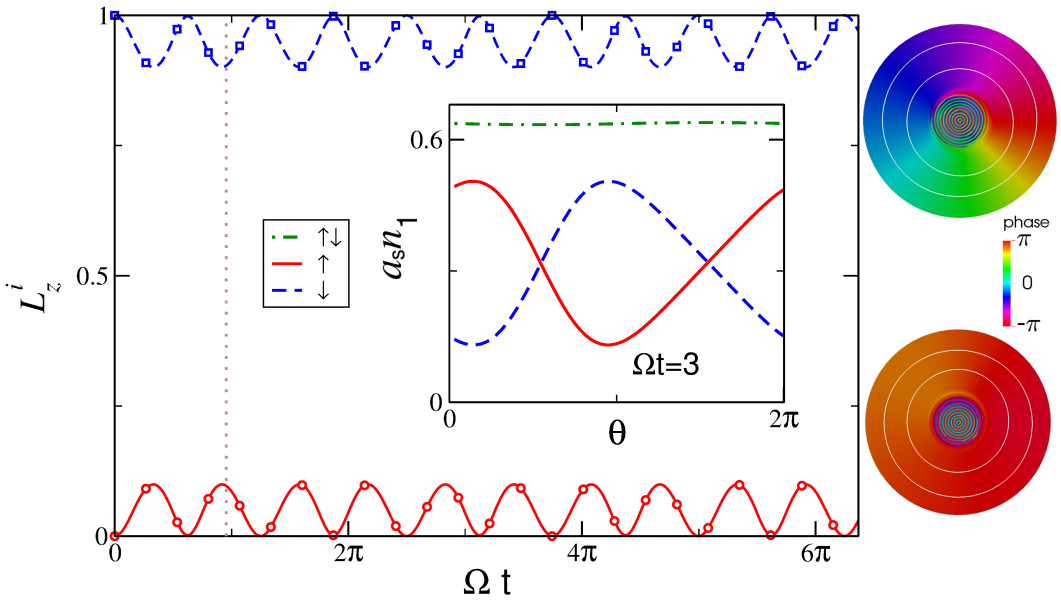

Figure 7.8: Mean angular momentum per particle of the ↑ (solid red line with circles) and ↓ (dashed blue line with squares) component, after solving the 2D Gross-Pitaevskii equation. In the inset, the azimuthal density, $a\,n_1 = (a/R)\int |\phi(\rho,\theta)|^2 \rho d\rho$, of the ↑ (solid red line), ↓ (dashed blue line) component, and the sum of both (dot-dashed green line), at $\Omega t = 3$ (indicated by the dotted vertical line). At the right side of the plot, snapshots of the corresponding phase pattern of the ↑ (top) and ↓ (bottom) component is represented by colours, and the isocontours at 5% of maximum density by the white lines. The effective chemical potential is $\mu_{\text{eff}} = \hbar\omega_\rho$ and the Rabi coupling is $\Omega = 2 \times 10^{-3}\omega_\rho$.

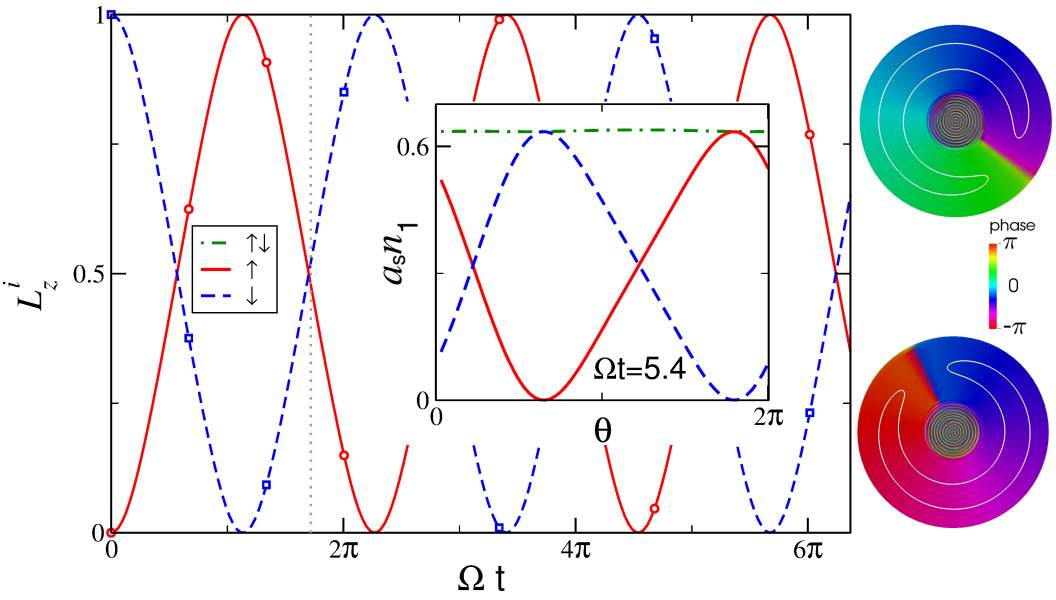

Figure 7.9: Same as Fig. 7.8 for $\Omega = 5 \times 10^{-3}\omega_\rho$ at $\Omega t = 5.4$.

phase slips. If this critical energy can not be transferred between components by the coherent coupling, vortices will be trapped, and the mean angular momentum per component will not oscillate around the value $(\kappa_1 + \kappa_2)/2$.

Fig. 7.8 shows a typical case representative of the trapping regime. It corresponds to the point A indicated in Fig 7.1, for the coupling $\Omega = 2 \times 10^{-3}\omega_\rho$. As can be seen, the mean angular momentum of each component oscillates near the initial value, and the corresponding densities (shown in the inset after integration along the transverse section of the torus) present variations without nodal points. Although the interaction between components translate into currents inside each component (see the phase maps on the right of the figure), they are not enough to drive phase slips. Finally it is worth to note that during all the time evolution the total density remains approximately constant along the torus.

When the Rabi coupling takes intermediate values, $\Omega \gtrsim \Omega_c$, stable CQPS will not manifest in the dynamics, and the system enters the NCQPS regime. In this case, the coherent coupling is large enough to produce phase slip events that exchange the winding number between spin components. However, the time frequency of these events is lower than Ω. This features are reflected in the case displayed in Fig. 7.9, corresponding to the point B of Fig. 7.1. Now the spin densities can show nodal points leading to phase slips, whereas the total density remains again approximately constant, although a small oscillation is present. As a consequence, and in contrast to the CQPS regime, the position of such nodal points for both components are not located at diametrically opposed positions. As the coherent coupling strength increases the frequency for phase slips approaches to Ω.

In addition, as the Rabi coupling decreases, approaching the critical Rabi frequency, the excitation of solitary waves (see panels (d)-(i) in Fig. 7.7) are responsible for the damping of the exchange of angular momentum between components. As a consequence, the system can

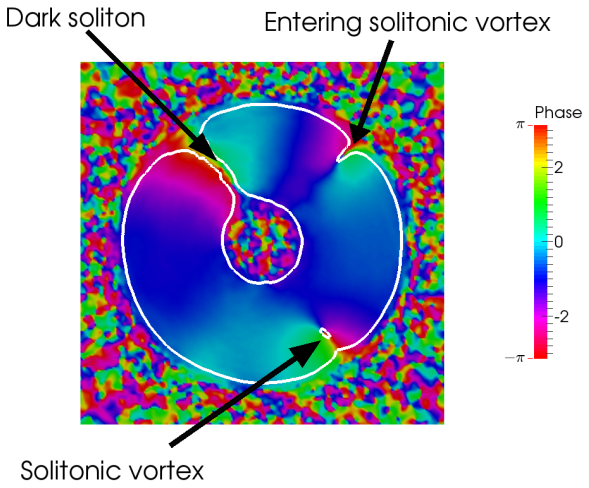

Figure 7.10: Density isocontour at 5% of maximum density and phase (colour) of the ↑ component of a condensate of $N = 5 \times 10^4$ atoms and $\Omega = 60\,\mathrm{Hz}$ after $2\,s$ of evolution, with the state $|\kappa_1{=}1, \kappa_2{=}0\rangle$ as the initial state. Two solitonic vortices and a dark soliton appear in the wave function.

deviate from the quasi-stationary path and explore other regions of the phase space. Different topological objects are generated, and then, the long-time dynamics will bring the condensate to an out-of-equilibrium quantum gas. Notice that in this regime many angular momentum modes are excited and the two-mode approach (7.5) is no longer valid. In Fig. 7.10 we show a characteristic snapshot of the density and the phase of the ↑-component of a condensate with $N = 5 \times 10^4$ atoms and Rabi coupling $\Omega = 60\,\mathrm{Hz}$ after $2\,\mathrm{s}$ of evolution from the initial state $|\kappa_1{=}1,\ \kappa_2{=}0\rangle$. The white line traces the density isocontour at 5% of maximum density and the colours display the phase. In the figure one can also see that although the initial angular momentum imbalance is $\Delta\kappa = 1$, several kinds of solitary waves (a dark soliton and two solitonic vortices) are excited in the condensate in order to try to drive a single 2π-phase slip. One can see that the appearance of solitonic vortices do not accomplish with the azimuthal dependence of the density predicted by Eq. (7.9), and as a consequence, it is not compatible with CQPS.

Chapter 8

Static and dynamic properties of topological states in spin-orbit coupled Bose-Einstein condensates

In Chap. 3, we have characterized the main topological states that can appear in single-component Bose-Einstein condensates. However, in coherently-coupled two-component Bose-Einstein condensates [Son02, Aba15], new topological states can appear. Among them, Josephson vortices, due to their relevance in superconducting systems [Bar82], have been studied in atomic gases [Kau05, Kau06, Su13, Ach13, Gal16b]. Josephson vortices are dark soliton-like states, where the density does not completely vanish at the "soliton" plane, due to a small increase of the imaginary part of the condensate wave function that provides nonzero relative current at the vicinity of this plane. In coherently-coupled Bose gases, both the dark soliton and the Josephson vortex are solution of the time-independent Gross-Pitaevskii equation (4.2), although Josephson vortices are energetically favourable. However, when there is spin-orbit coupling in the system, the dark soliton is no longer a solution of the Gross-Pitaevskii equation, but the Josephson vortex still remains as a solution.

In this section, we will study the physics of Josephson vortices in two coherently-coupled pancake-shaped Bose-Einstein condensates confined in a 2D harmonic trap. We will characterize the static properties of these states and analyze their stability and decay. Josephson vortices decay through the snake instability, producing vortices, as dark solitons. We will study the subsequent dynamical evolution of these vortices [Fet15] as a function of the Rabi coupling Ω, the direction of the Rashba-Dresselhaus spin-orbit coupling and its strength, given by k_L. This provides the main features of the ground state, by means of the phase diagram discussed in Chap. 3.

In order to describe the system, we consider two-component condensates in the mean-field regime, described by two coupled Gross-Pitaevskii equations for each condensate wave function $\Psi_\uparrow(\mathbf{r},t)$, and $\Psi_\downarrow(\mathbf{r},t)$, given by Eq. (4.1) but substituting the single-particle part by Eq. (4.25),

which is the hamiltonian for a Rashba-Dresselhaus spin-orbit coupled Bose gas in k_x. This equation reads in real space, as:

$$
\begin{aligned}
i\hbar\left(\frac{\partial}{\partial t}-\frac{\hbar k_L}{m}\frac{\partial}{\partial x}\right)\Psi_\uparrow &= \left(\mathcal{H}_0+g|\Psi_\uparrow|^2+g_{\uparrow\downarrow}|\Psi_\downarrow|^2\right)\Psi_\uparrow+\frac{\hbar\Omega}{2}\Psi_\downarrow \\
i\hbar\left(\frac{\partial}{\partial t}+\frac{\hbar k_L}{m}\frac{\partial}{\partial x}\right)\Psi_\downarrow &= \left(\mathcal{H}_0+g|\Psi_\downarrow|^2+g_{\uparrow\downarrow}|\Psi_\uparrow|^2\right)\Psi_\downarrow+\frac{\hbar\Omega}{2}\Psi_\uparrow,
\end{aligned}
\tag{8.1}
$$

where $\mathbf{k}_L=(k_L,0,0)$ is the laser wave vector characterizing the spin-orbit coupling. The confinement of the system will be provided by a cylindrically symmetric harmonic trap,

$$
V_{\mathrm{trap}}(\rho,z)=\frac{1}{2}m(\omega_\rho^2\rho^2+\omega_z^2z^2)\,, \tag{8.2}
$$

with the following characteristic lengths $a_{\mathrm{ho}}=a_\rho=\sqrt{\hbar/m\omega_\rho}$ and $a_z=\sqrt{\hbar/m\omega_z}$. The stationary states of Eq. (8.1) will be written as $\Psi_i(\mathbf{r},t)=\exp(-\mu t/\hbar)\,\psi_i(\mathbf{r})$, where μ is the chemical potential, and the number of particles N will be fixed by the wave function normalization $\sum_i\int\psi_i^*(\mathbf{r})\psi_i(\mathbf{r})d\mathbf{r}=N$. In this equation, one can get a dimensionless number $\alpha=m\Omega/\hbar k_L^2$ that quantifies the ratio between the strength of the Rabi coupling and the spin-orbit coupling.

As we have seen in Chap. 4, there three main phases in a spin-orbit coupled Bose gas. In what follows, we select a Rabi coupling Ω in order for the system to be either in the single-minimum or the plane-wave regime, where the ground state presents a smooth density profile. As we will see, in these regimes, the 3D Gross-Pitaevskii equation admits Josephson vortex solutions as excited states. They present a localized depletion of the density along with an associated phase jump for each condensate component. Their appearance can be understood by following a dynamical process in which, for a given k_L, the linear coupling Ω is adiabatically increased. Starting in the stripe phase regime, the length between density peaks increases with Ω, up to some critical value Ω_c, where dark soliton-like structures evolve from the ground state of the system [Cao15]. Above the critical value, the solitonic structure can persist as an excited state in the other phases of the system, the single-minimum or the plane-wave phases.

8.1 1D Josephson vortices

The main properties of static Josephson vortices can be easily identified in 1D condensates, where analytic solutions to the Gross-Pitaevskii equation are available in the absence of spin-orbit coupling ($k_L=0$). In contrast to static dark solitons, Josephson vortices, are excited states with lower energy than dark solitons, and have complex wave functions that denote the presence of interspecies (spin) currents in the condensate.

Without spin-orbit coupling

It is instructive to start considering a two-component system with $k_L=0$. Then, the homogeneous ($V_{\mathrm{trap}}=0$) Gross-Pitaevskii equation (8.1) admits two types of analytic stationary solitonic solutions (that have been addressed in the literature for the particular case $g_{\uparrow\downarrow}=0$

[Kau05, Qad12]), namely a dark soliton state:

$$\psi^{DS}_{\uparrow,\downarrow}(x) = \pm\sqrt{n}\,\tanh(x/\xi_\mu)\,, \tag{8.3}$$

having a density-dependent healing length[1] $\xi_\mu = \hbar/\sqrt{m\mu_{\rm eff}}$, with $\mu_{\rm eff} = \mu + \hbar\Omega/2$, and valid for all values of the coherent coupling $\Omega \geq 0$. In contrast, the wave function corresponding to a Josephson vortex state is:

$$\Psi^{JV}_{\uparrow,\downarrow}(x) = \sqrt{n}\left(\pm\tanh(x/\xi) + i\sqrt{1-\frac{2\hbar\Omega}{\mu_{\rm eff}}}\,{\rm sech}(x/\xi)\right)\,, \tag{8.4}$$

with a limited range of existence $\mu_{\rm eff} > 2\hbar\Omega$, and a healing length depending on the coherent coupling $\xi = \hbar/\sqrt{2m\hbar\Omega}$. In both states, the $\pm$ signs stand for the components $\uparrow$ and $\downarrow$ respectively. The total density is constant $n = n_\uparrow + n_\downarrow = \mu_{\rm eff}/(g + g_{\uparrow\downarrow})$, and there is no population imbalance $n_\uparrow = n_\downarrow = n/2$. We have defined $\mu_{\rm eff}$ as an effective chemical potential [Gal16c], which is related to the condensate density. For every single value of $\mu_{\rm eff}$ there exists a unique dark soliton state, but several Josephson vortices associated to different values of the Rabi coupling Ω.

Dark soliton states in the absence of spin-orbit coupling, Eq. (8.3), show the same symmetry between condensate components as the ground state, since from $\Psi^{GS}_\uparrow = -\Psi^{GS}_\downarrow$ we get the corresponding spin-antisymmetric solitonic state $\Psi^{DS}_\uparrow = -\Psi^{DS}_\downarrow$. In the case of Josephson vortices, they fulfill $\Psi^{JV}_\uparrow = -(\Psi^{JV}_\downarrow)^*$, which involves time reversal symmetry along with spin antisymmetry. In the range of coexistence of dark solitons and Josephson vortices, the healing length linked to density is narrower than that associated to the coherent coupling, $\xi_\mu < \xi$, and, as a result, dark solitons possess higher energy ($\propto \hbar^2/m\xi_\mu^2$) than Josephson vortices. This fact affects their stability, making the Josephson vortices dynamically stable states all along their range of existence in 1D, and turning dark solitons into dynamically unstable ones whenever $\mu_{\rm eff} > 2\hbar\Omega$. As we will see in the next sections, Josephson vortices can decay in multidimensional systems by snake instabilities, in the same manner as dark solitons do, in spite of the fact that the latter are still more energetic than the former.

The presence of a harmonic trapping potential does not modify qualitatively the type of solitonic solutions in two-component condensates without spin-orbit coupling. There also exist stationary states with the same symmetries as those discussed in the homogeneous case (Eqs. (8.3) and (8.4)). The main difference arises from the static continuation of such solitonic states from the noninteracting to the interacting regime (see left panel of Fig. 8.1). Even in this linear case, the system admits both, (real) spin antisymmetric solutions $\Psi_\uparrow = -\Psi_\downarrow$:

$$\psi^{n}_{\uparrow,\downarrow}(x) = \pm\, e^{-x^2/2a_{\rm ho}^2}\, H_n(x/a_{\rm ho})\,, \tag{8.5}$$

where H_n is the normalized Hermite polynomial of order n, and current states with the stronger symmetry $\Psi_\uparrow = -\Psi^*_\downarrow$:

$$\psi^{n,m}_{\uparrow,\downarrow}(x) = e^{-x^2/2\xi^2}\,\left(\pm\alpha H_n(x/\xi) + i\beta H_m(x/\xi)\right)\,, \tag{8.6}$$

[1] In this case, we use the subindex μ, in order to stress that the energy scale associated to this length is the chemical potential, in contrast to Josephson vortices, whose characteristic healing length is associated with the Rabi coupling

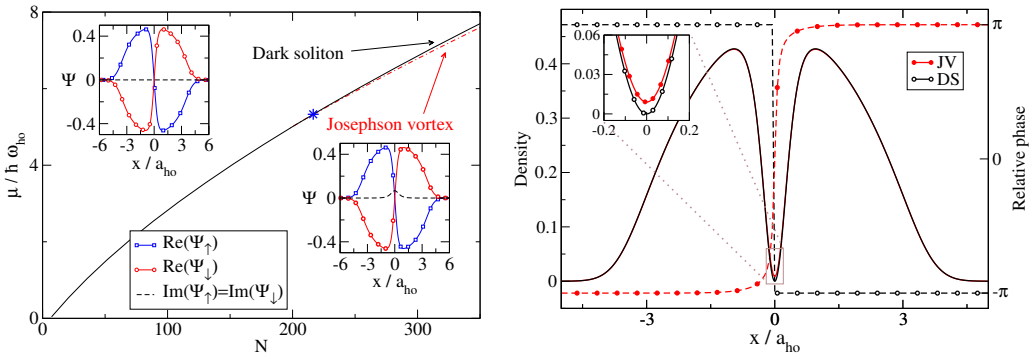

Figure 8.1: Family of 1D dark solitons and Josephson vortex states for two-component condensates, in the absence of spin-orbit coupling, confined by a harmonic potential of frequency $\omega_{\rm ho} = 2\pi \times 200$ Hz, and coupled by a Rabi frequency $\Omega/\omega_{\rm ho} = 3.5$. Left panel: trajectories in the $\mu - N$ plane (main graph), and two nearby representative examples (insets, dark solitons at the left and Josephson vortices at the right) corresponding to the (blue) star symbol. Right panel: total density (solid line) and relative phase (dashed line) of the dark solitons (open circles) and the Josephson vortices (filled circles). The inset zooms in the density depleted regions of both cases.

where n and m with $n \neq m$ label the states, and α and β are real coefficients satisfying $\alpha^2+\beta^2 = 1$. While states corresponding to Eq. (8.5) exist, with $\mu_{\rm eff} = \hbar\omega_{\rm ho}(n + 1/2)$, for every value of Ω, the stronger symmetry of Eq. (8.6), having $\xi = a_{\rm ho}$, requires that $\Omega = (n-m)\,\omega_{\rm ho}$, so that $\mu_{\rm eff} = \hbar\Omega\,(2n+1)/2(n-m)$. We have checked that states (8.5) and (8.6), which constitute a big manifold of excited states, persist, and even extend their range of existence, in the nonlinear regime. In particular, the nonlinear families of states starting from $\psi^{1}_{\uparrow,\downarrow}(x) = \pm e^{-x^2/2a_{\rm ho}^2} H_1(x/a_{\rm ho})$ and $\psi^{1,0}_{\uparrow,\downarrow}(x) = \pm e^{-x^2/2\xi^2}\,(\pm\alpha H_1(x/\xi) + i\beta H_0(x/\xi))$ are the confined counterpart of the solitonic states Eq. (8.3) and Eq. (8.4), respectively. As an example, the left panel of Fig. 8.1 shows their trajectories in the μ–N plane for $\Omega/\omega_{\rm ho} = 3.5$, and two representative cases (in the insets) for an interaction $g_{1D}N/a_{\rm ho} = 30\,\hbar\omega_{\rm ho}$, labeled by a blue star symbol, close to the bifurcation.

As can be seen in the graph of relative phase (right panel of Fig. 8.1), Josephson vortex states present a 2π-jump characteristic of the sine-Gordon solitons [Bar82]. In fact, it has been shown that the linear equations in the relative phase, obtained by perturbing Eq. (8.1), admits solutions containing domain walls (or *kinks*) with a length scale that depends on the coherent coupling [Son02]. The simplest of such solutions, made of a single kink, produces the referred 2π-jump in the relative phase, whereas higher phase jumps can be introduced in the system by generating either several single kinks, or a bound state of a kink and an antikink (*breather*) [Bar82, Qad16]. Recently, the dynamical generation of nonlinear excitations resembling the sine-Gordon breathers has been reported in coupled Bose-Einstein condensates [Su15]. Here, we show that doubly-charged Josephson vortices are stationary solutions of the Gross-Pitaevskii equation (8.1), which consist in a bound state of two kinks, making a doubly-charged (4π-phase jump) soliton. They can be obtained by introducing additional structure in the core of the Josephson vortex, where by core we mean the spatial region of the condensate showing a depleted density (see Ref. [Rod15] for Josephson vortex cores in superconductors). In terms of the singly-charged Josephson vortices (given by Eq. (8.4)), the core is enclosed in a healing length extension ξ defined by the hyperbolic

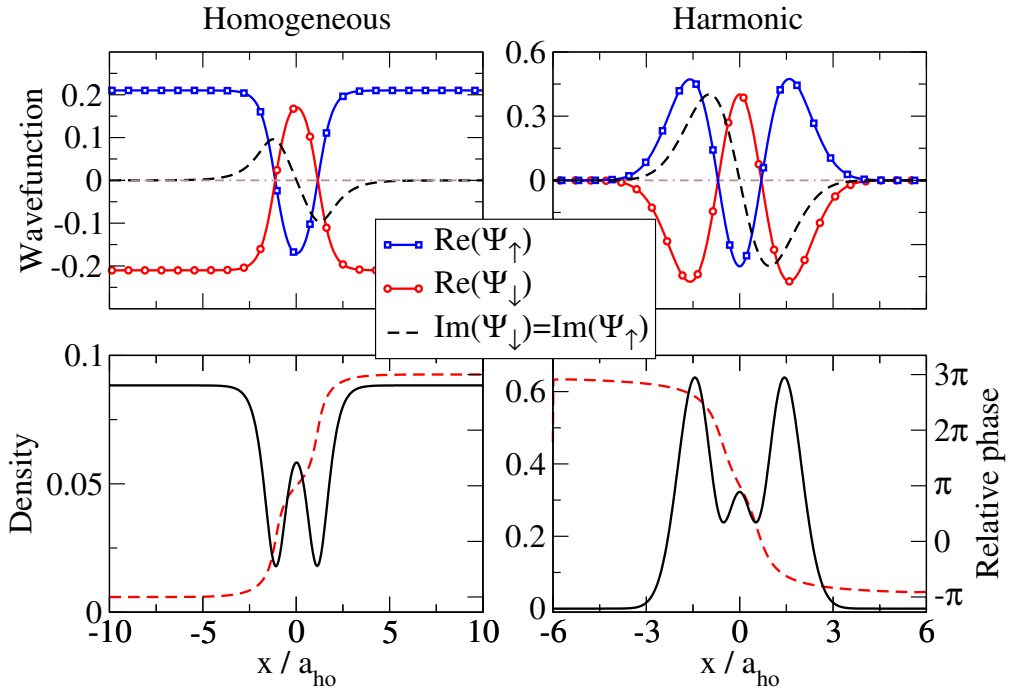

Figure 8.2: Doubly charged Josephson vortices in homogeneous (left) and trapped (right) settings in the absence of spin-orbit coupling. Top panels show the condensate wave functions, and bottom panels depict the total densities (solid lines) and relative phases (dashed lines). For the sake of comparison, the same (harmonic oscillator) units have been used in all the graphs. Homogeneous case: $\mu = 1.77\,\hbar\omega_{\rm ho}$, $g_{\uparrow\downarrow} = 0.2\,g$, and $\Omega/\omega_{\rm ho} = 0.7$. Trapped case: $\mu = 2.22\,\hbar\omega_{\rm ho}$, $g_{\uparrow\downarrow} = 0.9954\,g$, and $\Omega/\omega_{\rm ho} = 1.0$.

tangent shape of the wave function (in the homogeneous condensate), and is characterized by a density profile without zeros, described by the hyperbolic secant in the homogeneous case or the Hermite polynomial $H_0(x)$ in the (linear) trapped one. In contrast, a doubly-charged Josephson vortex state must present zeros in the imaginary part of the wave function inside the core, as it is the case of the examples represented in Fig. 8.2. They correspond to doubly-charged Josephson vortices for homogeneous and trapped systems, obtained by numerically solving the 1D Gross-Pitaevskii equation (8.1). Both states have no population imbalance. By direct observation of the wave function of the trapped condensate (top right panel), it follows that this state belongs to the family $\psi^{2,1}_{\uparrow,\downarrow}(x) = \pm\, e^{-x^2/2\xi^2}\,(\,\pm\alpha H_2(x/\xi) + i\beta H_1(x/\xi)\,)$. States of this type have been previously studied as solutions of the parametrically driven nonlinear Schrödinger equation [Bar03, Bar07].

With spin-orbit coupling

The laser coupling k_L introduces a significant difference in the nature of the possible solitonic solutions to Eq. (8.1). Dark solitons of the type described by Eq. (8.3) are no longer possible, since their symmetry ($\Psi^{DS}_{\uparrow} = -\Psi^{DS}_{\downarrow}$) is not fulfilled by the equation of motion. Contrary to dark solitons, the symmetry of Josephson vortices ($\Psi^{JV}_{\uparrow} = -(\Psi^{JV}_{\downarrow})^*$) is preserved by the spin-

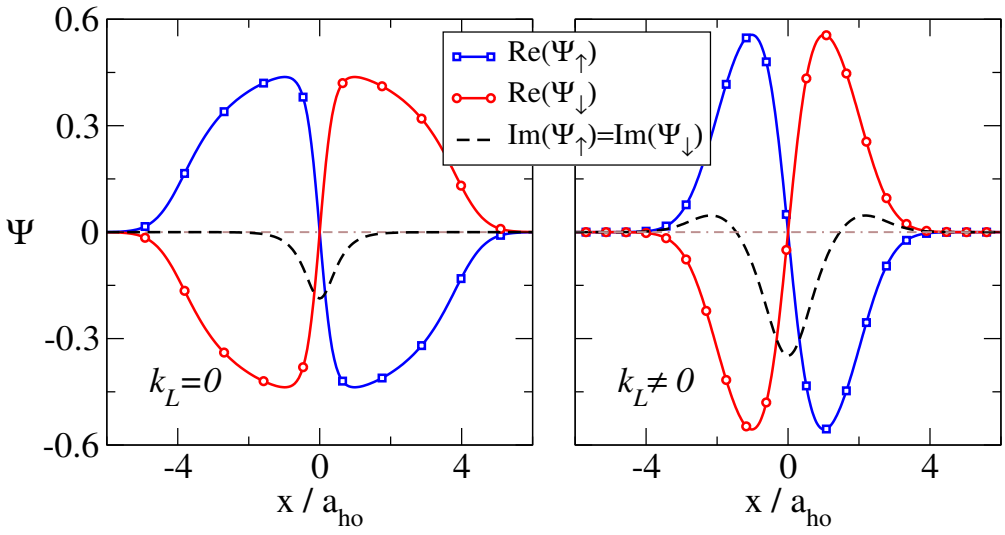

Figure 8.3: Left panel shows the Josephson vortices in the absence ($k_L = 0$) of spin-orbit coupling for $\Omega/\omega_{\rm ho} = 3.5$, and $\mu = 6.6\,\hbar\omega_{\rm ho}$. Right panel shows the Josephson vortices in the presence ($k_L \neq 0$) of spin-orbit coupling for trapped condensates with $\Omega/\omega_{\rm ho} = 2$, and $\mu = 1.7\,\hbar\omega_{\rm ho}$, within the single-minimum phase. The interaction strengths are the same in both cases, $g_{\uparrow\downarrow} = 0.9954\,g$.

orbit coupling. The wave functions of Josephson vortices, both in the homogeneous and trapped systems, are very similar to those shown in Fig. 8.1. The main difference is the appearance of zeros (out of the soliton core) in their imaginary parts, as a result of the relative momentum introduced by $\pm\hbar k_L$. This feature can be seen in Fig. 8.3, where we have plotted Josephson vortices in the absence of spin-orbit coupling, on the left, and in the presence of spin-orbit coupling, for $a_{\rm ho}k_L = 0.5$, on the right, for two different number of particles and coherent coupling. As it is reported below, multidimensional solitons present the same features (see Fig. 8.4) discussed below.

8.2 Josephson vortices in multidimensional condensates

Multidimensional Bose-Einstein condensates, composed of two coherently coupled (spin) components, can exhibit topological states in correspondence with the 1D ones presented before. In general, their existence depends on the interaction. As detailed below, our numerical results show that in harmonically trapped systems static dark solitons and Josephson vortices can be found in the absence of spin-orbit coupling ($k_L = 0$), but only static Josephson vortices survive to nonzero values of k_L.

In order to find solitonic states, we evolve the full-3D Gross-Pitaevskii Eq. (8.1) in imaginary time, from the initial ansatz:

$$\psi_\uparrow(\mathbf{r}) = -\psi_\downarrow(\mathbf{r}) = \chi_\perp(y,z)\tanh(x/\xi(y,z)), \tag{8.7}$$

where $\chi_\perp(x=0,y,z)$ is a transverse ground state, and $\xi(y,z) = \hbar/\sqrt{mg|\chi_\perp|^2}$ a local healing length. This ansatz, which corresponds to a dark soliton state in the x-direction (situated

at $x = 0$), follows from the approach proposed in Ref. [Mun14] for scalar condensates, and, apart from being a real function, captures the main features of the solitonic solution (phase jump and density depletion) we are searching for. In particular, for the high-interaction regime, $\chi_\perp(x = 0, y, z)$ is explicitly defined through the Thomas-Fermi wave function

$$\chi_{TF}(y, z) = \sqrt{(\mu_{\text{eff}} - V_{\text{trap}}(x = 0, y, z))/(g + g_{\uparrow\downarrow})}\,. \tag{8.8}$$

In the case of solitons in the y-direction, x and y swap places in Eq. (8.7). Figure 8.4 shows a 3D Josephson vortex in a spin-orbit-coupled system, obtained by following the procedure previously described. The condensate, which contains $N = 500$ ^{87}Rb atoms trapped by an external harmonic potential of frequency $\omega_\rho = 2\pi \times 200$ Hz and aspect ratio $\lambda = 4$, belongs to the single-minimum phase, with $\alpha = 2.36$ ($\Omega = 30$ kHz). This is a stationary solution of the Gross-Pitaevskii equation (8.1) with a non-trivial phase, given by a complex wave function (right panel of Figure 8.4) which involves the existence of inter-spin currents in the system. Comparing this state with the 1D Josephson vortex without spin-orbit coupling, represented in Fig. 8.1, the only difference comes from the zeros (out of the soliton core) in the imaginary part of the wave function.

8.2.1 Stable Josephson vortices

In the same way as it occurs with dark solitons in scalar Bose-Einstein condensates, it is possible to find dynamically stable Josephson vortex states below an interaction threshold, or equivalently, below a critical value of the effective chemical potential μ_{eff}. Above this, Josephson vortices are unstable topological states, whose decay leads to the appearance of vortex lines in the system.

In order to demonstrate the stability of multidimensional Josephson vortices, we have analyzed spin-orbit coupled condensates in quasi-2D systems. Our results show that the critical value of μ_{eff} for stability depends strongly on the presence of spin-orbit coupling, and specifically on the strength of the Rabi coupling. Without spin-orbit coupling, and for $\Omega = 30$ kHz, Josephson vortices are stable in 2D condensates containing up to $N_{2D} = 250$ particles. In the presence of spin-orbit coupling, however, stability is dramatically reduced. Moreover, the richer phase diagram produces differences on the stability for the same μ_{eff}, and provides different dynamical scenarios in the decay.

In Fig. 8.5 we show the real time evolution of Josephson vortices, across the x-direction, in the presence of spin-orbit coupling (with the wave vector $\mathbf{k}_L$ also lying on x). For the initial state, at time $t = 0$, we have added uniform noise $\delta(\mathbf{r})$ to the stationary wave function $\psi(\mathbf{r}) \to \psi(\mathbf{r})[1 + 0.01\delta(\mathbf{r})]$, that we will refer to as 1%-strength noise. The dimensionless density of the spin-$\uparrow$ component, integrated over the coordinate y perpendicular to the soliton, $n_x(x) = \int |\psi_\uparrow(x, y)|^2 dy$, is represented against time, given in harmonic oscillator units. The left panel of Fig. 8.5corresponds to a stable Josephson vortex in a 2D condensate containing $N_{2D} = 50$ atoms, confined by a harmonic trap of frequency $\omega_\rho = 2\pi \times 200$ Hz and aspect ratio $\lambda = 4$. The spin-orbit number is $\alpha = 0.79$ ($\Omega = 10$ kHz), situating the system inside the plane-wave phase. The horizontal dark line halving the atomic cloud marks the position of the Josephson vortex, which remains unaltered during the whole evolution. The case represented in the right panel of Fig. 8.5 is more peculiar. It has the same parameters as the condensate in the left panel except for a higher coherent coupling $\Omega = 30$ kHz, which puts the system within the single-minimum

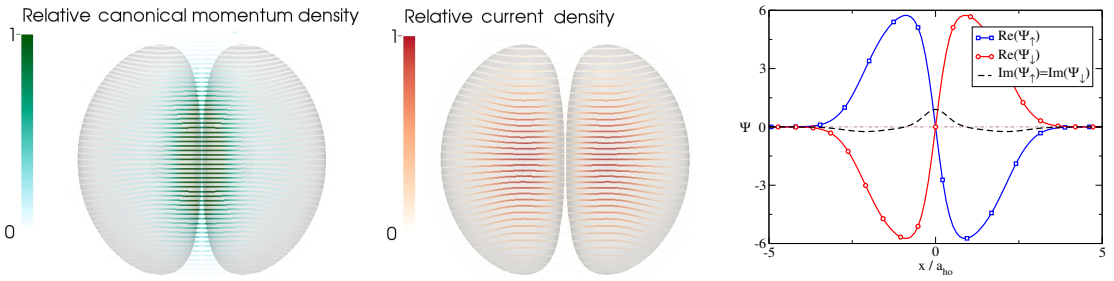

Figure 8.4: 3D Josephson vortex in a two-component condensate made of $N = 500$ ^{87}Rb atoms, trapped by a harmonic potential of frequency $\omega_\rho = 2\pi \times 200$ Hz and aspect ratio $\lambda = 4$, with a spin-orbit coupling characterized by $\lambda_L = 1064$ nm and $\Omega = 30$ kHz. Left panel: streamlines of the relative canonical momentum density $\hbar[n_\uparrow \vec{\nabla}\arg(\Psi_\uparrow) - n_\downarrow \vec{\nabla}\arg(\Psi_\downarrow)]/m$ in the x-y plane, colored by magnitude (in arbitrary units) over the density isocontour at 5% of maximum density. Middle panel: streamlines of the relative current density $\hbar[n_\uparrow(\vec{\nabla}\arg(\Psi_\uparrow) - \vec{k}_L) - n_\downarrow(\vec{\nabla}\arg(\Psi_\downarrow) + \vec{k}_L)]/m$ in the x-y plane, colored by magnitude (in arbitrary units) over the density isocontour at 5% of maximum density. Right panel: real (solid) and imaginary (dashed) part of the wave functions (blue squares for spin-↑ and red circles for spin-↓) along the x-axis (for $y = z = 0$). The imaginary part of the wave functions for both components are overlapped.

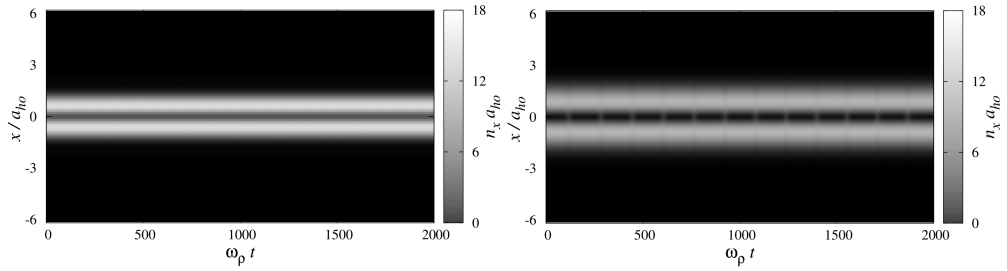

Figure 8.5: The left (right) panel shows the real time evolution of the integrated density over the y-direction of a Josephson vortex across the x-direction in a 2D system with spin-orbit coupling, for $\Omega = 10\,\text{kHz}$ ($30\,\text{kHz}$) inside the plane-wave (single-minimum) phase. Common parameters: $N_{2D} = 50$, $\omega_\rho = 2\pi \times 200\,\text{Hz}$, $\gamma = 4$, and $\lambda_L = 1064\,\text{nm}$.

phase with $\alpha = 2.36$. Small periodic deviations from the initial (perturbed) state can be observed in the graph. Nevertheless, the stationary configuration is rapidly recovered, and the Josephson vortex persists as a robust state.

8.2.2 Decay dynamics

Josephson vortices in multidimensional systems are unstable against transverse modes with long wavelengths. In this sense, the decay of Josephson vortices follows qualitatively that of dark solitons in scalar condensates, by distorting the soliton plane and producing vortex lines inside the system [Kuz88]. In elongated condensates, the decay of a dark soliton generates a solitonic vortex [Bra01, Mun14], which survives as a dynamically stable state. However, in scalar disk-shaped condensates a single vortex can not be generated after the soliton decay, because of angular

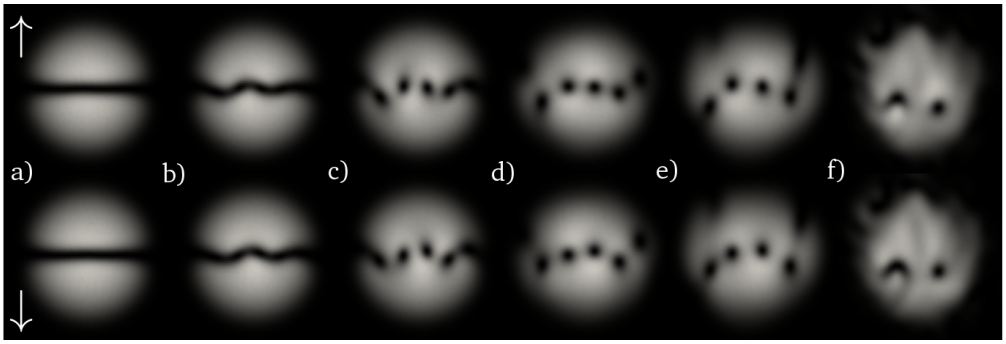

Figure 8.6: Decay of a Josephson vortex, in the y-direction of a two-dimensional system with spin-orbit coupling, by snake instability of the soliton plane. Condensate parameters: $N_{2D} = 2000$, $\omega_\rho = 2\pi \times 200\,\mathrm{Hz}$, $\gamma = 4$, $\lambda_L = 1064\,\mathrm{nm}$, and $\Omega = 30\,\mathrm{kHz}$. The spin-↑ (top) and spin-↓ (bottom) density snapshots, from (a) to (f), correspond to times $\omega_\rho t = 3.5,\ 4.3,\ 5,\ 6,\ 8,$ and 20, respectively.

momentum conservation; instead, a vortex dipole, constituted of a vortex and an antivortex, is left over [Kuz95, Hua03]. As we will demonstrate in what follows, this is also the case for disk-shaped spin-orbit coupled condensates. A vortex dipole per component is the remainder of the Josephson vortex at the last stage of its decay.

Figure 8.6 shows the whole time sequence of decay, from (a) to (f), for a Josephson vortex across the y-direction in a 2D condensate containing 2000 ^{87}Rb atoms. As can be seen, the two components follow a synchronized decay. After the snaking of the soliton plane, several pairs of vortex dipoles appear, almost overlapped, for each spin component. The vortices situated at the same position are connected by domain walls in the relative phase [Son02]. Finally, only one vortex dipole per component survives, and its subsequent evolution depends both on the particular regime of the system [Nee10, Fre10, Mid11, Tor11, Nav13] (i.e. either the single-minimum or plane-wave phase), and on the orientation of the Josephson vortex plane with respect to the direction of the laser wave vector $\mathbf{k}_L$.

For the sake of comparison, we consider first the decay dynamics in the absence of spin-orbit coupling. In Fig. 8.7 we show the real time evolution of a stationary Josephson vortex after adding a 1%-strength noise. The two lower panels represent the dimensionless density $a_{\mathrm{ho}} n_x(x)$ (left) and $a_{\mathrm{ho}} n_y(y)$ (right) for one condensate component (spin-↑). After few $\omega_\rho t$ cycles, the Josephson vortex (thick black line) decays into a vortex dipole (upper snapshots of Fig. 8.7) that describes a zigzag path (one per vortex) in the x and y coordinates. The dynamics of the vortex dipole consists in a superposition of a rotation around the center of the trap (low frequency oscillation in the graph), due to the rotational symmetry of the condensate, and a vibration of the relative position of the vortices (high frequency oscillation).

When spin-orbit coupling is switched on, the rotational symmetry is broken, and the vortex dipole that emerges after the decay of the Josephson vortex can not rotate freely. The term $-\hat{\mathbf{p}}\Psi_i \cdot \hbar\mathbf{k}_L$ that appears in the Gross-Pitaevskii equation (8.1) can be recognized as the potential of a magnetic dipole $-\boldsymbol{\mu}_S \cdot \mathbf{B}$, where $\boldsymbol{\mu}_S$ is the magnetic moment of a spin-1/2 particle and $\mathbf{B}$ is the static magnetic field. In this way, the velocity of the vortex dipole $-\hat{\mathbf{p}}\Psi_i$, which is perpendicular

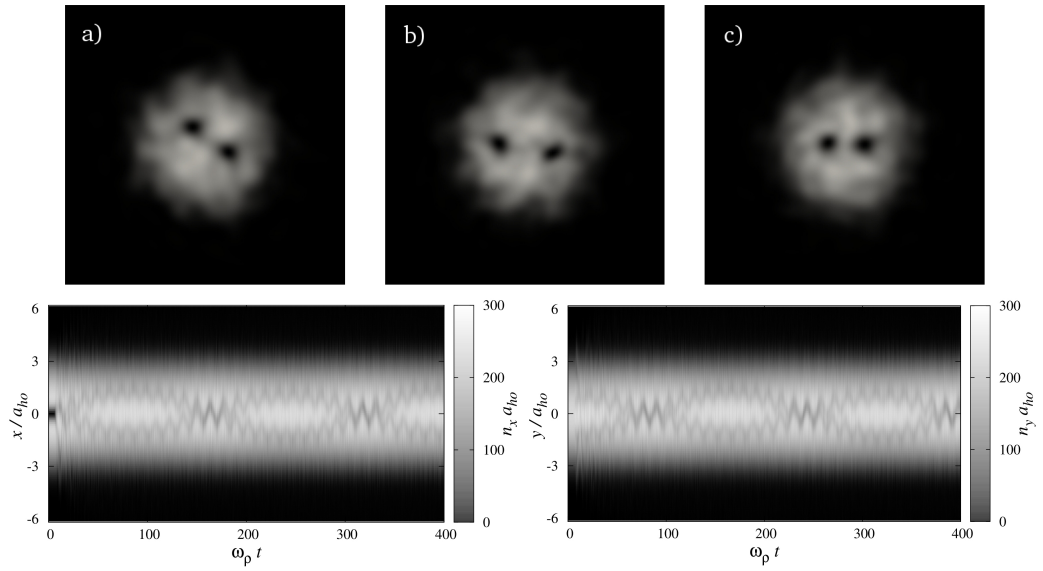

Figure 8.7: Real time evolution of a Josephson vortex in the x-direction, in a 2D condensate without spin-orbit coupling, and parameters: $N_{2D} = 2000$, $\omega_\rho = 2\pi \times 200\,\mathrm{Hz}$, $\gamma = 4$, $\lambda_L = 1064\,\mathrm{nm}$, and $\Omega = 10\,\mathrm{kHz}$. Upper panel: spin-↑-density snapshots, from (a) to (c), at times $\omega_\rho t = 51,\ 73$, and 78, respectively. Bottom panels: non-dimensional spin-↑ density integrated over the y (left) and x (right) directions.

to the dipole direction, interacts with the spin-orbit momentum $\mathbf{k}_L$, generating an aligning torque given by $\hat{\mathbf{p}}\Psi_i \times \hbar\mathbf{k}_L$. Therefore, the orientation of the Josephson vortex is crucial for the later dynamics of the emergent vortex dipoles, since their alignment follows the Josephson vortex one. Given that this orientation and the velocity field of the dipoles are the same for both components, the opposite laser momentum $\pm\hbar k_L$, yields to energies and acting torques with different signs. For this reason, in what follows, we address the decay of Josephson vortices in different dynamical regimes, and with different orientations of the soliton plane, along the laser wave vector (x-axis) and perpendicular to it (y-axis).

Josephson vortices in the single-minimum phase

In the single-minimum phase, the ground state of the system does not present population imbalance and the density profiles of both condensate components coincide. This is also the case for the excited states containing Josephson vortices. As can be seen in Fig. 8.8, the imaginary-time evolution of our initial ansatz Eq. (8.7) reaches the energy plateaus of Josephson vortices, represented in the insets Fig. 8.8(a), for the two orientations considered, x in the upper panel of the figure and y in the lower one, before falling to the ground state of the system, depicted in the insets Fig. 8.8(b). During the whole evolution, obtained for the coherent coupling $\Omega = 30\,\mathrm{kHz}$ and spin-orbit number $\alpha = 2.36$, the population imbalance remains zero.

Josephson vortex states have a nonzero mean momentum. Therefore, their mean energy depends on their orientation because of the term associated to the spin-orbit coupling. As a result, for the same parameters, a Josephson vortex across the y-direction has higher energy

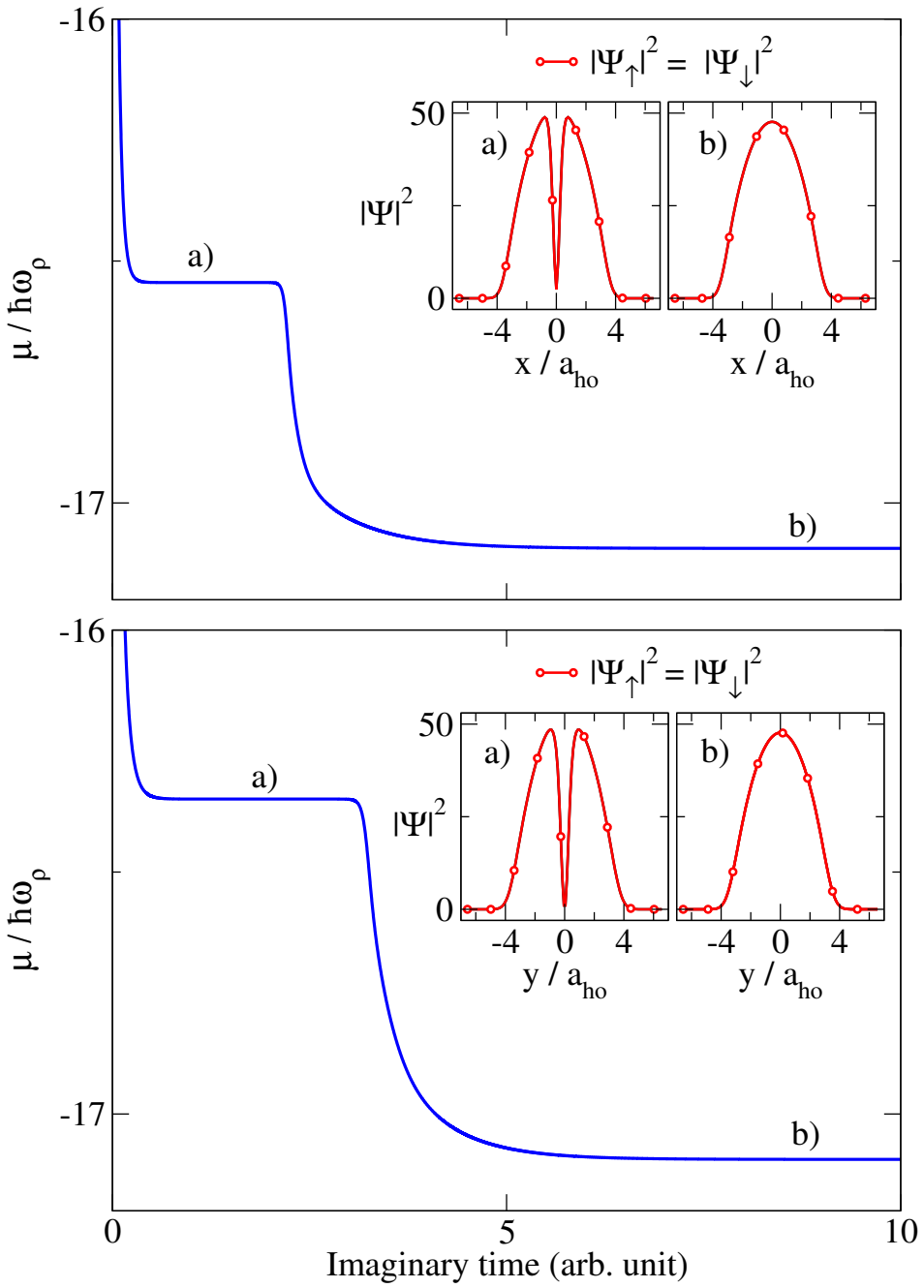

Figure 8.8: Imaginary time evolution of Josephson vortices, in the x (top) and y (bottom) directions, within the single-minimum phase, with parameters: $N_{2D} = 2000$, $\omega_\rho = 2\pi \times 200\,\mathrm{Hz}$, $\gamma = 4$, $\lambda_L = 1064\,\mathrm{nm}$, $\Omega = 30\,\mathrm{kHz}$. The insets, showing the spin densities along selected axis, correspond to different stationary states (labeled by (a) and (b)), from the initial Josephson vortex up to the final ground state.

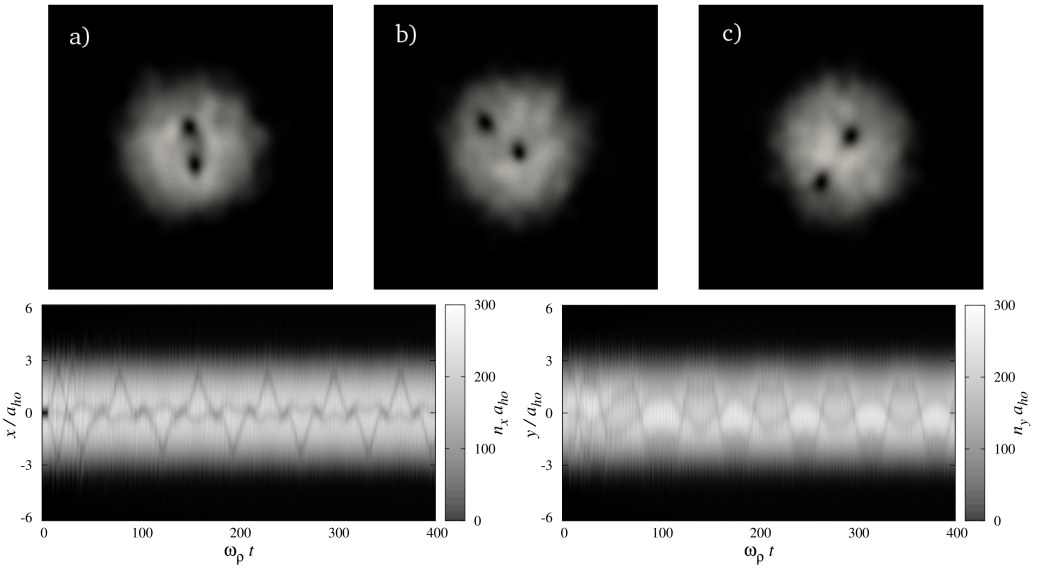

Figure 8.9: Real time evolution of the Josephson vortex, in the x-direction, shown in the top panel of Fig. 8.8. Upper panel: spin-↑-density snapshots, from (a) to (c), at times $\omega_\rho t =$ 99, 112, and 124, respectively. Bottom panels: evolution of the non-dimensional spin-↑ density integrated over the y (left) and x (right) directions.

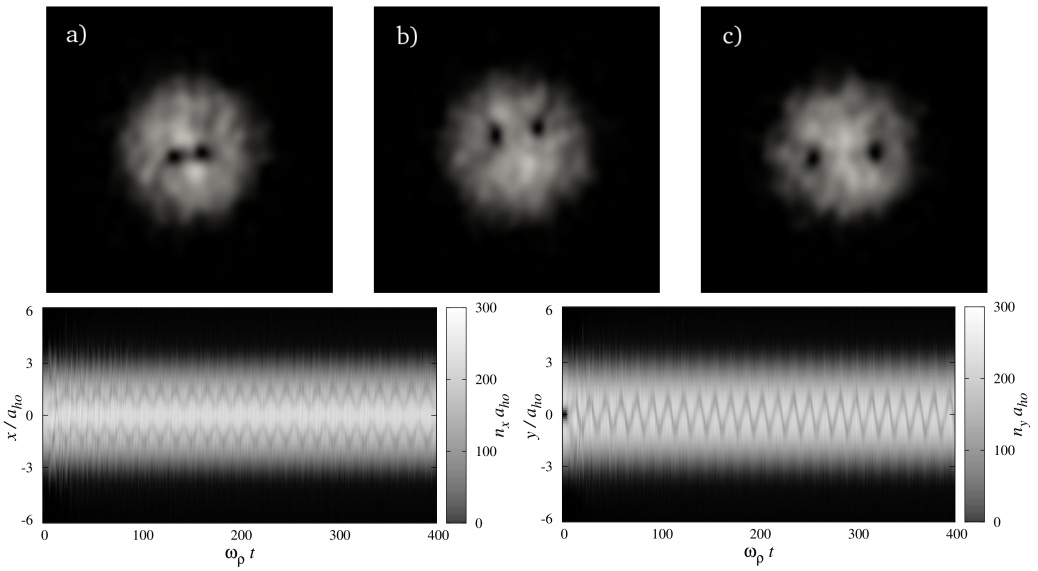

Figure 8.10: Same as Fig. 8.9, for the Josephson vortex, in the y-direction, shown in the bottom panel of Fig. 8.8. The snapshots, from (a) to (c), correspond to times $\omega_\rho t = 102,\ 108,$ and 112, respectively. This dynamical evolution corresponds to the same evolution represented in Fig. 8.6 but at longer times.

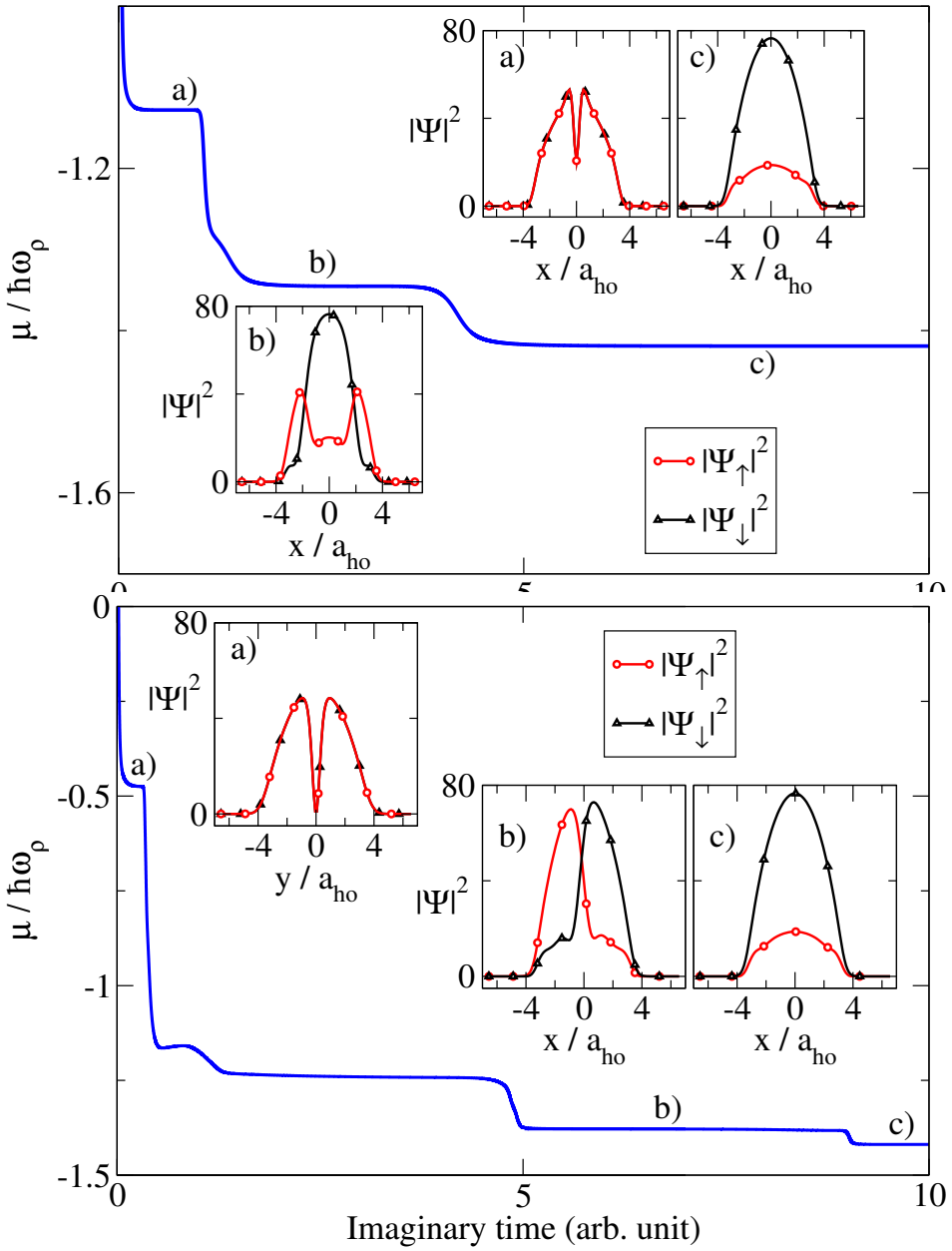

Figure 8.11: Same as Fig. 8.8 for Josephson vortices in the plane-wave phase ($\Omega = 10\,\mathrm{kHz}$).

than a Josephson vortex across x (as can be seen in the main graphs of Fig. 8.8). In the latter case, the momentum originated by the Josephson vortex is aligned with the laser wave vector, and then the energy of the system is reduced. On the other hand, for the Josephson vortex across the y-direction the spin-orbit coupling has no influence on the mean energy.

In order to analyze the dynamics of the Josephson vortices found in Fig. 8.8, we have performed their real time evolution by numerically solving the Gross-Pitaevskii equation (8.1),

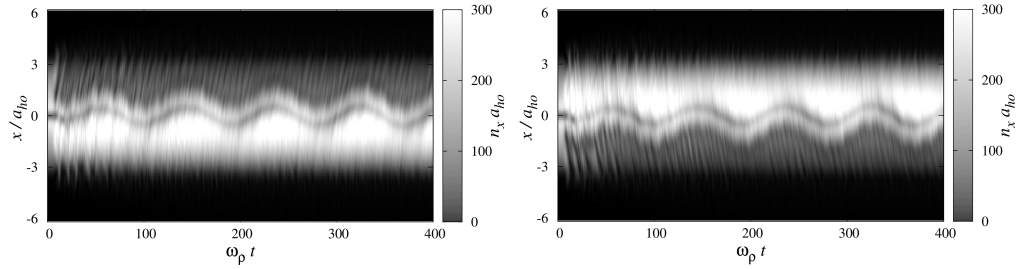

Figure 8.12: Real time evolution of the Josephson vortex, in the x-direction, shown in the top panel of Fig. 8.11. The left (right) panel shows the dimensionless, spin-↑ (spin-↓) density after integration over the coordinate y.

after adding a 1%-strength noise to the respective stationary states. The results are plotted in Fig. 8.9 for the Josephson vortex oriented across x, and Fig. 8.10 for the Josephson vortex oriented across y. In the former case the velocities of the emerging vortex dipoles are aligned with the laser wave vector. One of the dipoles lays on the energy minimum of the spin-orbit potential potential, whereas the other one occupies the energy maximum. This configuration is unstable and degenerate against exchange of the positions of the vortex and the anti-vortex. As a consequence, the system oscillates between one configuration and the other. The whole picture can be seen in the evolution of Fig. 8.9, where the peaked paths correspond to the motion of a vortex around the anti-vortex in order to exchange their positions.When the Josephson vortex is oriented across y (Fig. 8.10) the evolution resembles the case without spin-orbit coupling, except by the lacking of rotational motion of the dipoles around the center of the trap, because of the absence of rotational symmetry. The vortex dipoles are vibrating along with a small precession, keeping the orientation of the dipoles.

Josephson vortices in the plane-wave phase

As commented previously, the plane-wave phase is characterized by a ground state presenting population imbalance. However, the Josephson vortex states do not share this feature. Then, by evolving a Josephson vortex in imaginary time, it is possible to find new, intermediate excited states before reaching the ground state. Figure 8.11 represents this evolution for Josephson vortices (at insets (a)) across x (top panel) and y (bottom panel), having the coherent coupling $\Omega = 10\,\mathrm{kHz}$ and spin-orbit number $\alpha = 0.79$. The evolution finds several plateaus that correspond to solutions of the time-independent version of Eq. (8.1), and include population imbalance (at insets (b)). At the last stage of the evolution, the ground state is obtained (at insets (c)).

In the plane-wave phase, the Josephson vortex decay is different to the picture outlined before in Fig. 8.6. The characteristic population imbalance of the ground state plays a crucial role in the decay dynamics. For the Josephson vortex across y, a big population imbalance appears, the density of one of the components is highly depleted, and no vortices are finally left over. In contrast, the decay of the Josephson vortex across x is driven by phase separation. This phenomenon occurs at the first stage through the formation of new solitonic structures during the separation that finally decay into vortices. The resulting configuration presents again vortex dipoles that live near the surface of each condensate component. The vortex dipoles move

according to the oscillation of the boundary between components, but their orientation does not change in time because of the alignment of the dipole velocity and the laser wave vector. A whole evolution of this type is represented in Fig. 8.12, where the integrated density profile of both spin components are shown for the Josephson vortex across the x-direction of Fig. 8.11 (inset (a) of the top panel).

Chapter 9

Spin-orbit coupling in polariton condensates

In the previous chapters, we have studied different phenomena related to condensation and superfluidity appearing in atomic Bose-Einstein condensates. It is possible, however, to nucleate condensates of bosonic particles of different nature, as photons [Kla10], magnons [Dem06], or polaritons [Kas06]. In this thesis, we have investigated rotational properties and spin-orbit coupling in polariton condensates. Polaritons are quasiparticles that appear in semiconductor microcavities in the strong light-matter coupling regime. Semiconductors are materials characterized by an electronic band structure effectively represented by a valence band and a conduction band separated by a gap. The valence band, completely or almost completely occupied by electrons, is described by electron excitations or holes, which are quasiparticles associated to the absence of electrons in the valence band. In contrast, the conduction band is only occupied by few electrons that have been promoted from the valence band via the absorption of photons. When electrons of the valence band jump to the conduction band leaving holes behind, electron-hole pairs may form a bound state and constitute a composite particle called exciton, which obeys bosonic statistics to a good degree of approximation. These excitons can form a bound state with a photon in order to generate a polariton, which possesses properties characteristic of photons, as polarization, and also of excitons, such as a massive dispersion relation. Polaritons have been condensed by using a solid-state based semiconductor microcavity, which is a structure constituted by a quantum well between two structures of several thin layers with alterned refractive index, called Distributed Bragg Reflectors.

In this chapter we will introduce the main physics of polaritons, their dispersion relation and polarization, together with the (driven-dissipative) Gross-Pitaevskii equation that can describe a polariton condensate. After that, we will analyze the Transverse Electric - Transverse Magnetic (TE-TM) splitting, which leads to an effective spin-orbit coupling between the two polarization components of the polariton condensate. Afterwards, we will explain a phenomenon that appears due to this coupling: spin-to-orbital angular momentum conversion. This is an effect that manifests when we pump only one of the polarization components of the condensate (thus producing a spin imbalance). We will see that the TE-TM splitting permits the flip of the polarization, producing a vortex in the nonpumped component of the condensate. This effect can be derived

analytically in the case of homogeneous noninteracting condensates, and, in the case of polaritons trapped within a ring, it leads to a persistent current. After that, we will probe the superfluid behaviour of the polariton condensate by analyzing its response to the presence of disorder.

9.1 Polaritonic dispersion relation and polarization

In a semiconductor microcavity, cavity photons can remain for a long time, which is enough to generate excitons. The strong coupling between light and matter excitons gives rise to a new composite bosonic quasiparticle: the polariton. Polaritons can eventually form an out-of-equilibrium Bose-Einstein condensate when the pumping and losses are compensated, and drive the system to the lower energy state, which at the end gets macroscopically occupied [Car13]. Polaritons can exhibit interactions due to the excitonic fraction in the system. These interactions are short-range to a good approximation and, in experiments, the diluteness condition $na_s^3 \ll 1$, is commonly fulfilled. As a consequence, the mean-field theory applies (in its driven-dissipative version due to the short lifetime of polaritons, see below), and among its predictions, polaritonic Bose-Einstein condensates manifest superfluid behavior [Amo09, Wou10].

As commented above, polaritons exhibit both matter and light properties. Regarding the optical part, photons are relativistic particles, which imposes that their dispersion relation shows a linear increasing of the energy with the wave vector $E = \hbar\omega = \hbar ck$, where c is the speed of light in the cavity. However, since in the direction of the Distributed Bragg Reflectors, photons are confined due to the presence of the cavity, the wave vector in this direction gets quantized with

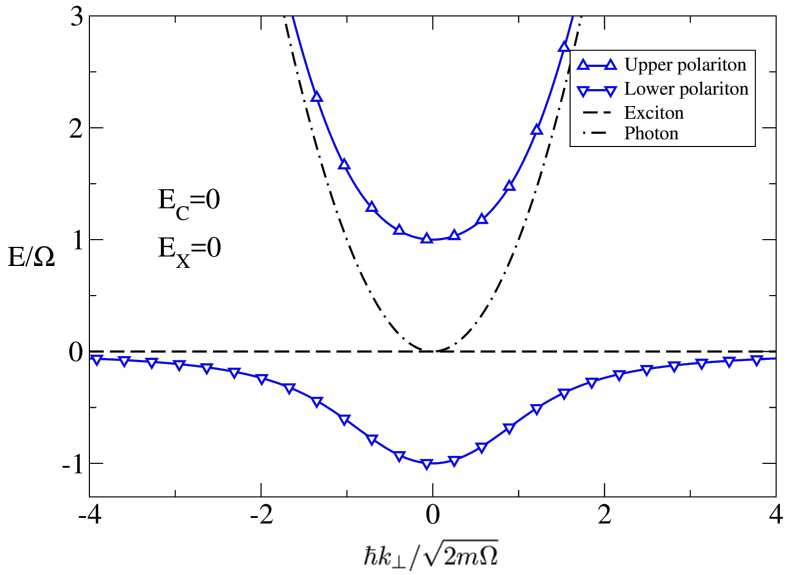

Figure 9.1: Dispersion relation of photons (black dot-dashed line), excitons (black dashed flat line) and polaritons (blue lines with down triangles for the lower polariton branch and up triangles for the upper polariton branch). The Rabi coupling gives the separation between both branches at $k_\perp = 0$. In this plot, $E_\mathrm{C} = E_\mathrm{X} = 0$.

a nonzero minimum value k_0. As a consequence, the dispersion, for low values of the in-plane wave vector $k_\perp$ is:

$$E = \hbar\omega = \hbar c\sqrt{k_\perp^2 + k_0^2} \approx \hbar c k_0 + \frac{\hbar c k_\perp^2}{2k_0}\,. \tag{9.1}$$

In the previous equation, a zero-point energy $E_{\rm C} = \hbar c k_0$ can be defined, and one can observe that, as a function of the in-plane wave vector, the photonic dispersion relation (9.1) is no longer linear but quadratic, with an effective mass $m_{\rm eff}$ that can be derived from the minimum cavity photon momentum: $m_{\rm eff}c = \hbar k_0$. Therefore, cavity photons behave as massive particles with an effective mass of the order of 10^{-5} times the electron mass. Excitons, as massive particles, are also well characterized by a quadratic dispersion relation. Nevertheless, since their mass (of the order of the electron mass) is much larger than the effective mass of the cavity photons, it is a good approximation to consider that its dispersion $E_{\rm X}$ is flat. When a linear (Rabi) coupling Ω is introduced between the dispersion relations of photons and excitons, the eigenvalues $E_{\rm pol}$ of the diagonalized system provide the dispersion relation of polaritons.

$$\begin{vmatrix} E_{\rm C} + \dfrac{\hbar^2 k_\perp^2}{2m_{\rm eff}} - E_{\rm pol} & \Omega \\ \Omega & E_{\rm X} - E_{\rm pol} \end{vmatrix} = 0\,, \tag{9.2}$$

which yields to

$$E_{\rm pol}^{\pm} = \frac{1}{2}\left(E_{\rm C} + E_{\rm X} + \frac{\hbar^2 k_\perp^2}{2m_{\rm eff}} \pm \sqrt{\left(E_{\rm C} - E_{\rm X} + \frac{\hbar^2 k_\perp^2}{2m_{\rm eff}} \right)^2 + 4\Omega^2} \right)\,. \tag{9.3}$$

The $\pm$ sign corresponds to the upper polariton and lower polariton branch, respectively. Figure 9.1 shows the flat dispersion relation of the excitons (black dashed line), the quadratic dispersion relation of the photons (black dot-dashed line), together with the two branches of the polaritons (blue lines with down and up triangles respectively), which, at $k_\perp = 0$ are separated by the Rabi coupling as 2Ω.

Photons are bosonic particles whose spin is commonly referred to as polarization. The polarization state of light can be projected onto a sphere, called Poincaré or Bloch sphere, where each point on its surface corresponds to a particular state of polarization with degree of polarization 1 (fully polarized), which decreases when approaching the center of the sphere (fully unpolarized). The six cardinal points in the Poincaré sphere (see Fig. 9.2) are associated to Horizontal (H) -Vertical (V) in the x-axis, Diagonal (D) -Antidiagonal (A) in the y-axis and Circular Right (σ^+) - Left (σ^-) in the z-axis.

The previous quantities are included in the so called Stokes vector, which has four components, $\vec{S} = (S_0, S_1, S_2, S_3)$. The first one, S_0 is associated to the radius of the Poincaré sphere itself, therefore, the light intensity (also called photoluminiscence). The other three components of the Stokes vector contain information about the degree of polarization in the three different bases introduced before. It is important to notice that the previous H-V, D-A and σ^+-σ^- bases are not independent. Only one of them is needed in order to fully describe the polarization state of light.

Some of the features of polaritons come from the photonic nature, since most of the properties

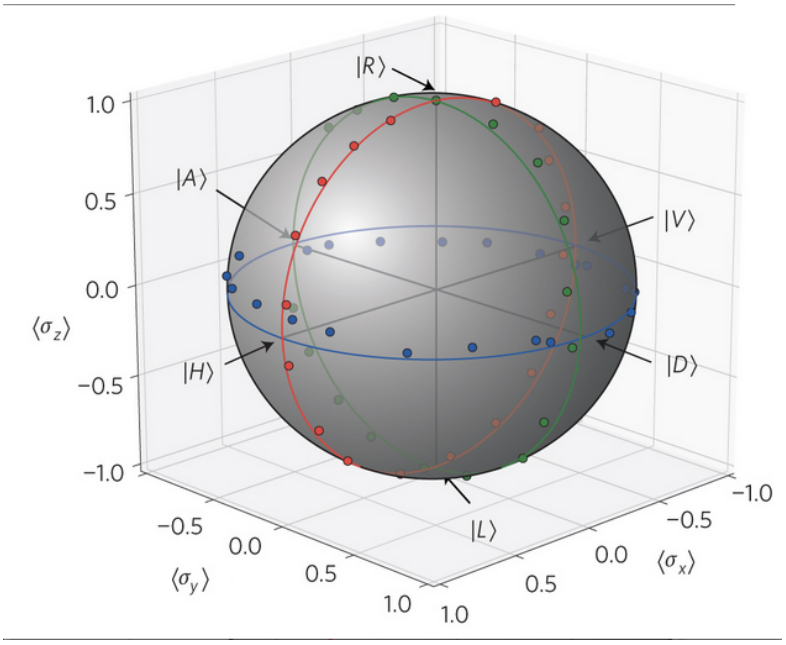

Figure 9.2: Different polarization states in the H-V, D-A and σ^+-σ^- (L-R in the figure) basis, projected on the surface of a Poincaré sphere.

of photons are also present in polaritons. Polarization is not an exception. Applied to the case of polaritons, the three last components of the Stokes vector constitute the pseudospin of the polariton. Due to the quantum nature of polaritons, wave functions can be assigned to the different fully-polarized states. However all of them can be written in terms of two. For instance, if we take the H-V basis, the D-A wave functions are related as: $\psi_{D,A} = (\psi_H \pm \psi_V)/\sqrt{2}$, and the σ^+-σ^- wave functions as: $\psi_\pm = (\psi_H \pm i\,\psi_V)/\sqrt{2}$, where the $+(-)$ sign refers to the D(A) and $\sigma^+(\sigma^-)$ polaritzation in the first and second case, respectively.

The Stokes vector can be written in terms of the Pauli matrices by using the following expression:

$$\vec{S} = \langle \Psi | \tilde{\sigma} | \Psi \rangle \,, \tag{9.4}$$

where Ψ concerns the spinor (polarization) wave function, and $\tilde{\sigma}$ is a quadrivector whose components are $(\mathbb{1}, \hat{\sigma}_x, \hat{\sigma}_y, \hat{\sigma}_z)$, being $\mathbb{1}$ the identity matrix and $\hat{\sigma}_{x,y,z}$ the three Pauli matrices. It is worth noticing that, since we have chosen the z-axis for the σ^+-σ^- polarization states, the last expression only works in this basis for the wave function. All these features can be shown in Fig. 9.2. The six cardinal points that fix the three polarization basis are located on the surface of a Poincaré sphere. At the same time, this sphere lives in a three-dimensional space whose basis is given by the Pauli matrices, showing the relation between the Pauli matrices and the three polarization basis in order to give the Stokes vector of light.

9.2 The driven-dissipative Gross-Pitaevskii equation of a polariton condensate with TE-TM splitting

Polaritonic Bose-Einstein condensates can be theoretically described within the mean-field framework by means of the Gross-Pitaevskii equation, as in the case of atomic condensates. However, in order to address this system, one has to take into account few differences in comparison to the atomic case. Polaritons have a finite lifetime that can not be neglected. As a consequence, in order to avoid having a permanently fading system, one has to pump the condensate to compensate losses. In addition, the polarization of photons also plays a crucial role in the polariton field, since there exist two spin projections of the polariton wave function, which leads to a spinor wave function that obeys two coupled Gross-Pitaevskii equations, as in the case of two-component spinor atomic Bose-Einstein condensates.

Apart from the differences previously commented, there is a term in the Gross-Pitaevskii equation whose expression differs in the polaritonic case. Atoms are massive particles with a quadratic dispersion relation, which yields to a kinetic term that can be written in real space in terms of a laplacian. For the case of polaritons, the dispersion is not quadratic (only at low momentum), and, in general, it can not be written as a laplacian. Therefore, one has to write this term as a matrix in the momentum space $T_{ij}(\vec{k})$, called kinetic tensor[1] in Ref. [Kav04].

After all these considerations, and as a function of the kinetic tensor, the *driven-dissipative* Gross-Pitaevskii equation[2] takes the form:

$$i\hbar\frac{\partial}{\partial t}\psi_\alpha(\vec{r},t) = [T_{\alpha\alpha}(\vec{k}) + V(\vec{r}) - i\hbar\gamma_\alpha]\psi_\alpha(\vec{r},t) + T_{\alpha\beta}(\vec{k})\psi_\beta(\vec{r},t) + (g_{\alpha\alpha}|\psi_\alpha(\vec{r},t)|^2 + g_{\alpha\beta}|\psi_\beta(\vec{r},t)|^2)\psi_\alpha(\vec{r},t) + iE_\alpha^{\text{field}}(\vec{r},t)\,. \tag{9.5}$$

In this equation, $\gamma_\alpha = 1/\tau_\alpha$, where τ_α is the lifetime of the polariton component α (α and β are indices that run over the two polarization components of the polariton condensate, fulfilling $\alpha \neq \beta$); and $E_\alpha^{\text{field}}(\vec{r},t)$ accounts for the pumping, which can possess a spatial distribution as well as temporal modulation, like a pulse. The rest of the parameters have the same meaning than the analogous ones in the two-component Gross-Pitaevskii equation.

TE-TM splitting in semiconductor microcavities

When light encounters a surface where there is a change of the medium of propagation, it suffers reflection and refraction, an effect that is described by the Fresnel equations. In the H-V polarization basis, one can decompose the entering wave vector in a component within the plane of the surface (also known as the Transverse Electric or TE mode) and a component vibrating along a direction perpendicular to the TE mode (called Transverse Magnetic or TM mode), that is not contained in surface plane if the incidence is not normal. Under these conditions, Fresnel equations predict a small splitting between the effective refractive index that both modes *feel* during the refraction process. However, this splitting is very small compared with other energy scales in the system, and can be neglected. Nevertheless, in Distributed Bragg Reflectors, which are constituted by many layers (also called multilayers) reflection and refractive processes occur

[1] It is important to recall that the expression of the kinetic tensor strongly depends on the polarization basis chosen for the polariton wave function.

[2] Also known as Lugiato-Lefever equation.

many times, and thus, the effect of the splitting between the TE and the TM modes is enhanced. As a consequence, one can no longer neglect such effect in semiconductor microcavities.

The different effective mass of the TE and the TM modes (due to the different refractive indices that both modes *feel*) yields to an anisotropic dispersion relation in $\vec{k}$-space when working in e.g. the H-V basis. The two polarization modes evolve in time according to their respective frequencies, which are different due to the different effective masses. Therefore, the pseudospin of a polariton suffers a precession as it goes over the condensate. This means that the pseudospin feels an effective magnetic field (known as Maialle field [Mai93]), which, in the cartesian plane, is proportional to $(\cos(2\theta), \sin(2\theta))$, being θ the angle between $\vec{k}$ and the x-axis. This effect describing the precession of the polariton pseudospin due to the TE-TM splitting is called Optical Spin Hall Effect, and was theoretically predicted in Ref. [Kav05] and experimentally detected in Ref. [Ley07]. Spin precession due to the Optical Spin Hall Effect can lead to the appearance of spin textures, as recently reported in Refs. [Kam12, Ant15, Duf15].

The TE-TM splitting changes dramatically the shape of the kinetic tensor. The main feature is that under these conditions, this tensor is no longer diagonal, which provides to the system an effective $\vec{k}$-dependent Rabi coupling between both components. As an example, in the H-V basis, this tensor is written as [Kav04, Kav05]:

$$T(\vec{k}) = \hbar \begin{pmatrix} \omega_{\mathrm{TM}}(\vec{k}) + (\omega_{\mathrm{TE}}(\vec{k}) - \omega_{\mathrm{TM}}(\vec{k}))\, k_x^2/k^2 & (\omega_{\mathrm{TE}}(\vec{k}) - \omega_{\mathrm{TM}}(\vec{k}))\, k_x k_y/k^2 \\ (\omega_{\mathrm{TE}}(\vec{k}) - \omega_{\mathrm{TM}}(\vec{k}))\, k_x k_y/k^2 & \omega_{\mathrm{TM}}(\vec{k}) + (\omega_{\mathrm{TE}}(\vec{k}) - \omega_{\mathrm{TM}}(\vec{k}))\, k_y^2/k^2 \end{pmatrix}, \tag{9.6}$$

where in the last expression, ω_{TE} (ω_{TM}) is a function of $\vec{k}$ that obeys the bare dispersion relation of the lower polariton branch with the effective mass corresponding to the TE (TM) mode (9.3). One can easily observe that this tensor is anisotropic on $\vec{k}$, which yields to an anisotropic Bogoliubov excitation spectrum [She06].

Interestingly, the kinetic tensor (9.6) expressed in the σ^+-σ^- basis is no longer anisotropic. However, the effective spin-orbit coupling induced by the $\vec{k}$-dependent Rabi coupling term, persists. In order to see these features, one has to change the basis of the kinetic tensor by means of the matrix that converts a state in the σ^+-σ^- basis into a state in the H-V basis:

$$A = \frac{1}{\sqrt{2}} \begin{pmatrix} 1 & i \\ 1 & -i \end{pmatrix}. \tag{9.7}$$

Performing the product $A\,T(\vec{k})\,A^{-1}$ yields to the kinetic tensor written in the circularly polarized basis:

$$T(\vec{k}) = \frac{\hbar}{2} \begin{pmatrix} \omega_{\mathrm{TM}}(\vec{k}) + \omega_{\mathrm{TE}}(\vec{k}) & (\omega_{\mathrm{TM}}(\vec{k}) - \omega_{\mathrm{TE}}(\vec{k}))\, (-k_x - i\, k_y)^2/k^2 \\ (\omega_{\mathrm{TM}}(\vec{k}) - \omega_{\mathrm{TE}}(\vec{k}))\, (-k_x + i\, k_y)^2/k^2 & \omega_{\mathrm{TM}}(\vec{k}) + \omega_{\mathrm{TE}}(\vec{k}) \end{pmatrix}, \tag{9.8}$$

and now the off-diagonal terms are linked to the effective spin-orbit coupling (notice the change of sign in front of k_y).

Figure 9.3 shows the splitting between the TM (ω_{TM}) and the TE (ω_{TE}) modes as a function of the in-plane wave vector (blue filled curve). These curve was first experimentally reported in Ref. [Pan99]. At low k limit, apart from the quadratic behavior of the dispersion relation, it is also licit to consider the strength of the spin-orbit coupling as a constant. However, it is no

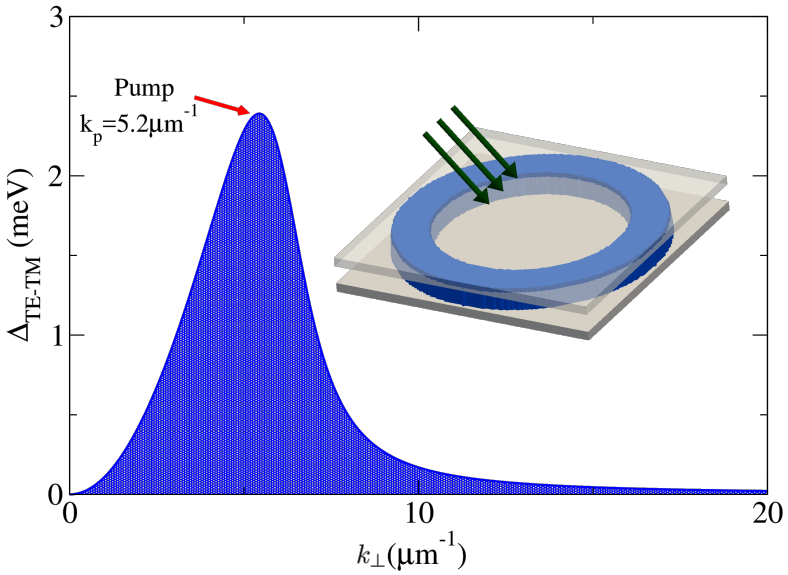

Figure 9.3: The blue filled curve shows the TE-TM splitting as a function of the in-plane wave vector. The red arrow points de radial wave vector of the pump k_p in setup sketched in the inset, which has been used in Sect. 9.3.2.

longer true when the momentum excitation is broader and contains large values of k.

9.3 Spin-to-orbital angular momentum conversion

One of the most striking effects that arise from the TE-TM splitting is the possibility to excite states with nonzero angular momentum (such as vortices [Lag08]) due to the effective spin-orbit coupling, which leads to a spin-to-orbital angular momentum conversion. In the case of spin-orbit coupling, the kinetic tensor couples the angular momentum difference between both components and the polarization in the circularly polarized basis. Moreover, in this case, the coupling occurs for a difference of winding number 2.

In this section, we will first analytically derive this effect for a noninteracting polariton condensate in a homogeneous system, and then, show the solution for an interacting polariton condensate trapped in a ring-shaped quantum well, where vortices translate into persistent currents along the ring [San10].

9.3.1 Noninteracting polaritons in a homogeneous quantum well

Spin-to-orbital angular momentum conversion is an effect that can be derived analytically in the homogeneous noninteracting case. Under these conditions, the only terms that appear in the driven-dissipative Gross-Pitaevskii equation are the kinetic tensor, the pump and the dissipation. The last term is proportional to the lifetime $\gamma = \gamma_+ = \gamma_-$, which we consider equal for both components.

$$i\hbar\frac{\partial}{\partial t}\Psi(\vec{k},t) = \left[T(\vec{k}) - i\hbar\gamma\mathbb{1}\right]\Psi(\vec{k},t) + iE(\vec{k},t)\,, \tag{9.9}$$

where $\Psi(\vec{k},t)$ and $E(\vec{k},t)$ are spinors that contain the wave function of each polarization component of the polariton condensate, and the pump in each component, respectively. The kinetic tensor (9.8) can be written as:

$$T(\vec{k}) = \hbar \begin{pmatrix} \omega(\vec{k}) & \Delta(\vec{k})e^{-i\,2\phi} \\ \Delta(\vec{k})e^{i\,2\phi} & \omega(\vec{k}) \end{pmatrix}, \tag{9.10}$$

where $k_x = k\cos\phi$ and $k_y = k\sin\phi$, and we have defined $2\omega(\vec{k}) = \omega_{\mathrm{TM}}(\vec{k}) + \omega_{\mathrm{TE}}(\vec{k})$ and $2\Delta(\vec{k}) = \omega_{\mathrm{TM}}(\vec{k}) - \omega_{\mathrm{TE}}(\vec{k})$. We can write $T(\vec{k}) - i\hbar\gamma\mathbb{1}$ in its diagonal form as $MD(\vec{k})M^{-1}$, where $D(\vec{k})$ is the diagonal matrix whose elements are the eigenvalues of $T(\vec{k}) - i\hbar\gamma\mathbb{1}$: $\hbar(\omega(\vec{k}) \pm \Delta(\vec{k}) - i\gamma)$, and M is the change of basis matrix.

At this point, we can rewrite the spinor wave function and the pump as $\Psi(\vec{k},t) = M\Phi(\vec{k},t)$ and $E(\vec{k},t) = MG(\vec{k},t)$. Since M is the matrix that diagonalizes the kinetic tensor, this transformation allows us to decouple the previous system of linear equations:

$$i\hbar\frac{\partial}{\partial t}\Phi(\vec{k},t) = D(\vec{k})\Phi(\vec{k},t) + iG(\vec{k},t)\,. \tag{9.11}$$

The solution of the homogenous part is

$$\Phi_H(\vec{k},t) = \Phi_0(\vec{k})\,\exp(-iD(\vec{k})t/\hbar)\,, \tag{9.12}$$

where $\Phi_0(\vec{k})$ is an initial condition for the polariton wave function, and the solution of the inhomogeneous part is:

$$\Phi_I(\vec{k},t) = \Phi_H(\vec{k},t)\int_0^t \frac{G(\vec{k},t')}{\hbar\Phi_H(\vec{k},t')}dt'\,, \tag{9.13}$$

with $\Phi(\vec{k},t) = \Phi_H(\vec{k},t) + \Phi_I(\vec{k},t)$. The solution for $\Psi(\vec{k},t)$ is then:

$$\begin{aligned}\Psi(\vec{k},t) =& M\Phi_H(\vec{k},t) + M\Phi_I(\vec{k},t) = M\Phi_0(\vec{k})\,\exp(-iD(\vec{k})t/\hbar) \\ &+ M\exp(-iD(\vec{k})t/\hbar)\Phi_0(\vec{k})\int_0^t \Phi_0(\vec{k})^{-1}\exp(iD(\vec{k})t'/\hbar)M^{-1}E(\vec{k},t)\,dt'\,.\end{aligned} \tag{9.14}$$

Due to the presence of the dissipative terms, which remain in the diagonal part of $D(\vec{k})$, one can see that the first term vanishes at long times. The second term of the sum simplifies as:

$$\Psi(\vec{k},t) = \int_0^t M\exp(-iD(\vec{k})(t-t')/\hbar)M^{-1}E(\vec{k},t)dt' = \int_0^t U(\vec{k},t-t')\exp(-\gamma t)E(\vec{k},t')dt'\,, \tag{9.15}$$

where $U(\vec{k},t) = e^{-iT(\vec{k})t}$ is the time evolution operator corresponding to the kinetic tensor, which can be shown to be:

$$U(\vec{k},t) = e^{i\omega(\vec{k})t}\begin{pmatrix} \cos(\Delta(\vec{k})\,t) & i\exp(-i2\phi)\sin(\Delta(\vec{k})\,t) \\ i\exp(i2\phi)\sin(\Delta(\vec{k})\,t) & \cos(\Delta(\vec{k})\,t) \end{pmatrix}. \tag{9.16}$$

When the system is pumping only one of the components of the σ^+-σ^- basis, the spinor corresponding to the pump will be $E(\vec{k},t) = f(\vec{k},t)(1\ ,\ 0)^T$. With the aim of demonstrating

the spin-to-orbital angular momentum effect, we will restrict the pump to the following shape: $f(\vec{k},t) = f_0\delta(k-k_p)\delta(t)$. The wave function in $\vec{k}$ can be calculated as:

$$\begin{pmatrix}\Psi_+(\vec{k},t)\\ \Psi_-(\vec{k},t)\end{pmatrix} = f_0\exp((i\omega(\vec{k})-\gamma)t)\delta(k-k_p)\begin{pmatrix}\cos(\Delta(\vec{k})t)\\ i\exp(i2\phi)\sin(\Delta(\vec{k})t)\end{pmatrix}. \tag{9.17}$$

The corresponding wave function in the real space is the inverse Fourier transform.

$$\begin{aligned}\begin{pmatrix}\Psi_+(\vec{r},t)\\ \Psi_-(\vec{r},t)\end{pmatrix} &= f_0\exp((i\omega(\vec{k})-\gamma)t)\int_0^{2\pi}d\phi\int_0^{\infty}kdk\,\delta(k-k_p)\exp(i\vec{k}\cdot\vec{r})\begin{pmatrix}\cos(\Delta(\vec{k})t)\\ i\exp(i2\phi)\sin(\Delta(\vec{k})t)\end{pmatrix}\\ &= f_0\,k_p\exp((i\omega(\vec{k})-\gamma)t)\int_0^{2\pi}d\phi\exp(ik_pr\cos(\theta-\phi))\begin{pmatrix}\cos(\Delta(\vec{k})t)\\ i\exp(i2\phi)\sin(\Delta(\vec{k})t)\end{pmatrix},\end{aligned} \tag{9.18}$$

where we have used that $\vec{k}\cdot\vec{r} = kr\cos(\theta-\phi)$, being θ and ϕ the orientation angles of $\vec{r}$ and $\vec{k}$, respectively. In order to solve the two integrals (one for each component), the following property of Bessel functions will be useful:

$$\mathcal{J}_n(\zeta) = \frac{1}{2\pi}\int_{-\pi}^{\pi}\exp(i(n\tau+\zeta\sin\tau))d\tau\,. \tag{9.19}$$

The final solution is then:

$$\begin{pmatrix}\Psi_+(\vec{r},t)\\ \Psi_-(\vec{r},t)\end{pmatrix} = 2\pi f_0\,k_p\exp((i\omega(\vec{k})-\gamma)t)\begin{pmatrix}\mathcal{J}_0(k_p\,r)\cos(\Delta(\vec{k})t)\\ -i\mathcal{J}_2(k_p\,r)\exp(i2\theta)\sin(\Delta(\vec{k})t)\end{pmatrix}. \tag{9.20}$$

We can see from the previous equation that when we pump one of the components, the wave function of the other component acquires a phase pattern with a winding number 2, which is a doubly-quantized vortex. This phenomenon has been already theoretically predicted in Ref. [Lie07], and experimentally observed in Ref. [Man11], in the case of non-trapped polariton condensates.

It is worth to comment the case where instead of pumping at a given modulus of $\vec{k}$ for all the possible angles in momentum space ϕ, the orientation of $\vec{k}$ is also fixed. In this case, a term $\delta(\phi-\phi_0)$, where ϕ_0 is the orientation direction of the pump wavevector, should be added to the pump. Then, the integral on ϕ when doing the inverse Fourier transform becomes trivial, and the solution is:

$$\begin{pmatrix}\Psi_+(\vec{r},t)\\ \Psi_-(\vec{r},t)\end{pmatrix} = 2\pi f_0\,k_p\exp((i\omega(\vec{k})-\gamma)t)\,\exp(ik_p\,r\cos(\theta-\phi_0))\begin{pmatrix}\cos(\Delta(\vec{k})t)\\ -i\exp(i2\phi_0)\sin(\Delta(\vec{k})t)\end{pmatrix}. \tag{9.21}$$

The previous solution does not content any vortex profile, hence, in order to nucleate a vortex, it is crucial not to fix the wavevector orientation and excite all the possible angles in momentum space. As an example, if we pump with the pump wavevector oriented along the x-direction, the phase pattern of the minority component will be the one of a plane wave travelling in the x-direction.

9.3.2 Interacting polaritons in a ring-shaped quantum well

We have seen that it is possible to generate a vortex state with winding number 2 in the σ^- component by pumping the σ^+ component, when the wave vector of the pump has a given modulus in a radial direction. In the case of a ring-shaped quantum well (inset of Fig. 9.3), vortex states translate into persistent currents. However, since in this case there is no analytical solution, one has to solve numerically the driven-dissipative Gross-Pitaevskii equation (9.5). In order to do this, we have used the following potential to describe the ring-shaped quantum well (in polar coordinates):

$$V(\rho) = V_0 \left(1 - \frac{\sinh(w/\xi)}{\cosh(w/\xi) + \cosh((\rho - R_0)/\xi)}\right) . \tag{9.22}$$

This potential corresponds to a ring with radius R_0, width w and depth V_0. The width of the edge of the ring is given by the parameter ξ, which we fix to be $w/10$.

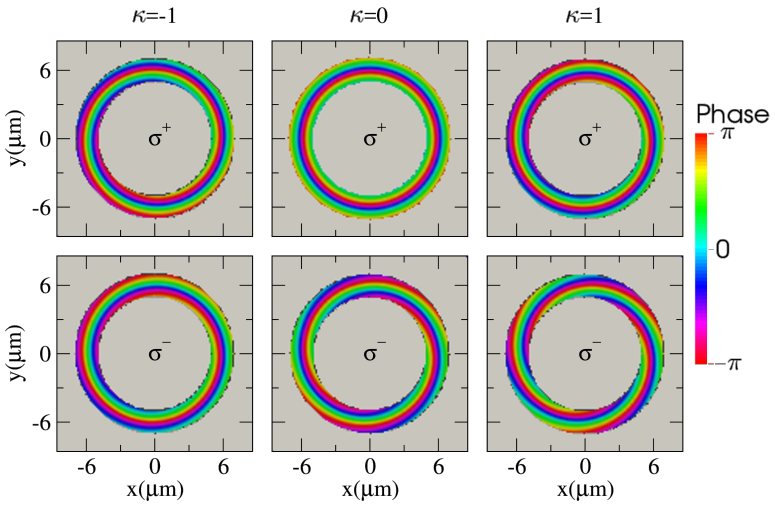

Figure 9.4: Phase profile of the σ^+ (top row) and the σ^- (bottom row) components, in the steady state for different values of the winding number associated to the Laguerre-Gauss beam of the pump. In the left panels, κ=−1, in the middle panels κ=0 and in the right panels κ=1. The winding number of the persistent current nucleated in the σ^- component is 2 units larger than that of the pump.

Regarding the pump scheme, and in order to control the angular momentum carried by the pump, we use a Laguerre-Gauss beam, pumping polaritons with σ^+ polarization, directly within the ring, with a radial wave vector $k_p = 5.2\mu$m (see Fig. 9.3) and imprinting a winding number κ:

$$E_+^{\text{field}}(\rho, \theta) = E_0\, e^{-\frac{(\rho - R_0)^2}{2w^2}} e^{ik_p\rho} e^{i\kappa\theta} . \tag{9.23}$$

We have numerically solved the two-dimensional driven-dissipative Gross-Pitaevskii equation to obtain the steady state of the system. In Fig. 9.4 we plot the phase profile of the polariton wave function of the σ^+ (top row) and the σ^- (bottom row) component inside the ring (i.e. for $|\rho - R_0| < w$, where there is an appreciable density well above zero). We represent the case

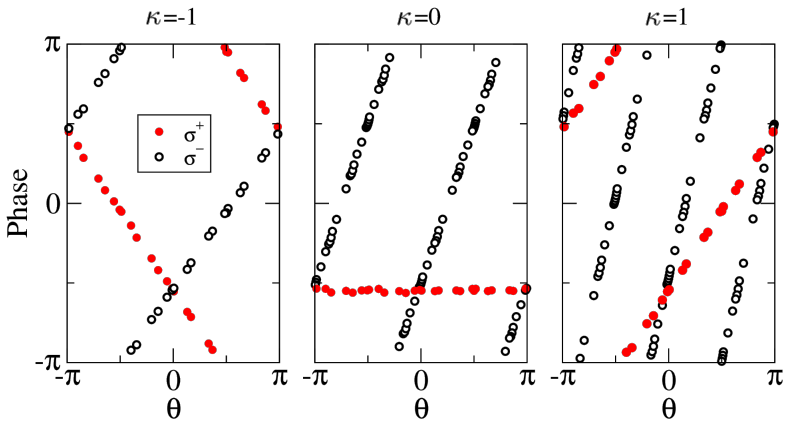

Figure 9.5: Plot of the phase of the σ^+ (red filled circles) and σ^- (black open circles) components as a function of the angle θ along the ring at $\rho = R_0$, for a Laguerre-Gauss pump with orbital angular momentum with winding number κ=−1 (left panel), κ=0 (middle panel) and κ=1 (right panel).

where the winding number of the angular momentum carried by the pump is κ=−1 in the left column, κ=0 in the middle column, and κ=1 in the right column. As expected, in the stationary state, the component co-polarized with the pump exhibits a persistent current with a winding number matching the pump. Interestingly, we find that the cross-polarized component exhibits a persistent current with winding number 1, 2 and 3 for the left, middle and right column, respectively. This is a two units increase with respect to the winding number of the pump, as in the homogeneous system. This property can be also seen in Fig. 9.5, where we show the phase $\phi\,(\rho = R_0, \theta)$ of the σ^+ polarized wave function (red filled circles) and of the σ^- wave function (black open circles) in the steady state. The winding number of the pump is κ=−1 (left panel), κ=0 (middle panel) and κ=1 (right panel). We see that the phase of the σ^- component winds by 2π, 4π and 6π, respectively, i.e. the winding number of the persistent current in the σ^- component is $\kappa = 1, 2$ and 3, as expected from Fig. 9.4.

9.4 Many-body localization under the presence of disorder

In the previous section, we have shown that when we excite the σ^+ polariton component into a mode carrying zero angular momentum in a smooth ring-shaped trap, the σ^- component acquires a persistent current with winding number 2. In this section we account for the fact that in realistic experiments, a disordered potential $V_{\rm dis}(\vec{r})$ experienced by polaritons is present within the ring. In order to generate a single realization of the disordered potential, we propose the following expression:

$$V_{\rm dis}(\vec{r}) = \mathrm{Re}\left[\mathcal{F}^{-1}[2\pi^2 l_c U_0 \exp(i\varphi_{\vec{k}}) \exp(-k^2 l_c^2/4)](\vec{r})\right] , \tag{9.24}$$

where U_0 is the strength of the disorder, l_c is the correlation length, which gives the order of magnitude of the distance between maxima and minima of the disorder potential, and $\varphi_{\vec{k}}$ is a

random matrix with phases uniformly distributed between 0 and 2π. We investigate the interplay of disorder and interactions on the polariton current along the ring.

In the simulations, we have fixed the polariton-polariton interaction to be 10 times larger in the co-polarized case than in the cross-polarized, i.e. $g = g_{++} = g_{--} = 10\, g_{+-}$. We use the pump to excite the σ^+ component with a Laguerre-Gauss beam with κ=0 orbital angular momentum. To monitor the persistent current induced in the σ^- component, we compute the expectation value of the angular momentum operator around the z-axis $I = \langle \hat{L}_z \rangle$, normalized to its maximum value. In the top panel of Fig. 9.6, we show the angular momentum computed from the average of ten dynamical simulations performed with different realizations of the disordered potential, as a function of the interaction strength g and the disorder strength U_0. We can see from the figure that there is a broad boundary (green region) in the (g, U_0) plane, with a positive slope, that separates two regions, and defines a critical disorder strength that increases for increasing interaction strength. Below this critical disorder (red region), the polariton current persists in spite of the disorder, as the latter is efficiently screened by the interactions. On the contrary, in the blue region above the critical disorder, the polariton current is suppressed as disorder overcomes the interaction [Dei10]. For each point of the top panel, we have computed the standard deviation σ_I of the different values of I obtained for each set of realizations of the disorder. The result is represented in the middle panel of Fig. 9.6. We see that when a persistent current exists, I does not fluctuate much from one realization to the next. Whereas in the regime where the disorder and the interactions compete equally, the actual value of I achieved is highly dependent on the details of $V_{\rm dis}(\vec{r})$.

The simulations show also that in the noninteracting regime, density hot spots build up as a result of Anderson localization [And58, Mod10], and the current along the ring is thus substantially reduced. An example of this regime is shown in the bottom panel of Fig. 9.6 where the density profile at $\rho = R_0$ is shown for $g = 0$ and $U_0 = 5$ meV (dot-dashed blue line). Then, upon increasing the interactions to $g = 0.6$ meVμm^2, the flow is restored and the polariton density becomes much more homogeneous within the ring (solid black line). This flow can be suppressed again by increasing the disorder amplitude to $U_0 = 8$ meV. In this case, the polariton density exhibits another hot spot (red dashed line).

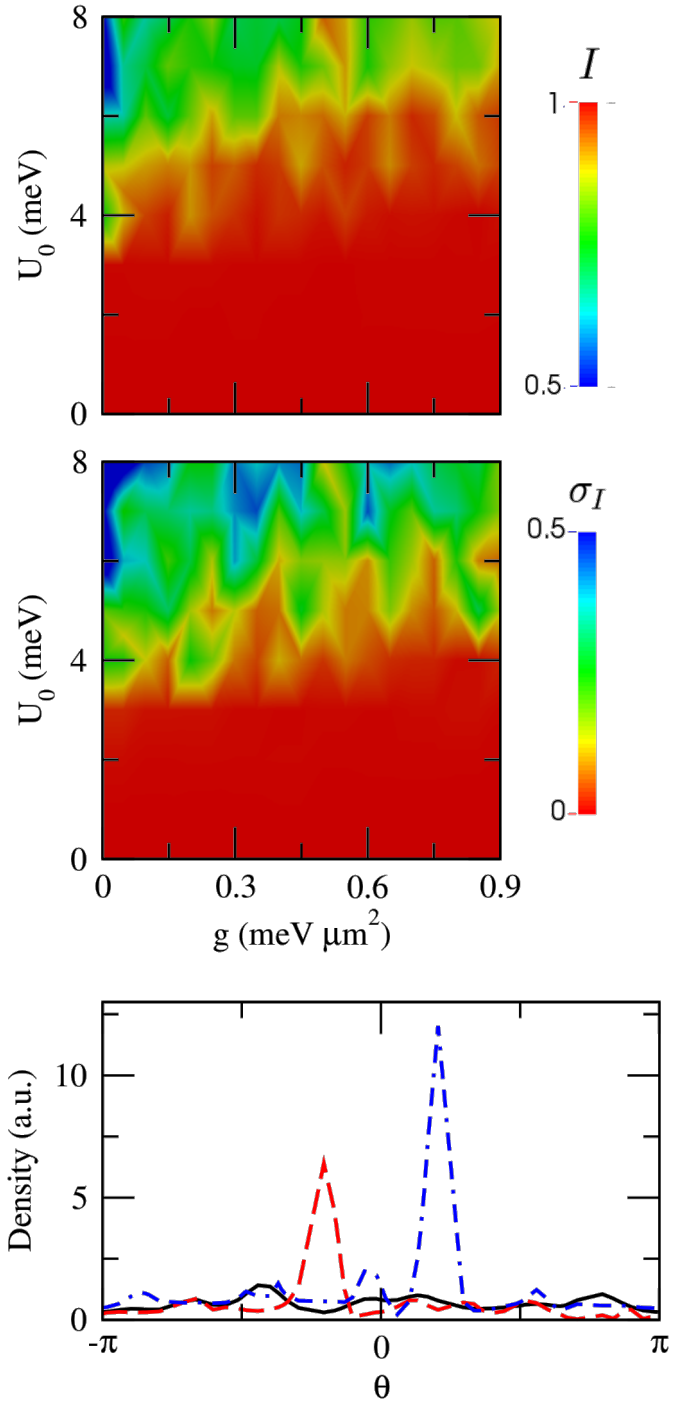

Figure 9.6: Top panel: magnitude of angular momentum I as a function of the interaction g and the disorder strength U_0. The value represented in the color map is the result of the average of ten dynamical simulations of the driven-dissipative Gross-Pitaevskii equation. Middle panel: standard deviation of σ_I in the numerical calculations. The bottom panel represents the density profile (in arbitrary units) along the ring at $\rho = R_0$ for different values of the interaction constant g and disorder strength U_0: $g = 0.6$ meVμm^2 and $U_0 = 5$ meV (solid black line), $g = 0$ meVμm^2 and $U_0 = 5$ meV (dot-dashed blue line) and $g = 0.6$ meVμm^2 and $U_0 = 8$ meV (dashed red line).

Chapter 10

Summary, conclusions and future perspectives

In this thesis we have numerically studied different aspects of the physics of Bose gases in multiply-connected geometries. In particular, we have investigated the appearance of topological states, such as vortices and solitary waves, for single-component and two-component systems. We have developed our calculations both in the strongly correlated regime, by solving the Bose-Hubbard model, and in the mean-field framework, by looking for solutions of the Gross-Pitaevskii equation. We have analyzed the case of atomic and polaritonic condensates, which differ in their lifetime, since atoms are stable for times much larger than the characteristic time scale of the system, whereas for polaritons, they survive for times of the order of the characteristic time scale of the system. Therefore, the latter allows us to study the physics of out-of-equilibrium condensates.

In the first part of this thesis, from Chapter 1 to 4 we have presented the different theoretical frameworks we have worked with. In the second part, from Chapter 5 to 9 we present and discuss the results we have obtained.

Chapter 1 has introduced the context in which the physics described in this thesis has been developed. This chapter also provides an outline of the thesis.

In Chapter 2, we have derived the Bose-Hubbard model, developed in order to theoretically analyze the physics of ultracold atoms in optical lattices in the strongly correlated regime. We have reviewed the first quantum phase transition of this model that was experimentally proben: the superfluid-to-Mott insulator transition. We have proposed extended versions of the Bose-Hubbard model, like the introduction in the hamiltonian of dipolar interactions. We provide also some physical magnitudes that can be extracted from this model that we will use along the thesis in order to analyze the main physics of our systems.

Chapter 3 summarizes the mean-field framework, and, in particular, we introduce the Gross-Pitaevskii equation for single-component condensates. We give an overview of the ground state properties in the regime of low and strong contact interactions (Thomas-Fermi approximation).

We introduce the Bogoliubov spectrum and the main topological states that have been reported in the literature, and some experimental techniques that have been used in order to nucleate them.

In Chapter 4, we have reviewed the case of two coupled components. We have analyzed the phase diagram in terms of the miscibility when there is no spin-flip, and polarizability when spin-flip is possible, and we have also obtained the Bogoliubov spectrum in the two-component case. We have derived the single-component hamiltonian in the case of spin-orbit coupling, and analyze the phase diagram in the absence and in the presence of interaction.

Chapter 5 is devoted to the study of the ground state properties of Bose gases loaded on few-site lattices. The main results obtained along this chapter are the following ones:

1. In the double-well case, we have seen that the hamiltonian of the system can be mapped onto the Lipkin-Meshkov-Glick hamiltonian, a spin model. We have performed finite-size scaling by using the population imbalance or the Schmidt gap, and we have observed that the critical exponents of the quantum phase transition that appears in the double-well hamiltonian has the same critical exponents than that of the Lipkin-Meshkov-Glick hamiltonian. Therefore, both transitions fall in the same universality class.

2. We have used the number of particles in the double well as the analog of the length in the spin model. We have also proposed an expression for the correlation function that provides a correlation length that behaves in a proper way far and close to the critical point.

3. In the case of dipolar atoms loaded on a triple well, we have seen that, as a function of the orientation of the dipoles, the phase diagram is very reach and displays several phases with different nature, among them, cat-like states. We have also seen that, in the case of large number of particles, the atomic limit is recovered.

4. Some quantum phase transitions of the triple well have been analyzed by performing finite-size scaling on the Schmidt gap, and we have observed that they display the same critical exponents that the double-well case, falling in the same universality class.

Although in the triple-well case, there are some transitions that possess the same critical exponents than the transition of the Lipkin-Meshkov-Glick hamiltonian, it is still unknown if it is possible to perform a mapping between both hamiltonians. Moreover, it is reasonable to think that it should be possible to propose an expression for the correlation function in the triple-well case, which is a future perspective of the present thesis. In addition, an extension to larger number of modes would provide more conclusions about the properties of quantum phase transitions in larger systems in different dimensions. Such analysis can give information about the role of on-site excited states in the value of the critical exponents of their corresponding transitions, as discussed in Ref. [Gar12].

In Chapter 6 we have studied the physics of ring-shaped Bose gases with a weak link both in the strongly correlated and the mean-field regime. The main results obtained in this section are:

1. In a Bose-Hubbard chain, when the sign of the tunnelling rate between two sites flips (which is experimentally feasible by manipulating the phase of the gas), the noninteracting ground state is a macroscopic superposition of a semifluxon and an antisemifluxon.

2. When the interaction is nonzero but small, the superposition of current flows is more robust against the fluctuation of the different parameters of the Bose-Hubbard hamiltonian. However, if the number of sites in the chain is too high, the excited states get closer to the semifluxon and the antisemifluxon states, and the mentioned superposition loses robustness.

3. In the mean-field approximation, winding number states are linked by solitonic states, such as dark solitons in 1D, and also solitonic vortices in 3D, that live in a swallow tail loop. However, in the presence of a potential barrier, solitonic vortices can not appear, and only dark solitons are possible.

4. The swallow tail loop generates an energy barrier that must be overcome in order to produce a phase slip between two winding number states. When the potential barrier rotates, phase slip events between two winding number states occur through dark solitons.

5. When realizing a protocol consisting in rotating the barrier in one direction to generate a phase slip and then rotate it in the other direction to recover the initial state, the rotation frequency at which this process occurs, appears at different values. It yields to a hysteresis cycle in the process.

6. A dark soliton in the torus in the 3D case decays into a solitonic vortex, emitting phonons in the process. Nevertheless, in the presence of the external barrier, a solitonic vortex decays into a dark soliton.

In the strongly correlated regime, it would be interesting to analyze the robustness of the macroscopic superposition in the thermodynamic limit, i.e. when $N \to \infty$, and compare the results with the mean-field case. In the continuous system, although we have recovered the hysteresis cycle measured in Ref. [Eck14], the results do not match quantitatively. It is still unknown if the main reason of the discrepancy between our results and those of the experiment is due to thermal excitations or quantum fluctuations [Fre97]. An alternative derivation in the strongly correlated regime of the hysteresis cycle is given in Ref. [Rou15]. A similar mean-field analysis of the hysteresis cycle can be found in Ref. [Zha16].

In Chapter 7, we investigate the physics of a coherently-coupled two-component Bose-Einstein condensate in a toroidal trap. We have studied the dynamical evolution of the system when persistent currents with different winding numbers are imprinted onto each component. The main results that have been obtained in this chapter are:

1. We have calculated the dynamical phase diagram as a function of the Rabi coupling and the chemical potential. We have identified three different regimes. At large values of the Rabi frequency compared to the chemical potential, the system exhibits oscillations in the mean angular momentum imbalance, by virtue of a transfer of vortices between both components. This effect is analogous to the Coherent Quantum Phase Slip [Ast12], which

has been recently observed in superconductors, by experimentally realizing the proposal of Mooij and Harmans, known as the Mooij-Harmans qubit [Moo05]. Therefore, we propose our system is an atomic analog of the Mooij-Harmans qubit.

2. We have developed an analytical model that describes the wave function in the Coherent Quantum Phase Slip regime, inspired by the two-mode approximation. We have observed an excellent agreement between the numerical results and the analytical model.

3. The system is analogous to two condensates trapped in two externally coupled toroidal potentials [Agh13].

4. We have shown that these system effectively behaves as a qubit, and a good control on the Rabi coupling is analogous to a quantum gate that operates on the qubit.

5. We have characterized the other two phases of the dynamical phase diagram: Non-Coherent Quantum Phase Slip regime and Trapping regime. We have seen that in the former phase, solitonic vortices take place in the system, and the appearance of such vortices is a clear signature of loss of coherence in the process of vortex transfer.

When analyzing the oscillation of the mean angular momentum imbalance as a function of time, it is possible to identify a clear transition that separates two regions. In one of them, the evolution follows the Jacobi elliptic function $\mathrm{dn}(t)$, whereas in the other region, the solution is the Jacobi elliptic function $\mathrm{cn}(t)$. These are also solutions of the Josephson problem [Rag99]. The possibility of mapping the problem onto the Josephson equations is still an open line of research.

Chapter 8 is devoted to the study of a particular solution of the two-component Gross-Pitaevskii equation in the presence of coherent coupling: Josephson vortices. We have analyzed the dynamical evolution of these states under the presence of spin-orbit coupling. The following points summarize the main results discussed in the chapter:

1. We have seen that Josephson vortices are states characterized by a noncomplete depletion per component at a certain point, where the relative phase suffers a sudden change of 2π. At the vicinity of the depletion, there is a nonzero current, due to the variation of the phase around this point. In the absence of spin-orbit coupling, both dark solitons and Josephson vortices are solutions of the Gross-Pitaevskii equation, but Josephson vortices needs a minimum value of the interaction energy to appear, and they have less energy than dark solitons in the range of coexistence.

2. In the presence of spin-orbit coupling, dark solitons disappear as solutions of the Gross-Pitaevskii equation since they do not follow the symmetry of the equation. In contrast, Josephson vortices do follow such symmetry, and thus they still appear as solutions of the Gross-Pitaevskii equation, although their expression is not analytical.

3. As dark solitons, Josephson vortices also decay through the snake instability in multidimensional systems. In pancake-shaped condensates, the product of the decay is a vortex dipole.

4. The subsequent evolution of the vortex dipole strongly depends on the orientation of the solitonic plane of the initial Josephson vortex, with respect to the orientation of the Rashba-Dresselhaus spin-orbit coupling. This evolution can be understood in terms of a precession of the velocity field of the condensate according to the spin-orbit coupling, which is analogous to a magnetic field.

In this chapter, we have only considered the case of pancake-shaped condensates. As a future work, it would be interesting to analyze the stability of Josephson vortices as a function of the aspect ratio of the harmonic confinement, and, in particular, the possibility of having as a result a solitonic vortex, since the velocity field that this state generates is much different than that of the vortex dipole. One can thus expect that the subsequent evolution would drastically change with respect to the case presented here.

In Chapter 9, we have addressed the fundamental physics concerning polariton condensates. We have studied a polariton condensate with spin-orbit coupling (due to TE-TM splitting) nucleated in a ring-shaped quantum well. The main results that can be extracted from this chapter of the thesis are:

1. When pumping one of circularly polarized components of the polariton condensate with a Laguerre-Gauss beam carrying no angular momentum, the cross-polarized component appears in the system but carrying a persistent current with winding number 2. This feature has been derived analytically in a homogeneous quantum well, and numerically in the ring-shaped quantum well.

2. For generic values of the winding number associated to the pump, the minor component of the polariton condensate nucleates a persistent current carrying an angular momentum with an associated winding number 2 units larger than that of the pump.

3. Under the presence of disorder, the persistent current in the minor component can be destroyed. However, the increase of the polariton-polariton interaction preserves such current. This effect can be understood in terms of many-body localization [And58, Bas06, Bas07]. These features have been analyzed in a dynamical phase diagram computed as a function of the interaction and the disorder strength.

This setup has been a proposal to be experimentally realized in the laboratories of the Néel Institute, in Grenoble. One of the perspectives of this work is first to develop a way to probe superfluidity in polariton condensates, and second, to design a possible experimental setup that can provide a more precise measure of the polariton-polariton interaction strength.

List of publications

Role of anisotropy in dipolar bosons in triple-well potentials
A. Gallemí, M. Guilleumas, R. Mayol and A. Sanpera
Phys. Rev. A **88**, 063645 (2013)

Propagation of collective modes in non-overlapping dipolar Bose-Einstein condensates
A. Gallemí, M. Guilleumas, R. Mayol and M. Pi
J. Phys.: Conf. Series **497**, 1 (2014)

Persistent currents supported by solitary waves in toroidal Bose-Einstein condensates
A. Muñoz Mateo, A. Gallemí, M. Guilleumas and R. Mayol
Phys. Rev. A **91**, 063625 (2015)

Fragmented condensation in Bose-Hubbard trimers with tunable tunnelling
A. Gallemí, M. Guilleumas, J. Martorell, R. Mayol, A. Polls and B. Juliá-Díaz
New J. Phys. **17**, 073014 (2015)

Coherent Quantum Phase Slip in two-component bosonic atomtronic circuits
A. Gallemí, A. Muñoz Mateo, R. Mayol and M. Guilleumas
New J. Phys. **18**, 015003 (2016)

Multidimensional Josephson vortices in spin-orbit coupled Bose-Einstein condensates: snake instability and decay through vortex dipoles
A. Gallemí, M. Guilleumas, R. Mayol and A. Muñoz Mateo
Phys. Rev. A **93**, 033618 (2016)

Robustness of discrete semifluxons in closed Bose–Hubbard chains
A. Gallemí, M. Guilleumas, J. Martorell, R. Mayol, A. Polls and B. Juliá-Díaz
New J. Phys. **18**, 075005 (2016)

Quantum spin models with mesoscopic Bose-Einstein condensates
A. Gallemí, G. Queraltó, M. Guilleumas, R. Mayol and A. Sanpera
Phys. Rev. A **94**, 063626 (2016)

Interaction-enhanced flow of a polariton persistent current in a ring
A. Gallemí, M. Guilleumas, M. Richard and A. Minguzzi
Work in progress

Bibliography

[Aba10] M. Abad, M. Guilleumas, R. Mayol, M. Pi and D. M. Jezek. Phys. Rev. A **81**, 043619 (2010).

[Aba13] M. Abad and A. Recati. Eur. Phys. J. D **67**, 148 (2013).

[Aba14] M. Abad, A. Sartori, S. Finazzi and A. Recati. Phys. Rev. A **89**, 053602 (2014).

[Aba15] M. Abad, M. Guilleumas, R. Mayol, F. Piazza, D. M. Jezek and A. Smerzi. Europhys. Lett. **109**, 40005 (2015).

[Aba16] M. Abad. Phys. Rev. A **93**, 033603 (2016).

[Ach13] V. Achilleos, J. Stockhofe, P. G. Kevrekidis, D. J. Frantzeskakis and P. Schmelcher. Europhys. Lett. **103**, 20002 (2013).

[Agh13] D. Aghamalyan, L. Amico and L.-C. Kwek. Phys. Rev. A **88**, 063627 (2013).

[Agh15] D. Aghamalyan, M. Cominotti, M. Rizzi, D. Rossini, F. Hekking, A. Minguzzi, L.-C. Kwek and L. Amico. New J. Phys. **17**, 045023 (2015).

[Aik12] K. Aikawa, A. Frisch, M. Mark, S. Baier, A. Rietzler, R. Grimm and F. Ferlaino. Phys. Rev. Lett. **108**, 210401 (2012).

[Alb05] M. Albiez, R. Gati, J. Fölling, S. Hunsmann, M. Cristiani and M. K. Oberthaler. Phys. Rev. Lett. **95**, 010402 (2005).

[Ami05] L. Amico, A. Osterloh and F. Cataliotti. Phys. Rev. Lett. **95**, 063201 (2005).

[Ami14] L. Amico, D. Aghamalyan, F. Auksztol, H. Crepaz, R. Dumke and L.-C. Kwek. Scientific Reports **4**, 4298 (2014).

[Amo09] A. Amo, J. Lefrère, S. Pigeon, C. Adrados, C. Ciuti, I. Carusotto, R. Houdré, E. Giacobino and A. Bramati. Nat. Phys. **5**, 805 (2009).

[And58] P. W. Anderson. Phys. Rev. **109**, 1492 (1958).

[And66] P. W. Anderson. Rev. Mod. Phys. **38**, 298 (1966).

[And95] M. H. Anderson, J. R. Ensher, M. R. Matthews, C. E. Wieman and E. A. Cornell. Science **269**, 198 (1995).

[Ant15] C. Antón, S. Morina, T. Gao, P. S. Eldridge, T. C. H. Liew, M. D. Martín, Z. Hatzopoulos, P. G. Savvidis, I. A. Shelykh and L. Viña. Phys. Rev. B **91**, 075305 (2015).

[Aru08] K. Y. Arutyunov, D. S. Golubev and A. D. Zaikin. Physics Reports **464**, 1 (2008).

[Arw14] G. Arwas, A. Vardi and D. Cohen. Phys. Rev. A **89**, 013601 (2014).

[Arw17] G. Arwas and D. Cohen. Phys. Rev. B **95**, 054505 (2017).

[Ash76] N. W. Ashcroft and N. D. Mermin. *Solid State Physics*, (Harcout: Orlando1976).

[Ast12] O. V. Astafiev, L. B. Ioffe, S. Kafanov, Y. A. Pashkin, K. Y. Arutyunov, D. Shahar, O. Cohen and J. S. Tsai. Nature **484**, 355 (2012).

[Bah13] S. Baharian and G. Baym. Phys. Rev. A **87**, 013619 (2013).

[Bar82] A. Barone and G. Paterno. *Physics and Applications of the Josephson Effect*, (Wiley and Sons Inc.1982).

[Bar03] I. V. Barashenkov, S. R. Woodford and E. V. Zemlyanaya. Phys. Rev. Lett. **90**, 054103 (2003).

[Bar07] I. V. Barashenkov, S. R. Woodford and E. V. Zemlyanaya. Phys. Rev. E **75**, 026604 (2007).

[Bas06] D. M. Basko, I. L. Aleiner and B. L. Altshuler. Ann. Phys. **321**, 1126 (2006).

[Bas07] D. M. Basko, I. L. Aleiner and B. L. Altshuler. Phys. Rev. B **76**, 052203 (2007).

[Bea13] S. Beattie, S. Moulder, R. J. Fletcher and Z. Hadzibabic. Phys. Rev. Lett. **110**, 025301 (2013).

[Bec08] C. Becker, S. Stellmer, P. Soltan-Panahi, S. Dörscher, M. Baumert, E.-M. Richter, J. Kronjäger, K. Bongs and K. Sengstock. Nat. Phys. **4**, 496 (2008).

[Ber11] D. Bercioux. *Spin-orbit interactions in semiconductor nanostructures* (2011).

[Bil13] T. P. Billam, A. L. Marchant, S. L. Cornish, S. A. Gardiner and N. G. Parker. *Progress in Optical Science and Photonics*, chapter Spontaneous Symmetry Breaking, Self-Trapping, and Josephson Oscillations, 403 (2013).

[Bjo74] J. E. Bjorkholm and A. A. Ashkin. Phys. Rev. Lett. **32**, 129 (1974).

[Blo73] F. Bloch. Phys. Rev. A **7**, 2187 (1973).

[Blo08] I. Bloch, J. Dalibard and W. Zwerger. Rev. Mod. Phys. **80**, 885 (2008).

[Boa12] O. Boada, A. Celi, J. I. Latorre and M. Lewenstein. Phys. Rev. Lett. **108**, 133001 (2012).

[Bot83] R. Botet and R. Jullien. Phys. Rev. B **28**, 3955 (1983).

[Bra01] J. Brand and W. P. Reinhardt. J. Phys. B: At. Mol. Opt. Phys. **34**, 4 (2001).

[Buo12] P. Buonsante, R. Burioni, E. Vescovi and A. Vezzani. Phys. Rev. A **85**, 043625 (2012).

[Bur99] S. Burger, K. Bongs, S. Dettmer, W. Ertmer, K. Sengstock, A. Sanpera, G. V. Shlyapnikov and M. Lewenstein. Phys. Rev. Lett. **83**, 5198 (1999).

[Bur02] S. Burger, L. D. Carr, P. Öhberg, K. Sengstock and A. Sanpera. Phys. Rev. A **65**, 043611 (2002).

[Byc84] Y. A. Bychkov and E. I. Rashba. Journal of Physics C: Solid State Physics **17**, 6039 (1984).

[Cal17] L. Calderaro, A. L. Fetter, P. Massignan and P. Wittek. Phys. Rev. A **95**, 023605 (2017).

[Cao15] S. Cao, C.-J. Shan, D.-W. Zhang, X. Qin and J. Xu. J. Opt. Soc. Am. B **32**, 201 (2015).

[Car13] I. Carusotto and C. Ciuti. Rev. Mod. Phys. **85**, 299 (2013).

[Chi00] M. L. Chiofalo, S. Succi and M. P. Tosi. Phys. Rev. E **62**, 7438 (2000).

[Com14] M. Cominotti, D. Rossini, M. Rizzi, F. Hekking and A. Minguzzi. Phys. Rev. Lett. **113**, 025301 (2014).

[Cor96] E. Cornell. J. Res. Natl. Inst. Stand. Technol. **101**, 419 (1996).

[Dal99] F. Dalfovo, S. Giorgini, L. Pitaevskii and S. Stringari. Rev. Mod. Phys. **71**, 463 (1999).

[Dav95] K. B. Davis, M.-O. Mewes, M. R. Andrews, N. J. van Druten, D. S. Durfee, D. M. Kurn and W. Ketterle. Phys. Rev. Lett. **75**, 3969 (1995).

[DeC12] G. DeChiara, L. Lepori, M. Lewenstein and A. Sanpera. Phys. Rev. Lett. **109**, 237208 (2012).

[Dei10] B. Deissler, M. Zaccanti, G. Roati, C. D'Errico, M. Fattori, M. Modugno, G. Modugno and M. Inguscio. Nat. Phys. **6**, 354 (2010).

[Del13] L. Dell'Anna, G. Mazzarella, V. Penna and L. Salasnich. Phys. Rev. A **87**, 053620 (2013).

[Dem06] S. O. Demokritov, V. E. Demidov, O. Dzyapko, G. A. Melkov, A. A. Serga, B. Hillebrands and A. N. Slavin. Nature **443**, 430 (2006).

[Den00] J. Denschlag, J. E. Simsariana, D. L. Feder, C. W. Clark, L. A. Collins, J. Cubizolles, L. Deng, E. W. Hagley, K. Helmerson, W. P. Reinhardt, S. L. Schneider and W. D. Phillips. Science **287**, 97 (2000).

[Dob99] L. Dobrek, M. Gajda, M. Lewenstein, K. Sengstock, G. Birkl and W. Ertmer. Phys. Rev. A **60**, 3381(R) (1999).

[Don91] R. J. Donnelly. *Quantized vortices in Helium II*, (Cambridge University Press1991).

[Don14] S. Donadello, S. Serafini, M. Tylutki, L. P. Pitaevskii, F. Dalfovo, G. Lamporesi and G. Ferrari. Phys. Rev. Lett. **113**, 065302 (2014).

[Dre55] G. Dresselhaus. Phys. Rev. **100**, 580 (1955).

[Dub12] R. Dubessy, T. Liennard, P. Pedri and H. Perrin. Phys. Rev. A **86**, 011602(R) (2012).

[Duf15] S. Dufferwiel, F. Li, E. Cancellieri, L. Giriunas, A. A. P. Trichet, D. M. Whittaker, P. M. Walker, F. Fras, E. Clarke, J. M. Smith, M. S. Skolnick and D. N. Krizhanovskii. Phys. Rev. Lett. **115**, 246401 (2015).

[Dum98] R. Dum, J. I. Cirac, M. Lewenstein and P. Zoller. Phys. Rev. Lett. **80**, 2972 (1998).

[Dus04] S. Dusuel and J. Vidal. Phys. Rev. Lett. **93**, 237204 (2004).

[Eck05] A. Eckardt, C. Weiss and M. Holthaus. Phys. Rev. Lett. **95**, 260404 (2005).

[Eck14] S. Eckel, J. G. Lee, F. Jendrzejewski, N. Murray, C. W. Clark, C. J. Lobb, W. D. Phillips, M. Edwards and G. K. Campbell. Nature **506**, 200 (2014).

[Eic14] C. Eichler, Y. Salathe, J. Mlynek, S. Schmidt and A. Wallraff. Phys. Rev. Lett. **113**, 110502 (2014).

[Emp87] P. Emplit, J. Hamaide, F. Reynaud, C. Froehly and A. Barthelemy. Opt. Commun. **62**, 374 (1987).

[Fet01] A. L. Fetter and A. A. Svidzinsky. J. Phys.: Condens. Matter **13**, R135 (2001).

[Fet09] A. L. Fetter. Rev. Mod. Phys. **81**, 647 (2009).

[Fet15] A. L. Fetter. J. Low Temp. Phys. **180**, 37 (2015).

[Fia12] O. Fialko, M.-C. Delattre, J. Brand and A. R. Kolovsky. Phys. Rev. Lett. **108**, 250402 (2012).

[Fis72] M. E. Fisher and M. N. Barber. Phys. Rev. Lett. **28**, 1516 (1972).

[Fis89] M. P. A. Fisher, P. B. Weichman, G. Grinstein and D. S. Fisher. Phys. Rev. B **40**, 546 (1989).

[Fra10] D. J. Frantzeskakis. J. Phys. A: Math. Theor. **43**, 213001 (2010).

[Fre94] J. K. Freericks and H. Monien. Europhys. Lett. **26**, 545 (1994).

[Fre97] J. A. Freire, D. P. Arovas and H. Levine. Phys. Rev. Lett. **79**, 5054 (1997).

[Fre10] D. V. Freilich, D. M. Bianchi, A. M. Kaufman, T. K. Langin and D. S. Hall. Science **329**, 1182 (2010).

[Gal13a] V. Galitski and I. B. Spielman. Nature **494**, 49 (2013).

[Gal13b] A. Gallemí, M. Guilleumas, R. Mayol and A. Sanpera. Phys. Rev. A **88**, 063645 (2013).

[Gal15] A. Gallemí, M. Guilleumas, J. Martorell, R. Mayol, A. Polls and B. Juliá-Díaz. New J. Phys. **17**, 073014 (2015).

[Gal16a] A. Gallemí, M. Guilleumas, J. Martorell, R. Mayol, A. Polls and B. Juliá-Díaz. New J. Phys. **18**, 075005 (2016).

[Gal16b] A. Gallemí, M. Guilleumas, R. Mayol and A. M. n. Mateo. Phys. Rev. A **93**, 033618 (2016).

[Gal16c] A. Gallemí, A. Muñoz Mateo, R. Mayol and M. Guilleumas. New J. Phys. **18**, 015003 (2016).

[Gal16d] A. Gallemí, G. Queraltó, M. Guilleumas, R. Mayol and A. Sanpera. Phys. Rev. A **94**, 063626 (2016).

[Gli65] A. J. Glick, H. J. Lipkin and N. Meshkov. Nucl. Phys. **62**, 211 (1965).

[Gol02] E. Goldobin, D. Koelle and R. Kleiner. Phys. Rev. B **66**, 100508(R) (2002).

[Gar02] J. J. García-Ripoll, V. M. Pérez-García and F. Sols. Phys. Rev. A **66**, 021602(R) (2002).

[Gar12] M. A. García-March, D. R. Dounas-Frazer and L. D. Carr. Frontiers of Physics **7**, 131 (2012).

[Gre02] M. Greiner, O. Mandel, T. Esslinger, T. W. Hänsch and I. Bloch. Nature **415**, 39 (2002).

[Gre13] D. Greif, T. Uehlinger, G. Jotzu, L. Tarruell and T. Esslinger. Science **340**, 1307 (2013).

[Hal06] D. W. Hallwood, J. Burnett and J. Dunningham. New J. Phys. **8**, 180 (2006).

[Hal10] P. L. Halkyard, M. P. A. Jones and S. A. Gardiner. Phys. Rev. A **81**, 061602(R) (2010).

[Hal11] D. W. Hallwood and J. Brand. Phys. Rev. A **84**, 043620 (2011).

[Ho96] T.-L. Ho and V. B. Shenoy. Phys. Rev. Lett. **77**, 3276 (1996).

[Ho11] T.-L. Ho and S. Zhang. Phys. Rev. Lett. **107**, 150403 (2011).

[Hos05] E. Hoskinson, Y. Sato, I. Hahn and R. E. Packard. Nat. Phys. **2**, 23 (2005).

[Hua03] G. Huang, V. A. Makarov and M. G. Velarde. Phys. Rev. A **67**, 023604 (2003).

[Hua16] L. Huang, Z. Meng, P. Wang, P. Peng, S.-L. Zhang, L. Chen, D. Li, Q. Zhou and J. Zhang. Nat. Phys. **12**, 540 (2016).

[Hub63] J. Hubbard. Proc. R. Soc. A **276**, 238 (1963).

[Jac11] A. D. Jackson, J. Smyrnakis, M. Magiropoulos and G. M. Kavoulakis. Europhys. Lett. **95**, 30002 (2011).

[Jak64] R. C. Jaklevic, J. Lambe, A. H. Silver and J. E. Mercereau. Phys. Rev. Lett. **12**, 159 (1964).

[Jak65] R. C. Jaklevic, J. Lambe, J. E. Mercereau and A. H. Silver. Phys. Rev. **140**, A1628 (1965).

[Jak98] D. Jaksch, C. Bruder, J. I. Cirac, C. W. Gardiner and P. Zoller. Phys. Rev Lett. **81**, 3108 (1998).

[Jak03] D. Jaksch and P. Zoller. New J. Phys. **5**, 56 (2003).

[Jon82] C. A. Jones and P. H. Roberts. J. Phys. A: Math. Gen. **15**, 2599 (1982).

[Jul10] B. Juliá-Díaz, D. Dagnino, M. Lewenstein, J. Martorell and A. Polls. Phys. Rev. A **81**, 023615 (2010).

[Kam12] E. Kammann, T. C. H. Liew, H. Ohadi, P. Cilibrizzi, P. Tsotsis, Z. Hatzopoulos, P. G. Savvidis, A. V. Kavokin and P. G. Lagoudakis. Phys. Rev. Lett. **109**, 036404 (2012).

[Kan09] R. Kanamoto, L. D. Carr and M. Ueda. Phys. Rev. A **79**, 063616 (2009).

[Kas06] J. Kasprzak, M. Richard, S. Kundermann, A. Baas, P. Jeambrun, J. M. J. Keeling, F. M. Marchetti, M. H. Szymanska, R. André, J. L. Staehli, V. Savona, P. B. Littlewood, B. Deveaud and L. S. Dang. Nature **443**, 409 (2006).

[Kau05] V. M. Kaurov and A. B. Kuklov. Phys. Rev. A **71**, 011601(R) (2005).

[Kau06] V. M. Kaurov and A. B. Kuklov. Phys. Rev. A **73**, 013627 (2006).

[Kav04] K. V. Kavokin, I. A. Shelykh, A. V. Kavokin, G. Malpuech and P. Bigenwald. Phys. Rev. Lett. **92**, 017401 (2004).

[Kav05] A. V. Kavokin, G. Malpuech and M. Glazov. Phys. Rev. Lett. **95**, 136601 (2005).

[Kha00] A. V. Khaetskii and Y. V. Nazarov. Phys. Rev. B **61**, 12639 (2000).

[Kin04] T. Kinoshita, T. Wenger and D. S. Weiss. Science **305**, 1125 (2004).

[Kla10] J. Klaers, J. Schmitt, F. Vewinger and M. Weitz. Nature **468**, 545 (2010).

[Kol06] A. R. Kolovsky. New J. Phys. **8**, 197 (2006).

[Ku14] M. J. Ku, W. Ji, B. Mukherjee, E. Guardado-Sanchez, L. W. Cheuk, T. Yefsah and M. W. Zwierlein. Phys. Rev. Lett. **113**, 065301 (2014).

[Ku16] M. J. Ku, B. Mukherjee, T. Yefsah and M. W. Zwierlein. Phys. Rev. Lett. **116**, 045304 (2016).

[Kuz88] E. A. Kuznetsov and S. K. Turitsyn. Sov. Phys. JEPT **67**, 1583 (1988).

[Kuz95] E. A. Kuznetsov and J. J. Rasmussen. Phys. Rev. E **51**, 4479 (1995).

[Lag08] K. G. Lagoudakis, M. Wouters, M. Richard, A. Baas, I. Carusotto, R. André, L. S. Dang and B. Deveaud-Plédran. Nat. Phys. **4**, 706 (2008).

[Lah09] T. Lahaye, C. Menotti, L. Santos, M. Lewenstein and T. Pfau. Rep. Prog. Phys. **72**, 126401 (2009).

[Lah10] T. Lahaye, T. Pfau and L. Santos. Phys. Rev. Lett. **104**, 170404 (2010).

[Lan67] J. S. Langer and V. Ambegaokar. Phys. Rev. **164**, 498 (1967).

[Lee06] C. Lee, T. J. Alexander and Y. S. Kivshar. Phys. Rev. Lett. **97**, 180408 (2006).

[Leg99] A. J. Leggett. AIP Conf. Proc. **477**, 154 (1999).

[Lep13] L. Lepori, G. DeChiara and A. Sanpera. Phys. Rev. B **87**, 235107 (2013).

[Lev07] S. Levy, E. Lahoud, I. Shomroni and J. Steinhauer. Nature **449**, 579 (2007).

[Lew07] M. Lewenstein, A. Sanpera, V. Ahufinger, B. Damski, A. D. Sen and U. Sen. Adv. Phys. **56**, 243 (2007).

[Lew12] M. Lewenstein, A. Sanpera and V. Ahufinger. *Ultracold Atoms in Optical Lattices. Simulating Quantum Many-Body Systems*, (Oxford University Press2012).

[Ley07] C. Leyder, M. Romanelli, J. P. Karr, E. Giacobino, T. C. H. Liew, M. M. Glazov, A. V. Kavokin, G. Malpuech and A. Bramati. Nat. Phys. **3**, 628 (2007).

[Li08a] H. Li and F. D. M. Haldane. Phys. Rev. Lett. **101**, 010504 (2008).

[Li08b] W. Li, M. Haque and S. Komineas. Phys. Rev. A **77**, 053610 (2008).

[Li12] Y. Li, L. P. Pitaevskii and S. Stringari. Phys. Rev. Lett. **108**, 225301 (2012).

[Li15] Y. Li, G. I. Martone and S. Stringari. *Annual Review of Cold Atoms and Molecules*, chapter SPIN-ORBIT-COUPLED BOSE-EINSTEIN CONDENSATES, 201 (2015).

[Lia11] R. Liao and J. Brand. Phys. Rev. A **83**, 041604(R) (2011).

[Lie07] T. C. H. Liew, A. V. Kavokin and I. A. Shelykh. Phys. Rev. B **75**, 241301 (2007).

[Lin11] Y.-J. Lin, K. Jiménez-García and I. B. Spielman. Nature **471**, 83 (2011).

[Lip65] H. J. Lipkin, N. Meshkov and A. J. Glick. Nucl. Phys. **62**, 188 (1965).

[Lu11] M. Lu, N. Q. Burdick, S. H. Youn and B. L. Lev. Phys. Rev. Lett. **107**, 190401 (2011).

[Mai93] M. Z. Maialle, E. A. de Andrada e Silva and L. J. Sham. Phys. Rev. B **47**, 15776 (1993).

[Man11] F. Manni, K. G. Lagoudakis, T. K. Paraïso, R. Cerna, Y. Léger, T. C. H. Liew, I. A. Shelykh, A. V. Kavokin, F. Morier-Genoud and B. Deveaud-Plédran. Phys. Rev. B **83**, 241307(R) (2011).

[Mat99] M. R. Matthews, B. P. Anderson, P. C. Haljan, D. S. Hall, C. E. Wieman and E. A. Cornell. Phys. Rev. Lett. **83**, 2498 (1999).

[Maz13] G. Mazzarella and L. Dell'Anna. Eur. Phys. J. Special Topics **217**, 197 (2013).

[McC70] D. E. McCumber and B. I. Halperin. Phys. Rev. B **1**, 1054 (1970).

[Mes65] N. Meshkov, A. J. Glick and H. J. Lipkin. Nucl. Phys. **62**, 199 (1965).

[Mid11] S. Middelkamp, P. J. Torres, P. G. Kevrekidis, D. J. Frantzeskakis, R. Carretero-González, P. Schmelcher, D. V. Freilich and D. S. Hall. Phys. Rev. A **84**, 011605(R) (2011).

[Mod10] G. Modugno. Rep. Prog. Phys. **73**, 102401 (2010).

[Moo05] J. E. Mooij and C. J. P. M. Harmans. New J. Phys. **7**, 219 (2005).

[Moo06] J. E. Mooij and Y. V. Nazarov. Nat. Phys. **2**, 169 (2006).

[Mot99] B. Mottelson. Phys. Rev. Lett. **83**, 2695 (1999).

[Mou12] S. Moulder, S. Beattie, R. P. Smith, N. Tammuz and Z. Hadzibabic. Phys. Rev. A **86**, 013629 (2012).

[Mue02] E. J. Mueller. Phys. Rev. A **66**, 063603 (2002).

[Mue06] E. J. Mueller, T. L. Ho, M. Ueda and G. Baym. Phys. Rev. A **74**, 033612 (2006).

[Mun07] A. Muñoz Mateo and V. Delgado. Phys. Rev. A **75**, 063610 (2007).

[Mun14] A. Muñoz Mateo and J. Brand. Phys. Rev. Lett. **113**, 255302 (2014).

[Mun15] A. Muñoz Mateo, A. Gallemí, M. Guilleumas and R. Mayol. Phys. Rev. A **91**, 063625 (2015).

[Mus10] G. Mussardo. *Statistical Field Theory. An Introduction to Exactly Solved Models in Statistical Physics*, (Oxford University Press2010).

[Nav13] R. Navarro, R. Carretero-González, P. J. Torres, P. G. Kevrekidis, D. J. Frantzeskakis, M. W. Ray, E. Altuntas and D. S. Hall. Phys. Rev. Lett. **110**, 225301 (2013).

[Nee10] T. W. Neely, E. C. Samson, A. S. Bradley, M. J. Davis and B. P. Anderson. Phys. Rev. Lett. **104**, 160401 (2010).

[Oru08] R. Orús, S. Dusuel and J. Vidal. Phys. Rev. Lett. **101**, 025701 (2008).

[Pan99] G. Panzarini, L. C. Andreani, A. Armitage, D. Baxter, M. S. Skolnick, V. N. Astratov, J. S. Roberts, A. V. Kavokin, M. R. Vladimirova and M. A. Kaliteevski. Phys. Rev. B **59**, 5082 (1999).

[Par03] G. S. Paraoanu. Phys. Rev. A **67**, 023607 (2003).

[Par04] B. Paredes, A. Widera, V. Murg, O. Mandel, S. Fölling, J. I. Cirac, G. V. Shlyapnikov, T. W. Hänsch and I. Bloch. Nature **429**, 277 (2004).

[Per97] S. V. Pereverzev, S. V. Loshak, S. Backhaus, S. Davis and R. E. Packard. Nature **388**, 449 (1997).

[Pet12] D. Peter, K. Pawlowski, T. Pfau and K. Rzazewski. Jour. Phys. B: At. Mol. Opt. Phys. **45**, 225302 (2012).

[Pia09] F. Piazza, L. A. Collins and A. Smerzi. Phys. Rev. A **80**, 021601(R) (2009).

[Pia13] F. Piazza, L. A. Collins and A. Smerzi. J. Phys. B: At. Mol. Opt. Phys. **46**, 095302 (2013).

[Pit03] P. Pitaevskii and S. Stringari. *Bose-Einstein Condensation*, (Oxford University Press2003).

[Pol15] J. Polo, P. Mason, S. Sridhar, T. P. Billam, V. Ahufinger and S. A. Gardiner. Phys. Rev. A **91**, 053626 (2015).

[Qad12] M. I. Qadir, H. Susanto and P. C. Matthews. J. Phys. B: At. Mol. Opt. Phys. **45**, 035004 (2012).

[Qad16] M. I. Qadir and U. Tahir. Can. J. Phys. **0**, 0599 (2016).

[Rad11] J. Radic, T. A. Sedrakyan, I. B. Spielman and V. Galitski. Phys. Rev. A **84**, 063624 (2011).

[Rag99] S. Raghavan, A. Smerzi, S. Fantoni and S. R. Shenoy. Phys. Rev. A **59**, 620 (1999).

[Ram11] A. Ramanathan, K. C. Wright, S. R. Muniz, M. Zelan, W. T. Hill, C. J. Lobb, K. Helmerson, W. D. Phillips and G. K. Campbell. Phys. Rev. Lett. **106**, 130401 (2011).

[Ras60] E. I. Rashba. Sov. Phys. Solid. State **2**, 1109 (1960).

[Rep64] J. D. Reppy and D. Depatie. Phys. Rev. Lett. **12**, 187 (1964).

[Res05] J. Reslen, L. Quiroga and N. F. Johnson. Europhys. Lett. **69**, 8 (2005).

[Rib02] F. Riboli and M. Modugno. Phys. Rev. A **65**, 063614 (2002).

[Rod15] D. Roditchev, C. Brun, L. Serrier-Garcia, J. C. Cuevas, V. H. L. Bessa, M. V. Milosevic, F. Debontridder, V. Stolyarov and T. Cren. Nat. Phys. **11**, 332 (2015).

[Rou15] A. Roussou, G. D. Tsibidis, J. Smyrnakis, M. Magiropoulos, N. K. Efremidis, A. D. Jackson and G. M. Kavoulakis. Phys. Rev. A **91**, 023613 (2015).

[Ryu07] C. Ryu, M. F. Andersen, P. Cladé, V. Natarajan, K. Helmerson and W. D. Phillips. Phys. Rev. Lett **99**, 260401 (2007).

[Sac99] S. Sachdev. *Quantum Phase Transitions*, (Cambridge University Press1999).

[San10] D. Sanvitto, F. M. Marchetti, M. H. Szymanska, G. Tosi, M. Baudisch, F. P. Laussy, D. N. Krizhanovskii, M. S. Skolnick, L. Marrucci, A. Lemaître, J. Bloch, C. Tejedor and L. Viña. Nat. Phys. **6**, 527 (2010).

[Sch11] C. Schenke, A. Minguzzi and F. Hekking. Phys. Rev. A **84**, 053636 (2011).

[Sco11] R. G. Scott, F. Dalfovo, L. P. Pitaevskii and S. Stringari. Phys. Rev. Lett. **106**, 185301 (2011).

[Sea07] B. T. Seaman, M. Krämer, D. Z. Anderson and M. J. Holland. Phys. Rev. A **75**, 023615 (2007).

[She06] I. A. Shelykh, Y. G. Rubo, G. Malpuech, D. D. Solnyshkov and A. Kavokin. Phys. Rev. Lett. **97**, 066402 (2006).

[Sim01] R. W. Simmonds, A. Marchenkov, E. Hoskinson, J. C. David and R. E. Packard. Nature **412**, 55 (2001).

[Sme97] A. Smerzi, S. Fantoni, S. Giovanazzi and S. R. Shenoy. Phys. Rev. Lett. **79**, 4950 (1997).

[Smy14] J. Smyrnakis, M. Magiropoulos, N. K. Efremidis and G. M. Kavoulakis. J. Phys. B: At. Mol. Opt. Phys. **47**, 215302 (2014).

[Sol94] F. Sols and J. Ferrer. Phys. Rev. B **49**, 15913 (1994).

[Son02] D. T. Son and M. A. Stephanov. Phys. Rev. A **65**, 063621 (2002).

[Sta08] T. D. Stanescu, B. Anderson and V. Galitski. Phys. Rev. A **78**, 023616 (2008).

[Su13] S.-W. Su, S.-C. Gou, A. Bradley, O. Fialko and J. Brand. Phys. Rev. Lett. **110**, 215302 (2013).

[Su15] S.-W. Su, S.-C. Gou, I.-K. Liu, A. Bradley, O. Fialko and J. Brand. Phys. Rev. A **91**, 023631 (2015).

[Szi14] G. Szirmai, G. Mazzarella and L. Salasnich. Phys. Rev. A **90**, 013607 (2014).

[Tor11] P. J. Torres, P. G. Kevrekidis, D. J. Frantzeskakis, R. Carretero-González, P. Schmelcher and D. S. Hall. Phys. Lett. A **375**, 3044 (2011).

[Tsu71] T. Tsuzuki. J. Low Temp. Phys. **4**, 441 (1971).

[Tyl16] M. Tylutki, L. P. Pitaevskii, A. Recati and S. Stringari. Phys. Rev. A **93**, 043623 (2016).

[Var15] E. Varoquaux. Rev. Mod. Phys. **87**, 803 (2015).

[vdW00] C. H. van der Wal, A. C. J. ter Haar, F. K. Wilhelm, R. N. Schouten, C. J. P. M. Harmans, T. P. Orlando, S. Lloyd and J. E. Mooij. Science **290**, 773 (2000).

[Wal08] R. Walser, E. Goldobin, O. Crasser, D. Koelle, R. Kleiner and W. P. Schleich. New J. Phys. **10**, 045020 (2008).

[Wil99a] J. E. Williams. *The Preparation of Topological Modes in a Strongly-Coupled Two-Component Bose-Einstein Condensate*. Ph.D. thesis, University of Colorado (1999).

[Wil99b] J. E. Williams and M. J. Holland. Nature **401**, 568 (1999).

[Wil99c] J. E. Williams, R. Walser, J. Cooper, E. A. Cornell and M. J. Holland. Phys. Rev. A **59**, R31(R) (1999).

[Woo12] S. J. Woo and Y.-W. Son. Phys. Rev. A **86**, 011604(R) (2012).

[Wou10] M. Wouters and I. Carusotto. Phys. Rev. Lett. **105**, 020602 (2010).

[Wri13] K. C. Wright, R. B. Blakestad, C. J. Lobb, W. D. Phillips and G. K. Campbell. Phys. Rev Lett. **110**, 025302 (2013).

[Wu15] Z. Wu, E. Zaremba, J. Smyrnakis, M. Magiropoulos, N. K. Efremidis and G. M. Kavoulakis. Phys. Rev. A **92**, 033630 (2015).

[Yak15] A. I. Yakimenko, K. O. Isaieva, S. I. Vilchinskii and E. A. Ostrovskaya. Phys. Rev. A **91**, 023607 (2015).

[Zha12] H. Zhai. Int. J. Mod. Phys. B **26**, 1230001 (2012).

[Zha15] H. Zhai. Rep. Prog. Phys. **78**, 026001 (2015).

[Zha16] X. Zhang, F. Piazza, W. Li and A. Smerzi. Phys. Rev. A **94**, 063601 (2016).

[Zin08] P. Ziń, J. Chwedeńczuk, B. Oleś, K. Sacha and M. Trippenbach. Europhys. Lett. **83**, 64007 (2008).